THE UNIVERSITY *of* EDINBURGH

Synthesis and High-Pressure Structural Studies of Bismuth Nanoparticles

Wanaruk Chaimayo

A thesis submitted in fulfilment of the requirements
for the degree of Doctor of Philosophy
to the
University of Edinburgh
August 2012

Abstract

Nanomaterials (NMs) are materials in which the size of at least one dimension is less than 100 nm. Examples include quantum dots, nanoparticles, "Buckminsterfullerene (C_{60})", carbon nanotubes, graphene and TiO_2 thin films. Many research groups have investigated the properties of NMs, and they have reported that some of them are clearly different to those of the bulk materials, and depend on the size of the NMs. Examples include melting temperatures, phase transition pressures, fluorescence spectra, catalytic properties and magnetic properties.

Recently, a high-pressure study of Te nano-cylinders revealed compressibility effects that are different to those observed in bulk-Te. Although this study reported an elevation of phase transition pressure compared to the bulk, the authors did not investigate the structures of the high-pressure phases, and it is unclear whether the incommensurate phase found at high pressures in bulk-Te was observed or not.

Indeed, it is completely unknown whether the incommensurate phases observed in a number of elements at high pressure also exist in nanoparticle samples of the same materials. The search for, and study of, such phases forms the subject of this thesis.

Initial studies of commercial selenium nanoparticles (nano-Se) revealed that the incommensurate phase of bulk selenium (Se-IV) is also found in nano-Se. The transition pressures in nano-Se are slightly higher than those of bulk-Se. However, the nano-Se samples were subsequently found not to have the sizes, shapes, and properties claimed by the vendor, which was confirmed by transmission and scanning electron microscopy. Further commercial samples of nano-Se and nano-Bi were also found to be of extremely poor quality. It was clear, therefore, that a detailed study of incommensurate phases in NMs would require us to make our own samples.

Bismuth nanoparticles (nano-Bi) with dimensions 51(6), 52(15), 92(13), 128(45), and 138(27) nm have been successfully synthesised by the author in collaboration with the Hybrid Nano Collöds group at the University of St. Andrews. On compression, the nano-Bi samples were found to have the same order of phases Bi-I, Bi-II, Bi-III, and Bi-V and phase transitions as found in bulk-Bi, but were found to exhibit larger phase coexistence. The phase transition pressures on pressure increase were higher than those of the bulk materials, and the smaller the diameter of nano-Bi, the higher the phase-transition pressure. This behaviour is similar to, but more extreme than, that found in CdSe nanoparticles.

The incommensurate Bi-III structure has been found in nano-Bi under increases in pressure. However, the diffraction patterns from Bi-III contain additional unaccounted-for peaks, and this phase is referred to as complex Bi-III. The Debye-Scherrer rings from complex Bi-III are smooth, and do not exhibit the spottiness observed in the diffraction patterns of Bi-III obtained from bulk-Bi. This enables full Rietveld refinement of Bi-III in the nano-samples. Complex Bi-III exists from 3 GPa up to 30 GPa, compared to the stable range of only 2.7 to 7.7 GPa of Bi-III in the bulk material. While such a large range of pressure enables the structure of nano-Bi-III to be studied over a much wider pressure range than bulk-Bi-III, such studies were hampered by the existence of the unaccounted-for peaks.

In order to get clean, single-phase patterns of Bi-III, samples of this phase were first prepared on pressure decrease from the higher-pressure Bi-V phase, before recompressing them. Single-phase samples of Bi-III were obtained and were found to be stable up to 14-18 GPa. However, because of phase coexistence, diffraction peaks from Bi-III were still visible at pressures as high as $\sim$30 GPa, which is $\sim$3 times larger than the upper limit pressure of existence of bulk-Bi-III. On pressure re-increase, nano-Bi-III has a higher bulk modulus than bulk-Bi-III. The bulk modulus was found to be size-dependent as it is higher when size decreases. Moreover, nano-Bi has a smaller value of the incommensurate wave vector, which is almost pressure independent, but is found to be particles size dependent. The incommensurate wave vector thus becomes another of the structural and physical properties of nanomaterials that is found to be sample-size dependent.

Declaration

I hereby declare that this thesis is my own original work and that it has not been submitted for any other degree. Unless otherwise stated, the research undertaken in this thesis was the unaided work of the author. Where other sources of information have been used, they have been acknowledged. Where the work was done in collaboration with others, a significant contribution was made by the author.

W. Chaimayo
August 2012

Acknowledgements

I would like to express my deepest thanks and respect to my supervisor Prof. Malcolm McMahon for his guidance, assistance and encouragement throughout my PhD and for introducing me to the field of high-pressure diffraction. Words cannot express my gratitude for his kind supervision, teaching, mind-opening discussion and moral support during the tough period of conducting the research and writing my thesis.

I also would like to express my appreciation to Dr John Loveday, my second supervisor, for his encouragement, cheer and support over the past four years.

I would like to thank all the members of the McMahon group: Dr Miriam Marques, for her late-night-working companionship, her chorizo, blanket and radiator; Dr Graham Stinton, for his support, thesis correction, valuable discussion, and sense of humour; Dr Lars Lundegaard, for his crystallographic expertise and considerable help in completing the x-ray diffraction studies; and Jenny Jeppsson, who introduced me to the PhD life when I first arrived in Edinburgh.

I am also grateful to Dr Olga Narygina and Dr John Proctor with whom the major x-ray diffraction experiments of this thesis were done, Emma McBride for her help and companionship in the wee small hours during experiments conducted at the Diamond Synchrotron and European Synchrotron Radiation Facility, and Rachel Husband who always created lively moments during the coffee times.

I am thankful to the professors and lecturers at the Department of Physics and Astronomy: Dr Ingo Loa, for our many worthy discussions; Dr Olga Degtyareva, for her strong support in thesis writing, her productivity tactics and her expertise in bismuth materials; and Dr Eugene Gregoryanz for his questions and suggestions during my first, second and third year panel reviews.

My gratitude also goes for Prof. Wilson Poon who put me on the right track when some critical research issues occurred, enabling me to complete my thesis.

I would like to express my heartfelt gratitude to Dr Pascal André who opened the nano-chemistry world to a physicist like me. I have learnt a large amount of chemistry from him, his guidance has been invaluable to this research, and his door has always been open for an unannounced discussion on any topic. Without him I could not have come this far.

I am thankful to Assist. Prof. Dr Thiti Bovornratanaraks, who introduced me to an academic life and to the field of high-pressure research, encouraged and supported me remotely from Thailand.

I am grateful to Salinee Khachonpisitsak and Uthaipat Piamphongsant for their great hospitality and accommodation during my quest for bismuth nanoparticles at St Andrews.

I would like to acknowledge the help and support I have received from my current office mates: Dr Graham Stinton for all-round questions; Ross Howie, for always answering my English grammar problems; Thomas Scheler, for being a role model of a hard working PhD student; Craig, for bringing in so many biscuits; and Donna Morton for keeping the office atmosphere lively and joyful.

Moreover, I am grateful to the former members of the CSEC: Dr Miriam Marques, Dr Anna Kusmartseva, Dr Petra Szilagyi, Dr Artur Bocian and Dr Gaétan Girait - for our amusing and happy times together.

I am also greatly indebted to the proofreaders of this thesis: Dr Rory Mckenzie, Rossalyn Mckenzie, Dr Shaun Evans, Dr Graham Stinton, Dr Teerasak E-Komon, Dr Thipnatee Sansawatt, Dr Angel Arevalo Lopez, Thomas Scheler, Craig Wilson, Sucheewin Chotchatchawankul, Teera Chantarojsiri, Chadtip Rodtassana, Anyanee Kamkaew, Wasin Sakulkoo, and Chidchanok Thepsoonthorn.

I would like to record my thanks to all those who have helped me in the course of this work. Particularly to the following: the technical staff at the University of Edinburgh, University of St. Andrews, the ESRF, and at the Rutherford-Appleton Laboratory; the administration and service staff at the University of Edinburgh and University of St. Andrews. Thanks to Steve Mitchell who trained me to use a Transmission Electron microscope. More importantly, I am also indebted to Jane Patterson, who made my everyday life during my PhD at the School of Physics and Astronomy run smoothly.

Thank you for the great financial support from School of Physics and Astronomy Studentship and Overseas Research Students Awards Scheme (ORSAS) and the

many extracurricular activities and courses provided by the Scottish Universities Physics Alliance (SUPA).

Thanks to all my Thai friends in Edinburgh for happy times during my study, and particularly to Arm, Pepe, Punim, Cheeze, Lek, Jo, Note, Golf, Ploysuay, for the companionship during this time.

Finally, I wish to express my deep gratitude to my wonderful family, my beloved parents, sisters, and grandmother, for their unfailing encouragement, loving consideration and support throughout; this thesis is dedicated to them. And special thanks to Chutikarn Thaisriwong for inspiration, moral support and her patience with me while I was chasing my dream and being far away from her.

Contents

List of Abbreviations

NM : Nanomaterial

NMs : Nanomaterials

NP : Nanoparticle

NPs : Nanoparticles

HP : High Pressure

XRD : X-Ray Diffraction

PXRD : Powder X-ray Diffraction

SXRD : Single-Crystal X-Ray Diffraction

HP-PXRD : High-Pressure Powder X-Ray Diffraction

SEM : Scanning Electron Microscopy

TEM : Transmission Electron Microscopy

DLS : Dynamic Light Scattering

DAC : Diamond Anvil Cell

CSEC : Centre for Science at Extreme Conditions

FWHM : Full Width at Half Maximum

KB mirror : Kirkpatrick-Baez mirror

Nano-Se : Selenium nanoparticles

Nano-Bi : Bismuth nanoparticles

Lyophilised nano-Se : Lyophilised selenium nanoparticles

HTP-TD : High-Temperature Polyol-Thermal Decomposition

Chapter 1

Introduction

1.1 Materials Science: The Science of Modern Human Life

In our complex modern world, the basic needs of human life are more than just food, shelter, clothing and medicine. Smart phones, personal computers, GPS systems and other forms of electronic consumer goods associated with information technology are also part of everyone's daily lives, at least in the developed world.

The understanding of materials, materials science, is the basis of all of this technology, and it has thus revolutionised society through the discovery of novel and advantageous materials with useful properties. There have been many inventions based on materials science research which have dramatically affected the global citizen, including computer hard drives, solid state drives (SSD), high resolution iPad screens, global positioning systems (GPS), modern batteries, and small powerful magnets.

Materials science is an interdisciplinary research field which links and describes the properties of matter using many branches of science and engineering. The study of materials science ranges from the atomic level, through microstructure, to the macroscopic behaviour of matter, and utilises statistical mechanics, thermodynamics, solid state physics and quantum mechanics.

In order to fully understand materials, their behaviour must be studied as a function of two important thermodynamic variables: pressure and temperature. Changes in either (or both) parameters can cause materials to have different states, volumes, crystal structures and electronic properties, resulting in changes of their

properties, such as the onset of superconductivity or magnetism.

The work described in this thesis focuses on the use of one of these variables, pressure, in the study of the behaviour of nanomaterials.

1.2 Pressure: An Important Thermodynamic Variable for Materials Science Studies

In the study of materials, high pressure is an under-utilised thermodynamic variable, as compared to temperature. This is unfortunate, as at high pressures, the physical properties of materials can be very different to those observed at ambient pressures. For example, oxygen (O_2) is a colourless gas at ambient pressures where it is essential for cellular respiration, while at high pressures it has a number of complex solid forms, some of which are magnetic [Klotz et al., 2010], and above 11 GPa, it adopts a form comprising $(O_2)_4$ structural units [Fujihisa et al., 2006, Lundegaard et al., 2006]. At much higher pressures, near 100 GPa, oxygen becomes a molecular metal [Weck et al., 2002], and is superconducting below 0.6 K [Shimizu et al., 1998]. Such changes cannot be induced by temperature alone, and the application of pressure thus provides access to novel phases with properties that would otherwise be unobtainable.

High-pressure conditions can be generated dynamically, by compressing samples for very short periods of time using laser-irradiation or high-speed projectiles, or statically, by compressing the sample slowly between hard anvils. The work described in this thesis uses only static compression methods, employing the diamond-anvil cell (DAC) technique.

In order to determine and understand the behaviour of novel phases induced by the application of pressure, it is essential to have a measurement technique that is well matched to the experimental methods required to apply the pressures. X-ray diffraction (XRD) is the best method for determining the structural behaviour of substances at the highest pressures, and for understanding structural transformations. In particular, the powder x-ray diffraction (PXRD) method is very well suited to the study of materials in diamond-anvil pressure cells, because many of the phase transitions observed at high pressure are strongly first order, resulting in the disintegration of samples that may have initially been loaded as single crystals. The PXRD method is relatively simple to use and, unlike

single-crystal x-ray diffraction (SXRD) methods, does not require the sample to be oriented into a wide range of different orientations while maintaining its alignment in the x-ray beam. If the pressure cells being used are heavy (which is necessary for multi-megabar pressures), or are located inside a cryostat, such reorientations may not be possible. In addition, the experimental facilities required for PXRD are relatively simple and are found in many scientific institutions, most importantly at synchrotron radiation facilities.

As mentioned above, one of the key research areas in high-pressure research is finding new materials with useful properties, or changing and optimising the properties of existing materials. Changes in physical properties can also be induced by altering the sizes of the individual crystallites of the substance. For example, gold appears gold-coloured in its bulk form, but has a red colour when it has nano-scale-sized particles (13-15 nm) [Pong et al., 2007]. The study of nano-scale behaviour currently lies at the forefront of materials science, fuelled in particular by the discovery of graphene [Novoselov et al., 2004], and promises to provide materials with remarkable new properties. As a result, the field is receiving considerable support from governments, particularly in the USA, UK and other European countries. The size of the individual particles is the critical factor in changing the physical properties, as will be described in the next section.

1.3 Nanomaterials: Recent Trends in Materials Science Research

Nanomaterials (NMs) are materials in which the size of at least one dimension is less than 100 nm [San-Miguel, 2006]. The era of nanomaterials started when Richard P. Feynman, the Nobel Laureate in Physics, gave a talk in 1959 entitled "There's Plenty of Room at the Bottom" [Feynman, 1992]. In this talk, he described the concept of individual atomic manipulation which many years later influenced the idea of nanotechnology. In 1974, Nario Taniguchi from the University of Tokyo was the first to use the term "nanotechnology", by which he meant the creation of production technology with ultra-fine accuracy and a precision of 1 nm [Booker and Boysen, 2005]. In 1985, the discovery of the easily-synthesised C_{60} molecule - buckminster fullerene, or buckyballs - brought nanotechnology to a much wider audience, and gained the Nobel Prize for Chemistry in 1996

[Kroto et al., 1985]. In 2004, the discovery of graphene [Novoselov et al., 2004] - a single layer of graphite comprising carbon atoms arranged in a 2D hexagonal crystal lattice, obtained via a non-complex synthesis method using only adhesive tape and graphite - has resulted in a further world-wide boost to nano-scale research. For their discovery, Andre Geim and Konstantin Novoselov were awarded the Nobel Prize for Physics in 2010 "for groundbreaking experiments regarding the two-dimensional material graphene". This latest discovery has proved particularly exciting for materials science because graphene has many potential applications[1].

The properties of NMs have been investigated by many research groups who have reported that some of them are clearly different from those of the bulk materials, and depend on the dimension of the NMs [San-Miguel, 2006]. For example, both the melting temperature [Goldstein et al., 1992] and phase transition pressures of CdSe [Tolbert and Alivisatos, 1995b], Fe_2O_3 [Clark et al., 2005], and Te [Deng et al., 2008] nanomaterials have been found to depend strongly on particle size. Consequently, size-dependent properties are key features of NMs which scientists around the world are hoping will enable them to tune the desired behaviours of materials by choosing a suitable size of NMs, e.g., particular sizes of InAs, InP, and CdSe nanoparticles emit specific fluorescence spectra which can be used as fluorescent labels in biological systems [Bruchez Jr et al., 1998].

Of direct relevance to the work described in this thesis is that, as noted above, the size of NMs has been found to strongly affect the pressures at which pressure-induced phase transitions occur; by decreasing the size of the nanocrystals, the solid-solid phase transition pressures are found to increase in the majority of nanomaterials, including CdSe [Tolbert and Alivisatos, 1995b], Ge [Wang et al., 2007], ZnO [Jiang et al., 2000b] nanomaterials. However, decreasing the size does not always lead to an increase in transition pressures. In a few materials, including Fe [Jiang et al., 2001a] and CoO [Liu et al., 2007], nanoparticles are found to have lower transition pressures than their bulk solids.

These size-dependent effects can be explained by surface energy and by the fact that the number of surface atoms is a large fraction of the total number of atoms in a nanocrystal. Moreover, the surface atoms mainly contribute to the free energy and the large changes in the thermodynamic properties of nanocrystals [Alivisatos, 1996].

[1]Such as components with the highest intrinsic strength [Lee et al., 2008], single molecule gas detector [Schedin et al., 2007], and ultra capacitors for energy storage [Stoller et al., 2008].

1.4 Research Questions

Over the last nine years, researchers in the School of Physics and Astronomy at The University of Edinburgh have discovered a variety of incommensurate structures in bulk elements such as Te, Se, Bi, and the alkali metals at high pressure [McMahon and Nelmes, 2006]. In this thesis, the work in extending these studies to nano-scale crystallites of selenium and bismuth is described with the aims of:

1. determining whether the incommensurate phases observed in the bulk materials at high pressure also exist in nanomaterials.

2. determining whether the crystal structures and transition pressures in the incommensurate nanomaterials are the same as those in the bulk.

PXRD techniques have been used to determine whether incommensurate structures exist in nanomaterials at high pressure. To investigate any differences in the phase transition pressure, compressibility and structure according to particle size, experiments have been conducted on various sizes of nanoparticles, both purchased from commercial suppliers and synthesised by the author.

The remainder of this thesis is arranged as shown in section 1.5.

1.5 Thesis Outline

- **Chapter 2 Nanomaterials Review**
  This chapter reviews the different types of nanomaterials, and the key factors which lead them to have distinctive properties compared to the bulk. It also reviews size-dependent properties, and previous high-pressure experiments on nanomaterials.

- **Chapter 3 Methodology and Experimental Techniques**
  This chapter outlines the high-pressure techniques used in this thesis; the theory of powder diffraction; the experimental set-up at the synchrotron; the x-ray diffraction methods used to determine incommensurate structures; data collection and data analysis methods. Moreover, the method for the determination of the particle size using dynamic light scattering (DLS),

transmission electron microscopy (TEM), scanning electron microscopy (SEM) and powder x-ray diffraction (PXRD) will be described.

- **Chapter 4 Studies of Commercial Selenium and Commercial Bismuth Nanoparticles**
  This chapter describes high-pressure powder x-ray diffraction (HP-PXRD) results on various types of commercially-available nanoparticles, i.e., selenium nanoparticles, lyophilised selenium nanoparticles, and bismuth nanoparticles.

- **Chapter 5 Bismuth Nanoparticles (Nano-Bi) Synthesis**
  This chapter describes the author's attempts to synthesise bismuth nanoparticles using recipes from the existing literature and then describes the modified synthesis methods developed by the author which lead to nanoparticles being successfully synthesised in the desired sizes and shapes.

- **Chapter 6 High-Pressure X-ray Diffraction Studies on Synthesised Bismuth Nanoparticles**
  This chapter contains four sections. In the first, HP-PXRD experiments are conducted on bulk bismuth to verify the results from the existing literature. In the second section, HP-PXRD results from polydispersed bismuth nanoparticles obtained from the synthesis methods described in Chapter 5 are given. In the third section, the experimental results from different sizes of monodispersed nano-Bi are compared with those from bulk-Bi. In the final section, a detailed study of the Bi-III structure is made using a re-pressurising process. Transition pressures, phase coexistence, size dependent compressibility of Bi-III and the pressure independence but size dependence of the incommensurate wave vector (q-vector) are described in detail.

- **Chapter 7 Conclusions**
  Conclusions from the work described in this thesis are given in this chapter, and possible further experiments and avenues of study are described.

Chapter 2

Nanomaterials Review

2.1 What are Nanomaterials?

Nanomaterials (NMs) are materials in which the size in at least one spatial dimension is less than 100 nm. The sizes can be a particle diameter (for a zero dimension, 0D NM), tube diameter (1D), or thickness of a layer (2D) [Andrievski and Glezer, 2001, Lövestam et al., 2010]. Bulk materials are classed as 3D because of their lack of a nano-scale size in any physical dimension. Consequently, in terms of dimensions, NMs can be classified in three categories, i.e., 0D, 1D and 2D NMs (see Fig. 2.1).

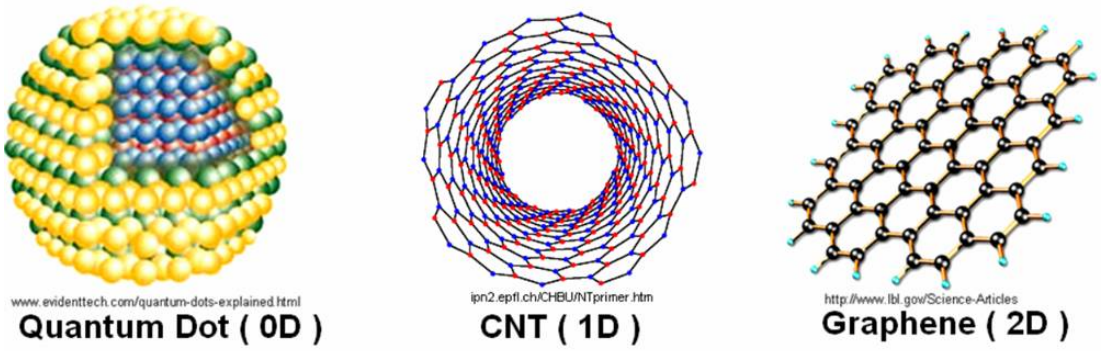

Figure 2.1: The three different kinds of NMs, e.g. quantum dot, carbon nanotube (CNT), graphene, which are categorised by the number of dimensions which have a nano-scale size.

2.1.1 Classification of Nanomaterials

- 0D NMs are materials in which all the dimension lengths are below 100 nm, as, for example, in a quantum dot, nanoparticle (NP), or "Buckyball" (or "Buckminsterfullerene" (C_{60})).
- 1D NMs are materials in which the lengths in two physical dimensions are below 100 nm, such as a carbon nanotube.
- 2D NMs are materials in which only one dimension length is below 100 nm, such as graphene, or TiO_2 thin films (with thickness below 100 nm).

NMs can be obtained by many methods, such as the membrane template method [Martin, 1994], mechanical attrition [Koch, 1993], the sol-gel process [Sanchez et al., 2000], chemical vapour deposition [Brumlik et al., 1994], or the flame or arc-discharge method [Li et al., 2001]. Each kind of NM is specifically produced using a certain method; for example, TiO_2 nanolayers are commonly produced using chemical vapour deposition (CVD) [Chen and Derking, 1993].

2.2 Why do Nanomaterials Behave Differently Compared to Their Bulk Counterparts?

NMs have been investigated by many research groups who have reported that some of their properties are clearly different to those of bulk materials, and depend on the size of the NMs [San-Miguel, 2006]. For example, both the melting temperature [Goldstein et al., 1992] and phase transition pressures [Tolbert and Alivisatos, 1995b, Jacobs et al., 2001, Clark et al., 2005, Deng et al., 2008] depend strongly on the particle size of the NMs. There are some theoretical models available to explain these phenomena which are:

1. The lengths of each dimension of NMs are comparable with the other critical lengths of the materials; for example, the mean free path of electrons and the coherence length of electrons in matter [San-Miguel, 2006].
2. The number of surface atoms is a large fraction of the total volume of atoms in the NM [Alivisatos, 1996, Roduner, 2006] (as seen in Fig. 2.2). This

aspect is the main factor in changes in free energy and thermodynamic properties compared to the bulk materials.

3. Electronic confinement by the nano-scale size of NMs causes the density of states (DoS) of the electrons to be discrete, while that of bulk materials is continuous [Alivisatos, 1996, Krahne et al., 2011]. This is illustrated in Fig. 2.3. From the discretisation in the DoS of electrons in NMs, electron-related properties, such as optical [Taneja et al., 2002] and electrochemical properties [Chirea et al., 2009], are different to those found in the extended bulk material. These are quantum confinement effects.

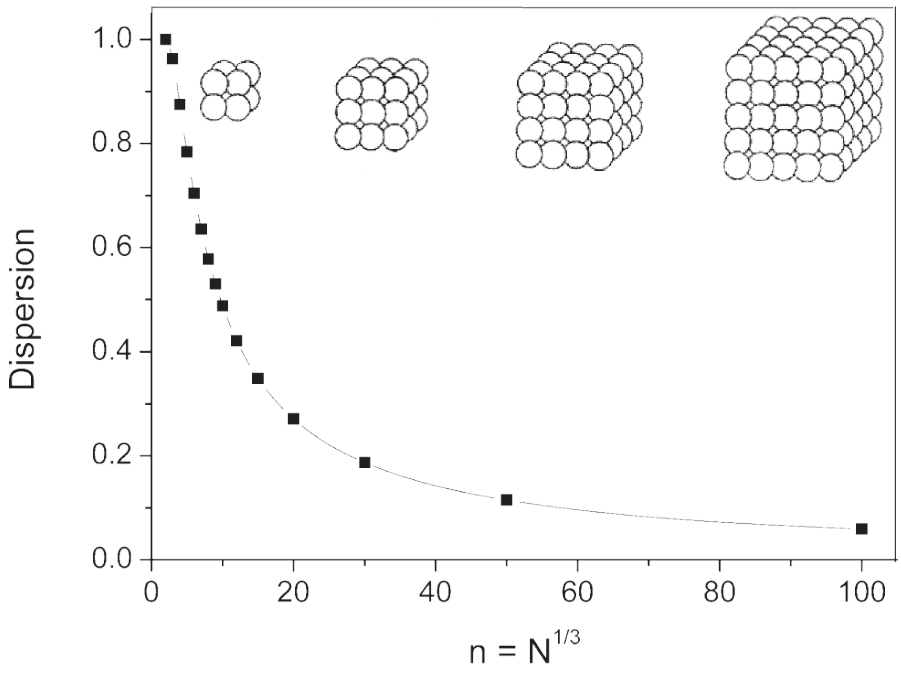

Figure 2.2: Progression of the dispersion (F) when $0<n<100$, F scales with surface area divided by volume in a cube as a function of n; n is number of atoms along an edge of the cube. And $N=n^3$, see more in [Roduner, 2006].

2.3 Size Dependent Properties of Nanomaterials

Size-dependent properties are the key features of NMs which scientists around the world hope will enable them to tune the desired properties of materials by

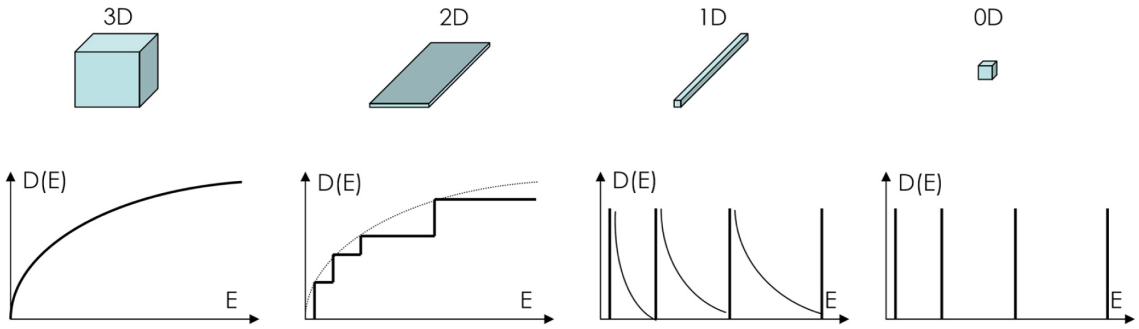

Figure 2.3: The density of states of electrons in (from left to right) bulk (3D), 2D NMs, 1D NMs and 0D NMs [Krahne et al., 2011].

choosing suitably-sized NMs. The size-dependent effects of many physical and chemical properties of NMs have been investigated, for instance:

Physical Properties: magnetic moment [Khanna and Linderoth, 1991], melting point [Nanda, 2009] and phase transition pressure [Tolbert and Alivisatos, 1994, Tolbert and Alivisatos, 1995a], etc.

Chemical Properties: catalytic ability [Valden et al., 1998], chemical reactivity [Rao et al., 1992], etc.

Some of the interesting size-dependent properties of NMs are further described in the following sections.

2.3.1 Catalytic Properties of Nanomaterials

Au is a noble metal in bulk form, but when the Au cluster size decreases to the nanoscale, Au nanocrystals, supported on a titania surface, show a catalytic ability in CO oxidation reactions [Valden et al., 1998]. This is illustrated in Fig. 2.4, demonstrating the effect of the size of the Au particles on the catalytic activity - that is, CO atoms/total Au atoms. An Au cluster diameter, or Au nanocrystal size, of about 3.5 nm shows the best performance (the highest activity) as a catalyst with titania substrate.

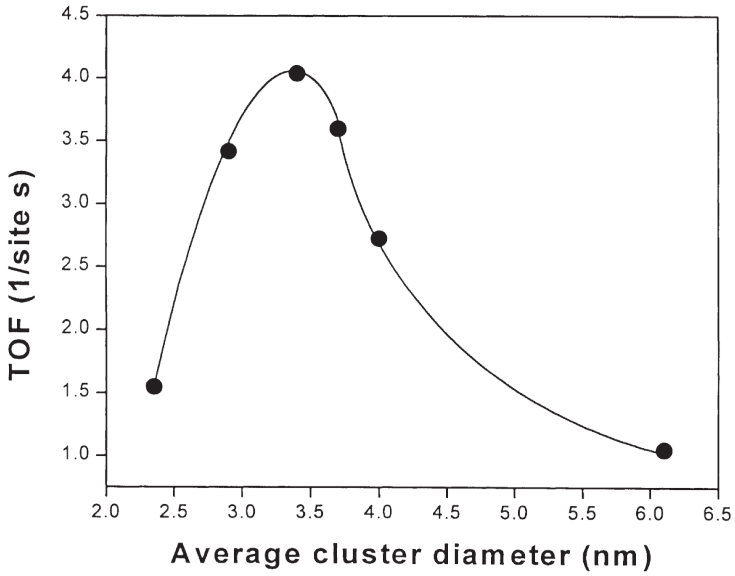

Figure 2.4: The change in activity (defined as the catalytic ability for CO oxidation reactions) and cluster size (nm) of Au at 350 K. The CO/O_2 mixture was 1:5 at total pressure of 40 Torr. The activity is defined as the specific reaction rate (product molecules/(surface site · second)) or turnover frequency (TOF) [Valden et al., 1998].

2.3.2 Magnetic Properties of Nanomaterials

In its bulk form, cobalt exhibits ferromagnetism [Kittel, 2004]. However, cobalt appears to be superparamagnetic[1] in the nano-scale because the coercivity of the NP decreases to zero. As can be seen from Fig. 2.5, the number of Co atoms in the cluster (the size of the cluster) has a clear effect on the magnetic moment per atom. It can be seen that the magnetic moment per atom (μ_B) decreases with the decrease of number of atoms in a Co cluster. Similar behaviours have been found in $Fe_{3-x}O_4$ (when x=$\frac{1}{3}$)[Demortiere et al., 2011] and in FePt [Rong et al., 2006] NPs. However, the opposite effect has been observed in $BiFeO_3$ [Park et al., 2007] and in Co_3O_4 [Ichiyanagi and Yamada, 2005] which is the decreasing in size leading to the increasing of saturation magnetization.

It should be noted, however, that no elevation of magnetic moment has been observed in $BiFeO_3$ [Park et al., 2007] and in Co_3O_4 [Ichiyanagi and Yamada, 2005]

[1]Superparamagnetism is similar to paramagnetism, but has larger saturation magnetisation. Superparamagnetism occurs in small ferromagnetic or ferrimagnetic nanoparticles.

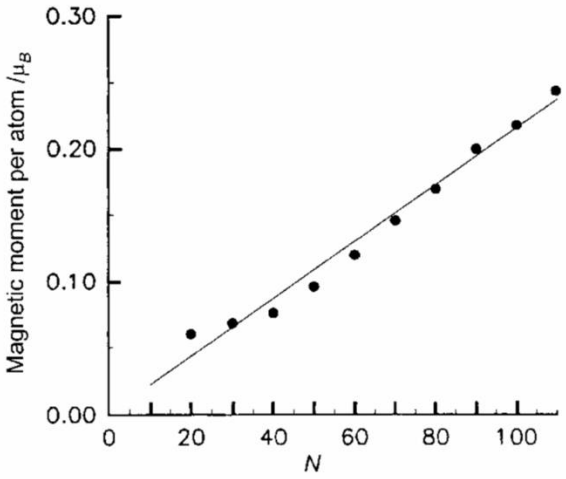

Figure 2.5: Magnetic moment per atom plotted against the number of atoms in a Co cluster at H=0.53 Tesla and Temperature=170 K. The solid line and solid dots are theoretical and experimental values, respectively. [Khanna and Linderoth, 1991].

when decreasing their sizes.

Not only do the nanoscale dimensions of NPs create distinctive magnetic properties compared to the bulk, but the interaction between the capping agent[2] used to produce the NP and the NP's surface also create changes in its magnetism. For instance, bulk gold is diamagnetic [Berkowitz and Kneller, 1969]; however, Crespo et al. reported that if they produced gold NPs according to the recipe of Brust et al. [Brust et al., 1994], with tetra-alkyl ammonium bromides (TOAB) as a stabilising agent and thiol as a capping agent, then thiol-capped Au NPs[3] (1.4 nm) show ferromagnetic properties. However, if only TOAB are used, then the NP exhibits the same diamagnetic properties as the bulk [Crespo et al., 2004].

A similar effect was reported by Yamamoto et al. [Yamamoto and Hori, 2006] who showed that Au NPs produced using polyallylamine hydrochloride (PAAHC) as a stabilising agent showed ferromagnetic behaviour in their shells and paramagnetic behaviours in their cores. The effect was explained by a weak interaction between the Au NPs surface and the PAAHC [Yamamoto and Hori, 2006].

[2]A capping agent is an organic material used to stop the growth of nanoparticles as it can bind strongly to the nanoparticles surface. It has been also used to stabilise nanoparticles in a solvent to prevent nanoparticles aggregation.

[3]Thiol-capped Au NPs are the Au NPs which have been synthesised using thiol as a capping agent which covers NPs at the surfaces.

2.3.3 Optical Properties of Nanomaterials

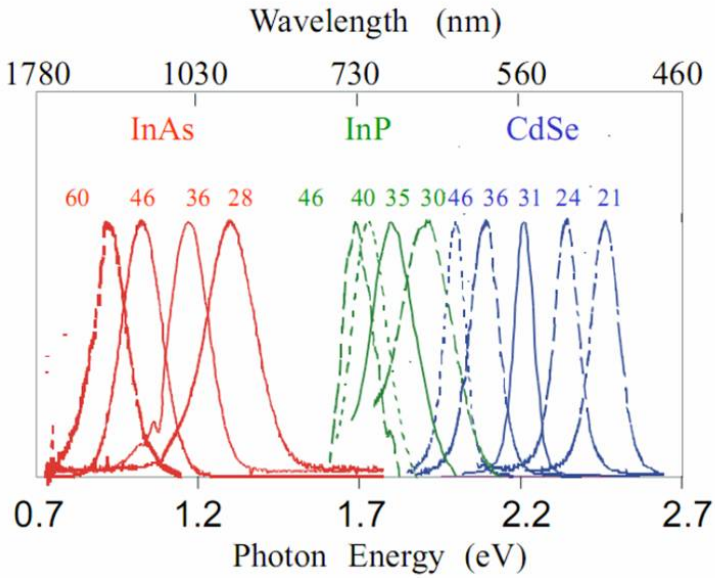

Figure 2.6: The variation in fluorescent spectra from InAs, InP, and CdSe nanoparticles with particle diameters. The diameters (in Å) are shown at the top of the peaks [Bruchez Jr et al., 1998].

When light interacts with NMs of different sizes, the resulting luminescence can have different wavelengths. For example, Bruchez et al. [Bruchez Jr et al., 1998] showed that NMs of InAs, InP, and CdSe give fluorescent spectra at the various photon energies seen in Fig. 2.6. This size-dependent fluorescence is of great benefit to biological science because of the use of fluorescent labels in biological systems. The NMs fluorescent labels are superior to dye-based labels (as previously used), as the emitted spectra is tuneable by varying the size of the NMs.

2.3.4 Thermodynamic Properties of Nanomaterials

Due to the theoretical reasons stated in section 2.2, namely that the number of surface atoms in a nanomaterial is a large fraction of the total and these atoms contribute substantially to the free energy, large changes in the thermodynamic properties of NMs relative to bulk are expected. When the size of a nanocrystal decreases, a decrease in melting temperature [Goldstein et al., 1992, Nanda, 2009], an increase in solid-solid phase transition pressure [Tolbert and Alivisatos, 1995b,

Jacobs et al., 2001, Clark et al., 2005, Deng et al., 2008], and structural distortions [Guo et al., 2008] have been observed.

This raises a number of questions:

- How does a large number of surface atoms relative to the number of enclosed atoms influence the structure of the interior of nanocrystals?
- Is it possible to manipulate the surface of nanocrystals so as to "trap" structures that might not be observed in the bulk?

To obtain the answers to these questions, phase transition experiments on NMs have to be carried out. By such means we may discover the scaling laws that relate the well-known phase transformations in bulk materials to the same, or newly-discovered, transitions in nanocrystals.

2.3.4.1 Melting Properties of Nanomaterials

The melting properties of bulk materials have been studied extensively, both theoretically [Anwar et al., 2003, Zhang and Maginn, 2012] and experimentally [Narygina et al., 2011, Guillaume et al., 2011]. For NMs, the melting temperature tends to decrease as the size of the NMs decreases [Goldstein et al., 1992, Martin et al., 1994, Nanda, 2009], as seen in Fig. 2.7.

In the melting process, surface atoms always move to minimise the surface area in the fluid phase. However, in the solid phase, strong-bond geometries result in very high energies for the atoms at the edges and corners of nanocrystals. The smaller the nanocrystal, the higher the fraction of atoms between edge and corner to volume, and thus the higher the surface energy. When nanocrystals are heated to melting point, therefore, smaller nanocrystals make larger contributions to the total energy of the system. Consequently, the melting temperature is lower for smaller-size nanocrystals [Tolbert and Alivisatos, 1995b, Alivisatos, 1996].

Other nanomaterials also show the same behaviour as CdS (as seen in Fig. 2.7). For example, silica-capped Au nanoparticles with a diameter of $\sim$3nm exhibit a melting point of only $\sim$630 K, whereas that of bulk gold is 1337.33 K, which agrees with the calculation of uncapped Au NPs [Dick et al., 2002]. In addition, organic nanocrystals, such as benzene, chlorobenzene, heptane, and naphthalene, confined in porous glass show the same trend as CdS [Jackson and Mckenna, 1990], and this has also been confirmed by calculation [Jiang et al., 1999b].

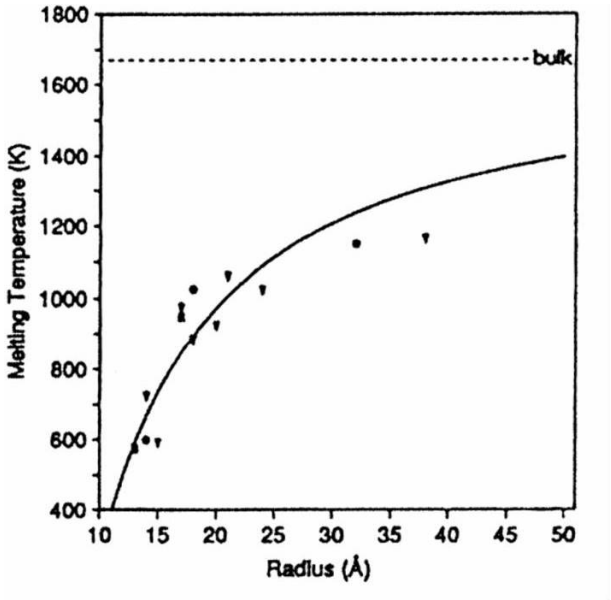

Figure 2.7: The melting temperature of CdS nanocrystals (0D) for a variety of different radii [Alivisatos, 1996, and references therein]. The solid line is the guide to the eye passing through the experimental data points which are represented by (•), (▼) and (■) symbols [Goldstein et al., 1992].

2.3.4.2 Bulk Modulus of Nanomaterials

Below are some of the reports on the size dependence of the bulk modulus in NMs (see Table 2.1). More extensive reviews and calculations were reported in the recently published paper by Gupta and Rana et. al. [Gupta and Rana, 2012]. The investigation of bulk modulii in NMs has mostly been studied during pressure-induced phase transition experiments, which are described further in section 2.4.

2.3.4.3 High Pressure Studies of Graphene

For completeness, I conclude this section with a summary of the high-pressure studies of graphene - perhaps the most studied of the NMs in recent years. I limit this discussion to high-pressure studies.

Proctor et al. [Proctor et al., 2009] reported the first result on graphene at high pressure. Variation in the number of layers and their adherence at different pressures in DAC were compared using Raman spectroscopy. The results show a clear trend for the Raman shift increasing with decreasing thickness of graphene.

Table 2.1: Dependence of nanomaterials bulk modulus with decreasing particle size.

Type	Substance	Bulk Modulus	Reference
Nano Element	Ag	increases	[Gu et al., 2008]
Nano Element	Au	increases	[Gu et al., 2008]
Nano Element	Ge	increases	[Wang et al., 2007]
Nano Metal Oxide	Fe_2O_3	increases	[Clark et al., 2005]
Nano Metal Oxide	$\beta-Ga_2O_3$	increases	[Wang et al., 2010]
Nano Metal Oxide	CoO	*decreases*	[Liu et al., 2006, Liu et al., 2007]
Nano Semiconductor	PbS	*decreases*	[Qadri et al., 1996, Jiang et al., 2000a]

Proctor et al. also proposed the possibility of using graphene as a stress sensor due to its adherence to many substrates. An extensive review of nano-carbon allotropes under high pressure can be found in [San-Miguel, 2006].

2.4 Pressure Induced Phase Transitions of Nanomaterials

Pressure can induce phase transitions to occur at values called the phase transition pressures (P_{tr}). In high-pressure experiments, P_{tr} is one of the important values that is investigated first.

CdS was the first nanomaterial [Zhao et al., 1991] to be studied under high pressure. A year later, CdS and CdSe nanomaterials were studied extensively by the Alivisatos group at the University of California, Berkeley [Haase and Alivisatos, 1992, Tolbert and Alivisatos, 1994, Tolbert and Alivisatos, 1995a].

The effect of particle size on a P_{tr} can be illustrated by the phase transition pressures of CdSe nanoparticles when changing from wurtzite (Coordination Number (CN) = 4) to the rock salt (CN = 6) structure, which are plotted against the 0D CdSe nanocrystals size (diameter) in Fig. 2.8. The transition pressures were taken from the middle point of the hysteresis[4] loop in the compression - decompression process [Tolbert and Alivisatos, 1994, Tolbert and Alivisatos, 1995b]. The graph shows a dramatic increase in the transition pressure with decreasing size of the

[4]Hysteresis - the transition pressure for a phase transition from phase A to phase B does not occur at the same pressure under compression and decompression, resulting in hysteresis on the volume vs. pressure plot for the sample.

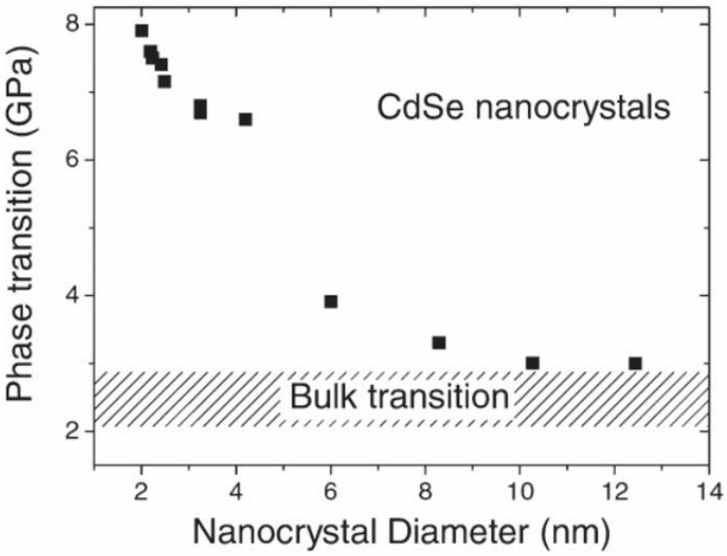

Figure 2.8: Size dependence of transition pressure of CdSe nanocrystals from wurtzite to the rock salt structure [Tolbert and Alivisatos, 1995b, San-Miguel, 2006].

nanocrystals. Above ∼11 nm, the phase transition behaviour of CdSe nanocrystals becomes almost like that of the bulk material [Jacobs et al., 2001].

In other studies, Clark et al. showed the same behaviour of P_{tr} [Clark et al., 2005], i.e., the transition pressure increases when the size of nanomaterials is decreased. For instance, the γ-Fe_2O_3 to α-Fe_2O_3 transition pressures are 27 GPa, 34 GPa, and 37 GPa for 7 nm, 5 nm, and 3 nm sized NPs diameter, respectively, compared to the bulk-Fe_2O_3 transition pressure of 24 GPa [Clark et al., 2005]. The CdSe [Tolbert and Alivisatos, 1994, Chen, 1997, Jacobs et al., 2001] and Fe_2O_3 [Clark et al., 2005] results of elevated transition pressures due to size dependence can be explained by theoretical works. For example, Gruenwald et al. used the transition path-sampling method to show that P_{tr} increases as CdSe NPs size decreases [Grüenwald and Dellago, 2009], while another work by Chen et al. also reported the same result; however, bond-order-length-strength (BOLS) theory was used [Chen et al., 2008].

More studies of the size dependence of transition pressures of nanomaterials are summarised in Table 2.2. This shows that the majority of nanomaterials have the same trend of increasing P_{tr} with decreasing particle size, with the exception of

CoO. It is unclear why CoO behaves differently compared to the other materials, as the authors did not provide any explanation; however, it could be assumed that the CoO NPs P_{tr} were probably not observed under true equilibrium conditions, resulting in an underestimation of P_{tr} or that the method in P_{tr} determination (interpolation) caused a large error. There are some nanomaterials in which the size dependence of P_{tr} is still controversial, such as SnO_2, α-Fe and CeO_2, because there has been some disagreement in the results.

Table 2.2: Dependence of nanomaterials transition pressure (P_{tr}) with decreasing particle size.

Type	Substance	P_{tr}	References
Nano Metal Oxide	ZnO	increases	[Jiang et al., 2000b, Kumar et al., 2007]
Nano Metal Oxide	Al_2O_3	increases	[Chen et al., 2002]
Nano Metal Oxide	Fe_2O_3	increases	[Clark et al., 2005]
Nano Metal Oxide	SnO_2	increases	[He et al., 2005]
Nano Metal Oxide	Ga_2O_3	increases	[Wang et al., 2010]
Nano Metal Oxide	CoO	*decreases*	[Liu et al., 2006, Liu et al., 2007]
Nano Semiconductor	CdSe	increases	[Tolbert and Alivisatos, 1995b]
Nano Semiconductor	PbS	increases	[Qadri et al., 1996, Jiang et al., 2000a]
Nano Semiconductor	ZnS	increases	[Jiang et al., 1999a]

The reason for the elevation in phase transition pressure in CdSe is explained by the hypothesis of Tolbert et. al. [Tolbert and Alivisatos, 1994] that there is a higher surface energy in nanomaterials compared to the bulk in the high pressure phase. In contrast, the decrease in phase transition pressure was described by the idea of large volume collapse by [Olsen et al., 1999] in the case for TiO_2. Moreover, Olsen et al. also suggested that the change in transition pressure can occur either way, depending on the system [Olsen et al., 1999]. This shows that there are many factors which can lead experiments on the same nanomaterials to have different high-pressure behaviours.

From the experience of the author, the same type of nanoparticles might not have the same high-pressure properties due to the way that the sample was produced; for example, mechanical attrition could lead NPs to have more intrinsic strain in the particles while NPs produced by chemical synthesis have no such strain. Alternatively, the stabilising agent or capping agent used to chemically produce NPs could also affect the variation in P_{tr} or bulk modulus. Clear evidence of the capping agent effect on nanoparticles was reported in [Crespo et al., 2004],

where the thiol capping agent can be utilised to synthesise diamagnetic Au NPs to have ferromagnetic property, as mentioned earlier. Therefore, when comparing the nanomaterials experiments under high pressure, all aspects of each experiment have to be taken into account, such as the method of sizing and error on size, the detection of phase transition, the method of nanomaterial production, etc. Due to uncertainties regarding the experimental data and the divergence of explanations, computer simulation is needed to explain the exact mechanism of size dependence in P_{tr}. The kinetics of the phase transition of CdSe NPs were studied extensively by Gruenwald et al. [Grüenwald and Dellago, 2009]. However, there are no specific kinetic studies on many other nanoparticles.

As mentioned in section 1.4, the aim of this thesis is to extend the studies of the high-pressure phases of elements that are known to have incommensurate structures in the bulk, such as Te, Se, and Bi [McMahon and Nelmes, 2006] to nano-scale regime. Some of those elements (Te and Se) previously studied as nanomaterials are shown in Table 2.3.

Table 2.3: Effect on the nanomaterials transition pressure (P_{tr}) when decreasing nanomaterials particle size for a number of different nanomaterials.

NMs	Shape	Sizing[a]	P_{tr}	P_{tr} det.[b]	References
Si	N/A	TEM	increases	ADXRD	[Tolbert et al., 1996]
Te	cylinder	TEM, SEM	increases	ADXRD[c]	[Krstic et al., 2007]
Te	particle	TEM[d]	increases	Resistance[e]	[Deng et al., 2008]
Ge	N/A[f]	EDXRD[g]	increases	XRD[h]	[Wang et al., 2007]
Se	wire	SEM[i]	increases	Raman	[Dai et al., 2011]
Fe	plate	TEM, SEM	*decreases*	ADXRD	[Sun et al., 2011]
Fe	N/A	N/A	*decreases*	ADXRD	[Jiang et al., 2001a]
Ni	N/A	N/A	no change	EDXRD	[Rekhi et al., 2001]
Si	wire	TEM	not found	Raman	[Khachadorian et al., 2011]

[a]Method of size measurement
[b]Method for P_{tr} determination
[c]ADXRD : Angle Dispersive X-ray Diffraction
[d]TEM : Transmission Electron Microscopy
[e]Electrical Resistance
[f]The author(s) did not mention about this detail
[g]EDXRD : Energy Dispersive X-ray Diffraction
[h]XRD : X-ray Diffraction
[i]SEM : Scanning Electron Microscopy

For determining structural transformation in NMs, as listed in Table 2.3, there are a number of experimental methods that have been used: Energy Dispersive X-

ray Diffraction (EDXRD), Angle Dispersive X-ray Diffraction (ADXRD), Raman spectroscopy and electrical resistance measurement. As can be seen in Table 2.3, the majority of the studies of nanomaterials under high pressure have used powder x-ray diffraction techniques, generally with an Angle Dispersive X-ray Diffraction (ADXRD) experimental set up. This validates our choice of techniques used to study nanomaterials in this thesis as follows:

- Powder x-ray diffraction (PXRD) (as mentioned earlier in section 1.2) can be used with nanomaterials (this is discussed further in section 3.1.2)
- Angle dispersive x-ray diffraction (ADXRD) is the most efficient technique to use to determine structural properties in nanomaterials (further discussion in section 3.1.1.4)

2.5 Conclusions

Nanomaterials have been reported to have distinctive properties compared to their bulk counterparts. This chapter has revealed that many kinds of nanomaterials have been investigated in various experiments and in some theoretical works.

In high-pressure studies of nanomaterials, increases and decreases in transition pressure (P_{tr}) or bulk modulus with decreasing size of nanomaterials are the current trend of interest. For this thesis, these two parameters will be studied alongside the main purpose of this thesis, which is the study of incommensurate structure of nanomaterials.

Most of the reviewed high-pressure studies of nanomaterials employed the angle dispersive powder x-ray diffraction, and this will also be used in this thesis. In addition, the sizing of nanoparticles is crucial because ineffective sizing procedures could lead to misinterpretation of size-dependent properties.

In the next chapter, detailed high-pressure techniques, x-ray diffraction experiments data collection and valid nanoparticles sizing methods will be discussed.

Chapter 3

Methodology and Experimental Techniques

3.1 High-Pressure Powder X-ray Diffraction (HP-PXRD) Techniques

3.1.1 High-Pressure Techniques

Modern high-pressure research was pioneered by P.W. Bridgman, who received the Nobel Prize in Physics in 1946 for "the invention of an apparatus to produce extremely high pressures, and for the discoveries he made therewith in the field of high-pressure physics" [Bri, 1964].

Bridgman pioneered the use of opposed-anvil pressure cells to obtain pressures above 9.8 GPa [Bridgman, 1950, Bridgman, 1952] and in a career that spanned six decades he studied an extremely wide range of materials, both solids and liquids, resulting in the publication of some 200 papers[1]. However, it was the invention of the diamond-anvil cell (DAC) in 1959 by Jamieson et al. [Jamieson et al., 1959] and Weir et al. [Weir et al., 1959] that heralded the modern era of high-pressure science [McMahon, 2011].

[1]The search was carried out through ISI Web of Science with the following set of keywords:"(AU=bridgman PW)" search completed on 16th April 2012.

3.1.1.1 The Diamond-Anvil Cell (DAC)

Successful high-pressure research depends critically on equipment and instrumentation, particularly that which is necessary to generate the high pressures required. While pressure cells have evolved over the last 50 years since the pioneering work of Bridgman, and a wide range of different pressure-generating devices have been developed (e.g. opposed-anvil cells [Bridgman, 1950, Bridgman, 1952], belt presses [Hall, 1960], multi-anvil cells [Liebermann, 2011], and the Paris-Edinburgh cell [Besson et al., 1992]), it is the DAC that has allowed researchers in a wide range of scientific disciplines to achieve pressures higher than those at the centre of the Earth[2] [Akahama and Kawamura, 2010]; to study materials at high pressure at both high and low temperatures [Sanloup et al., 2008, Datchi et al., 2009]; and to measure a wide range of physical properties at high pressures [Nelmes et al., 1993, Lobban et al., 1998, Goncharenko, 2005, Mirebeau, 2007].

While the pressure cell to be used for any particular study depends on the exact measurements required (e.g. neutron diffraction studies of hydrogen-containing materials require the compression of large volumes of sample, and thus the use of piston-cylinder or Paris-Edinburgh cells), DACs are particularly well suited to structural studies using x-ray powder diffraction techniques. Therefore, they are the pressure cells of choice for the work described in this thesis.

There are many kinds of DAC available commercially, such as Mao-Bell [Mao and Bell, 1978], Merrill-Bassett [Merrill and Bassett, 1974] and DXR-4, DXR-5, DXR-6 [Adams, 2012]. In this thesis, DXR-5 and DXR-6 (as shown in Fig. 3.1) DACs purchased from Diacell (now Easylab) were used for the selenium nanoparticles' high-pressure powder x-ray diffraction (HP-PXRD) experiments described in Chapter 4, while Merrill-Bassett cells (as shown in Fig. 3.2) were used for the bismuth nanoparticles' HP-PXRD experiments which will be described in Chapter 6.

DACs are particularly well suited to HP-PXRD studies, because:

- Diamond is the hardest known material.
- Diamond has a low absorption coefficient for x-rays with wavelengths < 0.7 Å [Brister, 1997], and the x-ray beam therefore has maximum access to the sample through the diamonds.

[2]Centre of the Earth pressure ∼350 GPa [Bundy, 2000]

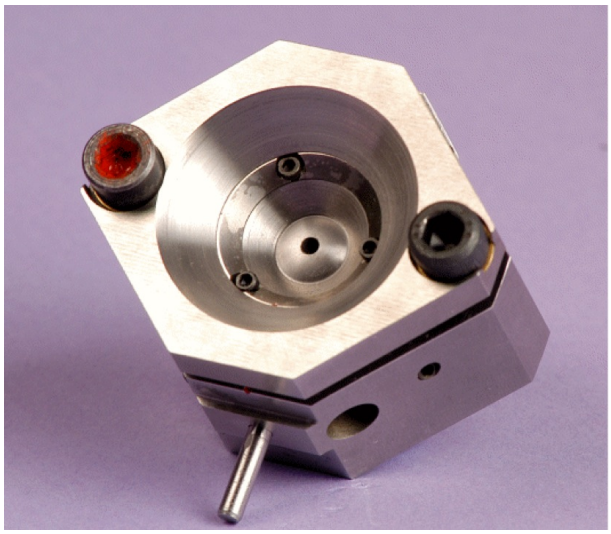

Figure 3.1: DXR diamond-anvil cell from Diacell Products.

- Diamond is transparent to visible light, allowing optical access to the sample for either visual observation or pressure measurement (see section 3.1.1.3).
- The diamond anvils are single crystals and give very little additional scattering to contaminate the diffraction pattern from the powder sample.
- Only a very small amount of sample material ($\sim$1-10 μg) is required.
- As a result of the small sample size and small culet size, DACs allow diffraction studies to pressures as high as 400 GPa [Akahama and Kawamura, 2010].
- DACs have small physical dimensions and are thus well-suited to use on synchrotron radiation sources.

Diamond-Anvil Cell Components

The basic design of all DACs is the same, and is described below using the Merrill-Basset DAC as an example.

The Merrill-Basset DAC was invented in 1974 [Merrill and Bassett, 1974], and was specifically designed for single-crystal x-ray diffraction studies of minerals as the cell was somewhat smaller than the pressure cells in use prior to 1974 (thus allowing its use on standard single-crystal diffractometers). The cell comprises the lower plate, the lower backing seat, the lower-diamond anvil, the tungsten (W)

or rhenium (Re) gasket, the upper-diamond anvil, the upper-backing seat, the upper plate, and three Allen screws, as shown in Fig. 3.2.

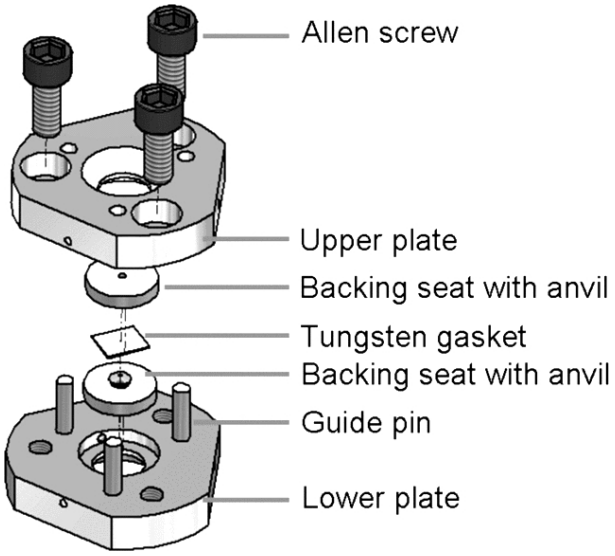

Figure 3.2: Exploded view of a Merrill-Basset DAC [Moggach et al., 2008].

The Cell Body The cell body comprises the upper and lower plates, which are made of hardened steel. These plates, the relative alignment of which is maintained by the three guide pins, are pulled together by tightening the Allen screws to generate the pressure. In other cell designs, including the DXR-5 and DXR-6 DACs used in this thesis, the upper and lower plates are in a piston-cylinder design, with the alignment of the plates being maintained by the close fitting of the piston within the cylinder.

The Backing Seats Prior to 1974, the backing seats of DACs were typically made of hardened steel or tungsten carbide to provide strong support to the diamond anvils themselves. However, such seats are not transparent to x-rays, and so are wholly unsuited to single-crystal x-ray diffraction, where diffracted x-rays must be measured to high diffraction angles. A key feature of the Merrill-Bassett DAC was the use of beryllium to make the DAC backing seats, as its low x-ray absorption allowed high-angle diffraction data to be collected using the molybdenum x-ray radiation (wavelength 0.71 Å) available on most laboratory-based single-crystal diffractometers. A small (1 mm diameter) hole through the

Be seat allowed optical access to the sample, while maintaining support at the base of the anvil.

However, beryllium softens at temperatures above 500 K, and so is not suitable for high-pressure high-temperature experiments. Additionally, if the direct x-ray beam passes through the Be seat closest to the detector, then an intense Be powder diffraction pattern is observed on the detector, superimposed on the diffraction pattern from the sample. While the use of other low-absorption materials such as cubic boron nitride (cBN) can be used to overcome the problems of the softening of the Be at high temperatures [Yamanaka et al., 2001], problems with diffraction patterns from the backing seat remained. This problem has recently been overcome by the use of so-called "Boëhler-Almax[3]" backing seats [Boehler and Hantsetters, 2004], in which the diamond anvil is supported radially by a tungsten carbide seat (see Fig. 3.3). The seats have a large opening angle, 70°, through which the cell can be rotated without a diffraction pattern resulting from the direct x-ray beam. They are also better suited to high-pressure high-temperature studies, which are essential in our single-crystal diffraction study of Bi-IV at 465 K [Chaimayo et al., 2012]. As a result of these advantages, Boëhler-Almax seats have become very popular internationally since the first report of their development in 2004 [Boehler and Hantsetters, 2004].

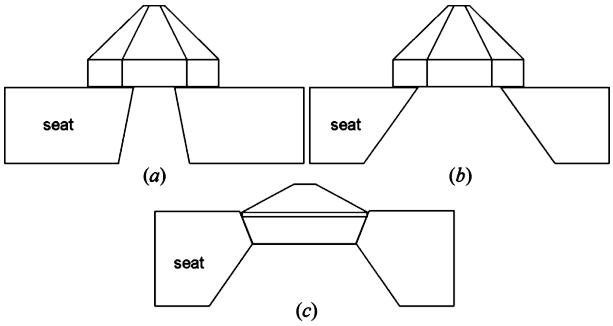

Figure 3.3: Different types of backing seats, (a) a beryllium backing seat with a modified brilliant-cut diamond anvil, (b) a tungsten carbide or steel backing seat with a modified brilliant-cut diamond anvil, and (c) a Boëhler-Almax diamond anvil with a tungsten carbide (Boëhler-Almax) backing seat which supports the anvil more efficiently than (a) and (b) due to its design [Moggach et al., 2008].

[3]Boëhler-Almax backing seat is compatible with Boëhler-Almax diamond anvil as they will match to each other.

Diamond Anvils The diamond anvils of a DAC have direct contact with the sample and the pressure transmitting medium (PTM) which surrounds the sample. As a result, the culet (tip) of the diamond, which has a diameter of 25-600 μm, experiences very high pressure. Diamond is thus the ideal material to be used for the anvils due to its outstanding properties: it is the hardest known material (level 10 on the Moh scale); it is highly transparent to hard x-rays[4]; it is impervious to abrasion, transparent to optical spectrum for visual inspection, and transparent to UV and IR[5] radiation. If ultra-high pressures are required ($>$ 1 Mbar), then bevelled-cut diamond culets, as introduced by Mao and Bell in 1978 [Mao and Bell, 1978], are normally used, as this culet design reduces the stresses at the culet edges. The only limitations for diamond usage in high pressure research are their brittleness and their expense.

In the work described in this thesis conducted with Merrill-Basset and DXR-5/6 DACs, Drukker standard-design and Brilliant design diamond anvils with 300-μm and 400-μm culets have been used with beryllium backing seats. Some data were also collected with Merrill-Basset DACs equipped with Boëhler-Almax diamond backing seats, containing diamonds with 300-μm and 400-μm culets.

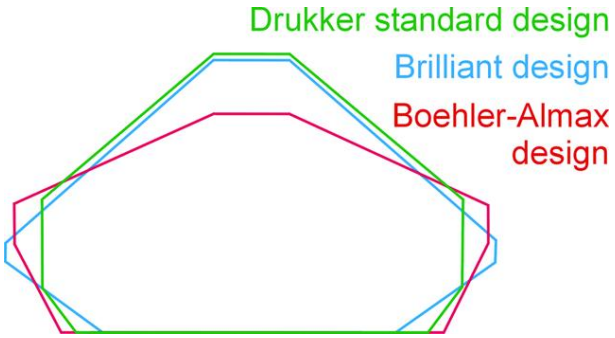

Figure 3.4: Different designs of diamond culets [Katrusiak, 2007].

Gasket Initially, DACs were not equipped with gaskets, and the sample was compressed directly between the diamond culets [Jamieson et al., 1959]. The idea of the metal-gasketted DAC was introduced by van Valkenburg in 1962

[4]Hard x-rays are typically defined as x-ray with energies greater than around 10 keV (from http://hesperia.gsfc.nasa.gov/sftheory/xray.htm)

[5]A special diamond type IIA with low nitrogen content is most suitable for infrared (IR) and Raman spectroscopy

[Valkenburg, 1962], and allowed samples to be studied to higher pressures and to be loaded with a pressure-transmitting medium for obtaining hydrostatic pressure conditions. Gaskets also allowed samples that were initially liquids or gases to be studied. The gasket is a thin metal foil, with an initial thickness of ∼0.2 mm, which is indented by the diamond anvils to a thickness of 0.02 mm (20 μm) before the sample chamber of diameter $\sim \frac{1}{3}$ of the culet diameter, is drilled in the centre of the indent using laser drilling or spark erosion with an Electric Discharge Machine (EDM). The gasket can be made of tungsten, rhenium, hardened steel, or alloys thereof [Katrusiak, 2007], and the choice of gasket material will depend on the highest pressure required, and the non-reactiveness of the gasket material to the sample or pressure transmitting medium.

Allen Screws As can be seen in Fig. 3.2, Merrill-Bassett DACs have three Allen screws which are used to pull the upper and lower plates together, thus pressurising the sample. The three Allen screws have to be tightened equally in order to maintain the parallelism between the culets of the upper and lower diamond anvils. In the DXR-5/6 DACs, there are two screws with opposite threads which are tightened simultaneously to pull the diamonds together.

Principles of the DAC Operation

The simplest definition of pressure is:

$$Pressure\,(Pa) = \frac{Force\,(N)}{Area\,(m^2)} \tag{3.1}$$

Thus, the smaller the area on which a force is applied, the higher the pressure attained, and a DAC with diamond anvils with smaller culets will generally generate higher pressures than a cell fitted with larger-culet diamonds. For example, for the majority of work described in this thesis, Merrill-Bassett DACs equipped with anvils with 400 μm culets routinely reached pressures of up to 30 GPa. For work above this pressure, DXR-5 and DXR-6 DACs fitted with 300-μm-size-culet anvils were used, and these reached pressures of ∼50 GPa. The maximum attainable pressure also depends on the thickness of the gasket between the culets and the diameter of the gasket hole that contains the sample, as shown in equation (3.2) and in Fig. 3.5. It can be seen that the maximum pressure is inversely proportional to the sample thickness, and thus the volume of the

sample illuminated by the x-ray beam. The higher the pressure required, therefore, the weaker the diffraction signal. For optimum diffraction data, different cells equipped with samples of different thicknesses are required.

$$Attainable\ Pressure \propto \left(\frac{2h}{D-d}\right)^{-1} \text{[Katrusiak, 2007]} \tag{3.2}$$

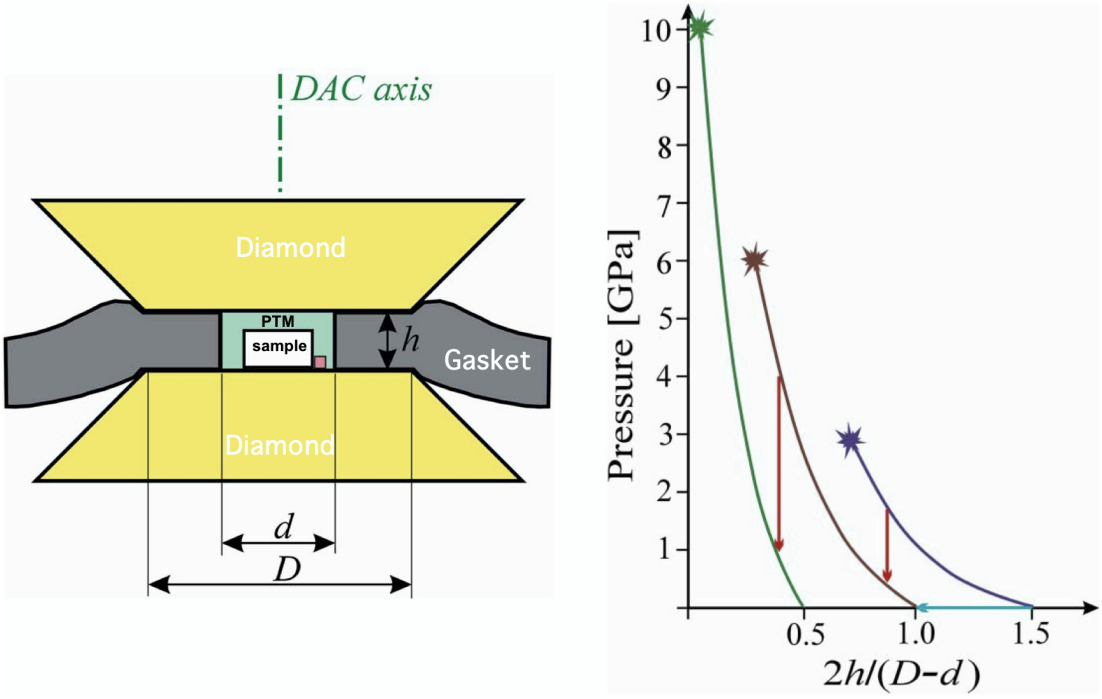

Figure 3.5: (left) Cross-sectional diagram of a DAC showing compositional elements in the pressure chamber. (right) The graph illustrates the relationship between the initial high-pressure chamber dimensions h, D and d. The parameters are incorporated into the term $2h/(D-d)$. The small star signs represent the attainable pressures. The vertical red arrows point out pressure changing by cycling pressure and the blue arrow indicates the changes in h, chamber height, by the gasket pre-indentation. This figure is edited from [Katrusiak, 2007].

As stated previously, in order to achieve sample pressures of up to 30 GPa and 50 GPa, diamond anvils equipped with culets of 400 μm and 300 μm, respectively, were employed. Next, 10 mm×10 mm×0.2 mm-thick tungsten sheets were indented to a thickness of ∼20-25 μm using the diamond anvils in the DAC, and a gasket hole of diameter ∼110-125 μm was then drilled at the centre of the indent using an Electrical Discharge Machine (EDM).

In order to increase the pressure, the Allen screws have to be tightened equally to let the upper and lower cell body move toward each other. The axial thrust will then force diamond anvils to apply pressure to the hydrostatic fluid, which consequently pressurises the sample, see Fig. 3.6(a).

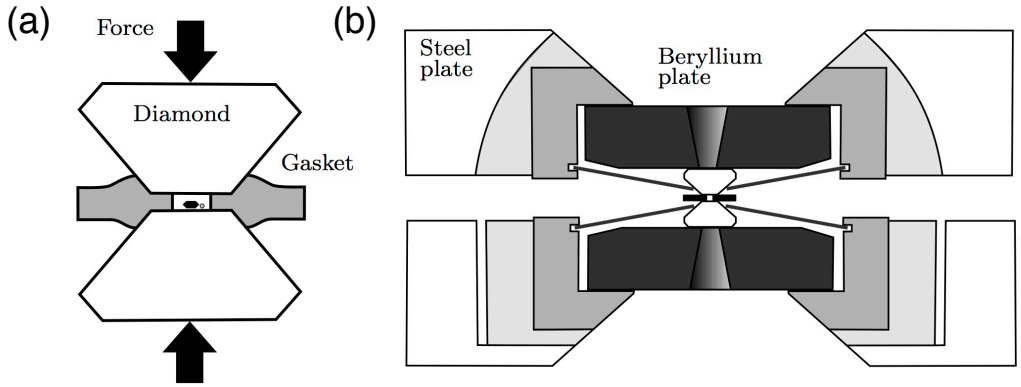

Figure 3.6: Schematic diagram of a DAC [Lundegaard, 2008].

3.1.1.2 Pressure Transmitting Media (PTM)

When the diamonds in the DAC are pulled/pushed together, the reduction in the volume of the sample chamber increases the pressure on the sample. To ensure that every point in the pressure chamber experiences the same pressure conditions (and thus the pressure is hydrostatic), the crystalline sample should be surrounded by a liquid, called the pressure transmitting media (PTM), which is loaded into the sample chamber in addition to the sample itself. Without the PTM, the uniaxial nature of the compression by the diamonds can lead to substantial pressure gradients in the sample resulting in peak broadening in the collected diffraction patterns, or to *hkl*-dependent peak shifts which can make indexing and fitting the diffraction data impossible.

Truly hydrostatic conditions are obtained by using a light and inert gas (such as helium (He)) as the PTM. But He solidifies at 12 GPa at 300 K [Mao et al., 1988, Klotz et al., 2009]. *All* PTMs are solids above this pressure, and so do not give truly hydrostatic conditions. Recently, Klotz et al. [Klotz et al., 2009] critically reviewed the most frequently-used PTMs using the broadening and splitting of the fluorescence peaks from a ruby pressure calibrant (see section 3.1.1.3)

to quantify the non-hydrostaticity of the solids/liquids PTM. While Klotz et al. [Klotz et al., 2009] studied a wide range of PTMs (1:1 and 5:1 isopentane-n pentane, 4:1 deuterated methanol−ethanol, 16:3:1 deuterated methanol−ethanol-water, 1:1 FC84 Fluorinert-FC87 Fluorinert, Daphne 7474, silicone oil, as well as nitrogen, neon, argon and helium), within the Centre for Science at Extreme Conditions (CSEC), only 4:1 methanol-ethanol, 16:3:1 methanol-ethanol, nitrogen (N_2) and helium (He) are typically used as PTMs, and these are focused on below:

4:1 methanol-ethanol is the best-known PTM because it is easy to handle and load, and is very cheap. The medium can go hydrostatically up to 10 GPa [Piermarini et al., 1973]. The deuterated form is used for neutron diffraction experiments.

16:3:1 methanol-ethanol-water is easy to make and also inexpensive. The addition of a small amount of water was initially reported to extend the hydrostatic limit some 4 GPa above the limit of 4:1 deuterated methanol-ethanol. However, a more recent study by Klotz et al. reported that methanol-ethanol-water and methanol-ethanol have the same hydrostatic limit of 10 GPa [Klotz et al., 2009, and references therein]. The 16:3:1 mixture is also used in its deuterated form, but only in neutron diffraction experiments.

Nitrogen (N_2) can provide hydrostatic conditions up to 13 GPa [Lesar, 1979], a limit confirmed by [Klotz et al., 2009]. It is typically loaded into the sample chamber as a cryogenic liquid.

Helium (He) has long been regarded as the best PTM. It is typically loaded as a high-pressure (few kbar) gas rather than a cryogenic liquid, and specialist equipment is required, but this can be purchased commercially from SITEC company [Sitec, 2012]. Although it solidifies at 12 GPa, helium provides a hydrostatic environment up to 12 GPa at 300 K, and a quasi-hydrostatic medium to considerably higher pressures [Klotz et al., 2009].

In the work described in this thesis, a 4:1 methanol-ethanol [Piermarini et al., 1973] PTM was used, because, during the synthesis process (see Chapter 5), water was found to give unwanted reactions with the bismuth nanoparticles during their

formation. While more hydrostatic conditions would have been obtained using a He PTM, the CSEC gas loader was not available during the work reported.

3.1.1.3 Pressure Measurement

Although the sample pressure in a DAC could, theoretically, be calculated from the applied force and the area of the diamond culets, in practice this is not possible, because losses due to friction and elastic deformation of the gasket and anvils cannot be accurately accounted for. In addition, while an absolute pressure scale can be obtained from the volume and compressibility, by integration of the bulk modulus [Eremets, 1996], the most commonly-employed methods to determine pressures in crystallographic experiments are to use an internal diffraction standard or the ruby fluorescence technique.

Commonly-used internal diffraction standards are NaCl, CsCl, CaF_2 and MgO [Katrusiak, 2007], because they are strongly scattering crystals, and a number of elemental metals such as Pt, Au, Cu and Ta may also be used [Ming et al., 1983, Heinz and Jeanloz, 1984, Holzapfel, 2005], most widely in ultrahigh-pressure studies. The sample pressure (which is assumed to be the same as that of the calibrant) is obtained by determining the atomic volume of the calibrant using diffraction, and then determining the pressure from its known equation of state (EoS).

While an internal calibrant enables the sample pressure to be obtained from diffraction data collected simultaneously to that of the sample, the pressure cannot be determined without access to an x-ray beam. However, the optical access to the sample chamber in a DAC means that it is possible both to excite fluorescence in a material and to measure its wavelength. This is the basis of the ruby fluorescence technique for measuring pressure. In this technique, a small ($\sim$5 μm) piece of ruby is enclosed along with the sample in the gasket hole of the DAC. Ruby fluoresces strongly when illuminated by a laser, and the wavelength of the R_1 and R_2 fluorescence doublet is pressure dependent. A schematic diagram of a typical ruby fluorescence set-up for pressure measurement is shown in Fig. 3.7.

To calculate the pressure from the measured fluorescence spectrum, the

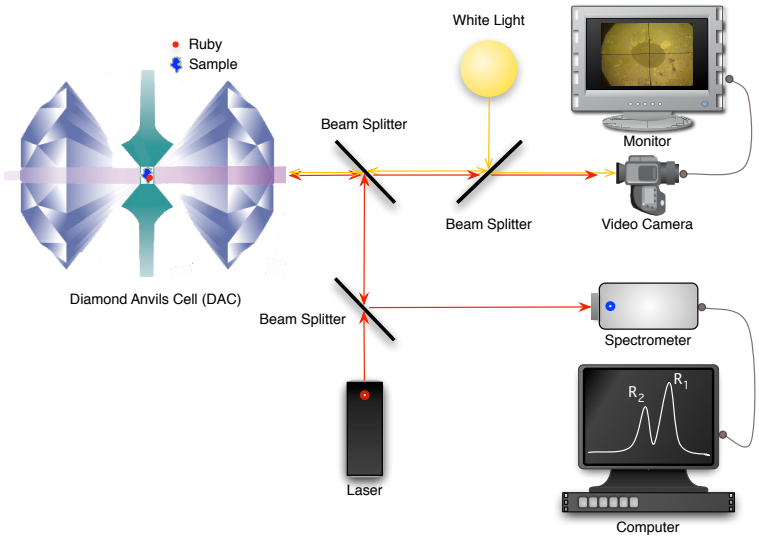

Figure 3.7: Schematic diagram of a fluorescence pressure measurement system.

following equation (3.3) is used [Mao et al., 1986].

$$P(bar) = \frac{19040}{B}\left[\left(\frac{\Delta\lambda}{\lambda_0}+1\right)^B - 1\right] \tag{3.3}$$

where $\Delta\lambda$ is the wavelength shift (in Å) of the ruby $R_{1,2}$ fluorescence line from its ambient-pressure value. The constant, B, has the value 7.665 for quasi-hydrostatic condition and 5 for non-hydrostatic conditions; and λ_0 is the wavelength measured at 1 bar (Å) and is equal to 6942 (Å) for the R_1 line and 6928 (Å) for the R_2 line.

3.1.1.4 High-Pressure X-ray Diffraction at Synchrotron Radiation Sources

While x-ray diffraction has been used to determine the high-pressure behaviour of materials since the earliest days of the DAC [Jamieson et al., 1959], it was the use of synchrotron radiation in the late 1970s and early 1980s that enabled diffraction data to be collected to very high pressures. Prior to 1990, diffraction data were typically collected using energy dispersive diffraction techniques, where the data were obtained as a function of energy at a fixed Bragg angle using the full polychromatic (or "white") beam from the synchrotron. The intensity of the white beam overcame the weakness of the diffraction signal from the very small samples,

and enabled diffraction data to be collected in minutes or seconds. However, the inherent limitations of the energy dispersive technique - particularly its poor resolution and poor powder averaging - meant that the information obtainable from the diffraction data was limited to lattice type and, perhaps, spacegroup.

In 1990, the angle-dispersive method for collecting high-pressure powder data was pioneered in Japan. This technique uses monochromatic synchrotron radiation and an area detector, such as an image plate, to collect the full 2-dimensional Debye-Scherrer (D-S) diffraction pattern. This is subsequently integrated azimuthally around the D-S rings to give a standard 1D diffraction profile. The integration process results in each data point in the final profile being the average of, potentially, many thousands of pixels in the raw D-S image. This averaging process greatly improves the signal-to-noise ratio and gives more accurate peak intensities. Combined with the inherently higher resolution of the technique, angle dispersive-methods are ideally suited to the detailed study of structures and transitions at high pressures. As a result, these methods are now employed for high-pressure studies at all synchrotron radiation sources around the world. In particular, the techniques are used on all of the synchrotron high-pressure beamlines used in this thesis, i.e., I15 at Diamond, ID09A at the ESRF, and ID27 at the ESRF.

All of these beamlines have been built specifically to conduct high-pressure diffraction experiments. On all three, the x-ray beam can be focussed or collimated to $30\times30\mu m^2$ on I15, $10\times10\mu m^2$ on ID09A (ESRF) and $2.7\times1.7\mu m^2$ on ID27 (ESRF); this reduces the likelihood of the incident beam hitting the metallic gasket and producing an intense diffraction pattern from it. Each beamline provides a low divergence x-ray beam with a wavelength of $\sim$0.41 Å, which is currently believed to be the ideal wavelength at which to collect high-pressure powder diffraction data.

3.1.2 Theory of Powder Diffraction

Powder x-ray diffraction is the main tool used in this thesis to study the incommensurate structures of nanomaterials. While not as powerful as single-crystal techniques for determining completely unknown crystal structures, powder methods are, of course, ideally suited to nanocrystalline powdered samples. Powder x-ray diffraction is also a method which is easier to perform experimentally and

from which it is easier to analyse the data compared to single crystal x-ray diffraction methods.

In the studies described in this thesis, preliminary powder x-ray diffraction studies were carried out with a Bruker D8 x-ray diffractometer located in CSEC, the University of Edinburgh. These "in-house" studies were used to determine the quality of the nanoparticles in terms of the elemental composition, and the particle size using the Scherrer equation (which will be discussed in section 3.3.4). Once identified, the highest quality samples (i.e. monodispersed in size and shape) were prepared for high-pressure powder x-ray diffraction at a synchrotron, i.e., Diamond (Oxfordshire, UK) and the ESRF (Grenoble, France).

The Debye-Scherrer method is the powder diffraction technique that has been used throughout this thesis. This technique can be described briefly as follows. The x-ray beam passes though the powdered sample, which has many single crystals in random orientations. Each single crystal will give a number of diffraction spots on the detector, and so many randomly-orientated single crystals will give a number of diffraction rings at positions according to Bragg's Law.

3.1.2.1 Bragg's Law

Bragg's Law is named after W.H. Bragg and W.L. Bragg (1912) who developed the theory of diffraction in crystals. Bragg's Law can be explained using simple geometrical considerations which are not physically correct. However, this is the simplest explanation and gives the correct result for crystallography studies. Bragg's equation is:

$$2d_{hkl}sin(\theta) = n(\lambda) \tag{3.4}$$

If Bragg's Law is satisfied, there will be constructive interference between the x-rays diffracted by two crystallographic planes (A and B in Fig. 3.8) separated by a distance d_{hkl}. This will occur at a unique value of θ - the angle of the incident beam to the sample's crystallographic planes.

3.1.2.2 The Reciprocal Lattice and the Reciprocal Space

The reciprocal lattice and reciprocal space are efficient tools used in understanding and interpreting the diffraction of x-rays from matter. It is unfortunate that

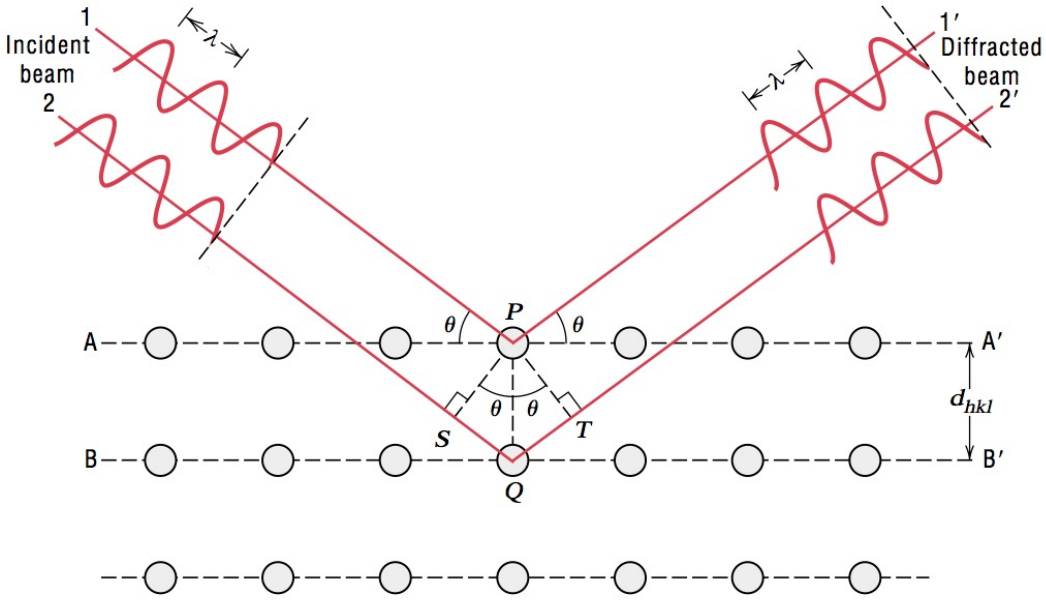

Figure 3.8: Schematic diagram of x-ray and crystal geometry used in Bragg's Law, when λ is wavelength, n is the order of the reflection, d_{hkl} is the distance between adjacent atomic planes with Miller indices (hkl) and θ is incident angle and reflected angle measured from the considered atomic plane [Callister Jr, 2001].

a crystal structure cannot be directly imaged in real space. Instead, x-ray diffraction images the structure in the inverse of the crystal real space − reciprocal space. Therefore, the reciprocal lattice is a powerful tool for understanding the crystallographic results in this thesis.

In reciprocal space, the Miller Indices of the planes from which x-rays are diffracted become the coordinates of reciprocal lattice points. Moreover, the reciprocal lattice can be used to identify the direction of the diffraction beam, obtain information on the crystallite size, and image strain effects and crystal orientation for both single crystals and powder samples. The reciprocal lattice vectors $(\vec{a}^*, \vec{b}^*, \vec{c}^*)$ can be formulated in equation (3.5).

$$\vec{a}^* = \frac{\vec{b} \times \vec{c}}{\vec{a} \cdot \left(\vec{b} \times \vec{c}\right)} \tag{3.5}$$

where $\vec{a}$, $\vec{b}$ and $\vec{c}$ are basis translation vectors in real space. Some important

properties of real space and reciprocal space are given in equation (3.6) and in equation (3.7).

$$\vec{a} \cdot \vec{a}^* = \vec{b} \cdot \vec{b}^* = \vec{c} \cdot \vec{c}^* = 1 \tag{3.6}$$

$$d^*_{hkl} = \frac{1}{d_{hkl}} \tag{3.7}$$

3.1.2.3 Criteria for Accurate Structure Determination

The structures of all the nanomaterial samples in this thesis were determined using x-ray diffraction. For the sake of accuracy in structure determination, considerable care must be taken in every step of the data collection, i.e., accurate sample intensities, no additional peaks, low background intensity, high signal-to-noise ratio, and high signal-to-background ratio - which are achieved using the methods described in the following sections. The procedures of x-ray diffraction workflows used in this thesis are more or less identical to those used previously in many successful experiments by the members of high-pressure research group at Edinburgh [Degtyareva et al., 2004, Hejny et al., 2006, Bovornratanaraks et al., 2006, McMahon et al., 2007, Evans et al., 2009].

The high intensity x-ray beam available at any synchrotron source allows any experiment to have high a signal-to-noise ratio. Moreover, the short exposure times of only a few seconds results in no changes in the sample conditions during the data collection.

A specific energy of the x-ray beam can be chosen to suit each experiment. The x-ray wavelength of 0.41 Å($\sim$30 keV) has been widely used because it is short enough to provide reasonable access to reciprocal space. Moreover, the maximum flux from synchrotron undulators is typically in the range of 30 to 50 keV, and x-rays of these wavelengths can be focussed relatively easily [Mezouar, 2010]. A still shorter wavelength is, of course, able to give better access to reciprocal space, but synchrotrons typically provide lower intensities at such wavelengths, and there are increased difficulties in focussing and/or collimating the beams. Detectors such as image plates are also less sensitive at such wavelengths.

The focussing, collimation, and small size of the x-ray beam play a vital role in preventing equipment near to the x-ray beam from being illuminated and

generating background. In particular, since the diameter of the sample chamber in a DAC is ~ 100 μm in diameter, the incident x-ray beam must be considerably smaller than this in order not to hit the strongly-scattering gasket and produce intense diffraction rings from tungsten or rhenium.

The pressure cell is oscillated around a vertical axis by rocking a few degrees during the x-ray exposure. This results in a better powder pattern (i.e. more homogeneous powder rings) because the oscillation brings more of the sample crystallites into the Bragg condition, resulting in diffraction from more of them, and smoother diffraction rings. However, for a very fine powder, such as that from a nanocrystalline sample, sample oscillation might not be as necessary. Despite this, for all the data collected in this thesis the sample was oscillated $\pm$ 3° or $\pm$ 5° around a vertical axis.

Integrating the 2D diffraction patterns azimuthally gives 1D powder diffraction profiles with an extremely high signal-to-noise ratio, and more accurate peak intensities. In the 1D integrated diffraction profile, the intensity at any given 2θ value typically results from the averaging of thousands of pixels in the 2D image.

Accurate calibration of the experimental equipment is vital if accurate results are to be obtained. The sample-detector distance, x-ray wavelength, detector tilts, and the position of the straight-through x-ray beam on the detector (which gives the centre of the Debye-Scherrer pattern) are obtained on beamline I15 at Diamond and on beamlines ID09A and ID27 at the ESRF, by collecting a diffraction pattern from a silicon standard sample. The ruby fluorescence pressure measuring systems used in these HP-PXRD experiments are calibrated with a neon lamp which has a wavelength of 550 nm and silicon standard which gives a Raman peak at 520 cm^{-1}.

3.1.3 Experimental Set Up, Data Collection and Data Analysis

3.1.3.1 Experimental Set Up

At a synchrotron (see Fig. 3.9), high-energy electrons circulate around a storage ring. When a bunch of electrons are forced to change direction by passing

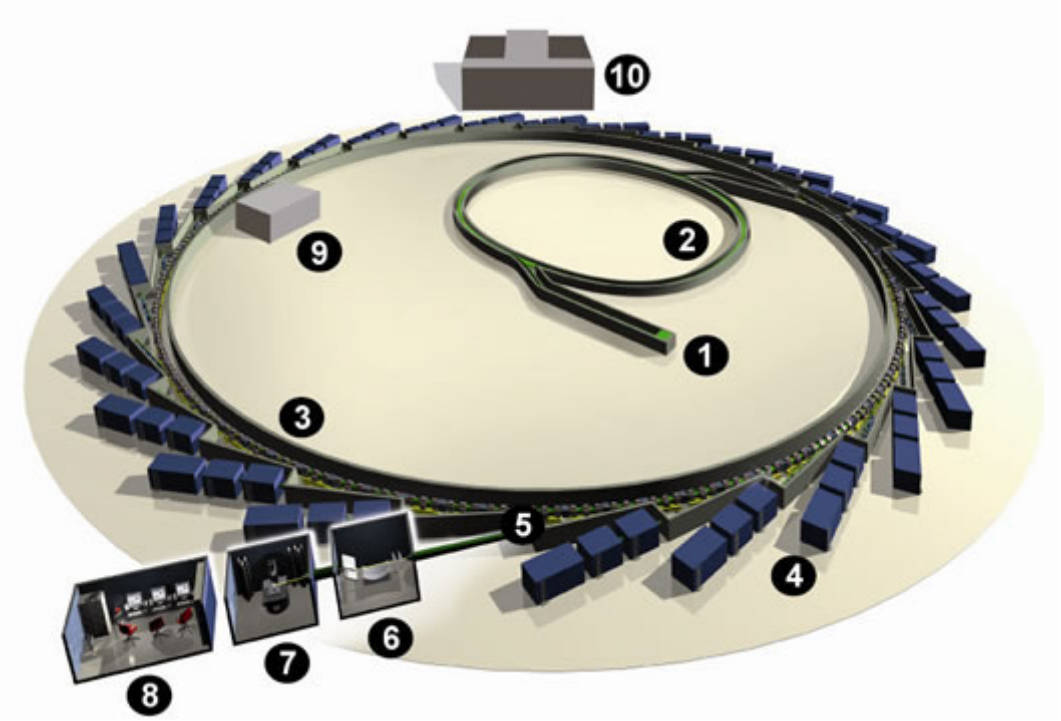

Figure 3.9: Diagram describing the components of a synchrotron. 1) injection system - the electron gun and the Linac, 2) booster ring, 3) storage ring, 4) beam line, 5) front ends, 6) optics hutch, 7) experimental hutch and 8) control room, and 9) radio frequency (RF) cavity [Website, 2009].

through a bending magnet (or an insertion device such as an undulator), the resulting acceleration results in the emission of radiation over a wide range of the electromagnetic spectrum. This radiation is then delivered to the optics hutch (see Fig. 3.10) where it is incident on a Si (111) monochromator. Only that very small part of the spectral bandwidth that meets the Bragg condition is diffracted by the monochromator, resulting in a monochromatic outgoing x-ray beam which is then collimated and focused by a Kirkpatrick-Baez (KB) geometry focussing mirror system[6]. The focussed x-ray beam is then further collimated by a platinum (Pt) pinhole made of many layers of Pt, before it is incident on the DAC placed on the sample stage. The sample stage can translate precisely in micron steps

[6]Kirkpatrick-Baez (KB) optics consist of two elliptical silicon-coated-substrate mirrors aligned perpendicular to each other. In the KB geometry, the x-rays from the synchrotron are placed at one focal point of the optics, and are reflected from the mirror surfaces to the second focal point, resulting in a two-dimensionally-focused beam.

along the x, y, z directions, and can also rotate around the vertical z axis (see Fig. 3.11).

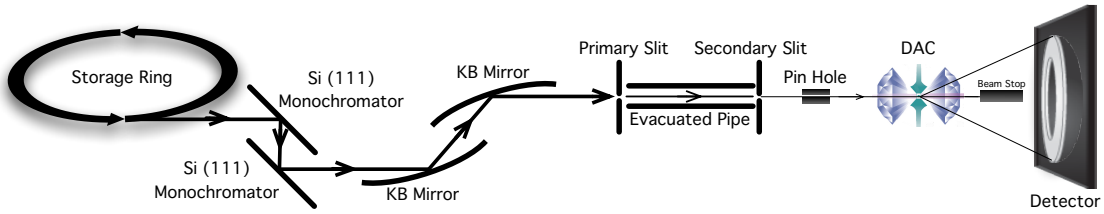

Figure 3.10: Schematic diagram of high-pressure beamline for powder x-ray diffraction at I15, Diamond, Oxfordshire, UK.

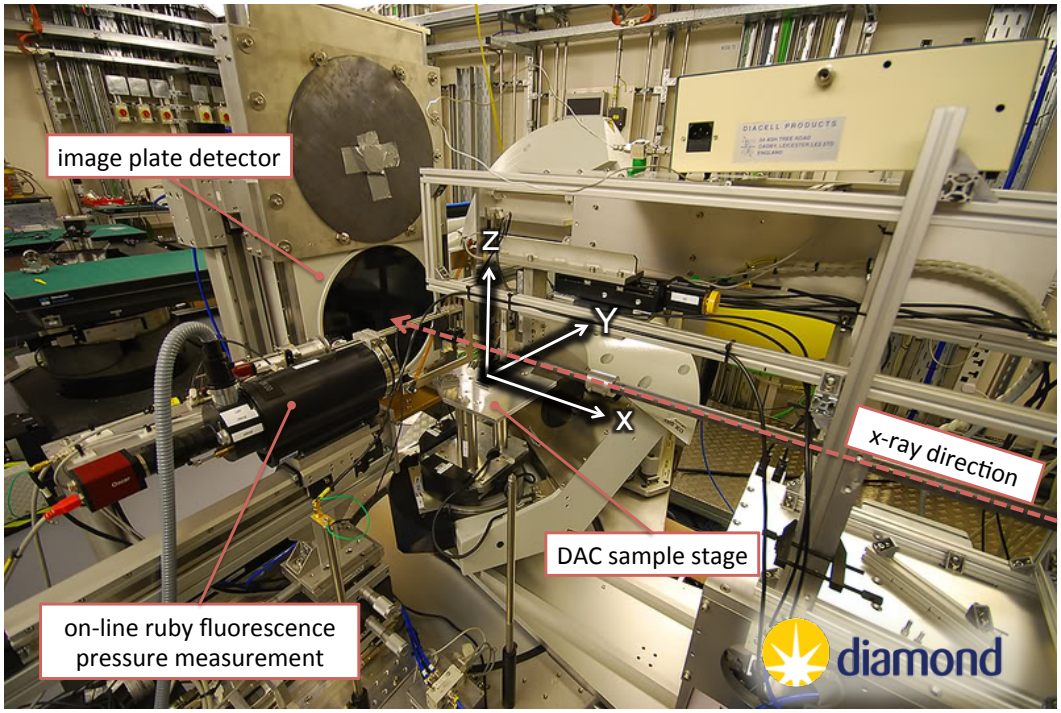

Figure 3.11: Photograph of the experimental hutch on beamline I15, at the Diamond synchrotron, Oxfordshire, UK. Important components on the beamline are labelled.

For high-pressure powder x-ray diffraction studies, an area detector is essential, as it enables the whole Debye-Sherrer diffraction pattern to be collected simultaneously. The detector is placed 300-500 mm behind the sample after the

beam stop - the small piece of Pb which is placed in front of the detector to stop the intense primary beam that has not been diffracted by the sample. Two kinds of area detector have recently been used in this field: an image plate (IP) and a charge couple device (CCD) detector.

An image plate (IP) is a plastic film consisting of doped phosphoric material ($BaF(Br,I):Eu^{2+}$) in which trapped colour centres are created by incident x-rays. When illuminated by a He-Ne laser, the trapped electrons decay and visible light is emitted. The laser is scanned over the image plate in a raster or spiral pattern resulting in a digitised 2D image of the diffraction pattern. The pixel size is typically 100 μm.

CCD detectors have some advantages over image plates, in particular their much shorter readout time ($\sim$1200 msec for a CCD and 80 sec for an IP). However, CCDs are typically smaller than image plates and must therefore be placed closer to the sample in order to collect the full diffraction image. This reduces the resolution of the diffraction images. The electronic noise and background in a CCD detector is also higher than that obtained with an image plate detector. Almost all of the diffraction data presented in this thesis was collected with a MAR345 image plate detector made by MarResearch GmbH.

3.1.3.2 Data Collection

In this section I will describe the data collection methods used at the Diamond Synchrotron, Oxfordshire, UK, to obtain most of the diffraction data presented in this thesis.

Equipment Calibration Before collecting any diffraction data from a sample, the diffraction setup was calibrated with a silicon standard sample[7]. The Si standard was aligned and exposed to the x-ray beam, resulting in a powder x-ray diffraction pattern. From the known lattice parameters, and the known incident x-ray wavelength (set via an absorption edge) the sample-to-detector distance, the beam centre position, and the tilt of the detector to the incident beam can be obtained using a program called "FIT2D[8]". For ruby fluorescence pressure

[7]Silicon standard sample is silicon powder obtained from National Institute of Standards and Technology (NIST) with code SRM640. It is supplied as a reference standard, with known calibrated lattice parameters.

[8]FIT2D is a free program running under LINUX and Windows, developed by Hammersley et al. [Hammersley et al., 1996], which is used worldwide for viewing and integrating 2D diffraction

measurements, the spectrometer system was calibrated using the emission lines from a neon lamp and the Raman peak from a Si single crystal. The zero-pressure position of the ruby fluorescense peaks was also determined.

Sample Alignment In order to ensure that the sample is perfectly centred on the x-ray beam, and that rotation around the vertical axis does not move the sample, and that all samples are the same distance from the detector, it is essential that the sample is centred on the rotation axis of the sample stage.

The sample is first centred relative to the x-ray beam in the y and z directions (y: across the beam horizontally, z: across the beam vertically, x: along the beam) by scanning the pressure cell across the x-ray beam while monitoring the intensity of the straight-through beam with a Si diode placed downstream of the DAC. As the sample is less absorbing than the gasket, a "top-hat" intensity profile is obtained, with the centre of the top-hat being the centre of the sample. This centres the sample in y and z. The sample is then rotated around the vertical axis to access a positive angle between 5° and 25°, the sample is rescanned in y, and the y-position of the centre of the sample noted. The y scan is then repeated at the equivalent negative angle, and the position of the sample centre is noted. If the sample is not located on the rotation axis, then these two centres will be at different y positions. The two y values are then used to calculate the necessary correction in the DAC position in x, and the two y scans at ±5-25° are then repeated at this new x position to ensure that they now give the same y value for the sample centre. At this point, the sample is centred on both the rotation axis and the x-ray beam.

Collecting Data The powder x-ray diffraction (PXRD) data shown in this thesis were collected using the image plate (IP) method (MAR345) on the high-pressure beamline ID27 at the ESRF and on I15 at the Diamond Synchrotron, and using a MAR555 flat-panel detector on beamline ID09A at the ESRF. The incident x-ray wavelengths were between 0.3 Å- 0.4 Å and the beam diameter was between 3 and 60 μm, depending on the beamline.

For every sample, PXRD data were first collected at ambient pressure to check sample quality. Then the DAC was pressurised in steps of 4 GPa from 0.1 GPa - 50 GPa for nano-Se, and in steps of 0.3 GPa from 0.1 GPa to 30 GPa for nano-Bi. In

images.

normal operation, two or three diamond-anvil cells were used in rotation during an experiment. This allowed data to be collected from one sample while the pressure was being increased in other samples and allowed to stabilise for ∼20 minutes.

The sample pressure was measured using the ruby fluorescence technique [Mao et al., 1986] immediately before and after performing x-ray diffraction, and the two values averaged. During the PXRD data collected, the samples were oscillated ±3° to ±5° around the vertical axis to improve the powder averaging. Data collection times were typically 5-10 seconds, a time which was optimised to give the most intense Bragg reflection just below the saturation limit of the detector, while also allowing very weak modulation reflections to be visible.

3.1.3.3 Data Analysis

To extract crystallographic information from the 2D PXRD patterns, the following procedure has to be carried out using the software detailed below.

1. The 2D diffraction patterns obtained at each pressure were viewed and integrated azimuthally using **FIT2D**, and reduced to 1D (x,y) data sets.

2. All 1D integrated diffraction profiles were plotted in a multi-curve waterfall plot using **Origin**, which enabled one to clearly see the changes in diffraction patterns caused by applied pressures, and by phase transitions.

3. In order to index the powder patterns, the 2θ values of selected diffraction peaks were determined and input into the **DICVOL** program [Boultif and Louër, 2004], which tries to determine the Bravais lattice and approximate unit cell parameters.

4. In order to determine the spacegroup, the indexed powder profiles were studied, and **systematic absences** were used to determine the spacegroup symmetry.

This information was then used for profile fitting of the diffraction data.

For Profile Fitting In order to extract crystallographic parameters, fitting of the 1D integrated diffraction profiles using the Le Bail and Rietveld methods was conducted using **JANA2006**[9] [Petricek et al., 2006].

[9]JANA2006 performs multivariate least-squares minimisation of an observed 1D integrated diffraction profile to a calculated diffraction profile according to just the obtained Bravais lattice,

1. The best-fitting lattice parameters and peak-shape parameters were obtained using the Le Bail method within **JANA2006**, utilising the spacegroup and preliminary lattice parameters obtained from the earlier analysis steps.

2. Then, Rietveld refinement of the profiles, again using **JANA2006**, was used to obtain the atomic coordinates for each of the component atoms. The quality of refinements was quantified from the value of the R-factor, residual/difference plots and visual comparison of the observed and the calculated diffraction patterns.

3. The crystal structures were then plotted using **ATOMS**[10].

For Peak Position Fitting In some cases, the lattice parameters were obtained from least-squares fitting to the d-spacings of the diffraction peaks rather than from profile fitting. This method can only by used with the known structure. The sequence of steps in this case was as follows.

1. Positions of each peak in d-spacing of the 1D integrated diffraction profiles were determined by **XRDA**[11][Desgreniers and Lagarec, 1998]. Each peak was fitted with a Gaussian or a Lorenzian function.

2. The known Miller indices (hkl) and the corresponding peak positions were input into **UnitCell**[12], which performed a least-squares fit to the lattice parameters.

3. However, **UnitCell** only works with commensurate crystal structures and incommensurate host-guest structure. In order to perform a least-squares fit to the positions of both the main and satellite reflections in the diffraction profile from an incommensurate modulated structure, and thereby obtain both the lattice parameters and the q-vector, a weighted least-squares fit was implemented in an **Excel** spreadsheet.

pre-selected space group and symmetry by adjusting a large amount of parameters, e.g., cell parameters, background signal, peak shape, etc.

[10]ATOMS is a program for drawing atomic structures, including crystals, polymers and molecules. More details can be found at [Ato, 2012].

[11]XRDA is a program used for determining position of peaks (2θ or d-spacing) in 1D integrated diffraction profiles.

[12]A non-linear least squares cell refinement program with regression diagnostics.

3.2 Crystallography of Incommensurate Structures

3.2.1 Aperiodic Crystals

It has been known for a long time that a material is crystalline if it gives sharp diffraction peaks, which means all intensity from the incident radiation will be concentrated at Bragg peaks. However, in 1991, the definition for "aperiodic crystals" was added to the definition of "crystal" in the International Union of Crystallography's Report of the Executive Committee [IUCr, 1992] as follows:

> *... In the following by 'crystal' we mean any solid having an essentially discrete diffraction diagram and by 'aperiodic crystal' we mean any crystal in which three-dimensional lattice periodicity can be considered to be absent. As an extension, the latter term will also include those crystals in which three-dimensional periodicity is too weak to describe significant correlations in the atomic configuration, but which can be properly described by crystallographic methods developed for actual aperiodic crystals ...*

Aperiodic crystal structures have been found to occur in minerals, metals, alloys (quasicrystals), proteins, and macromolecules [Chapuis, 2010]. Aperiodic crystals are classified as incommensurate modulated, composite structure (which will be called "host-guest structure" in the rest of this thesis) and quasicrystal according to [Janssen et al., 2007]. This thesis focuses only on their incommensurate structures. The definition of incommensurate structures given by [Caracas and Gonze, 2005] is as follows:

> *...The incommensurate crystals are materials where some local property exhibits a spatially periodic modulations with a wavelength that is incommensurate with respect to the lattice constants of a corresponding averaged underlying structures....*

In other words, an incommensurate structure is a structure which has a long range order but lacks periodicity. Caracas and Gonze [Caracas and Gonze, 2005] divided incommensurate structures into five classes of modulation: orientation, displacement, interface, composition and intergrowth; which is more than those classed by [Janssen et al., 2007]. However, in this thesis, only two

important classes are focused on, these are: incommensurate modulated structure (displacement) and incommensurate host-guest structure (intergrowth). Incommensurate structures in metals will be focused on in the next section.

Diffraction peaks of commensurate (periodic) structures have only main peaks, while diffraction patterns from incommensurate structures contain both main and satellite peaks. Therefore, an x-ray diffraction pattern from a periodic crystal is indexed from its Bragg reflections using integers. On the other hand, for an incommensurate structure, not only does its pattern have to be indexed by the main Bragg peaks using the method above but it also has to index the "satellite" peaks using irrational numbers. Generally, the Bragg peaks are expressed by equation (3.8).

$$\mathbf{H} = h\mathbf{a}^* + k\mathbf{b}^* + l\mathbf{c}^* + m_1\mathbf{q}_1 + m_2\mathbf{q}_2 + \cdots + m_d\mathbf{q}_d \tag{3.8}$$

Where $\mathbf{H}$ is the reciprocal lattice position of a Bragg reflection, $\mathbf{a}^*$, $\mathbf{b}^*$,$\mathbf{c}^*$ are the basis vector of reciprocal space, and h, k, l are integers (the Miller indices). Reflections ($\mathbf{H}$) with $m_i = 0$; ($i = 1, 2, 3,\ldots$) are called the main reflections, whereas reflections with $m_i \neq 0$; ($i = 1, 2, 3,\ldots$) are the satellite reflections.

3.2.2 Incommensurate Structures in Elements at High Pressure

Of the more than one hundred elements in the periodic table (Fig. 3.12), there are 16 elements, highlighted with a black border, which have been found to have an incommensurate structure only at high pressure.

In this study, two nano-elements[13] are focused on, namely selenium and bismuth nanoparticles (see Fig. 3.13).

In the bulk materials,

- Selenium has an incommensurate modulated structure from 28 GPa to at least 70 GPa [McMahon et al., 2004]. In that pressure range, the structure has an incommensurate "sine-wave like" modulation (to an average structure), and is an example of a "incommensurate modulated structure".

- Bismuth has an incommensurate host-guest structure from 2.7 GPa to 7.7 GPa [McMahon et al., 2007]. In this pressure range, some bismuth

[13]nano-elements: particles of the element that have a diameter on the nanometer scale.

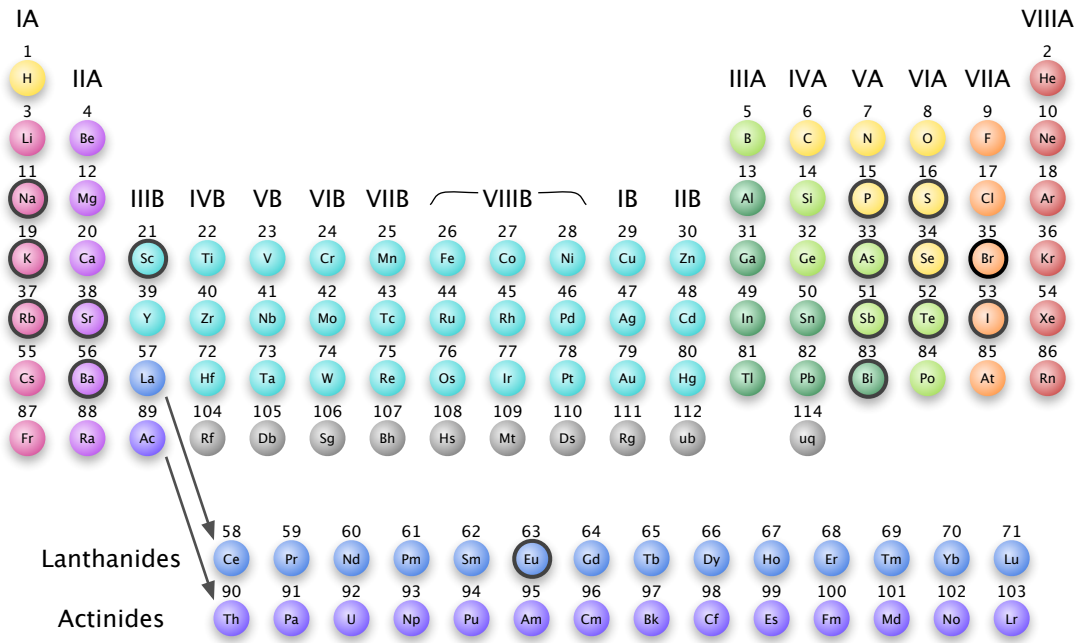

Figure 3.12: There are 16 elements (as labelled with black borders) known to have incommensurate structures at high pressure [McMahon and Nelmes, 2006, and references therein]. It should be noted that Eu has recently found to have incommensurate structure at high pressure [Husband et al., 2012].

atoms act as a host structure and some others as a guest structure. The host and guest structures are each commensurate, but they are incommensurate with respect to each other.

3.2.3 Incommensurate Modulated Structures

This structure type looks like a periodic structure, but with a "wave-like" incommensurate modulation (see Fig. 3.14). This type of structure can be found in some elements at high pressure; for example, the high-pressure phase of selenium is found to have an incommensurate monoclinic structure, Se-IV, which is stable from 28 GPa to at least 70 GPa [McMahon et al., 2004]. Moreover, Te-III is isostructural to Se-IV and is stable from 4.5 to 29.2 GPa [Hejny and McMahon, 2003]. (see incommensurate modulated structure of Se, Se-IV, diffraction pattern in Fig. 4.4 in Chapter 4).

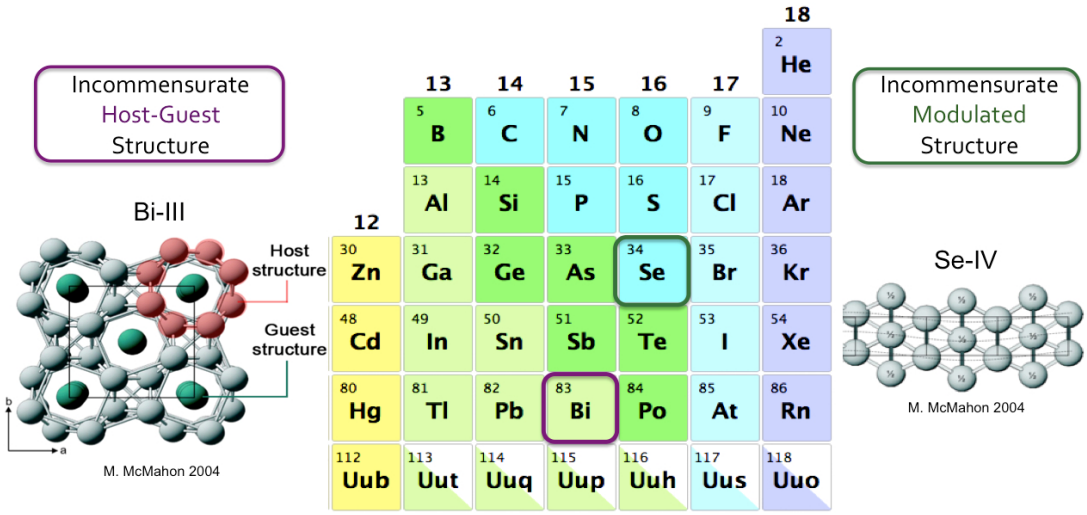

Figure 3.13: The elements of interest in this thesis are selenium and bismuth. Bulk selenium has an incommensurate modulated structure from 28 GPa to at least 70 GPa [McMahon et al., 2004]. Bulk bismuth exhibits an incommensurate host-guest structure from 2.7 GPa to 7.7 GPa [McMahon et al., 2007].

3.2.4 Incommensurate Host-Guest Structures

Incommensurate host-guest structures, also called incommensurate composite structures, are structures that consist of two different periodic crystal structures existing within each other, see Fig. 3.15. One of these periodic structures is called the "host" while the other is called the "guest".

This type of structure can be found in some other elements at high pressure; for example, Ba-IV from 12 - 25 GPa [Nelmes et al., 1999] and Rb-IV from 16 - 21 GPa [Lundegaard, 2008]. Bi-III has a body-centred tetragonal (bct) host and a bct guest structures from 2.7 - 7.7 GPa [McMahon et al., 2007].

3.3 Particle Size Determinations

To quantify the quality of purchased nanoparticles (NPs) or synthesised NPs, the size of the individual nanoparticles has to be measured efficiently and accurately. The following methods were used for this.

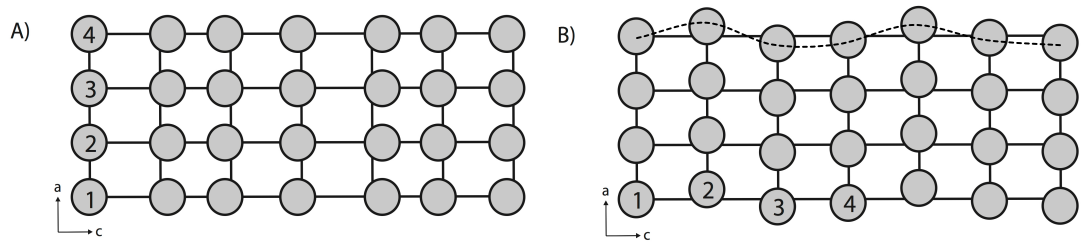

Figure 3.14: Incommensurate modulated structures with A) longitudinally and B) transversally modulated atomic displacement. The modulation can be define by sine function, $u = Asin(2\pi \boldsymbol{q} \cdot \boldsymbol{r})$ where A is the amplitude of the modulating wave u, $\boldsymbol{q}$ is the incommensurate wave vector and $\boldsymbol{r}$ is the position vector of an atom in three-dimensional space. Figure edited from [Lundegaard, 2008].

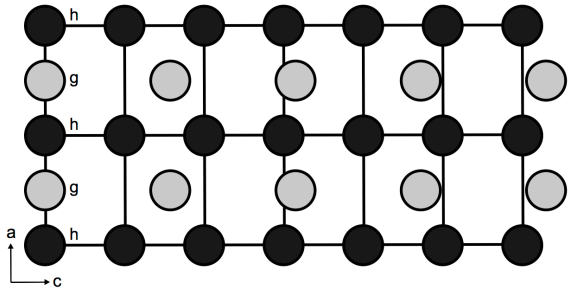

Figure 3.15: Diagram of an incommensurate composite structure showing the two different lattices repeat of the host and guest components [Lundegaard, 2008].

3.3.1 Dynamic Light Scattering (DLS)

Dynamic Light Scattering (DLS) is an indirect method to determine the size of the NPs. With this means, the NPs have to be suspended in a solution. The Brownian motion of the nanoparticles, caused by their collision with solvent molecules in random thermal motion, is related to their sizes. A schematic diagram of the experimental set up is shown in Fig. 3.16.

In a DLS measurement, a high intensity laser was used as a monochromatic light source. When the incoming beam hits the NPs which are moving randomly in Brownian motion, the variations in scattered intensities with time are detected at a fixed scattering angle (typically 90° to incident beam). The correlation of the intensity and time is analysed resulting in the size of the NPs.

The advantage of the DLS method is its ease of sample preparation. However,

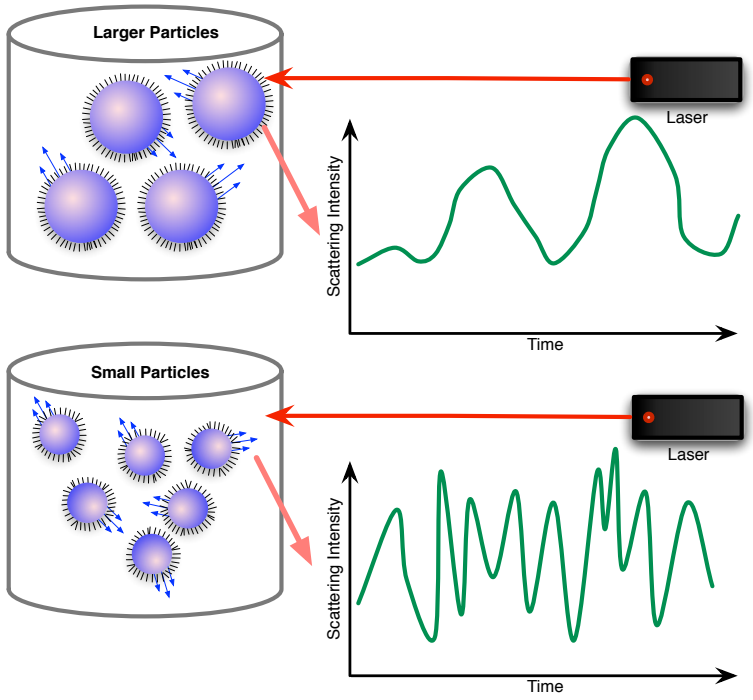

Figure 3.16: Schematic diagram of a Dynamic Light Scattering (DLS) experiment. The upper diagram shows a hypothetical result for large particle sizes; the lower for small particle sizes.

it should be noted that the result of DLS is the average particle size for a whole system with a certain size distribution. Therefore, the reported size might not be the actual size of each particle. In particular, the surface structure, such as the stabiliser used in nanoparticle production, also contributes to the measurement, resulting in an overestimation of the NPs size.

Dynamic Light Scattering (DLS) is the accessible technique available to measure the NPs size available at the School of Physics and Astronomy at The University of Edinburgh. The method was used to determine the size before progressing to a more accurate re-examination of the size by transmission electron microscopy (TEM).

For the work in this thesis, the NP samples were prepared by mixing 0.01 g of the NPs with 5.2 g of 100% ethanol. Next, the mixtures were sonicated for about 1 minute. Then a sample was put in a cuvette and placed in the DLS sample chamber for the process of measurement.

3.3.2 Transmission Electron Microscope (TEM)

Transmission Electron Microscope (TEM) works like a slide projector. In a typical TEM, a tungsten filament produces an electron beam in a vacuum chamber located the top of the microscope. An electrical potential accelerates emitted electrons from the electron gun to follow the vertical vacuum path and to travel through electromagnetic fields and collimators, which focus and narrow the beam down toward the very thin (less than 100 nm) slice of material (in this case, NPs do not need this special preparation). Only certain parts of the electron beam are transmitted from certain parts of the sample. These transmitted electrons are then detected by a phosphor screen, CCD or film on the other side to produce an image.

The TEM provides more accurate size determination than DLS, because the size of each particle can be measured individually using TEM.

Samples for the TEM measurement were prepared in the same way as for the DLS experiments. TEM copper grids were placed into the mixtures of nanoparticles and solvent (in this case ethanol), after which the solution was left to evaporate, leaving the dry NPs to stick to the grid.

The TEM used for the NPs characterisation in this thesis is located at the Institute of Molecular Science at The University of Edinburgh. It should be noted that access to the TEM was limited.

3.3.3 Scanning Electron Microscope (SEM)

A scanning Electron Microscope (SEM) is a microscope that uses an electron beam to form an image of a sample from a raster scan of the sample's surface. In a typical SEM, a beam of electrons is produced by a hot filament (electron gun) at the top of the microscope. An electric potential drives electrons from the electron gun to follow a vertical path (in vacuum) and pass through electromagnetic lenses and collimators which focus and collimate the beam toward the sample. Upon striking the sample surface, the sample emits a secondary electron, an auger electron, and a back-scattering electron, along with an x-ray photon.

The most common mode of using SEM is to image the sample with the secondary electron. SEMs typically have at least a secondary electron detector. However, the more expensive SEMs also have auger electron, back-scattering

electron, and x-ray detectors.

Unlike TEMs, SEMs can image the surface of NPs because their mode of operation uses a lower incident electron energy compared to that of TEMs (see more details in Appendix B.2.1). Nevertheless, an SEM is not as good as a TEM for size determination because the edges of particles cannot be seen clearly from the SEM image. Moreover, an SEM normally has lower magnification than a TEM. In this thesis, samples were prepared for SEM measurement by diluting them in a solvent (toluene or isooctane), after which the sample is spin-coated onto a conductive material; in this case, a silicon wafer.

SEM measurements for this thesis were conducted at the School of Physics and Astronomy at the University of St. Andrews. The method was the most readily accessible, so it was preferentially used to determine the NPs' size, while the NPs syntheses were performed at the University of St. Andrews (see Chapter 5 for more details).

3.3.4 Powder X-Ray Diffraction (PXRD)

Powder x-ray diffraction can give an estimate of the average NPs' diameter from the broadening of the diffraction peaks via the Scherrer equation (3.9).

$$\tau = \frac{\kappa\lambda}{\beta cos\theta} \tag{3.9}$$

where τ is the mean size of the crystalline domains (in this case, size of the NPs), κ is the dimensionless shape factor (it has a typical value of about 0.9, but varies with the actual shape of the crystallite), λ is the incident x-ray wavelength (Å), β is the line broadening at half maximum intensity (FWHM) in radians of 2θ scale, and θ is the Bragg angle [Patterson, 1939]. It is important to note that the Scherrer equation is limited to nano-scale materials, because it is not applicable to particles larger than 0.1 μm.

3.3.5 Evaluations of Size Determination Methods

An accurate determination of the size of the nanoparticles was a crucial step in both the synthesis of bismuth nanoparticles, and for the size-dependent study of incommensurate structures in this thesis. Without a reliable and accurate size measurement procedure, it would have been very difficult to optimise the bismuth

synthesis procedures and to establish whether there is a relationship between particle size and structure and/or transition pressure.

The best way to determine the size of NPs is to use a TEM or an SEM. In this study an SEM was more easily accessible, although it is generally considered to have less ability than TEM. However, the relative availability of the SEM and the reduced cost (free of charge vs. £40 per hour for the TEM) made the SEM the more appropriate choice for this work, even with its diminished ability at NP size determination.

The use of XRD to determine NPs size has the advantage that it could be used to determine the composition of the NPs at the same time. However, the NPs size obtained from the Scherrer equation (3.9) is the average size for the whole volume of the sample probed by the x-ray beam, and not the size of individual particles. As a result, this method cannot provide any information on the distribution of sizes within the sample.

DLS is the quickest way to measure the size of NPs. However, the NPs have to be well dispersed in solution, have monodispersity, and have no organic contamination on their surface. This is because with DLS, the largest NPs or the largest parts in the mixture will dominate the light scattering, resulting in an overestimation of the size.

In summary, for samples that have not previously been tested, an SEM was used first to see the morphology of the NPs together with XRD to probe the elemental composition and the structure of the sample. The TEM was then used to obtain the most precise determination of the diameter of NPs due to the well-defined edges given in the TEM image, and its higher resolution and higher magnification compared to the SEM. Finally, DLS was used only on known and well-dispersed samples.

3.4 Conclusions

Using diamond-anvil cells as the pressure generator and the x-ray diffraction techniques on a synchrotron as the probing tool is the most efficient method by which to study the crystallographic structure of materials at high pressure. The incommensurate structures recently observed in bulk elements at high pressure have been revealed using these techniques. The study of incommensurate

structures in nanomaterials can also be carried out using the same methods. However, the nanomaterials have to be carefully characterised using in-house x-ray diffractometers and the nanoparticles' size measured carefully by SEM, TEM, or DLS before performing the high-pressure x-ray diffraction experiment.

Chapter 4

Studies of Commercial Selenium, Lyophilised Selenium and Bismuth Nanoparticles

4.1 Introduction

Before starting a programme of high-pressure powder x-ray diffraction (HP-PXRD) experiments, it was vital to find good quality nanomaterial samples. The ideal nanoparticles (NPs) for the planned experiments must be monodispersed[1] and spherical in shape, as shown in Fig. 4.1.

To obtain such samples, one can either buy them from a reputable supplier or synthesise them oneself. The advantages of the former method are the high quality of nanoparticles available, the large amount of time saved, the lower price compared to the self-synthesis method, a reliable service, and technical assistance. However, there is no guarantee that the company will have nanomaterials of the desired chemical composition, or the sizes that are needed. On the other hand, if one synthesises the nanoparticles oneself, one can be assured of getting the composition and sizes required. However, this option could be time consuming and expensive, and needs experience in nanoparticle synthesis.

At the start of this thesis, only three kinds of elemental nanoparticles whose

[1] A collection of NPs is called monodispersed if the NPs have the same size and shape (or close to with a narrow size distribution). On the other hand, a sample of NPs that have an inconsistent size and shape is called polydispersed.

bulk phases were known to have incommensurate phases at high pressure were available commercially: selenium, lyophilised selenium and bismuth. Therefore, samples of all three were purchased and used in HP-PXRD experiments.

The three samples purchased for this study have different sizes (in diameter) as described below:-

- Selenium nanoparticles (nano-Se)[2] of size 10 nm, 20 nm, 30 nm, 40 nm, 70 nm and 100 nm.
- Lyophilised selenium nanoparticles (lyophilised nano-Se) of size 10 nm.
- Bismuth nanoparticles (nano-Bi) of size 40 nm and 80 nm.

The "sizes" reported above are the values obtained from the corresponding suppliers. For each sample, HP-PXRD experiments were conducted and the samples were characterised subsequently to determine their size and morphology, using the appropriate methods which are described later in sections 4.2.2, 4.3.2 and 4.4.2.

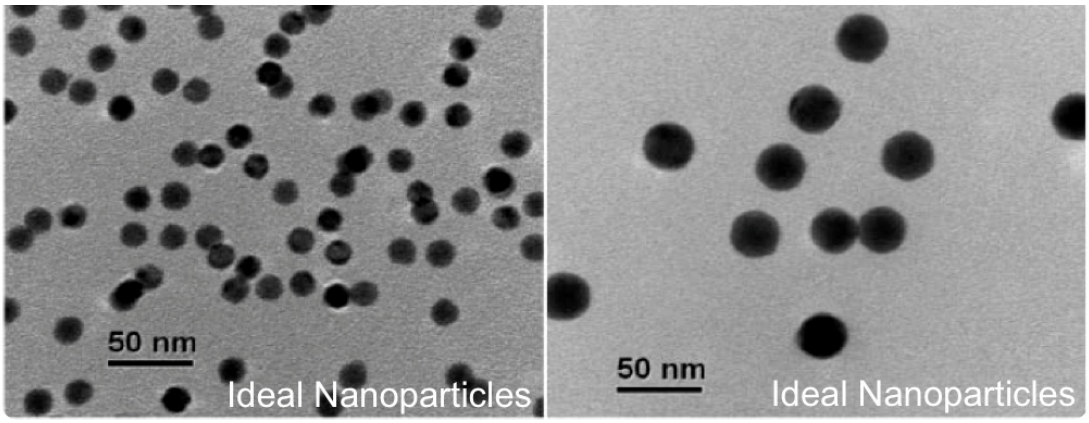

Figure 4.1: SEM images showing the ideal nanoparticles, which are monodispersed (low dispersity) and spherical. This type of nanoparticles is required for use in the HP-PXRD experiments. Images are edited from [Wang and Buhro, 2010].

[2]Only 10 nm and 70 nm were used in HP-PXRD experiments.

4.2 Selenium Nanoparticles (Nano-Se)

4.2.1 HP-PXRD Experiments

For this PhD project, two aspects of the phase transitions in nanocrystalline materials were to be studied: the (possible) variation of the transition pressures of different sizes of nanocrystals, and structural studies of nanocrystals along with crystallographic parameters in the (possible) incommensurate phase.

In this chapter, 10 nm-size selenium nanoparticles were used for testing the possibility of doing HP-PXRD experiments with a nanoparticle sample, and to determine whether the crystallographic properties of selenium nanoparticles (nano-Se) are different from those most recently reported in the bulk selenium (bulk-Se) [McMahon et al., 2004].

4.2.1.1 HP-PXRD Experimental Set Up and Data Collection

For this initial study, HP-PXRD experiments were performed at the ESRF synchrotron on beamline ID09A with nano-Se of size 10 nm. Powder x-ray diffraction data were collected on a MAR555 amorphous-Se detector, using an incident x-ray wavelength of 0.37378 Å, and an incident beam diameter of 3 μm.

The nano-Se sample was material of 99% purity obtained from the Canano LLC company. The sample was loaded with a methanol-ethanol (4:1) PTM into a 125-μm-diameter sample hole in a tungsten gasket in a DXR-6 diamond-anvil cell (DAC). The pressure cell was equipped with diamond anvils with 300 μm culets mounted on beryllium backing seats. A small piece of ruby was enclosed with the sample for pressure measurement via the ruby fluorescence technique [Mao et al., 1986]. X-ray diffraction data from the nano-Se were collected using $\pm 2^\circ$ oscillating scan around the vertical axis, with an exposure time of 30 seconds.

At ambient temperature, the 10 nm nano-Se were pressurised from ambient pressure up to $\sim$50 GPa, in 13 pressure steps. As illustrated in Fig. 4.2, the diffraction patterns showed quite smooth and clean powder rings. However, it should be noted that there were a fair amount of diffraction spots, which indicated the existence of larger crystallites. The diffraction patterns collected at each step of pressure were integrated azimuthally using **FIT2D** [Hammersley et al., 1996].

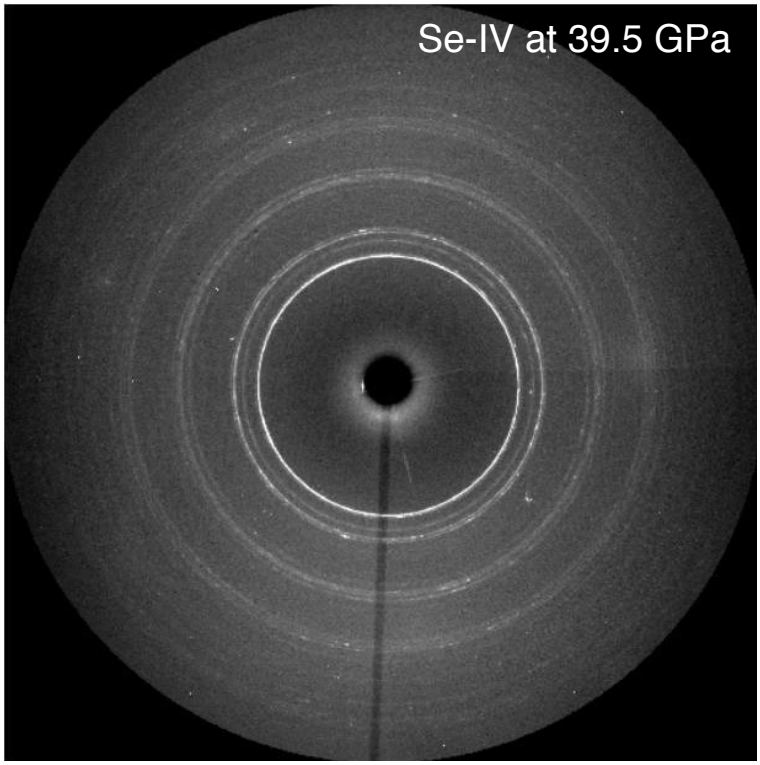

Figure 4.2: 2D diffraction image from the incommensurate phase of nano-Se at 39.5 GPa. Smooth rings indicate the good quality of the powder. However, there is some degree of spottiness which arises from some large crystallites (with a size >1 μm) in the nano-Se sample.

4.2.1.2 HP-PXRD Results and Discussion for 10nm nano-Se

The integrated diffraction patterns were plotted as a multi-curve waterfall graph from which it is possible to see the changes in the diffraction patterns brought about by the pressure applied. From the major changes in diffraction pattern on pressure increase seen in Fig. 4.3, the transition pressures were determined to be 19.9(1.8) GPa and 31.7(2.2) GPa on pressure increase.

For structure determination of the Se-IV observed above 31.7 GPa[3], the diffraction profile collected at 39.5 GPa was refined using the Le Bail [LeBail, 1992] method in **JANA2006** [Petricek et al., 2006], as seen in Fig. 4.4. The structure of Se-IV observed previously in a bulk sample [McMahon et al., 2004] was used as a starting model. The structure of the nano-Se-IV was found to have the same symmetry as bulk Se-IV, and is an incommensurate body-centred monoclinic cell, with superspacegroup $I2/m(0q0)s0$ and lattice parameters $a = 3.2818(4)$ Å, $b = 4.0076(6)$ Å, $c = 2.5845(3)$ Å, $\beta = 112.968(15)^\circ$ and $q = 0.2520(9)$ at 39.5 GPa. The Le Bail fit of this structure to the data is shown in Fig. 4.4, and is excellent with $R_{wp} = 0.56\%$.

All diffraction patterns of Se-IV collected between 29.6 GPa and 51.1 GPa, were then refined. From this analysis, the incommensurate wave vector (q-vector) was obtained from each diffraction profile and these are plotted against pressure, together with the q-vector values from the bulk [McMahon et al., 2004], in Fig. 4.5. Surprisingly, the q-vector behaviour of nano-Se is completely different from that of bulk-Se as reported in [McMahon et al., 2004]. In bulk Se-IV, the q-vector initially decreases rapidly from a value of 0.305 at 32 GPa to 0.280 at 50 GPa, and then varies little with pressure. In the nano-Se, the q-vector *increases* with pressure, from 0.220 at 30 GPa to 0.270 at 50 GPa. Due to the completely different and unexpected behaviour of the q-vectors seen in the nano and bulk materials, further careful and detailed analysis was conducted, as described in the following section.

4.2.1.3 Crystallographic Structural Refinement Investigation

The determination of the lattice parameters and q-vector described above used the Le Bail refinement of the full diffraction profiles using JANA2006, a refinement

[3]The transition pressure was calculated as the average between the last pattern with no high pressure phase and the first pattern showing some peaks of the high pressure phase.

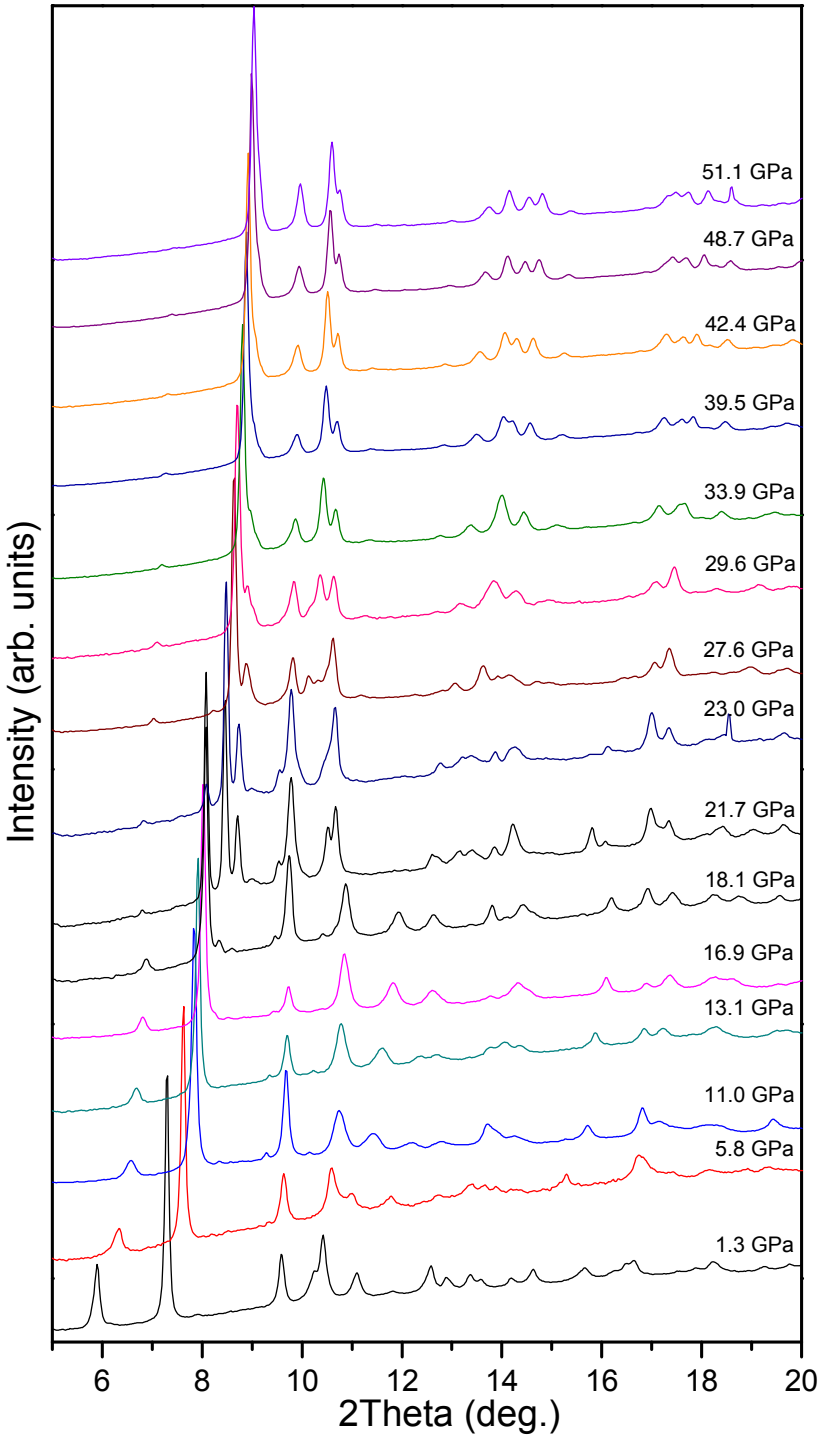

Figure 4.3: Waterfall plot showing integrated diffraction patterns obtained on pressure increase from 10 nm nano-Se. Phase transitions take place at 19.9(1.8) and 31.7(2.2) GPa.

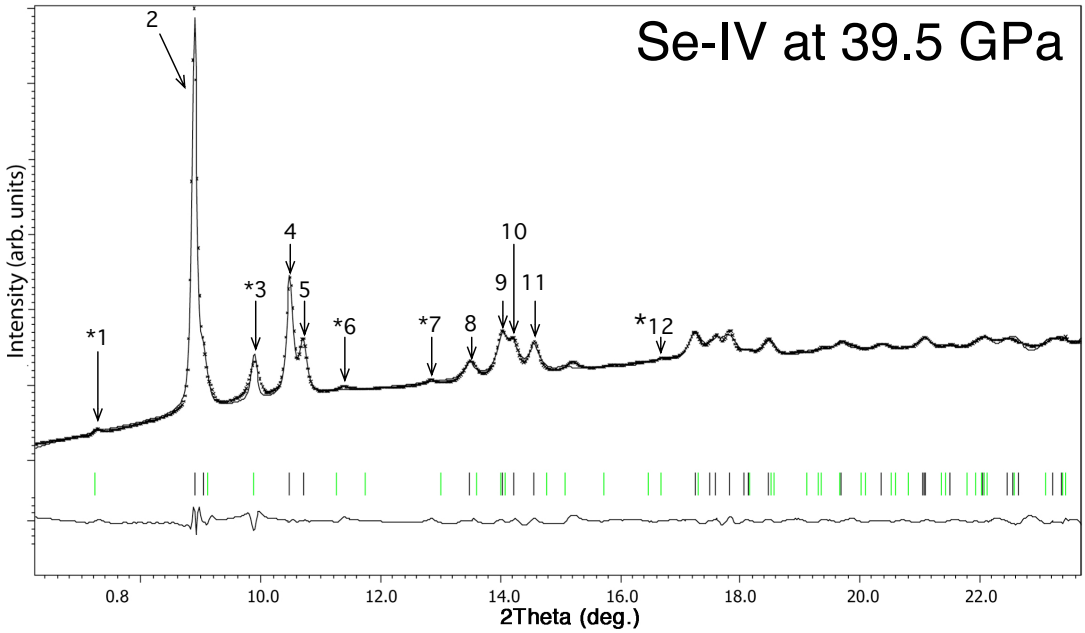

Figure 4.4: Le Bail fit to an integrated diffraction pattern from nano-Se at 39.5 GPa. The observed (dotted line) and calculated (solid line) diffraction patterns are shown. The difference between the experimental and calculated patterns is presented at the bottom of the graph. The tick marks below the pattern show the positions of main peaks (black) and satellites peaks (green). Significant diffraction peaks are labelled in order of decreasing d-spacing. The asterisks (*) identify the incommensurate satellite peaks.

package specifically written to analyse diffraction data from incommensurate structures. The Le Bail profile-fitting method minimises the difference in *intensity* between the observed and calculated profiles by adjusting the large number of parameters which affect calculated intensity, such as cell parameters, background, peak shape, q-vector and amplitude of the incommensurate modulation.

However, in order to determine only the lattice parameters and q-vector, which depend only on the positions of the diffraction peaks, but not their intensity, one can adjust those parameters that minimise the differences between the *positions* of the Bragg peaks. While software such as Unitcell [Holland and Redfern, 1997] exists to refine the lattice parameters of a commensurate structure from indexed peak positions, such software cannot deal with incommensurate structures, so simultaneous refinement of the q-vector and lattice parameters was therefore conducted using least-squares refinement using a spreadsheet.

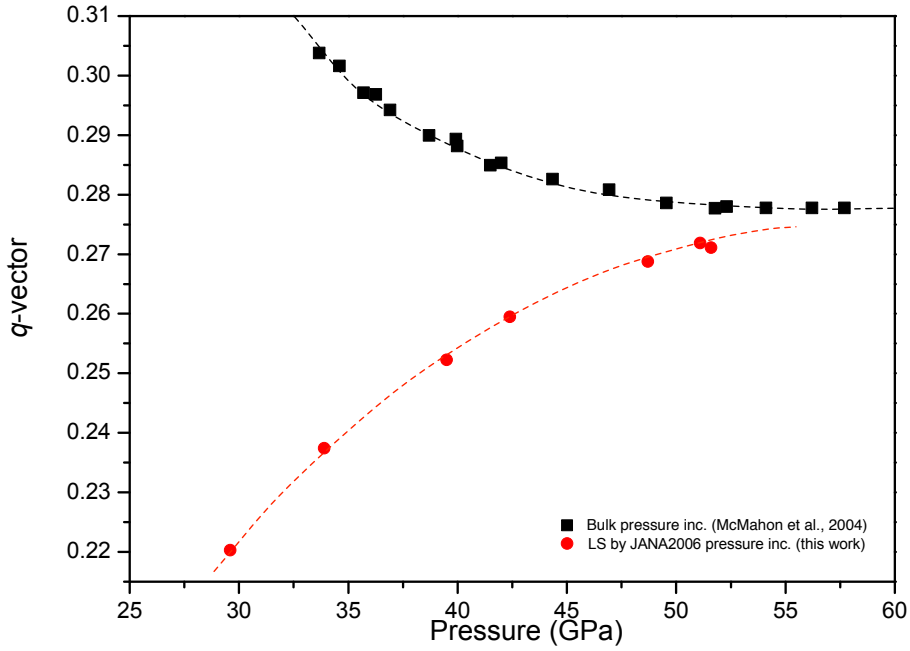

Figure 4.5: The pressure dependence of the q-vector of 10 nm-Se-IV (●) analysed by JANA2006 and bulk-Se-IV (■) analysed using JANA2000 (an older version of JANA2006). The bulk-Se-IV data are from [McMahon et al., 2004]. The dashed lines are guides to the eye. The uncertainties in the q-vector are smaller than the symbols used to plot the data, while the uncertainties in pressure are not more than 1 GPa.

These two methods (Le Bail fitting to the diffraction profile, and least-squares refinement of indexed peak positions) should, of course, give the same lattice parameters. However, previous experience shows that in the Le Bail method, the best overall fit is often obtained by fitting the strongest peaks at the expense of the weaker peaks, which includes the incommensurate satellite reflections. This bias does not affect the fitting of peak *positions*, as no information on the peak intensities is used in this method, and strong and weak peaks are therefore treated equally.

To investigate the differences in the best-fitting parameters obtained from the two different analysis methods, each was used to analyse nano-Se diffraction data collected on beamline ID09A at the ESRF. Four sets of data were collected at the beamline, namely compression and decompression of both 10 nm and 70 nm-sized nano-Se samples (see section 4.2.1.7).

4.2.1.4 Process of Refinement

JANA2006: Nano-Se 2D diffraction patterns at each pressure were integrated azimuthally and the resulting 2θ vs. intensity data were fitted using the Le Bail method in JANA2006. Initial values for the cell parameters and q-vector were taken from [McMahon et al., 2004].

Spreadsheet: From the same azimuthally-integrated data as used above, the peak positions of both main and satellite reflections were obtained by fitting Gaussian or Lorentzian peak shapes (as appropriate) using the XRDA peak-fitting program. Again using initial values for the cell parameters and q-vector taken from McMahon et al. [McMahon et al., 2004], initial estimates were made of the calculated positions of the same peaks. The differences between the observed and calculated positions were then minimised using a least-squares(LS) algorithm within Excel. No information on the intensity of the diffraction peaks was given.

4.2.1.5 10 nm Nano-Se Results and Discussion

The compression data from the 10 nm nano-Se were analysed first. Those patterns from the Se-IV phase were read into JANA2006 and refined using superspace group $I2/m(0q0)s0$ as in [McMahon et al., 2004]. The resulting dependence of the q-vector with pressure is shown in Fig. 4.5.

As was observed in the initial analysis, the q-vector increases with pressure, from 0.22 at 30 GPa to 0.27 at 50 GPa. At approximately 37 GPa, the q-vector passes through the commensurate value of 0.25, with no apparent lock-in or discontinuity in the pressure dependence.

The completely different trend compared to that seen previously in bulk-Se could result from the nanoparticle nature of the material, and would be a striking example of a structural difference between a bulk and nanomaterial. However, as discussed previously, it might also arise from a problem with fitting the data. To distinguish between these two possibilities, the pressure dependence of the q-vector was also determined by least-squares fitting to measured peak positions (d-spacing) from Excel spreadsheet. Surprisingly, the pressure dependence of the q-vector obtained from this second method shows a completely different trend to that obtained using profile fitting with JANA2006 as seen in Fig. 4.6.

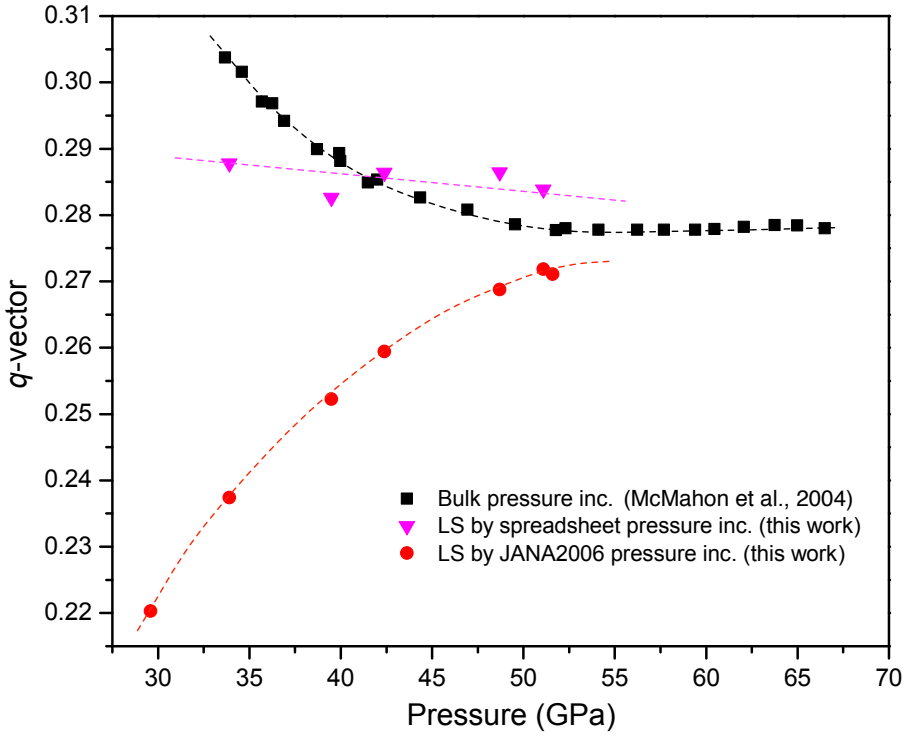

Figure 4.6: The q-vector values of bulk-Se (■), 10 nm nano-Se analysed with profile fitting using JANA2006 (●), and 10 nm nano-Se analysed by fitting to peak positions (▼). The dashed lines are guides for the eye. The uncertainties in the q-vector using JANA2006 are smaller than the symbols used to plot the data, while the uncertainties from the least-squares fitting in the spreadsheet are 0.002. The uncertainties in the pressure are no more than 1 GPa.

4.2.1.6 Why Do The Two Methods Give a Different Trend in q-vector?

To answer this question, a comparison was made between the calculated peak positions determined from the lattice parameters obtained from the Le Bail fit in JANA2006, and from the LS fitting to d-spacing in the Excel spreadsheet. The *calculated* peak positions from the two methods were then subtracted, peak-by-peak, from the *observed peak* positions, as determined from individual peak fitting. The differences were then squared to obtain positive values, and the resulting discrepancies, identified by the peak numbers labelled in Fig. 4.4, are shown in Fig. 4.7.

As can be seen in Fig. 4.7, there are large discrepancies between the observed and calculated positions of the three satellite peaks *1, *6, and *7 when using

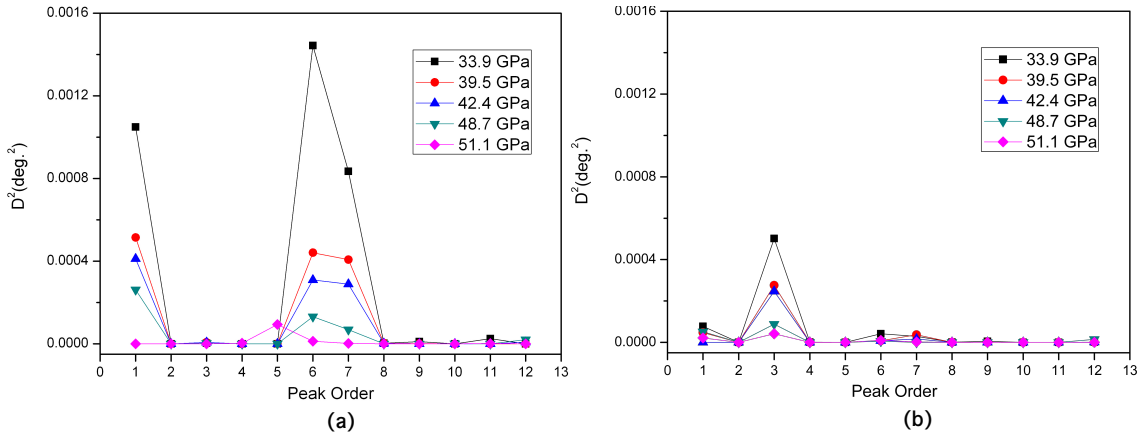

Figure 4.7: Discrepancies of peak 1-12 (as labelled in Fig. 4.4) between the observed and calculated profiles refined by JANA2006 (a) and from the Excel spreadsheet (b) of 10 nm nano-Se.

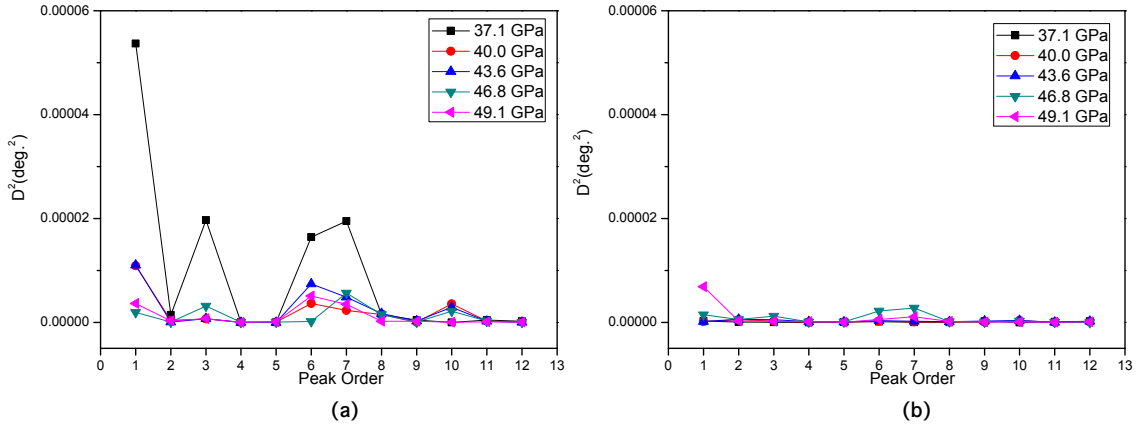

Figure 4.8: Discrepancies of peak 1-12 (as labelled in Fig. 4.4) between the observed and calculated profiles refined by JANA2006 (a) and from the Excel spreadsheet (b) of 70 nm nano-Se. Note that the y-scale in this figure is 32 times smaller than that of Fig. 4.7.

JANA2006. In contrast, the LS fitting to the d-spacings from Excel spreadsheet shows a substantial difference only in satellite peak *3 (as shown in Fig. 4.4). Note also that the maximum discrepancy obtained when fitting to the d-spacings is at least a factor of 2 smaller than that obtained when using JANA2006. The different discrepancies arise from the different methods used to fit the patterns. JANA2006 aims to minimise the overall intensity differences, and it fits the stronger (non-

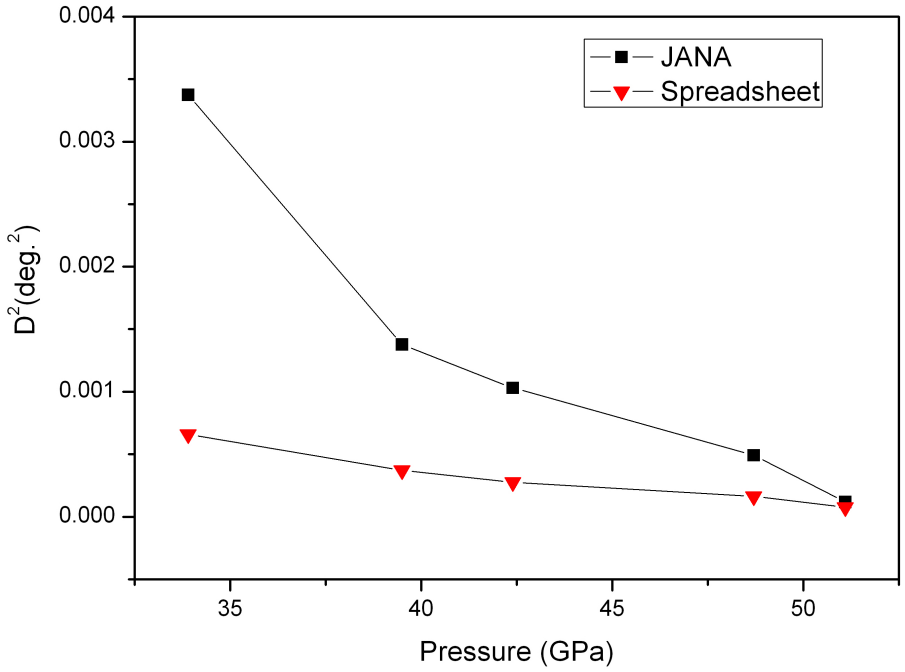

Figure 4.9: Trend of total discrepancies between experimental diffraction pattern and calculated pattern obtained from JANA2006 (■) and from the Excel spreadsheet (▼) of 10 nm Se.

satellite) peaks at the expense of the weaker (satellite) peaks. JANA2006 fits peak *3 reasonably well because it is the strongest of the satellite peaks (at 39.5 GPa the peak intensity of *3 above background is 152 counts while those of *1, *6, *7 are 32, 18 and 27 counts, respectively). Meanwhile, LS fitting to the d-spacings from Excel spreadsheet treats all peaks equally, no matter how intense they are, and whether or not they are satellite peaks. As a result, peaks *1,*6,*7 are very well fitted, while peak *3 has the only substantial misfit, although it is at least a factor of two smaller than the largest misfits obtained when using JANA2006. Note also from Fig. 4.9 that the size of the total discrepancies[4] from both methods decreases at higher pressure. This suggests that the two analysis methods will agree more with each other at the higher pressure, which is indeed what happens, as can be seen in Fig. 4.6 and Fig. 4.9.

More analysis was conducted to determine the influence of peak *3 on the lattice parameters and q-vector, and two investigations were performed (Fig. 4.10).

[4]The summation of discrepancies from every peak (peak 1 to 12) labelled in Fig. 4.4.

In the first, LS fitting to peak positions was performed, but with peak *3 omitted. This resulted in a slight increase in the value of q obtained at all pressures, and a generally poorer agreement with the values obtained from bulk-Se. In the second analysis, LS fitting to the peak positions was performed, but this time the only incommensurate peak included was *3, and so the value of q depended only on this peak. As expected, the values of q obtained were very close to those obtained when using JANA2006, where the determination of q is dominated by the high intensity of peak *3.

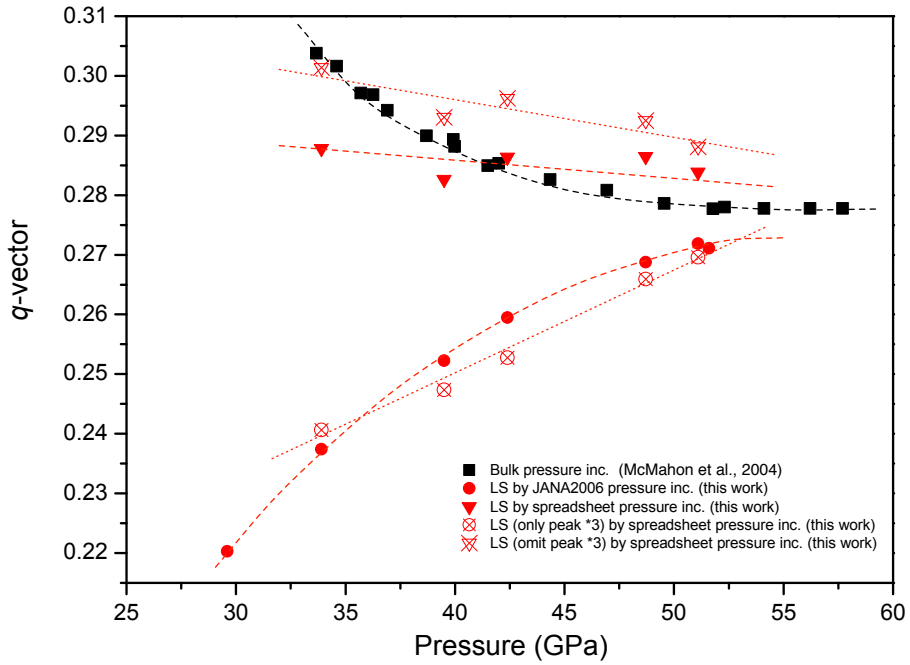

Figure 4.10: Pressure dependence of the q-vector of 10 nm nano-Se-IV and, for comparison, of bulk Se-IV [McMahon et al., 2004]. Analysis of the nano-Se-IV was performed using profile fitting with JANA2006 (●) and by LS fitting to the measured d-spacings of both main and satellite peaks (▼). Further analyses were conducted LS fitting to d-spacings by omitting satellite peak *3 (⧖), and also omitting all incommensurate peaks except *3 (⊠). The dashed lines are guides to the eye. The uncertainties in the q-vector using JANA2006 are smaller than the symbols used to plot the data, while the uncertainties from the least-squares fitting in the spreadsheet are 0.002. The uncertainties in the pressure are not more than 1 GPa. It is worth mentioning that "LS by JANA2006" seen in the graph's legend refers to the profile fitting which also uses least square(LS) method to obtain the minimum difference between observed and calculated diffraction profiles.

From Fig. 4.10, it is clear that the position of satellite peak *3 behaves anomalously, leading to q-vectors that are different to those obtained from bulk Se-IV. However, there is no clear or obvious reason for this anomalous behaviour. The displacement of the position of peak *3 could be because of contamination from a material used for producing the nano-sample. However, no additional peaks are observed in the diffraction profiles, which strongly suggests that there is no obvious contaminant phase present.

Diffraction data collected from the 10 nm nano-Se sample on pressure decrease were also analysed. On pressure decrease, it shows almost the same trends of discrepancies in each peak of each method. The pressure dependence of the monoclinic cell parameters is shown in Fig. 4.11, as determined using JANA2006, and Fig. 4.12 as determined using LS-fitting to peak positions.

It is clear that the lattice parameters, i.e., a, b, c, β and q-vector, are not in good agreement with those obtained from bulk-Se, as reported in [McMahon et al., 2004]. One possible cause of this discrepancy is the pressure measurements obtained using the ruby fluorescence technique, and the pressure values and fluorescence spectra were therefore re-examined. At 48.7 GPa, the ruby fluorescence profile was a good doublet, reflecting a hydrostatic pressure (or at least not a non-hydrostatic pressure) in the sample. Therefore, close-to-hydrostatic conditions persisted up to 48.7 GPa, a pressure well beyond the hydrostatic limit of only $\sim$10 GPa [Klotz et al., 2009] for this PTM (16:3:1 Methanol:Ethanol:Water). As the spectra in the bulk-Se experiment were equally sharp (M.I. McMahon, Private Communication), non-hydrostatic pressures do not then seem able to explain the differences seen between the bulk- and nano-Se lattice parameters in Fig. 4.11 and Fig. 4.12.

However, it is clear that there is a considerable hysteresis in the measured lattice parameters, that the agreement between bulk and nano-Se samples is a lot better on pressure decrease than on increase, and that the data collected almost immediately after starting pressure decrease agrees very well with the bulk data. Such behaviour can arise if there are strongly non-hydrostatic conditions within the sample, particularly if the ruby crystal used to determine the pressure is "bridged" between the two diamond anvils. However, while this normally results in an over-estimation of the pressure on pressure increase, it also results in a broadening of the ruby fluorescence spectrum, which, as said, is not observed.

However, as pressure is decreased and the ruby stops being "bridged", more accurate pressures are once again observed. The observed behaviour is thus unusual, and unlike that seen previously in bulk materials. The most likely explanation for the different behaviour observed on pressure increase and decrease is the development of non-hydrostatic pressure effects on compression, and their disappearance on pressure decrease - even though this is not reflected in the broadness of the ruby fluorescence spectrum. However, relatively little is known about the effects of non-hydrostaticity in nano-crystalline samples, and a more systematic study of such affects would be needed before definitive conclusions could be drawn.

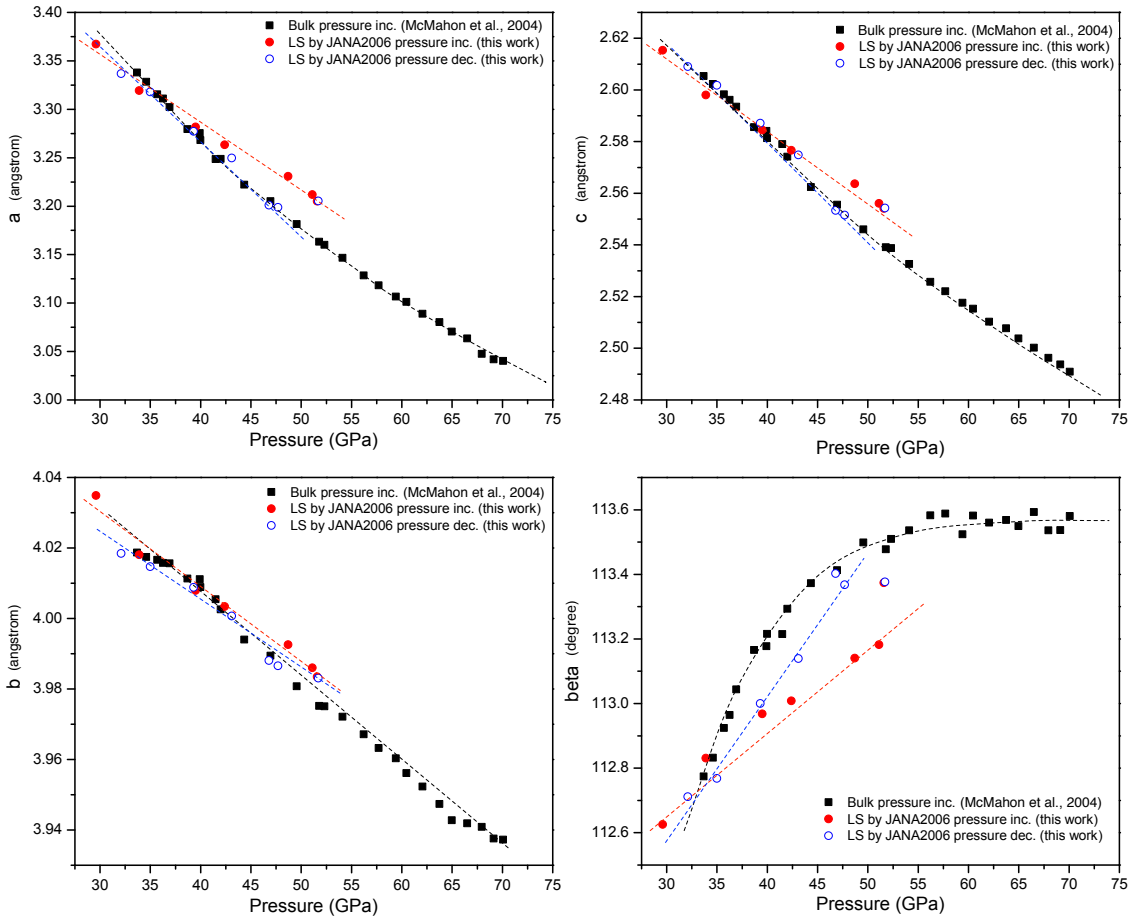

Figure 4.11: The lattice parameters of 10 nm nano-Se-IV as determined by JANA2006 on both pressure increase (●) and decrease (○). The corresponding values from bulk-Se-IV on pressure increase (■) are also shown [McMahon et al., 2004]. The dashed lines are guides for the eye. Uncertainties in the lattice parameters are smaller than the symbols used to plot the data points. The uncertainties in pressure are no more than ±1 GPa.

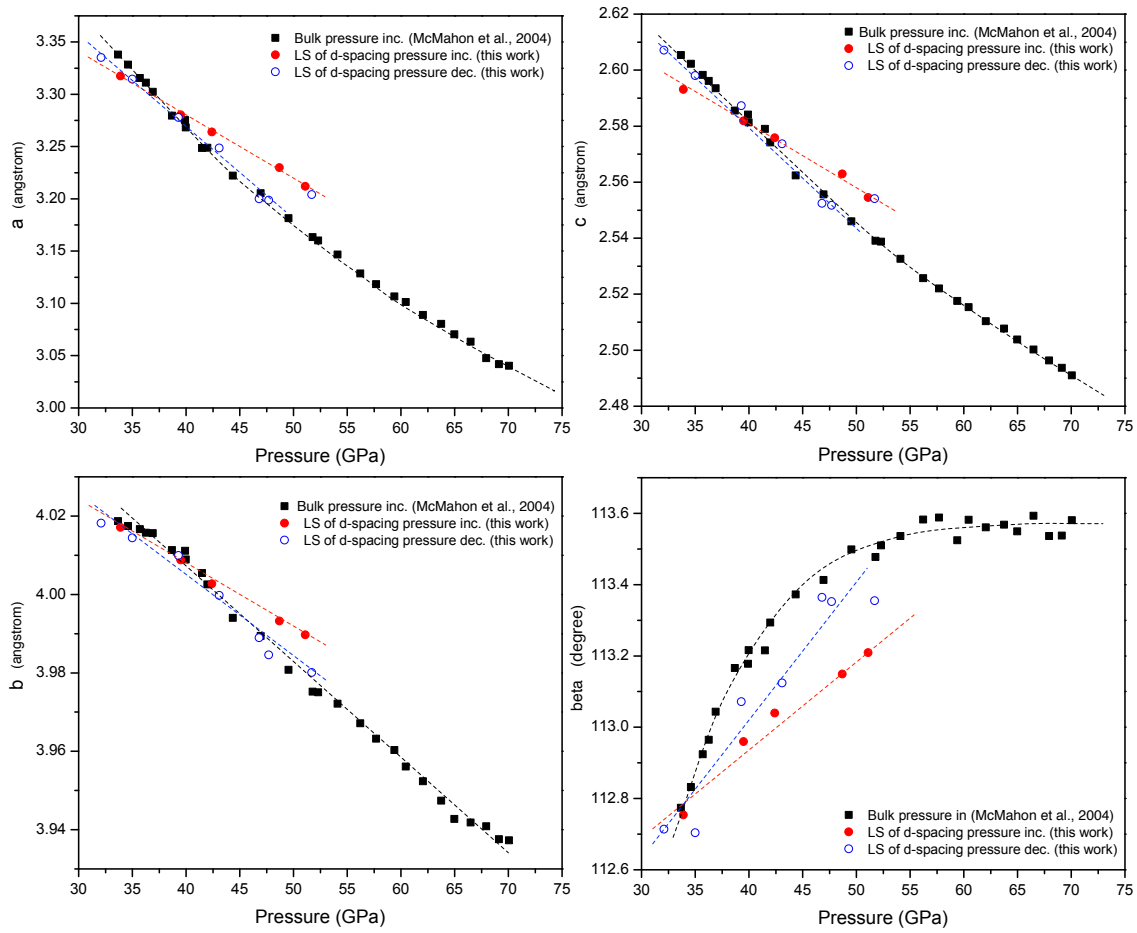

Figure 4.12: The lattice parameters of 10 nm nano-Se-IV as determined by least-squares fitting to the peak positions (d-spacing) from Excel spreadsheet on both pressure increase (●) and decrease (○). The corresponding values from bulk-Se-IV on pressure increase (■) are also shown [McMahon et al., 2004]. The dashed lines are guides for the eye. Uncertainties from LS fitting to d-spacing from Excel spreadsheet are 0.01 Å for a, b, c and 0.01 degree for beta. The uncertainties in pressure are no more than ±1 GPa.

4.2.1.7 70 nm nano-Se Results and Discussion

The same analysis methods as described for the 10 nm nano-Se were also applied to a sample with 70 nm crystallites. On pressure increase there is considerably better agreement between the q-vector (Fig. 4.13) and lattice parameters (Fig. 4.14) obtained from the nano and bulk samples, and from the q-vector and lattice parameters obtained by both profile fitting with JANA2006 and LS fitting to measured d-spacings from Excel spreadsheet. However, the sample again exhibits considerable hysteresis in the parameters on pressure decrease, with the result that the lattice parameters and q-vector obtained on pressure decrease are very different to those obtained on compression.

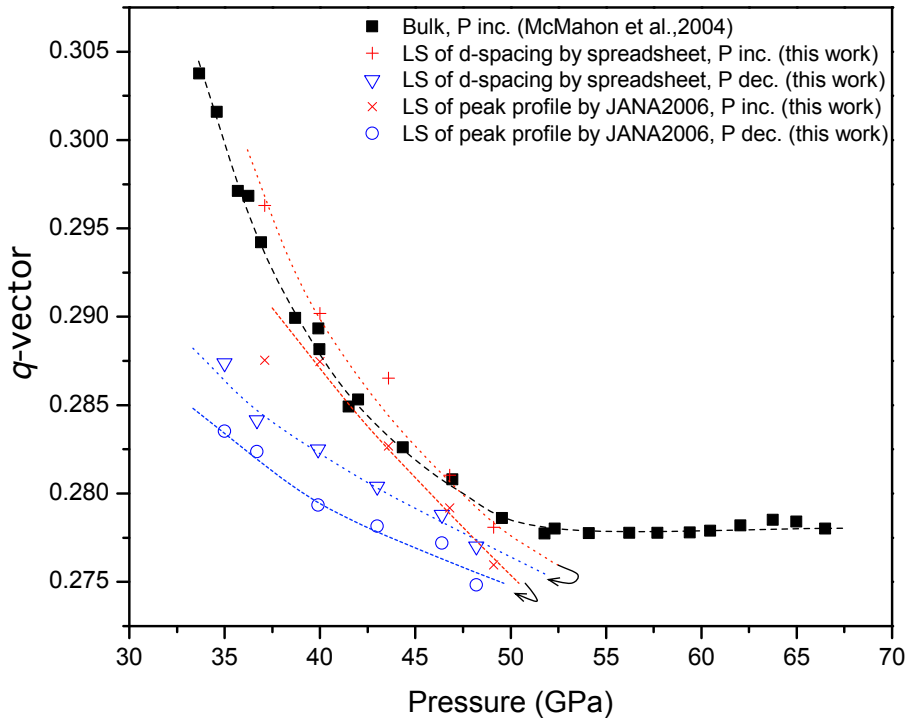

Figure 4.13: Pressure dependence of the q-vector of 70 nm nano-Se on pressure increase (red symbols) and decrease (blue symbols), as determined by profile-fitting using JANA2006 and LS fitting to measured d-spacings. The corresponding values for bulk-Se on pressure increase are also shown [McMahon et al., 2004]. The dashed lines are guides for the eye. Uncertainties in the lattice parameters as determined by JANA2006 are smaller than the symbols used to plot the data points, while the uncertainties from LS fitting to d-spacing from Excel spreadsheet are 0.002. The uncertainties in pressure are no more than ± 1 GPa.

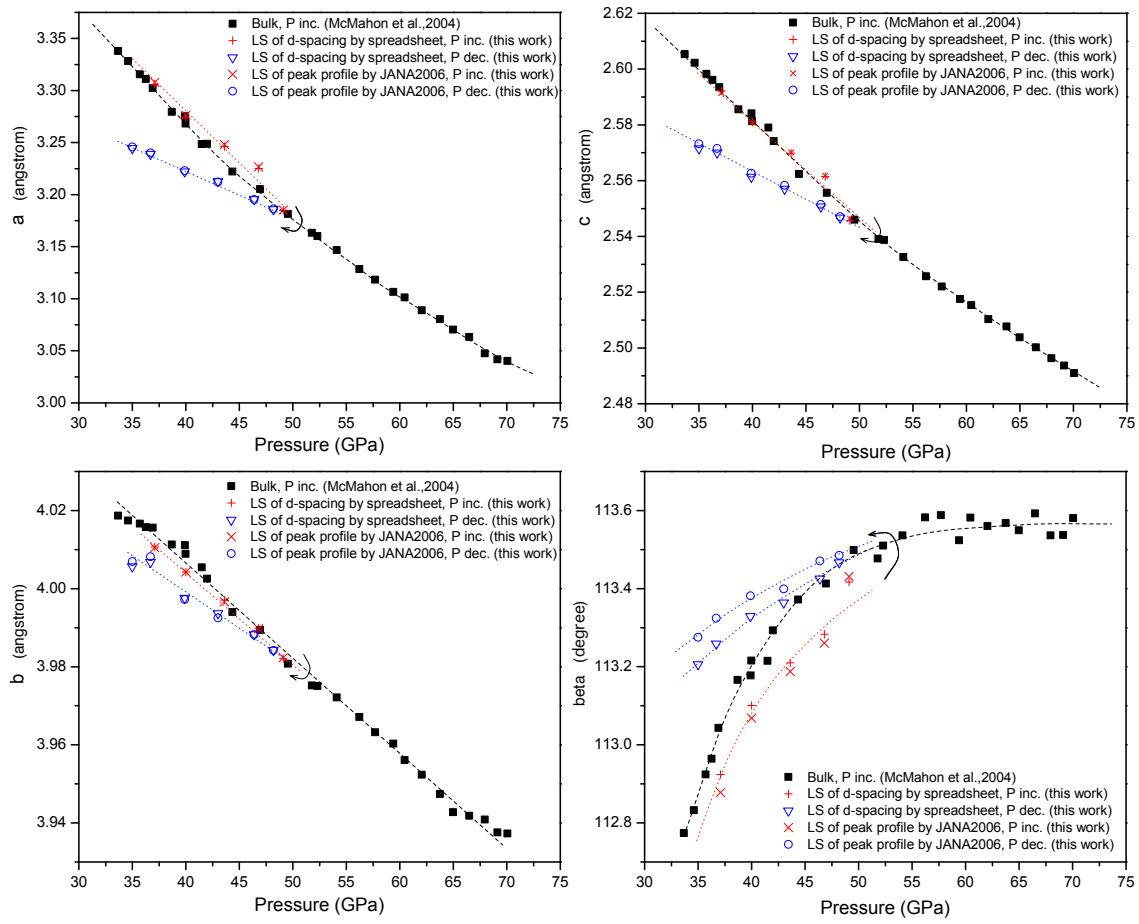

Figure 4.14: Pressure dependence of the lattice parameters of 70 nm nano-Se on pressure increase (red symbols) and decrease (blue symbols), as determined by profile-fitting using JANA2006 and LS fitting to measured d-spacings using Excel spreadsheet. The corresponding values for bulk-Se on pressure increase are also shown [McMahon et al., 2004]. The dashed lines are guides for the eye. Uncertainties in the lattice parameters as determined by JANA2006 are smaller than the symbols used to plot the data points, while the uncertainties from LS fitting are 0.01 Å for a, b, c and 0.01 degree for beta. The uncertainties in pressure are no more than ±1 GPa.

4.2.1.8 Selenium Nanoparticles (Nano-Se) HP-PXRD: Conclusions

The incommensurate Se-IV phase previously found in bulk-Se [McMahon et al., 2004] exists in both 10 nm and 70 nm nano-Se. This is the first observation of an incommensurate phase in a nanocrystalline sample. However, it is difficult to determine whether the detailed structures in the bulk and nano samples are the same. There is clearly a problem with incommensurate satellite peak *3 (as labelled in Fig. 4.4), as in the 10 nm nano-Se sample it is displaced from the position it would need to have at 34 GPa (see Fig. 4.10) in order for the q-vector to be the same at this pressure in the bulk and nano-sample. This displacement results in the value of the q-vector obtained by profile-fitting and fitting to peak positions giving different results, with neither agreeing very well with the results from the bulk sample. The misfitting of the satellite peaks is reduced at higher pressures, with the result that the q-vectors obtained from the two analysis methods agree better with each other, and with the earlier results from the bulk sample. Similar analysis performed on the 70 nm nano-Se sample shows the two methods give much more similar results, perhaps because the *3 peak is relatively weaker and is therefore weighted more lightly in the profile-fitting method. However, the hysteresis observed in the pressure dependence of the lattice parameters in the 10 nm nano-Se sample is also presented in the 70 nm nano-Se sample. Therefore, while the pressure dependence of the lattice parameters in the 10 nm nano-Se sample agrees with that of the bulk sample only on pressure decrease; the lattice parameters determined using the 70 nm nano-Se sample agree with the bulk sample on pressure increase, but not on pressure decrease.

These issues might arise from a non-hydrostatic pressure in the sample chamber. If there were strongly non-hydrostatic conditions, this could be the reason for the peak fitting issues because of micro-strains in the contact between each particle [Palosz et al., 2004]. However, the broadened ruby fluorescence spectrum that would arise under such conditions was not observed. A systematic study of these affects is needed, including the use of a more hydrostatic pressure medium like helium [Klotz et al., 2009]. Such a study was not performed, as there were clearly serious issues with the quality of the nano-Se samples, as will now be described.

4.2.1.9 Investigation of nano-Se sample: Good Nano-Powder or Not?

Parts of the 2D diffraction images from the 10 nm, 40 nm, 70 nm samples of nano-Se at low pressures (in phase Se-I) and high pressures (in phase Se-IV) are compared in Fig. 4.15. The Debye-Scherrer rings in all the images were expected to be completely smooth because of the very small crystallite size. However, the diffraction rings from each sample contain a degree of spottiness, especially in the 10 nm (Se-I and Se-IV) and in 40 nm (Se-I) samples. As the spotty lines are still from Se, this means that there are crystallites in all samples that are bigger than 1 μm. All of the samples are therefore clearly not 100% nanomaterials. To confirm this, we performed a detailed characterisation of all the nano-Se samples, especially the 10 nm and 70 nm samples, as described in the next section.

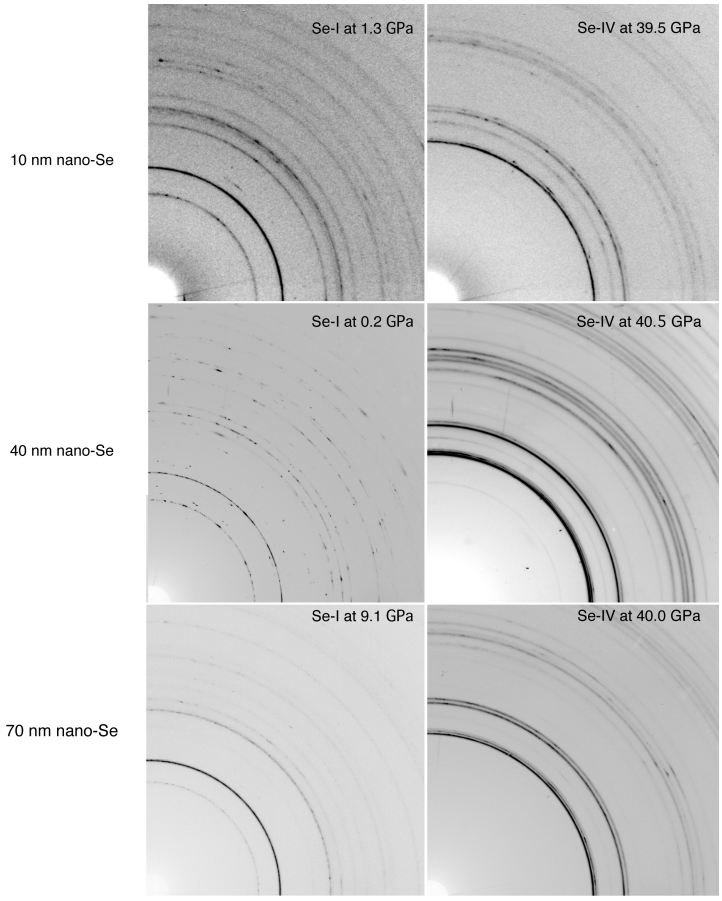

Figure 4.15: Quadrants of 2D diffraction images obtained from 10 nm, 40 nm, 70 nm commercial nano-Se samples in phase Se-I (left-hand images) and in phase Se-IV (right-hand images).

4.2.2 Characterisation Results

The size and shape of the claimed-to-be-nanoparticle materials (nano-Se in this case, but also all future nanomaterials studied in this thesis) have been characterised using the following facilities.

- Dynamic Light Scattering (DLS), Department of Physics and Astronomy, The University of Edinburgh.
- Transmission Electron Microscope (TEM), Institute of Molecular Plant Sciences, The University of Edinburgh.
- Scanning Electron Microscope (SEM), Department of Physics and Astronomy, University of St. Andrews.

First, for the 10 nm nano-Se sample, sonication and centrifugation (see further details in Appendix B.1.2) were performed with the hope that any particle clusters would be broken apart and each particle would then be separated and stabilised in a solution. This could potentially assist DLS to reveal the real size of the sample. From the DLS, the size of the (claimed) 10 nm nano-Se NPs varied from ∼140 nm (non-centrifuged) down to ∼80 nm (centrifuged). However, TEM of the sample showed many ∼10 nm particles and also a few ∼80-100 nm particles. This is consistent with the DLS results of ∼80 nm, because, particles of size ∼80-100 nm were the main contributors to light scattering.

The 10 nm, 30 nm, 40 nm, 70 nm and 100 nm nano-Se particles were also characterised by SEM. As a result, we have a clear understanding that not all of these samples are nanoparticles, as seen in Fig. 4.16. In Fig. 4.17, the 10 nm, 70 nm, and 100 nm nano-Se are polydispersed nanorods, some 30(±20) nm in width and 500(±300) nm in length. The 30 nm and 40 nm nano-Se have predominantly ball-like shapes, but with some random shapes as well. The approximate sizes of the particles in these two samples are 2-5 microns! (see Fig. 4.17)

4.2.3 Conclusions

Both the 10 nm and 70 nm selenium nanomaterial samples exhibit a high-pressure incommensurate modulated structure, as found in bulk-Se [McMahon et al., 2004]. However, the use of various characterisation methods reveals that none of the

nano-Se nanomaterials samples we have purchased have the sizes, shapes, and properties claimed by their suppliers.

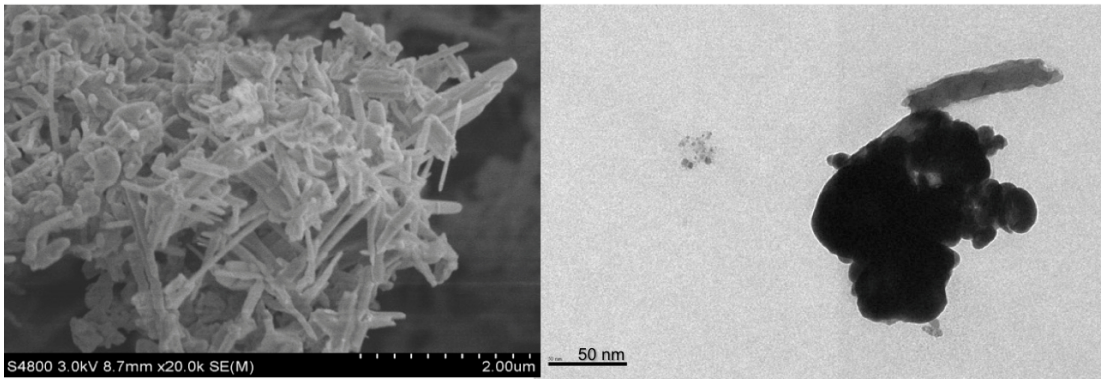

Figure 4.16: SEM (left) and TEM (right) images of purchased selenium nanoparticles which were claimed to be 10 nm in size, and to be monodispersed with a spherical shape. Microscopic images clearly reveal the sample crystallites to have a larger size, various shapes and polydispersity.

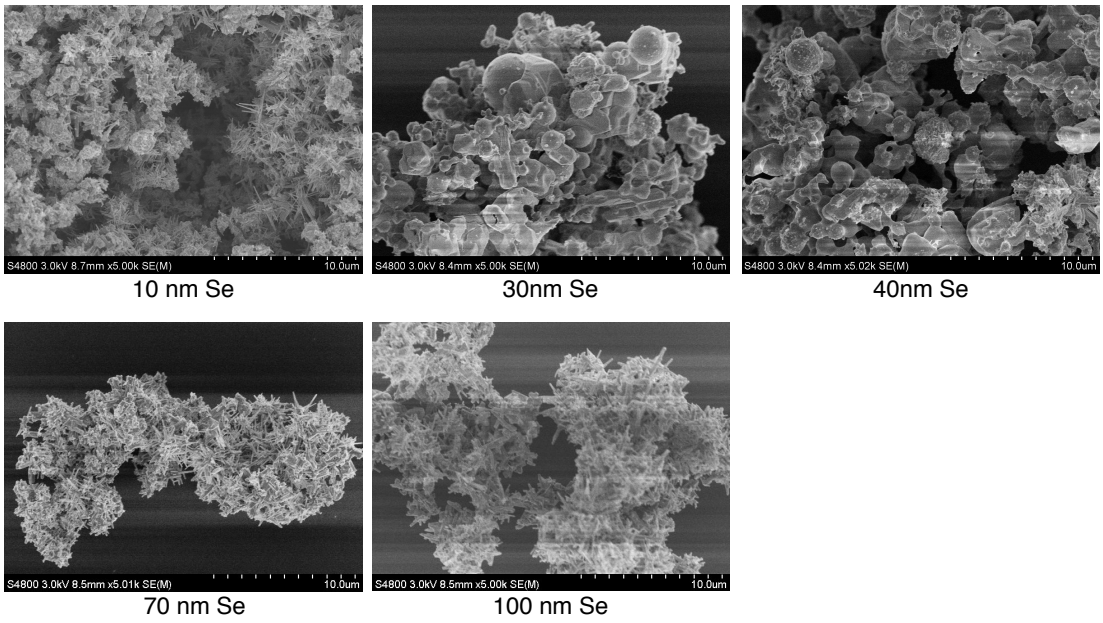

Figure 4.17: SEM images of purchased selenium nanoparticles which were claimed to be 10 nm, 30 nm, 40 nm, 70 nm, 100 nm in size, and to be monodispersed with a spherical shape. Microscopic images clearly reveal the sample crystallites to have a larger size, various shapes and polydispersity.

4.3 Lyophilised Selenium Nanoparticles (Lyophilised Nano-Se)

In the hope of obtaining a better quality of nano-Se, a second kind of nano-Se was purchased. This sample, lyophilised[5] nano-Se had a claimed particle size of ∼10 nm and monodispersity, and was purchased from Nanocs Inc. The sample was studied using HP-PXRD, TEM and DLS.

4.3.1 HP-PXRD Experiment

Lyophilised nano-Se were loaded into a DAC and HP-PXRD experiments conducted in the same manner as described in section 4.2.1. The 1D integrated x-ray diffraction profiles showed no evidence of any diffraction peaks, just a high background intensity. Two possible reasons for this could be either that the sample is amorphous selenium [Bandyopadhyay and Ming, 1996] rather than crystalline, or that size of the particles was too small to give a sharp diffraction peak. However, in both cases we might expect to see some evidence for a diffraction pattern, albeit with very broad peaks.

4.3.2 Characterisation Results

The sample was then characterised by TEM and DLS using the equipment described in section 4.2.2. From the TEM image (shown in Fig. 4.18), it is clear that layers of organic material, which is used to coat the particle in order to stabilise the nanoparticles in any polar-type solvent, cover each ∼10 nm particle. In addition, the DLS gave a very large particle size (∼10,000 nm) which could be caused by cluster formation due to hydrophobic interaction. Many attempts to separate the particles were made using centrifugation and sonication methods. However, neither technique was able to separate the clumps of organic materials (mixed with 10 nm particles) into individual particles.

[5]Lyophilisation (also known as freeze drying, lyophilization or cryodesiccation) is process of dehydration which is typically used to make the material more convenient for transport.

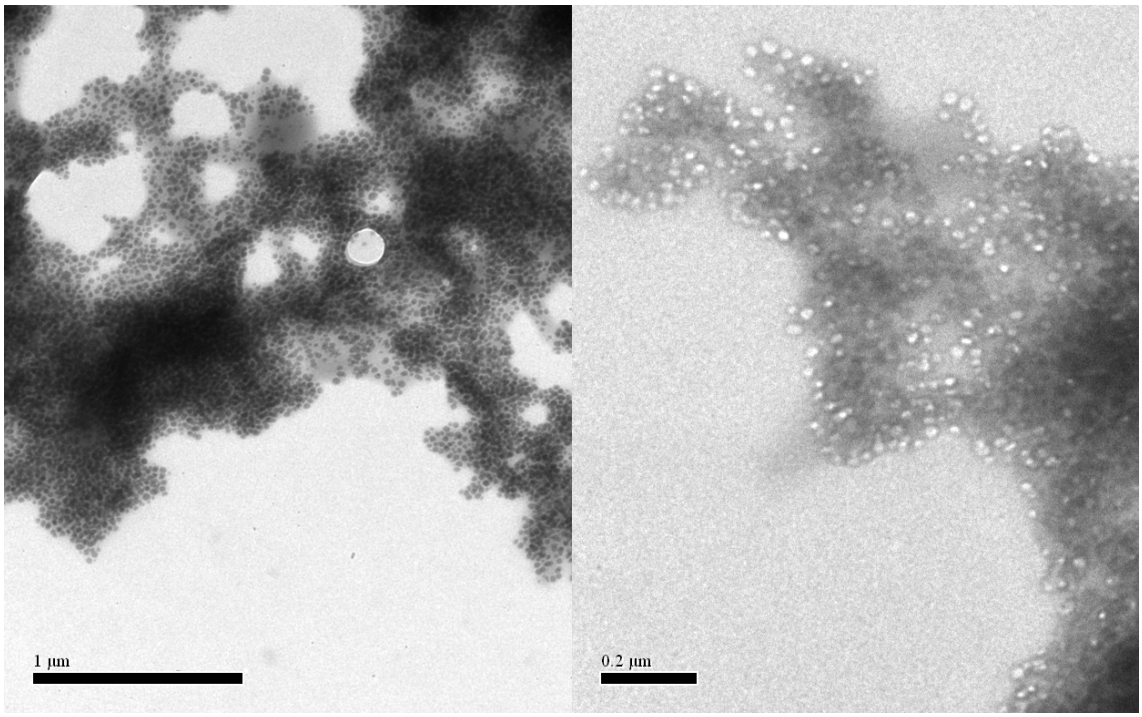

Figure 4.18: TEM micrograph of lyophilised nano-Se at ×4800 magnification (left) and at ×11,000 magnification (right). The organic materials surrounding the Se particles, and the clumpy nature of the sample are clearly evident.

4.3.3 Conclusion

This commercially available sample, despite its characterisation details, particle size information, and high price (£500/50mg), showed no evidence at all of crystalline nano-Se, and so was of no use for this work.

4.4 Bismuth Nanoparticles (Nano-Bi)

Bulk bismuth also exhibits a incommensurate phase at high pressures, with an incommensurate host-guest structure [Degtyareva et al., 2001]. After the failure to obtain commercial samples of nano-Se, attempts were made to purchase bismuth nanoparticles. Samples were subsequently purchased from Nanjing Jinling Goldfoil Co, Ltd[6] in China with a claimed nano-Bi diameter of 40 nm and 80 nm.

[6]Nanjing Jinling Goldfoil Co, Ltd, 321 South Zhongshang Road, Nanjing, 210001, China.

4.4.1 HP-PXRD Experiment

The 40 nm nano-Bi was loaded into a DAC and HP-PXRD conducted using the same techniques as described in section 4.2.1. Disappointingly, the 1D integrated x-ray diffraction profile obtained at ambient pressure did not have the profile expected from the ambient-pressure Bi-I phase [Tonkov and Ponyatovsky, 2004]. Instead, the diffraction pattern was clearly from a body-centred-cubic (bcc) structure (see Fig. 4.19), whereas bulk bismuth has a bcc structure only above 7.7 GPa [Degtyareva et al., 2004]. However, the lattice parameter of the commercial sample was very different to that of the bcc structure of bulk bismuth (bulk-Bi) reported in [Degtyareva et al., 2004].

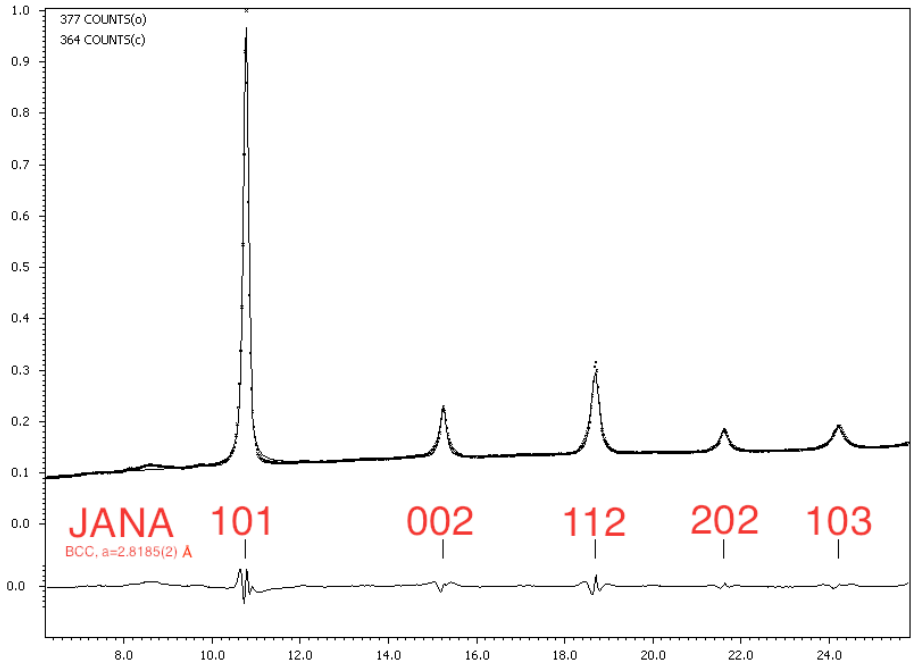

Figure 4.19: Le Bail refinement of 1D integrated x-ray diffraction profile obtained from the purchased nano-Bi. The pattern is clearly that from a body-centred-cubic (bcc) structure with $a = 2.8185(2)$ Å. The observed (dotted line) and calculated diffraction patterns (solid line) are shown. The difference between the experimental and calculated patterns is shown at the bottom most of the graph. Tick marks show the calculated peak positions.

4.4.2 Characterisation Results

The characterisation was carried out using the equipment described in section 4.2.2. The results revealed that there were many individual nanoparticles, as well as many clusters or clumps (organic materials mixed with bismuth particles), as can be seen in the SEM images shown in Fig. 4.20. The DLS also reported very large particle sizes (∼10,000 nm - 50,000 nm) which was due to the clumping. Centrifugation and sonication were once again performed in order to try and break down the clusters, but this was again unsuccessful.

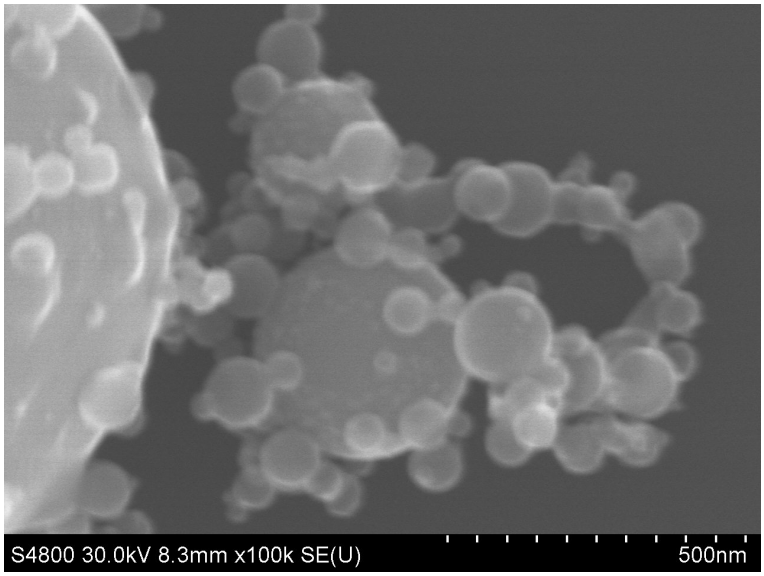

Figure 4.20: SEM image of the commercial nano-Bi samples showing the polydispersed nanoparticles stuck together in clusters.

4.4.3 Conclusion

The supposed Bi nanoparticles showed polydispersity in the SEM images and demonstrated aggregation and cluster formation, as shown in the DLS results. More importantly, the sample was clearly not bismuth as it had the wrong diffraction pattern. Therefore, this sample was useless for the work to be done in this thesis.

4.5 Conclusion

Although the incommensurate Se-IV phase was observed in the purchased nano-Se samples, none of these samples was truly nano-Se. Each contained particle sizes larger than expected. The lyophilised nano-Se sample showed absolutely no diffraction peaks, and the nanoparticles were covered in layers of organic material and were clumped together. The purchased nano-Bi sample also had too large particle sizes, was clumpy, and was not bismuth. The clear conclusion from all of this work was that commercially-available nanoparticles are not good enough to be used in this project. It was therefore decided that in order to have the well characterised and high-quality nanoparticles that were needed for this thesis it would be necessary to make our own via chemical synthesis. Consequently, a collaboration with Dr Pascal Andrè of the School of Physics and Astronomy, University of St. Andrews, was established to make bismuth nanoparticles. This is described in the following Chapter.

Chapter 5

Bismuth Nanoparticles (Nano-Bi) Synthesis

5.1 Introduction

The results of the previous chapter suggest that obtaining spherically-shaped and monodispersed nanoparticles of various sizes is not currently possible from commercial suppliers. And, none of the commercial samples provided the possibility of using sonication and centrifugation to select a specific size and shape from the commercial samples. It was therefore decided that the synthesis of our own samples was the best way forward.

Some 16 elements are now known to have incommensurate phases in their bulk form at high pressure, including Na, K, Rb, Sr, Ba, Sc, P, As, Sb, Bi, S, Se, Te [McMahon and Nelmes, 2006] and Eu [Husband et al., 2012]. For Na, K, Rb, Sr, Ba and Eu there have been no reports of nanoparticle synthesis. Moreover, these elements are also difficult to handle due to their air-sensitivity at ambient conditions. Thus, nanoparticle samples would be extremely reactive. In contrast, there is a considerable literature on the synthesis of group 15 and 16 element nanoparticles, i.e., Bi, Se, and Te. After discussion with Dr André Pascal at the Hybrid Nano Collöds group, Department of Physics, the University of St. Andrews, we decided to focus on the synthesis of bismuth nanoparticles with controlled morphology (spherical, cubic or pyramided) and low polydispersity.

More than 90 different syntheses have been completed. Three main chemical approaches were used which eventually led to the synthesis of one spherical and

polydispersed and four spherical and monodispersed NP samples of a suitable size for HP-PXRD study which will be further described in Chapter 6.

5.2 A Review of Bismuth Nanomaterial Synthesis

5.2.1 Introduction

Bismuth nanomaterials have been of interest to scientific research for over 30 years, and the number of publications per year has increased rapidly since 2000. Bismuth nanomaterial-related literature[1] has been reported in the ISI Web of Science from 1980 to 2011, as can be seen from Fig. 5.1. There are a total of 2,454 records over the past 30 years, with the number of publications having increased dramatically since 2005.

Bismuth-related nanomaterials have been synthesised with various compositions and in diverse shapes and forms. Such materials have been synthesised as oxides [Soltanzadeh and Morsali, 2010], alloys [Ould-Ely et al., 2005], or pure bismuth itself [Wang et al., 2008], and are produced as spheres [Wang et al., 2008], rods [Soltanzadeh and Morsali, 2010], cubes [Wang et al., 2006], and core-shell [Grebinski et al., 2004] nano structures.

From a practical point of view, bismuth has been used in electrodes, and in sensors and detectors for electroanalysis that utilise its unique properties, such as its insensitivity to the presence of oxygen, and the excellent mechanical stability of metallic bismuth [Švancara et al., 2010]. Nano-bismuth (nano-Bi) has been used as a seeding crystal to help produce nanowires of other nanomaterials, such as CdSe [Wang and Buhro, 2010] InAs, GaP, GaAs, and InP [Fanfair and Korgel, 2005], with applications in electronics. Moreover, by heating bismuth nanoparticles with single-walled carbon nanotubes, it has been shown that hybrid inorganic-organic bismuth-filled carbon nanotubes can be produced [Kiang, 2000].

Despite these applications, the preparation of bismuth nanoparticles with a controllable size and shape has remained a key concern, and this has led to the

[1]The search was carried out through the ISI Web of Science with the following set of keywords: "(TS=bismuth) and (TS=(quantum dot*) or TS=quantum-dot* or TS=QD or TS=QDs or TS=Qdot* or TS=nanoparticle* or TS=nano-particle* or TS=nanocrystal* or TS=nano-crystal* or TS=nanocylinder* or TS=nano-cylinder* or TS=nanorod* or TS=nano-rod* or TS=nanoneedle* or TS=nano-needle* or TS=nanocolloid* or TS=nano-colloid* or TS=colloid* or TS=nano-wire* or TS=nanowire* or (TS=nanotube* or TS=nano-tube* not ts=carbon)) and py=1980-2011" search completed on 4th January 2012.

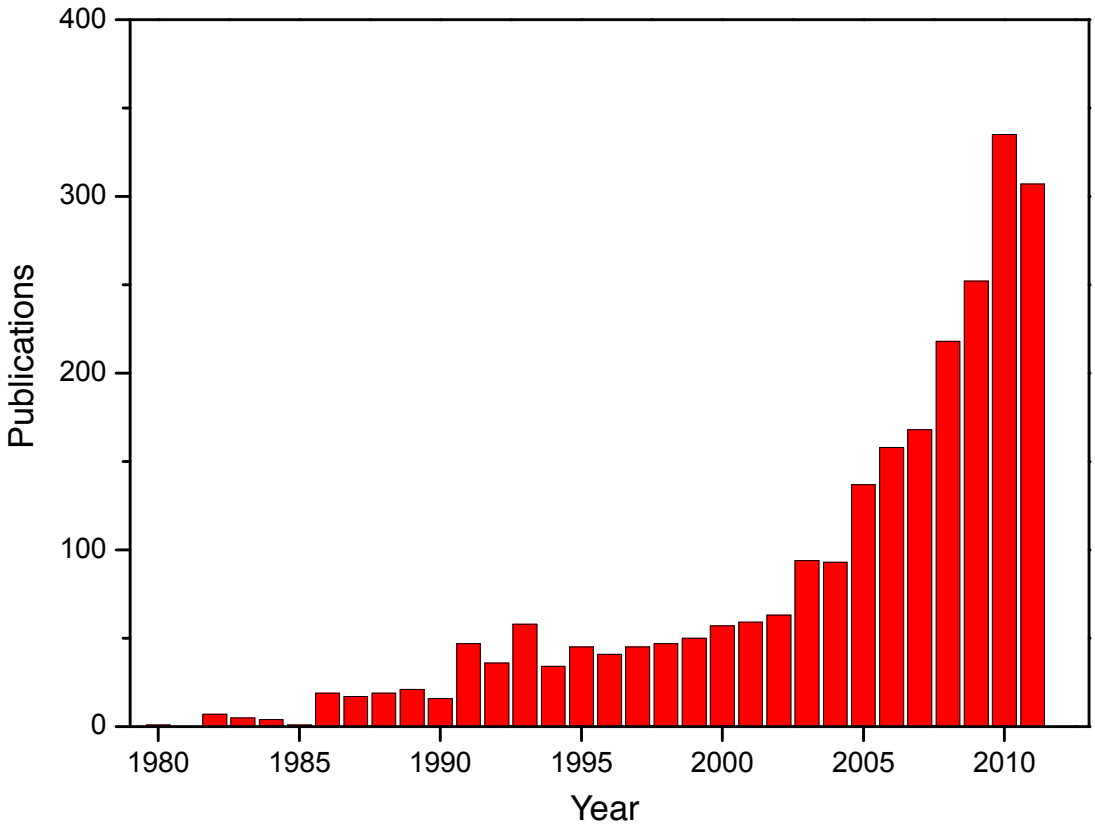

Figure 5.1: Number of bismuth-related nanomaterial publications from 1980-2011.

development of many different synthesis pathways. In this review section, synthesis methods will be categorised in three different pathways, that is, aqueous bismuth synthesis, non-aqueous bismuth synthesis, and high-temperature polyol-thermal decomposition synthesis.

In addition to these chemical approaches, there are other techniques such as laser ablation [Reppert et al., 2007], arc discharge [Matkasymova et al., 2009], and electrodeposition [Tharamani et al., 2008] for nano-Bi synthesis. However, chemical pathways have been proved to be very effective, as they provide higher control and enable different sizes and shapes to be prepared with relatively low polydispersity.

5.2.2 A Review of Aqueous Bismuth Synthesis Approach

Aqueous bismuth salt synthesis approach relies on the use of water as a solvent, and can be considered as a simple method based on the production of microemulsions. The reagents used in this approach are the precursor, surfactant (surface active agents), reducing agent, and solvent. The mechanism of this method is described in Fig. 5.2.

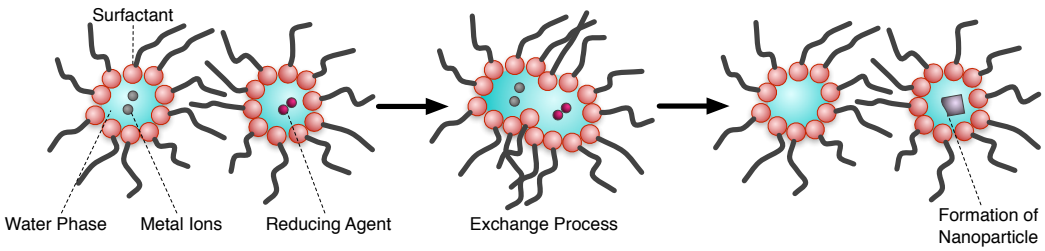

Figure 5.2: A nanometre-sized water droplet is surrounded by a chosen surfactant to form a micelle. Bismuth ions (Bi^{3+}) which are dissociated from the bismuth precursor are present in the water droplet. The reducing agent, which is later put into the system, reduces Bi^{3+} to bismuth metal in nanometre sizes.

Fig. 5.2 shows "polar in non-polar solvent" droplets stabilised by a layer of surfactant localised at the interface of the two solvents, e.g., water and isooctane. In this reverse microemulsion structure, it is then possible to stabilise chemicals in the aqueous core, hence confining them within a very small volume.

In this approach, the shape and size of the nanoparticles are often wrongly thought to be similar to the microemulsion, which in the past was thought to be acting as a template. In fact, the size of the nanoparticles is not the same as the size of the microemulsion, as proved by Stubenrauch et al. [Stubenrauch et al., 2008].

A wide range of bismuth precursors, such as $BiCl_3$, $Bi(NO_3)_3$, $Bi(CH_3CO_2)_3$, BiOCl, and $C_{15}H_9BiO_6S_3$ (bismuth thiolate), can be used [Son et al., 2010], and the solubility of these different precursors can alter the effectiveness of the particle production. In some cases, if the precursor itself has a low solubility in water, the additional of a small amount of acid has been shown to be beneficial. For example, water-insoluble BiOCl can be dissolved in water with the addition of 6 M of HCl [Diemente, 1997].

Examples of the different surfactants used in this type of synthesis are TOP (trioctylphosphine) [Son et al., 2010] and NaAOT (sodium bis-(2-ethylhexyl)-

sulfosuccinate). The choice of reducing agent depends on its strength and its solubility in the aqueous phase. For example, hydrazine hydrate ($N_2H_4 \cdot H_2O$) has been used as a reducing agent with a bismuth precursor to synthesise bismuth nanorods and nanotubes [Ma et al., 2010].

5.2.3 A Review of Non-Aqueous Bismuth Synthesis Approach

The non-aqueous approach uses a non-polar solvent to synthesise NPs such as CdSe, Au and Ag. However, this method has not previously been used to synthesise bismuth NPs. This section, therefore, introduces how other nanomaterials are synthesised by non-aqueous method, which inspired the non-aqueous approach for the bismuth nanoparticles synthesis described in section 5.4.

The reagents required for synthesis include a metal precursor, a non-polar solvent, and an amine or an amine and an acid. The amine, or amine and acid, serve as a stabiliser to control the growth of nanoparticles. For example, for Au and Ag NP synthesis [Hiramatsu and Osterloh, 2004], tetrachloroauric acid or silver acetate, oleylamine, and toluene were utilised. However, another type of amine, dodecylamine, can also work equally well in the reaction, but oleylamine was chosen because it is commercially available and is inexpensive [Hiramatsu and Osterloh, 2004]. In another case, for Au NP synthesis by Leff et al. [Leff et al., 1996], dodecylamine, oleylamine, chloroauric acid ($HAuCl_4$-$3H_2O$), sodium borohydride ($NaBH_4$), tetraoctylammonium bromide ($N(C_8H_{17})_4Br$), and toluene were used. The role of the amine or amine/acid is mainly as a stabilising agent [Leff et al., 1996]. However, in some cases, it can also reduce the metal precursor [Hiramatsu and Osterloh, 2004].

The size of the NPs depends upon the concentration of precursor used. For example, a high concentration of Au precursor will give smaller particles because more seed particles form at the beginning of the reaction [Hiramatsu and Osterloh, 2004]. However, when the reaction is prolonged, larger particles grow at the cost of smaller ones, which is called the Ostwald ripening process [Hiramatsu and Osterloh, 2004].

The products of this approach are amine-capped gold and silver NPs with sizes of 6-21 nm and 8-32 nm, respectively [Hiramatsu and Osterloh, 2004]. Moreover, amine-capped gold nanocrystals with a size of 2.5-7.0 nm, whose surfaces are

coated with primary amine[2], were obtained by [Leff et al., 1996].

The effect of the amine to the characteristics of nanoparticles has also been studied. For example, long-chain primary amines are found to boost emission of fluorescence of CdSe [Talapin et al., 2002]. Moreover, using a long chain amine (e.g. dodecylamine) might cause high oxidation at the surface of nanoparticles, as O_2 can go to the surface easily. Thus a branched structured amine (e.g. dioctylamine) can prevent O_2 reaching the surface of nanoparticles [Yu et al., 2003], leading to a non-oxidised nanoparticle surface. The effect of the amine on the surface of the nanoparticles has been studied using FTIR. For instance, there is a study using FTIR techniques with oleylamine-capped FePt particles which results in the confirmation of the binding between NH_2 of amine and the FePt NPs' surface [Shukla et al., 2003].

5.2.4 A Review of High-Temperature Polyol-Thermal Decomposition Synthesis Approach

This method mainly uses poly-alcohols as both the solvent and the reducing agent. Ethylene glycol and 1,5-pentanediol each contain two alcohol groups, and are most commonly used in polyol-based materials synthesis. While the details of the mechanism of polyol synthesis have been well studied, its details have remained elusive and have not been verified for a large range of materials. The method takes advantage of the relative solubility of the metal precursors in the partially-polar solvent, and utilises a coating agent to control the growth of the nanoparticles. Table 5.1 shows some common ingredients that have been used in this type of bismuth synthesis. One should note that additives could also be used to boost nanoparticle formation. Although this generic approach has been reported for many years, the exact mechanism, and the effects of the solvent and coating agent, remain elusive.

To get different sizes of nano-Bi, many parameters in the synthesis have to be taken into account. For example, a faster stirring rate during the synthesis results in smaller particle sizes [Wang and Xia, 2004], and the more rapid the synthesis, the smaller the particle size obtained [Richards et al., 2010]. Systematically changing the synthesis conditions - such as the molar ratio of PVP to $BiCl_3$, the concentration

[2]A primary amine is an amine which has one hydrogen atom in an ammonia molecule replaced by an alkyl chain.

Table 5.1: Examples of high-temperature polyol-thermal decomposition synthesis.

Product	Bi Precursor	Additives[a]	Coating Agent	Reference
s[b], M[c]	Bi Acetate	EG[d]	PVP	[Wang and Xia, 2004]
s, M	Bi Chloride	$Na[N(SiMe_3)_2]$	PHD-*co*-PVP	[Richards et al., 2010]
s, M	$Bi[N(SiMe_3)_2]_3$	$NaN(SiMe_3)_2$	PHD-*co*-PVP	[Wang and Buhro, 2010]
s, M	$Bi[N(SiMe_3)_2]_3$	$Li[N(SiMe_3)_2]$	HDA[e]	[Yarema et al., 2010]
s, P[f]	Bi Chloride	-	Dodecanethiol	[Carotenuto et al., 2009]
s, P	Bi Citrate	EG and Urea	PVP	[Cheng et al., 2009]
s, N/A[g]	Bi Chloride	$NaBH_4$	PVP	[Wang et al., 2005]
w[h], P	Sodium Bismuthate	EG[i]	PVP	[Wang et al., 2004]

[a]acts as reducing agent
[b]nanoparticles with spherical shape
[c]Monodispersed
[d]Ethylene Glycol
[e]Hexadecylamine
[f]Polydispersed
[g]No size distribution presented
[h]nano wires
[i]ethylene glycol served as both solvent and reducing agent.

of $BiCl_3$ [Wang et al., 2005], varying the amounts of $BiCl_3$ and $NaN(SiMe_3)_2$, and using different concentrations of the ingredients [Wang and Buhro, 2010] can also affect the size of nanoparticles. For example, it was reported that the morphologies of the Bi products can also be controlled by adjusting the quantity of NaOH used in the solution [Wang and Kim, 2008]. Moreover, bismuth nanowires were obtained when using ethylene glycol (EG), while nanobelts with a rectangular cross section were obtained when using glycerol as an extra reducing agent.

5.3 Aqueous Bismuth Synthesis Approach

5.3.1 Introduction

The synthesis of bismuth nanoparticles in aqueous media was chosen first for this study because it is easy to set up and manipulate the experiment. The synthesis can also be done at room temperature, and has a short reaction time. In the present study, many variations of the room-temperature aqueous bismuth syntheses procedures were carried out.

5.3.2 Experimental Method

The synthesis approach mainly uses five different types of chemical reagents, as described in Table 5.2. Moreover, the structures and formulae for all chemical reagents can be found in section 5.7. The amount of substances used in this synthesis is presented in Appendix B.1.1.

Table 5.2: Reagents used in the aqueous bismuth synthesis approach.

Types	Chemical Reagents	Functions
Bi precursors	BiOCl, $BiNO_3$, $BiCl_3$	A precursor of nano-Bi
Surfactants	NaAOT, NP5	To form small micelles
Reducing Agents	$NaBH_4$	To reduce Bi^{3+} to form Bi metal
Capping Agent	Dodecanethiol	To prevent aggregation
Solvents	Isooctane, Water, Ethanol	To solubilise the solid reagent

Each type of reagent has its own function in the synthesis, as shown in Fig. 5.2 of section 5.2.2 and Table 5.2 in this section. In addition, two types of surfactants are used, NaAOT and NP5, the structures of which are shown in Fig. 5.3.

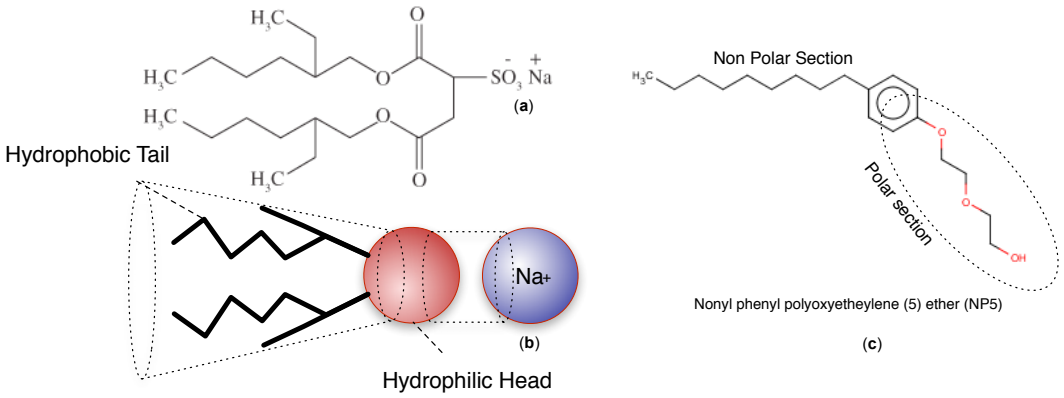

Figure 5.3: (a) The chemical structure of NaAOT, a single surfactant molecule, which consists of a hydrophilic head and a hydrophobic tail. (b) The schematic structure of NaAOT. (c) A single surfactant molecule of NP5 (Nonyl phenyl polyoxyethelene (5) ether), which consists of polar and non-polar sections.

AOT[3] (of NaAOT) and NP5 are two typical surfactants. AOT is ionic, whereas NP5 is a non-ionic, and both have been used for the synthesis of nano-Bi.

[3]AOT is the organic part of NaAOT

NaAOT has been used previously in the synthesis of many different nanomaterials, including Fe [Baroli et al., 2007], Co [Eastoe et al., 1994, Eastoe et al., 1996, Legrand et al., 2000], and Cu [Cason et al., 2001, André et al., 2002].

NaAOT was used as a part of the ionic surfactant approach of this synthesis, leading to an inverse micelle formation as shown in Fig. 5.4(a), the hydrophobic tails containing hydrocarbon chains align outwards while the hydrophilic heads containing sodium sulfonate arrange themselves inwards to be in contact with the water droplet. NP5 was used as a part of the non-ionic surfactant approach, as shown in Fig. 5.4(b). NP5 has a polar region and a non-polar chain, when the polar region (the -O- and OH- arm) is aligned towards the water droplet.

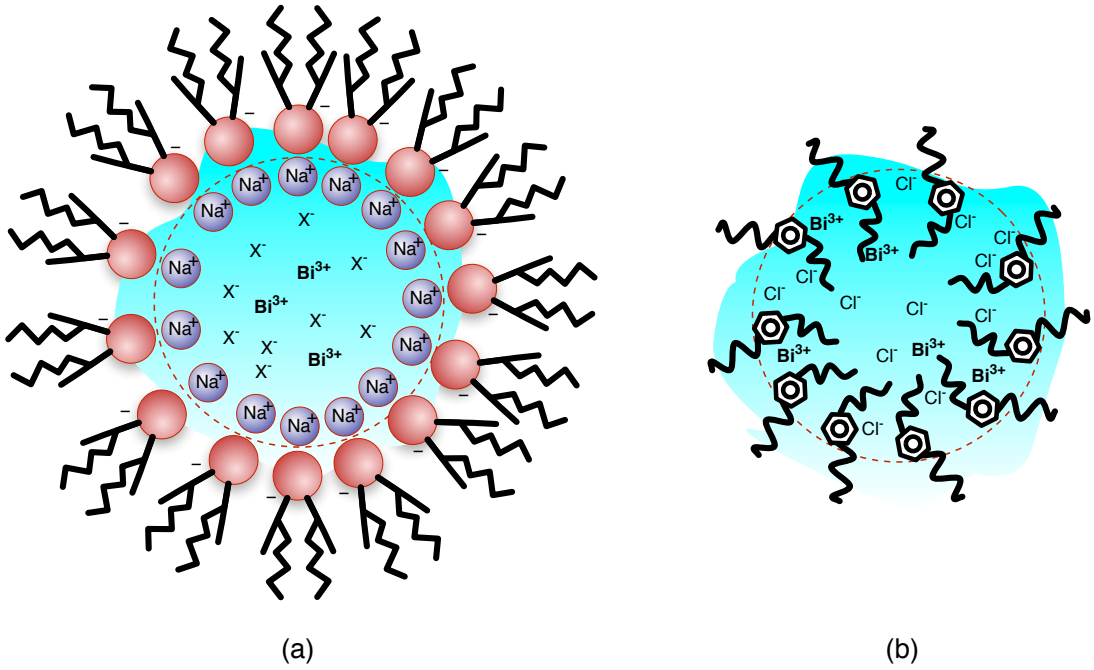

Figure 5.4: (a) The inverse micelle structure formed from the ionic surfactant, NaAOT, containing a water droplet of Bi^{3+} solution. The reagents are isooctane, NaAOT, $Bi(NO_3)_3$ or $BiCl_3$ or BiOCl, Water, $NaBH_4$; X^-=$(NO_3)^-$ or Cl^- or $(1/3)OCL^-$, (b) The inverse micelle structure formed from the non-ionic surfactant, NP5, containing a water droplet of Bi^{3+} solution. The reagents are isooctane, NP5, $BiCl_3$ or BiOCl, water, and $NaBH_4$. It should noted that (b) represents only the case when using $BiCl_3$ as a precursor.

The synthesis was performed in a glovebox under an inert atmosphere of N_2 that was O_2 and H_2O free. In a typical synthesis, a surfactant solution was

prepared by being mixed with isooctane and subsequently with water. Bismuth precursor was then added to surfactant/isooctane/water system to obtain the desired Bi^{3+} concentration. The mixture was stirred at 250 rpm using a magnetic stir bar, followed by the swift injection of the reducing agent ($NaBH_4$/NaAOT or $NaBH_4$/NP5). Stirring continued at room temperature for 15 minutes. The syntheses were completed with a variety of concentrations of bismuth precursor (from 0.025 M to 0.2 M) whilst keeping the concentration of NaAOT constant, and vice versa, to tune the size of the nanoparticles. During all syntheses the solutions turned black, indicating the reduction of the Bi ions to Bi metal. Dodecanethiol (200 μL) was then injected and the solution was stirred for a further five minutes at 250 rpm. The resulting nano-Bi particles were then precipitated by centrifugation in the presence of ethanol (see Appendix B.1.2). This step was repeated several times to extract the product from the surfactant solution. A detailed example of the nano-Bi preparation protocol, precipitation process and characterisation techniques is given in Appendix B.1. To visualise the morphology, and quantify the composition of the nano-Bi, the product of each synthesis was dissolved in isooctane, sonicated briefly and then characterised by scanning electron microscopy (SEM) and x-ray diffraction (XRD).

5.3.3 Experimental Results

As can be seen in Fig 5.5, SEM revealed that the product of the reaction was inhomogeneous. Although it showed nano-size material, there was clustering with an undefined shape and size. Unfortunately, the common features in all of the nanomaterials produced by this approach were high polydispersity and the appearance of various sizes and shapes.

5.3.4 Discussion

Although the inverse-micelle process is simple in principle, it presents significant challenges in practice [Chen, 2011]. In addition to the polydispersity and various particle shapes, XRD analysis of the sample synthesised using $BiCl_3$ and water/NaAOT/isooctane showed it to contain NaCl and B_2Cl_4, which could arise from the chlorine in $BiCl_3$, the sodium in NaAOT, and boron in $NaBH_4$ (see Fig. 5.6).

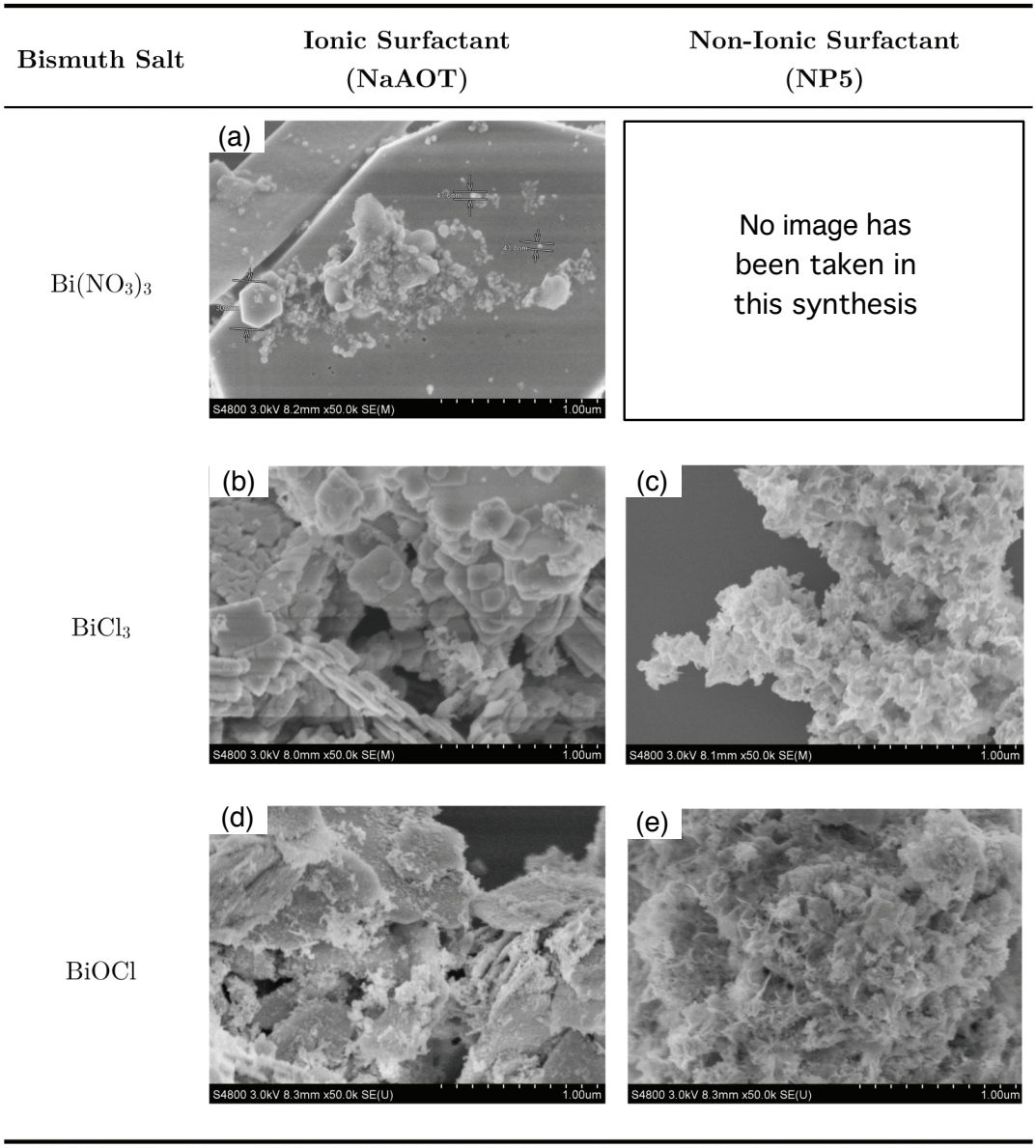

Figure 5.5: SEM images showing the different synthesised products obtained using aqueous synthesis. The figure compares the products obtained from different bismuth precursors, $Bi(NO_3)_3$, $BiCl_3$, and BiOCl, and two different surfactants, NaAOT and NP5. It is worth mentioning that synthesis using $Bi(NO_3)_3$ with NP5 was not carried out resulting in no related SEM image shown.

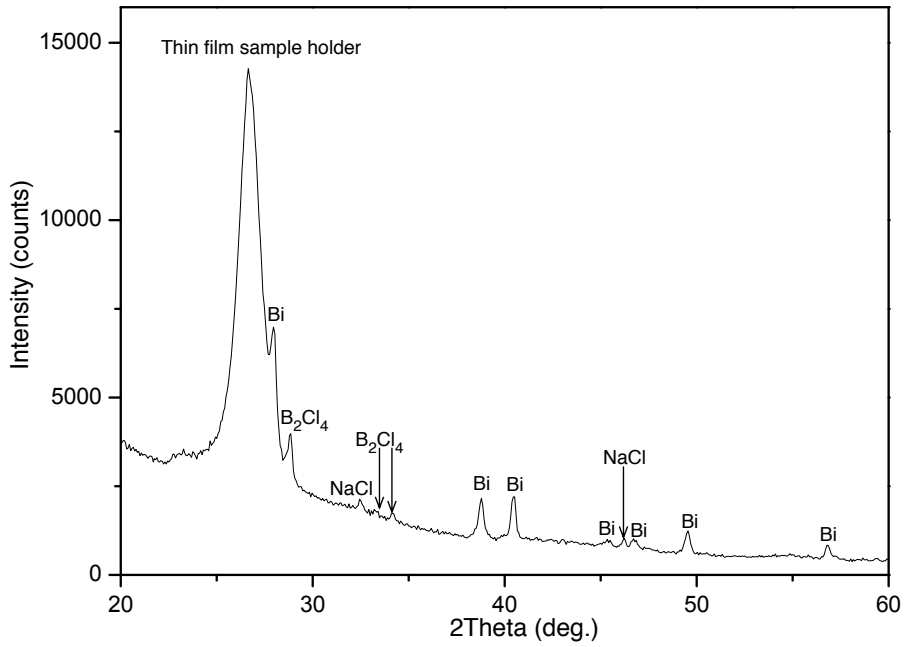

Figure 5.6: X-ray diffraction pattern obtained from the in-house x-ray diffractometer (D8) showing the pattern from nano-Bi sample synthesised using $BiCl_3$, $NaBH_4$, NaAOT, water and isooctane. It should be noted that NaCl and B_2Cl_4 were also obtained as by-products.

Moreover, from the synthesis using the BiOCl, $NaBH_4$ and water/NaAOT/isooctane, XRD patterns from the samples show unreacted BiOCl remaining in the final product (see Fig. 5.7). SEM images also confirmed the existence of BiOCl by comparing the morphology of pure BiOCl with that of nano-Bi produced using BiOCl as a precursor (see Fig. 5.8). Diemente also confirmed that BiOCl is not a water-soluble compound [Diemente, 1997]. It is believed that unreacted BiOCl remained in the final product of NP5 system as well.

Besides the solubility issue of BiOCl, the solubility of the bismuth precursors also needed to be considered. From Table 5.3, only $BiCl_3$ shows good solubility in the solvent used in the experiment.

5.3.5 Conclusions

The goal of this study was to synthesise nano-Bi. From this synthesis approach, bismuth metal was successfully obtained when $BiCl_3$ (see Fig. 5.6) was used as a precursor with NaAOT as a surfactant. However, from the SEM images of the

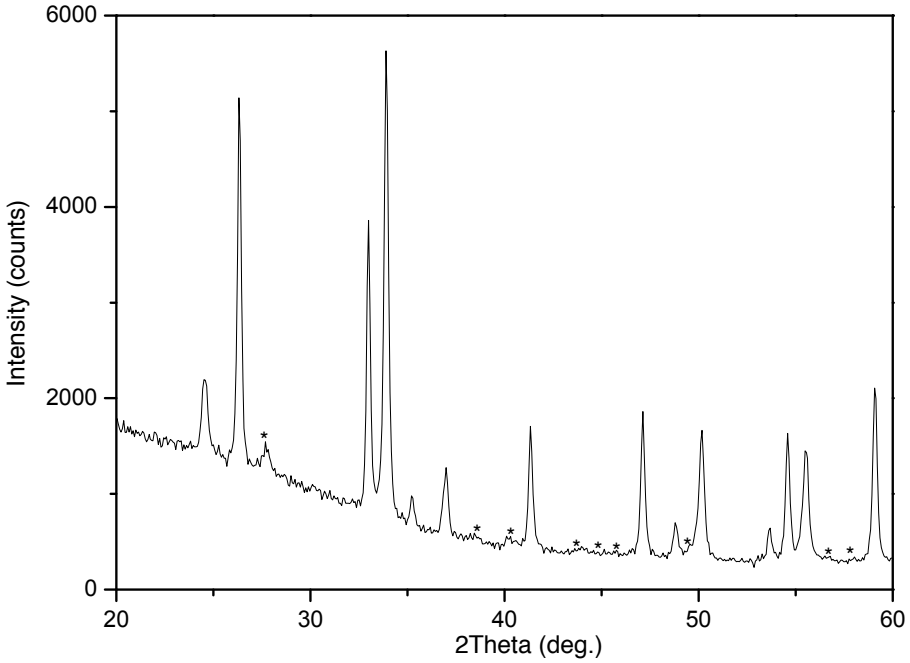

Figure 5.7: X-ray diffraction pattern obtained from the in-house x-ray diffractometer (D8) showing the diffraction pattern of nano-Bi sample synthesised using BiOCL, water, $NaBH_4$ and NaAOT. The asterisks '*' label the positions of BiOCl precursor peaks.

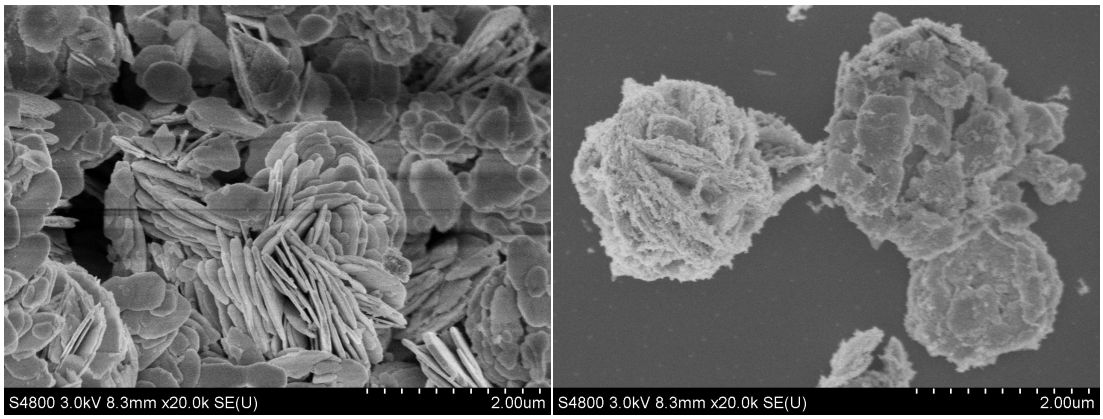

(a) BiOCl powder (b) Product of nano-Bi synthesis using BiOCl as a precursor

Figure 5.8: SEM images of (a) pure BiOCl powder, and (b) nano-Bi synthesised using BiOCl as a precursor. The plate-like shape of the product in (a) strongly suggests that unreacted BiOCl exists as an end-product of the synthesis. Both SEM images were taken using ×20k magnification.

Table 5.3: Water solubility of bismuth precursors used in the aqueous bismuth synthesis. In this solubility test, bismuth precursor : water is 50 mg : 4 g.

Bismuth Precursor	Solubility in Water	Reference
$Bi(NO_3)_3$	Reacts with water	observation and [Lide, 2008]
$BiCl_3$	Yes	observation
BiOCl	No	observation and [Diemente, 1997]

samples (see Fig. 5.5(b)), it can be seen that the shape of the nano-Bi is not as spherical as expected. Moreover, NaCl and B_2Cl_4 were found to exist in the final products of syntheses. Moreover, because BiOCl has very low solubility in water, unreacted BiOCl still remained in the reaction solution. Similarly, $Bi(NO_3)_3$ was insufficiently dissolved in water, leading to only a small amount of high quality nano-Bi in the syntheses (low yield). Because of these limitations, another method was attempted, as described in the next section.

5.4 Non-Aqueous Bismuth Synthesis Approach

5.4.1 Introduction

From the first synthesis approach it was clear that having water as the only solvent in the system was not optimum because it was unable to dissolve some of the bismuth precursors efficiently and the nano-Bi product does not reach a desired quality. Therefore, we turned our attention to the use of non-polar solvents. Toluene was selected for use in this non-aqueous bismuth approach, whilst the different reducing agents were employed in this method to observe the potential of reduction of converting the bismuth ions into bismuth metal. However, the toluene might affect the reducing power of each reducing agent because it provides a different solvation to each of them.

This approach was inspired by the non-aqueous synthetic pathway of Au nanoparticles, which were successfully synthesised using amine/acid with $NaBH_4$ as the reducing agent [Leff et al., 1996].

This synthetic approach is non-aqueous at room temperature because of the use of no water (or a reduced amount of water). Alkyl amine and acid molecules were

used instead of a surfactant to stabilise and control the growth of the nanoparticles. The acid and amine groups were selected because of their ability to form a complex with the Bi surface atoms in a similar way as chemisorption[4].

5.4.2 Experimental Method

This procedure mainly uses four different types of chemical reagents, as shown in Fig. 5.9. It should be noted that dodecanethiol was also sometimes used as an additional reagent to monitor nanoparticles aggregation. Bismuth acetate was used as a bismuth precursor, and toluene was used as a non-aqueous solvent. Decanoic acid was utilised, together with dodecylamine or dioctylamine, to act as ligands to be the stabiliser in the synthesis. In addition, various kinds of reducing agent were used, including hydrazine monohydrate, sodium borohydride, tetrabutylammonium borohydride and phenyl hydrazine (see Fig. 5.9).

Solvent	Bismuth Salt	Ligands	Reducing Agents
Toluene $C_6H_5CH_3$	Bismuth Acetate $Bi(CH_3CO_2)_3$	Dodecylamine $CH_3(CH_2)_{11}NH_2$	Hydrazine Monohydrate $NH_2NH_2 \cdot H_2O$
		Dioctylamine $CH_3(CH_2)_7NH(CH_2)_7CH_3$	Sodium Borohydride $NaBH_4$
		Decanoic Acid $CH_3(CH_2)_8COOH$	Tetrabutylammonium Borohyride $(CH_3CH_2CH_2CH_2)_4N(BH_4)$
			Phenyl Hydrazine $C_6H_5NHNH_2$

Figure 5.9: Overall reagents used in this synthesis including solvent, bismuth precursor, ligands and reducing agents.

The synthesis was established in a glovebox under O_2 and H_2O free. In a typical synthesis, two separate solutions were prepared. In the first, the reaction

[4]Chemisorption is a sub-class of adsorption. It is driven by a chemical reaction occurring at the exposed surface.

mixture of a bismuth acetate solution was prepared by mixing the bismuth acetate precursor first with decanoic acid, and subsequently with toluene. Similarly, the second mixture contained dodecylamine or dioctylamine, toluene and bismuth acetate. Both reaction tubes were then stirred vigorously. When the solutions became homogenous, they were mixed into one reaction tube. The reducing agent was added to the mixed solution and the solution was stirred at room temperature for 15 minutes until it turned black. Dodecanethiol was then injected into the solution which was then mixed for a further five minutes. The nano-Bi was then precipitated by adding toluene and methanol, followed by centrifugation (see more details in Appendix B.1.2). The product was purified by re-precipitation several times. Similar protocols were followed until the syntheses were completed using a number of different reducing agents and amines. A detailed example of the nano-Bi preparation protocol, precipitation process and characterisation techniques is given in the Appendix B.1.1.

To study different synthesis conditions, the initial amine and acid molar ratios were varied whereas the concentration of bismuth acetate was kept constant. In one particular synthesis, two reducing agents were used in sequence in an attempt to create a nucleation first by the role of a strong reducing agent, followed by a slower growth of NPs by the role of the weaker reducing agent. In addition, in some cases, a small amount of H_2O was used to assist the solubility of the reducing agent.

To visualise the morphology of the nano-Bi, and to verify its composition, the product of each synthesis was re-dispersed in isooctane and then characterised by SEM and XRD, in the manner described in the previous section.

5.4.3 Experimental Results

After the injection of the reducing agent, the solution turned black in all cases within 4-10 minutes. The appearance of the black solution was interpreted as being associated with the formation of nano-Bi. In addition, small plates[5] of bismuth appeared as evidence of a fast reduction by $TBABH_4$ (tetrabutylammonium borohydride) resulting in the aggregation of bismuth metal after only 4 minutes of the synthesis.

[5]Plate refers to the small, irregularly shaped aggregation of synthesis product with the approximate size of 0.5×0.5 cm^2.

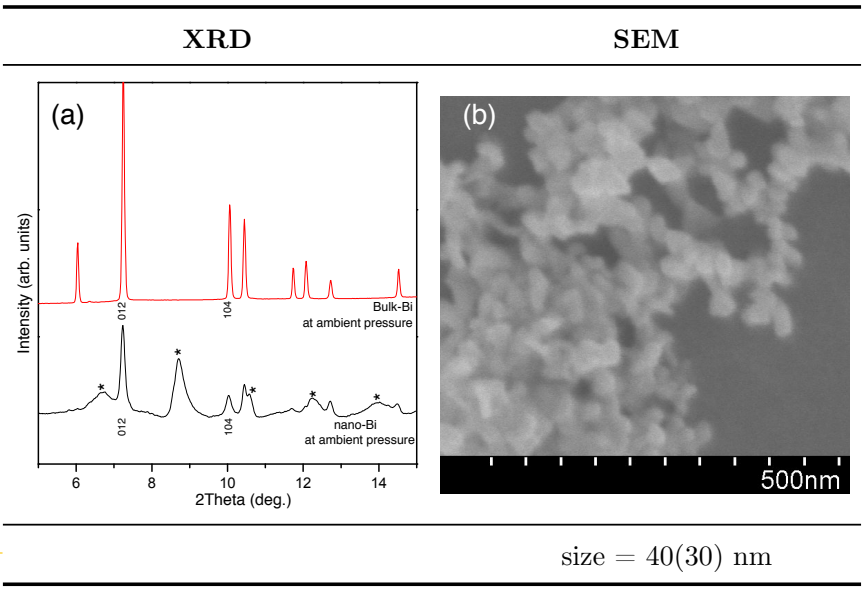

Figure 5.10: (a) X-ray diffraction pattern of synthesised nano-Bi in Bi-I ($hR2$ As-type structure [Degtyareva et al., 2004]). The asterisks '*' label the positions of non-Bi peaks. (b) The SEM image (at $\times$100k magnification) of the synthesis product obtained using the non-aqueous bismuth approach (bismuth acetate, $NaBH_4$, decanoic acid and dodecylamine) shows the average size to be 40(30) nm, with small Bi NPs fused to each other.

Using $NaBH_4$ as the reducing agent seemed to be the most successful method, as the $NaBH_4$ was very effective in reducing bismuth acetate to nano-Bi, as confirmed by the XRD diffraction pattern shown in Fig. 5.10(a). However, the $NaBH_4$ cannot be used to successfully synthesise spherical and low polydispersity nano-Bi, as fusions of nano-Bi were found (see Fig. 5.10(b)) in all of the samples after synthesis. It should be noted that the additional non-Bi peaks in Fig. 5.10(a) could be NaCl, which is formed from a chlorine ion from $BiCl_3$ and a sodium from $NaBH_4$, as well as excess organic materials used in the synthesis.

In general, the SEM images revealed that all the nano-Bi samples synthesised using this non-aqueous method showed aggregation, and were inhomogeneous with various sizes of NP and various sizes of clusters. In order to investigate nanoparticle fusion, dodecanethiol, a strong ligand for the surface of Bi metal, was added to the nano-Bi solution to prevent aggregation. However, aggregates still formed, indicating that aggregation must happen during the synthesis and before the dodecanethiol is added.

5.4.4 Discussion

The solubility of the reagents in the synthesis dramatically affects its yield, as all the reagents must be well dissolved in solution to control the reaction. The solubility of the majority of reagents used in this approach in toluene is quite good. Bismuth acetate is soluble in toluene as it contains non-polar groups which point outwards towards the toluene. Moreover, dodecylamine or dioctylamine and decanoic acid are also soluble in toluene due to their alkyl chains, as are $TBABH_4$, N_2H_4 monohydrate and phenyl hydrazine. However, $NaBH_4$ is not naturally soluble in toluene, but can be made soluble by adding a small amount of H_2O.

The alkyl amine/acid were presumed to act as the nano-Bi's stabilising agent, as, in a similar reaction (but at high temperature), oleic acid, another kind of acid to the one used in this study, was proven to be the ligand which coated the bismuth nanoparticles in a high-temperature synthesis [Yarema et al., 2010]. Therefore, the decanoic acid and dodecylamine or dioctylamine used in this synthesis are likely to have the same function.

Many reducing agents have been used (Fig. 5.9), leading to different nanoparticle formation due to the different reducing strengths. The reducing strength of each reducing agent is compared in the Table 5.4. The N_2H_4 and Phenyl-N_2H_4 are comparatively weaker than $NaBH_4$ and $TBABH_4$. Moreover, $NaBH_4$ is stronger than $TBABH_4$. In addition, the polarity is one of the key factors for an efficient reaction because a well-solvated reducing agent will lead to a more efficient reaction.

From the results, $TBABH_4$ can reduce bismuth acetate faster than $NaBH_4$ as seen from the fast-reaction plate aggregates in 4-10 minutes after starting the reaction, although $TBABH_4$ is a weaker reducing agent (Table 5.4). This is because $TBABH_4$ has higher solubility in toluene due to having less polarity while $NaBH_4$ is not well soluble in toluene because of its higher polarity.

A stronger reducing agent is necessary to reduce a process of reduction with its large reduction potential (E^0). From Table 5.5, it is likely that Bi^{3+} will be reduced directly to Bi^0 (No. 3), rather than reduced to the intermediate step of Bi^+ (No. 4) when $NaBH_4$ is used as a reducing agent. However, when a weaker reducing agent, N_2H_4, is used, the reducing power is just enough to reduce Bi^{3+} to Bi^+. It should be noted that the values in Table 5.5 are from water-based

Table 5.4: Reducing strength of each reducing agent used in the non-aqueous bismuth synthesis.

Reducing agents	States	Qualitative Strength[a]	Polarities
$N_2H_4{\cdot}H_2O$	liquid	++	Polar
Phenyl-N_2H_4	liquid	++	Polar / nonpolar
$NaBH_4$	powder	>+++	Polar
$TBABH_4$	powder	+++	Polar / nonpolar

[a]Qualitative Strength - The ability to reduce bismuth precursor obtained from experimental observations.

reduction [Lide, 2008]. Therefore, the reduction potential in toluene solvent might be slightly different. However, these numbers can be used to discuss in general.

Table 5.5: Standard redox potentials of related reagents [Lide, 2008] in the non-aqueous bismuth approach.

No.	Chemical Reaction	E^0 (V)
1	$BH_4{}^- + 3H_2O \leftrightarrow B(OH)_3 + 7H^+ + 8e^-$	-1.73
2	$N_2H_4 \cdot H_2O \leftrightarrow N_2 + 5H^+ + 4e^- + OH^-$	-0.23
3	$Bi^{3+} + 3e^- \leftrightarrow Bi^0$	0.308
4	$Bi^{3+} + 2e^- \leftrightarrow Bi^+$	0.2
5	$Bi^+ + e^- \leftrightarrow Bi^0$	0.5

In an attempt to overcome the aggregation problem as mentioned earlier, various ratios of decanoic acid/dodecylamine, and another kind of amine (dioctylamine), were employed. However, there was no significant difference in the outcome, and, ultimately, we could not circumvent this problem.

The aggregation might be due to the extremely fast kinetics of the synthesis and the weak interaction of the amine/acid stabiliser and the Bi NP's surface. Therefore, the rate of nanoparticle formation could not overcome the rate of reduction to Bi metal by the strong reducing agents, $NaBH_4$ and $TBABH_4$, resulting in an aggregated sample. Also, the size of the nanoparticles could not be controlled very efficiently.

5.4.5 Conclusions

In this work, we sought to synthesise Bi nanoparticles using the non-aqueous bismuth approach to overcome the limitations of the previous aqueous method. It is evident that bismuth metal of nanometre sizes was successfully obtained, as illustrated in Fig. 5.10(a) and Fig. 5.10(b). The synthesis which gave the best nanoparticles was that using bismuth acetate, dodecylamine, decanoic acid and $NaBH_4$. However, the particles were very polydispersed and fused to one another. Further investigation into aggregate formation was undertaken, but the problems could not be solved.

Future work using this method should include finding a reducing agent which is strong enough to reduce the Bi ions to Bi metal, but weak enough to allow slow growth for better control of the nano-Bi particle size.

5.5 High-Temperature Polyol-Thermal Decomposition Synthesis Approach

5.5.1 Introduction

High-temperature polyol-thermal decomposition (HTP-TD) synthesis was inspired by recent literature which reported the formation of nano-Bi using a co-polymer (PHD-*co*-PVP : Poly(1-vinylpyrrolidone)-graft-(1-hexadecene) [Wang and Buhro, 2010] and the synthesis of nano-Ag using the PVP (polyvinylpyrrolidone)-stabilised polyol pathway [Wiley et al., 2004]. HTP-TD method has a longer reaction time, leading to slower formation of bismuth NPs, and better control of the sample purity and nanoparticle size. In this section, the chemical methods developed over the course of this research to allow the formation of nano-Bi particles, are reported.

5.5.2 Experimental Method

The four groups of reagents used in this synthesis are shown in Fig. 5.12. Six types of bismuth precursor, ($Bi[N(SiMe_3)_2]_3$, $BiCl_3$, BiOCl, $Bi(NO_3)_3$, $Bi(CH_3CO_2)_3$ and $NaBiO_3$) and four kinds of solvent/reducing agent[6] (octadecene (ODE),

[6]In this synthesis, the solvent is believed to act as reducing agent as well.

diisopropylbenzene (DIPB), ethylene glycol (EG), and 1,5-pentanediol) were used. $NaN(SiMe_3)_2$ in THF was employed as an assisting reducing agent. Moreover, PVP and PHD-*co*-PVP, which is the derivative of PVP, were also utilised.

This synthesis approach could be considered as a polyol or a thermal decomposition approach, or as a combination of the two, as the only difference is the choice of solvent/reducing agent used in the synthesis (see Fig. 5.12). If 1,5-pentanediol or ethylene glycol (EG) are the only reducing agents used in the synthesis, this synthetic pathway will be called "polyol synthesis". However, if $NaN(SiMe_3)_2$ is also used, it will be called "polyol and thermal decomposition synthesis", because of the thermal decomposition caused by $NaN(SiMe_3)_2$. On the other hand, if octadecene (ODE) or diisopropylbenzene (DIPB) is utilised as the solvent/reducing agent, and whether $NaN(SiMe_3)_2$ is used or not, this chemical synthesis should be called "thermal decomposition synthesis".

For clarity, it is worth mentioning that high-temperature polyol-thermal decomposition (HTP-TD) is used to described both "high-temperature polyol and thermal decomposition synthesis" and "high-temperature thermal decomposition synthesis".

Bismuth precursors	Solvent/Reducing Agents	Assisting Reducing agent	Coating agents
$Bi[N(SiMe_3)_2)]_3$ $BiCl_3$ BiOCl $Bi(NO_3)_3$ $Bi(CH_3CO_2)_3$ $NaBiO_3$	octadecene (ODE) diisopropylbenzene (DIPB) ethylene glycol (EG) 1,5 pentanediol	$NaN(SiMe_3)_2$	PVP PHD-co-PVP

Figure 5.11: Reagents used in the high-temperature polyol-thermal decomposition (HTP-TD) synthesis.

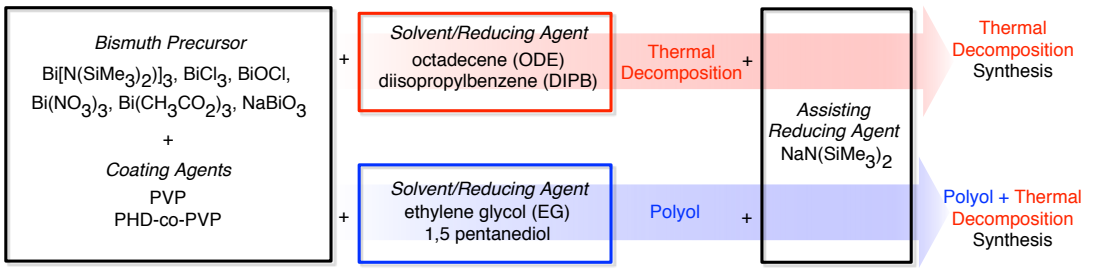

Figure 5.12: Schematic diagram showing the polyol synthesis and thermal decomposition synthesis methods.

5.5.3 Experimental Results

5.5.3.1 Choosing the Right Solvent

To optimise the synthesis conditions, PVP was first used as a coating agent, because the molecular structure of PVP is simpler than that of PHD-*co*-PVP, which has a PHD polymeric group. The solubility of PVP was assessed in a wide range of solvents, including DIPB, ODE, EG, and 1,5-pentanediol. As 1,5-pentanediol gave the best solubility for PVP powder, the later syntheses focused on using 1,5-pentanediol as a solvent/reducing agent.

5.5.3.2 High-Temperature Polyol and Thermal Decomposition Synthesis: Using PVP and 1,5-pentanediol

Synthesis was performed in a glovebox under an inert atmosphere of N_2 that was O_2 and H_2O free. PVP was first mixed with 1,5-pentanediol at 165° C followed by stirring using a magnetic stirrer at 250 rpm. The PVP was soluble in 1,5-pentanediol. The solution was allowed to cool to room temperature before being added to the bismuth precursors (see Fig. 5.13(a) and Fig. 5.13(b)) followed by stirring at 750 rpm for 15 minutes. The system was then brought to 165° C again, and stirred at 750 rpm for 93 hrs, which is the so-called "stabilisation time of 93 hrs". Then the solution was cooled to room temperature. $NaN(SiMe_3)_2$ was then added and further stirring was applied for another 15 minutes at room temperature. Finally, the solution was immersed in a hot oil bath at 165° C and stirred at 750 rpm. At this stage, some solutions turned black within 5-10 minutes after immersion in the oil, which indicated the formation of nano-Bi. Samples were collected after 6 hrs, 20 hrs, and 43 hrs (see Fig. 5.13) of the synthesis for

characterisation.

For each of the sample collections, a washing process was then implemented to clean the product. Sonication and washing with different ratios of toluene and methanol were used to purify the collected solution. The purification process was repeated several times. Precipitation was performed by centrifugation and decantation (see Appendix B.1.2 for more details). To visualise the morphology, and to verify the composition of the synthesised nano-Bi, the solution was treated in the same way as described in section 5.3.2 while toluene was used to re-disperse the nanoparticles into the solution for future use, e.g., for SEM.

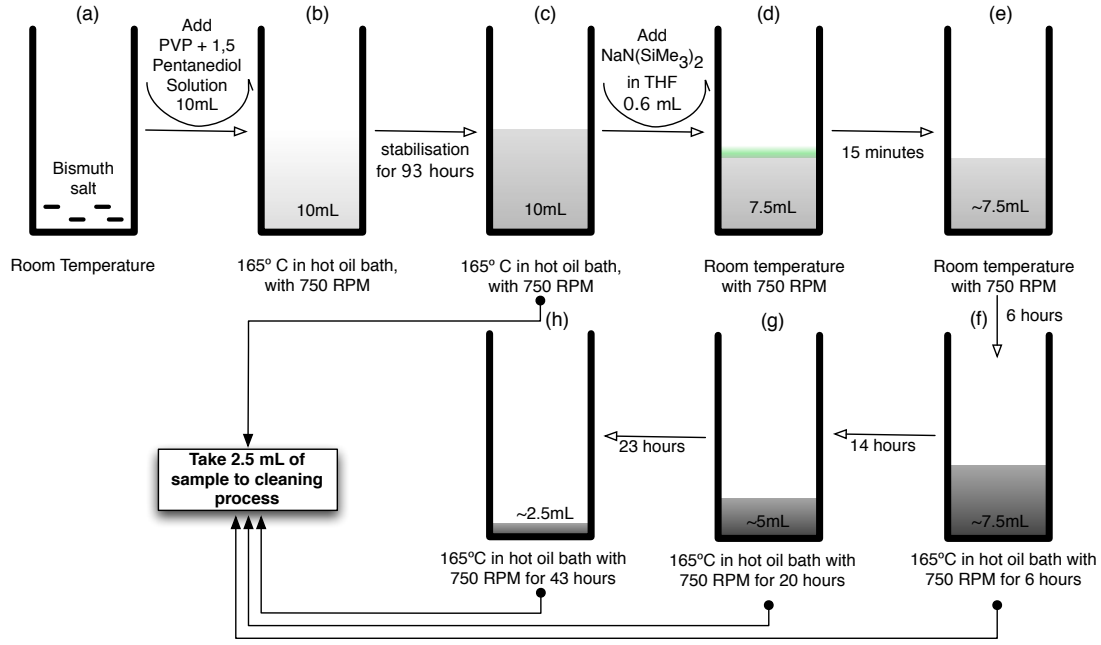

Figure 5.13: Schematic diagram of the mixing steps of the high-temperature polyol-thermal decomposition synthesis.

It should be noted that there was a solubility issue after mixing the 1,5-pentanediol with the bismuth precursor $BiCl_3$. From visual observation, $BiCl_3$ was not soluble in 1,5-pentanediol, resulting in uncommon morphology of the end product which is believed to be unreacted $BiCl_3$ at the end of synthesis (see Fig. 5.14). The SEM image of the $BiCl_3$ powder (Fig. 5.14(a)) and the product synthesised using $BiCl_3$ with 20 hrs synthesis time (Fig. 5.14(b)) appeared to be quite similar.

Only $BiCl_3$ has such solubility problems, and the other bismuth precursors

SEM of $BiCl_3$	SEM of Synthesised Product of $BiCl_3$ as a precursor 20-hr Synthesis

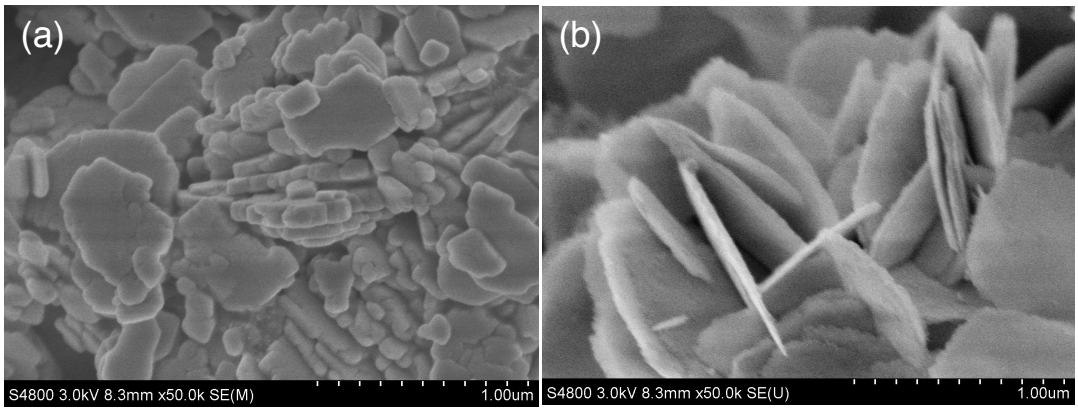

Figure 5.14: SEM images (a) the $BiCl_3$ precursor powder and (b) the product of the synthesis using $BiCl_3$ as a precursor, showing their similar morphology.

had sufficient solubility in 1,5 pentanediol. Considering all the results from all the reported synthetic approaches, this method appeared to be the most promising pathway. From this method, one polydispersed nano-Bi sample (128(45) nm) and three reasonably monodispersed and spherical nano-Bi samples (52(15) nm, 92(13) nm and 138(27) nm) were eventually successfully obtained.

The long stabilisation time was the key factor in the syntheses leading to the successful syntheses. Partial reduction of the bismuth precursor to nano-Bi by 1,5-pentanediol occurs during this period, and the long stabilisation time resulted in the production of more nano-sized particles as it allows the bismuth precursors to be thoroughly solubilised in the solvent (see Fig. 5.15). From Fig. 5.15, in the synthesis using $Bi(CH_3CO_2)_3$ (right panel), Fig. 5.15(c) shows fewer nanoparticles (lower yield) than Fig. 5.15(d) but more unreacted Bi precursor, because the product in Fig. 5.15(c) is from a much shorter stabilisation time. It should be noted that this comparison is done under the assumption that 18 hrs and 20 hrs of synthesis time are not significantly different.

The synthesis time (counting from the time when the assisting reducing agent, $NaN(SiMe_3)_2$, was added) became the second key factor in successful syntheses, and it was found that the size of nanoparticles increases when the synthesis time increases (see Fig. 5.16). In the left panel of Fig. 5.16, it can be seen that the size

of nano-Bi synthesised after 43 hr shown in Fig. 5.16(d) is larger than the nano-Bi seen in Fig 5.16(c), which is after 20 hrs of synthesis. Furthermore, there were also variations in the synthesised product due to the different bismuth precursors (see Fig. 5.16). From Fig. 5.16(a) and 5.16(e), $Bi(CH_3CO_2)_3$ was more prone to be partially reduced by 1,5-pentanediol than $NaBiO_3$ was. This was determined from the fact that unreacted $NaBiO_3$ was observed in Fig. 5.16(e). However, both $Bi(CH_3CO_2)_3$ and $NaBiO_3$ precursors give a high yield of spherical and low polydispersed nanoparticles after 20 hrs (see Fig. 5.16(c) and Fig. 5.16(g)) and 43 hrs (see Fig. 5.16(d) and Fig. 5.16(h)).

Stabilisation + (synthesis)	$Bi(NO_3)_3$	$Bi(CH_3CO_2)_3$
3hr + (18hr*)	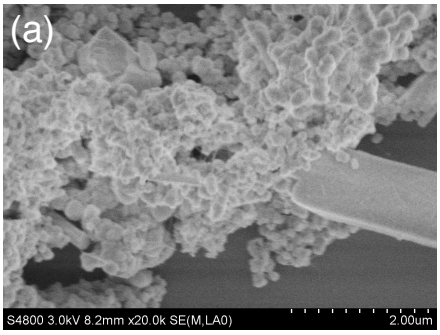	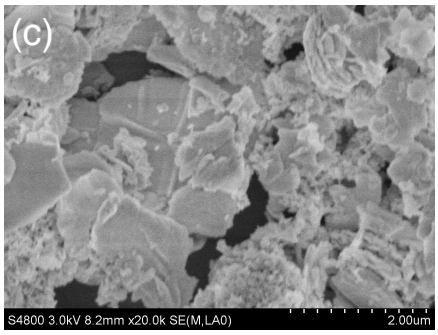
93hr + (20hr)	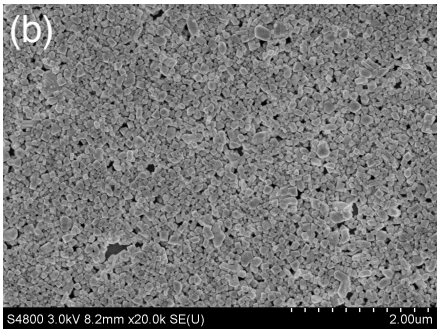	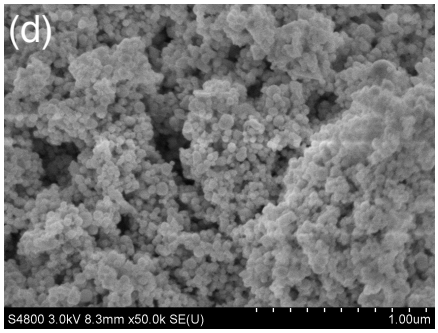

Figure 5.15: SEM images showing the different NPs obtained from syntheses with stabilisation times of 18 hrs and 20 hrs from $Bi(NO_3)_3$ (left panel) and $Bi(CH_3CO_2)_3$ (right panel). (a) Bismuth NPs with 2 μm×1 μm particles of unreacted $Bi(NO_3)_3$ (b) bismuth NPs (c) unreacted $Bi(CH_3CO_2)_3$ and a small amount of bismuth NPs (d) bismuth NPs. In the author's experience, 18 hrs and 20 hrs stabilisation times are indistinguishable. Comparison of the images suggests that the longer the stabilisation time, the more nanoparticles are obtained.

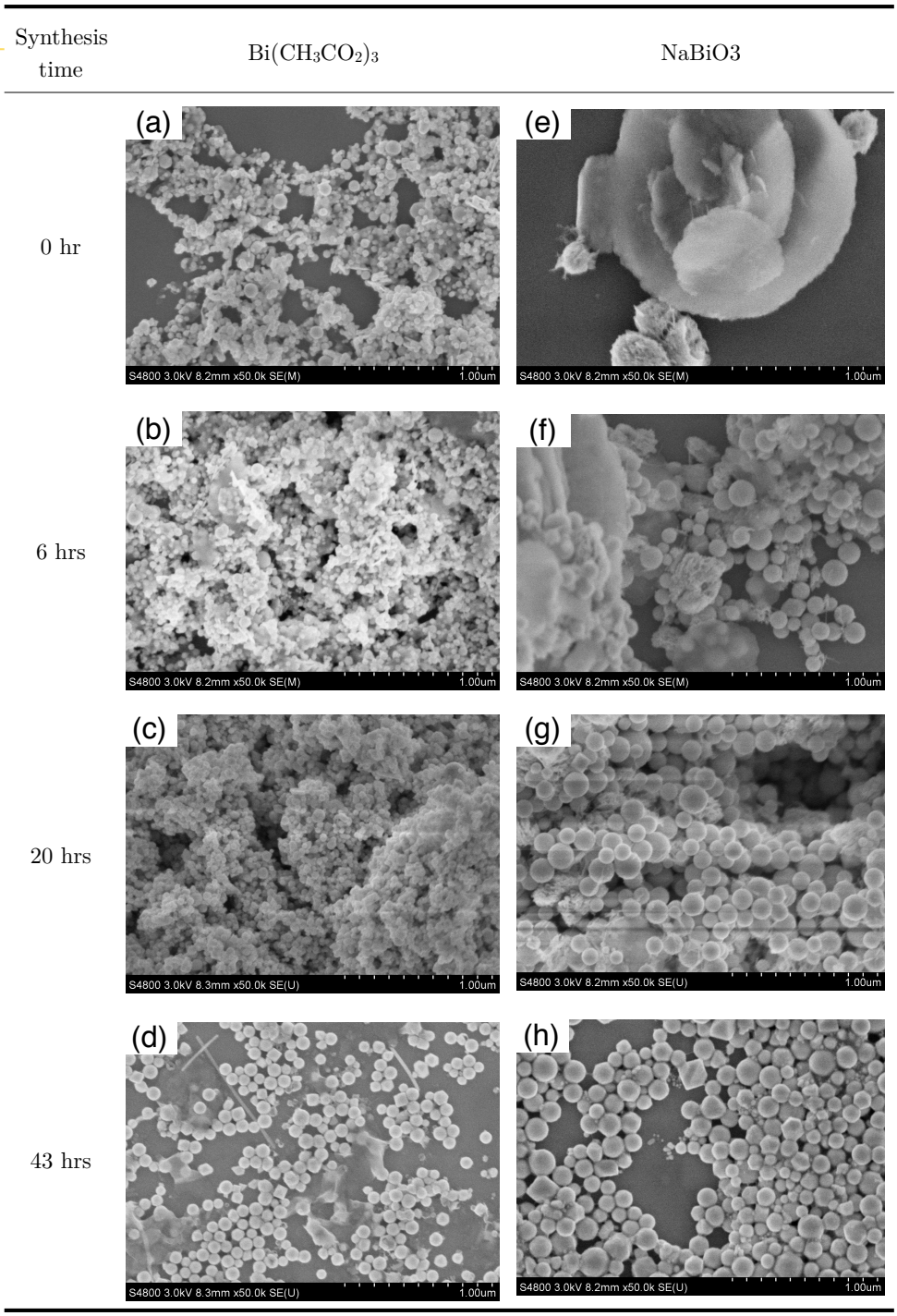

Figure 5.16: SEM images illustrating the differences in the synthesised samples obtained using the different bismuth precursors $Bi(CH_3CO_2)_3$ (left panel) and $NaBiO_3$ (right panel), and variations of synthesis times, including 0 hr, 6 hrs, 20 hrs and 43 hrs. Both syntheses had 93 hrs of stabilisation time.

5.5.3.3 High-Temperature Thermal Decomposition Synthesis: Using PHD-*co*-PVP and 1-octadecene (Buhro's Procedure)

Although successful syntheses were conducted using PVP, PHD-*co*-PVP, a more complex surfactant than PVP, was also utilised as it might have provided better control of the nano-Bi synthesis, as previously reported in [Wang and Buhro, 2010]. PHD-*co*-PVP is a PVP with an additional PHD polymeric group. A typical synthesis uses $BiCl_3$, PHD-*co*-PVP, THF (tetrahydrofuran), octadecene (ODE) and $NaN(SiMe_3)_2$ powder as the primary reagents.

The synthesis was performed in a glovebox under an inert atmosphere of N_2 that was O_2 and H_2O free. In a typical synthesis, $BiCl_3$ was loaded into a reaction tube equipped with a magnetic stirrer. Dried[7] and degassed THF was then put in to the tube, followed by shaking to obtain a homogeneous but milky suspension. The PHD-*co*-PVP in ODE was subsequently mixed with the suspension, and stirred at 750 rpm for one minute. After that, $NaN(SiMe_3)_2$ was added and stirred at 750 rpm. The solution was then stirred at 750 rpm and heated at 165° C in a temperature-controlled oil bath for 20 hrs. The solution turned black after 2-3 minutes, the usual sign that bismuth metal (either nano-Bi or bulk-Bi) has formed.

The purification step was achieved by precipitation of the particles using toluene and methanol as described in details in Appendix B.1.2. The nano-Bi was re-dispersed in toluene for SEM analysis. To determine the composition of the nano-Bi, the product of each synthesis was also characterised using x-ray diffraction (XRD).

SEM revealed spherical and monodispersed nano-Bi (see Fig. 5.17) which subsequent measurements revealed to have a diameter of 51(6) nm. The sample was characterised using PXRD at Diamond synchrotron indicating synthesised product to be bismuth.

5.5.4 Discussion

In the case of the 1,5-pentanediol, two reduction processes occurred, the first by 1,5-pentanediol during the stabilisation time and the second during the synthesis time after the $NaN(SiMe_3)_2$ was added.

[7]Dried THF is THF anhydrous (THF without any water).

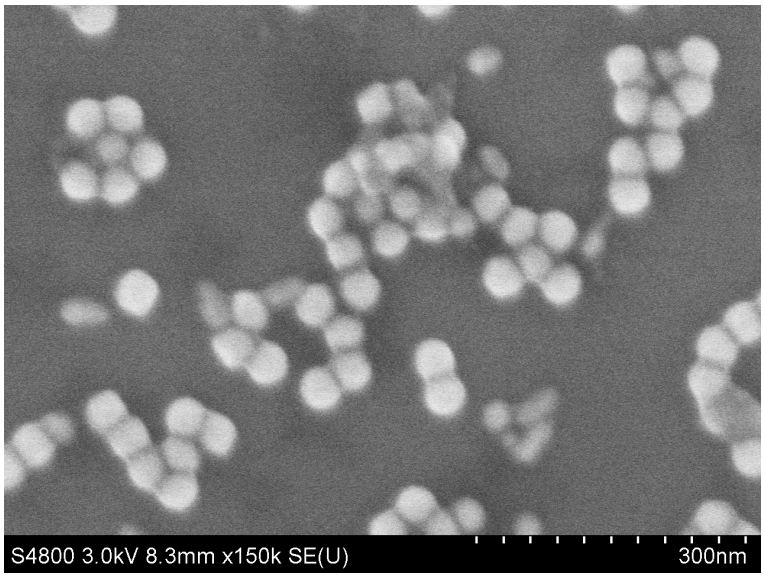

Figure 5.17: SEM image of nano-Bi synthesised using Buhro's procedure [Wang and Buhro, 2010]. The nano-Bi particles are spherical and monodispersed with a size of 51(6) nm.

The type of bismuth precursor used was shown to affect the size of nanoparticles produced (see Fig. 5.15 and Fig. 5.16). In addition, the longer the synthesis time, the larger the size of NPs produced, as found in bismuth acetate ($Bi(CH_3CO_2)_3$). From Fig. 5.16 (left column), the particles are largest after 43 hrs of synthesis time and are smallest at 0 hr of synthesis time.

However, it should be noted that Buhro's process, which was claimed to provide very monodispersed nano-Bi with a size of 4.8 nm, 8.0 nm, 11.3 nm and 15.3 nm with 10-15% polydispersity in size, could not be exactly reproduced in this study. The size of NPs produced by this method in our work is 51(6) nm, some three times larger than the largest size reported in [Wang and Buhro, 2010]. The failure to reproduce these earlier results could be due to the dissimilarity of the syntheses conditions, as presented in Fig. 5.18. From Fig. 5.18, it can be seen that the washing and the precipitation procedure is one of the key dissimilarities because the previous study did not discuss this process in detail. It is possible, therefore, that the very small size and monodispersed particles reported in [Wang and Buhro, 2010] were obtained by size selection during the washing and precipitation procedure.

PHD-*co*-PVP could be used to successfully synthesise nano-Bi in the presence of

ODE. To obtain even better quality and smaller-sized nano-Bi, the 1,5-pentanediol used previously with PVP could have been used with PHD-*co*-PVP. However, time constraints prevented further investigation of the PHD-*co*-PVP in 1,5-pentanediol system. To investigate the interaction between PVP or PHD-*co*-PVP with the nano-Bi surface, Fourier transform infrared spectroscopy (FTIR) is needed. The method was used successfully by Borodko et al. [Borodko et al., 2006], who identified the interaction between PVP and platinum nanoparticle surfaces. An understanding of the bonding interaction of PVP or PHD-*co*-PVP with the nano-Bi particles would lead to a mechanistic understanding of nano-Bi formation using this synthesis approach.

Similarity	Dissimilarity
	Heating rate
Same type of reagents	$BiCl_3$ solubility in THF ($BiCl_3$ in THF was observed to be turbid (this work) while it was reported to be clear solution earlier.)
Mixing steps	Synthesis temperature (200^o C vs 165^o C (this work))
	Synthesis time (17 hrs *vs* 20 hrs (this work))
	Washing and precipitation procedure

Figure 5.18: Comparison of the conditions used in high-temperature thermal decomposition synthesis (Buhro's synthesis) [Wang and Buhro, 2010] and the work in this thesis.

5.5.5 Conclusions

HTP-TD syntheses, including "high-temperature polyol and thermal decomposition synthesis" and "high-temperature thermal decomposition synthesis", provided the best control over the particle sizes and shapes. The type of bismuth precursor, the stabilisation time and the synthesis time were the main factors that could be used to tune the nanoparticle size.

5.6 Conclusions

Three different synthesis methods, aqueous-based synthesis, non-aqueous based synthesis, and high-temperature polyol-thermal decomposition (HTP-TD) synthesis, have been used to make Bi nanoparticles. The high-temperature polyol-thermal decomposition method was found to be the most efficient way to produce nano-Bi, and five samples with particle sizes of 51(6) nm, 52(15) nm, 92(13) nm, 128(45) nm and 138(27) nm were made by this method (as shown in Fig. 5.19). It was these samples that were used for the HP-PXRD experiments described in the Chapter 6. It should be noted that, in this thesis, 128(45) nm was called polydispersed nano-Bi as it has very high polydispersity. Moreover, this polydispersed sample was used in HP-PXRD experiments before any other nano-Bi samples because it was obtained earlier than the others, as described in section 6.3. The rest of the samples have lower polydispersity (so-called monodispersed nano-Bi) and was subsequently used in HP-PXRD experiments described in section 6.4 and section 6.5. A comprehensive investigation of the mechanism by which the nano-Bi particles were formed has not yet been made, both because of time constraints and because the synthesis mechanism was not the main purpose of this thesis, which focuses instead on the behaviour of nano-Bi under pressure.

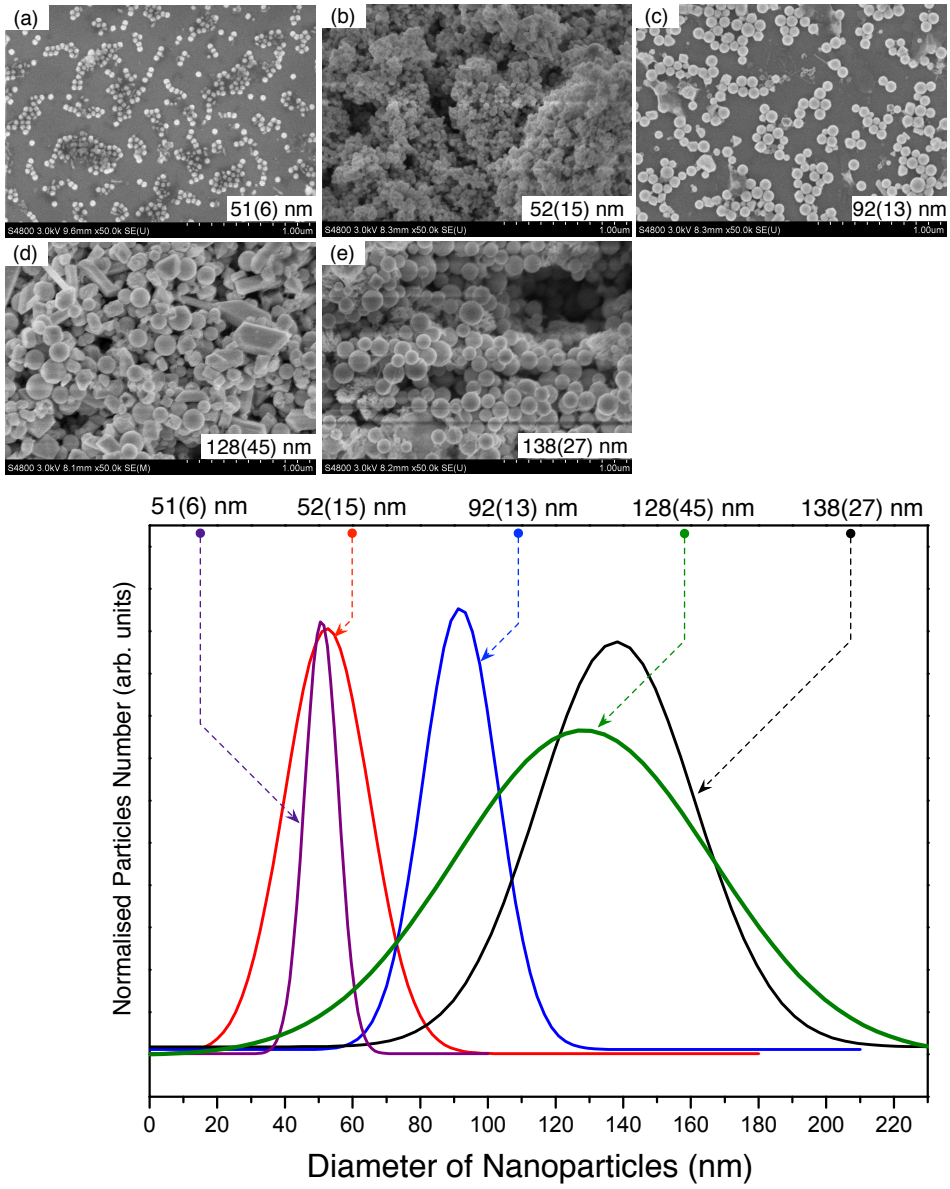

Figure 5.19: (top panel) SEM images of the polydispersed, i.e 128(45) nm, and monodispersed, i.e. 51(6), 52(15), 92(13), and 138(27) nm, nano-Bi samples used for the HP-PXRD experiments. The 51(6) nm sample was obtained from high-temperature thermal decomposition synthesis (Buhro's procedure), and the 52(15) nm, 92(13) nm, 128(45) nm, and 138(27) nm samples were obtained via high-temperature polyol-thermal decomposition synthesis. (bottom panel) Gaussian curves show the particle size distribution of each sample. The sizes were determined by sampling 400-1000 particles, and the uncertainty in the size is calculated from FWHM/2.

5.7 Glossary of Chemical Formulae and Structures

Reagent	Formula (Trade name, Supplier)	Structural formula
Bismuth Precursors		
Bismuth (III) nitrate pentahydrate	$Bi(NO_3)_3 \cdot 5H_2O$ Bismuth(III) nitrate pentahydrate, ACS reagent, ≥98.0%, Sigma-Aldrich	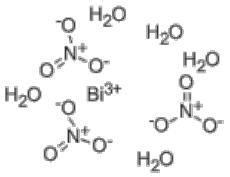
Bismuth acetate	$Bi(CH_3CO_2)_3$ Bismuth(III) acetate ≥99.99%, Sigma-Aldrich	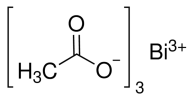
Bismuth (III) chloride	$BiCl_3$ Bismuth(III) chloride, reagent grade, ≥98%, Sigma-Aldrich	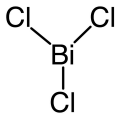
Bismuth (III) oxychloride	BiClO Bismuth(III) oxychloride, 99%, Sigma-Aldrich	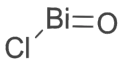
Sodium bismuthate	NaBiO3 Sodium bismuthate ACS reagent, ≥80.0%, Sigma-Aldrich	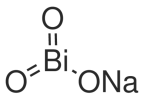

Figure 5.20: Bismuth precursors used in these nanoparticles syntheses.

Reagent	Formula (Trade name, Supplier)	Structural formula
Aqueous Bismuth Salt Approach		
Sodium bis(2-ethylhexyl) sulfosuccinate (NaAOT)	$C_{20}H_{37}NaO_7S$ Bis(2-ethylhexyl) sulfosuccinate sodium salt Dioctyl sulfosuccinate sodium salt (NaAOT), 98% Sigma-Aldrich	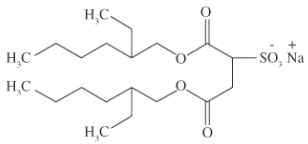
Nonylphenol Polyoxyethylene ether (NP5)	$C_{19}H_{32}O_3$ IGEPAL® CO-520 (NP5), Sigma-Aldrich	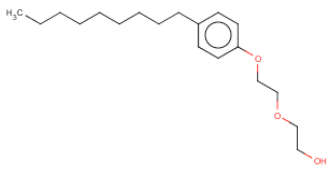
1-Dodecanethiol	$CH_3(CH_2)_{11}SH$ 1-Dodecanethiol, 98%, Sigma-Aldrich	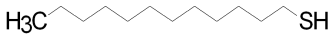

Figure 5.21: Reagents used in the aqueous bismuth synthesis approach.

Reagent	Formula (Trade name, Supplier)	Structural formula
Non Aqueous Bismuth Salt Approach		
Toluene	$C_6H_5CH_3$ Toluene ACS reagent, ≥99.5%, Sigma-Aldrich	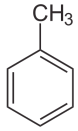
Dodecylamine	$CH_3(CH_2)_{11}NH_2$ Dodecyl amine, 98%, Acros	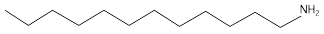
Dioctylamine	$CH_3(CH_2)_7NH(CH_2)_7CH_3$ Dioctylamine 98%, Sigma-Aldrich	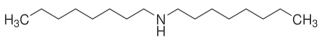
Decanoic Acid	$CH_3(CH_2)_8COOH$ Decanoic acid, 99%, Acros	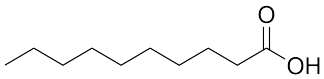
Hydrazine (N_2H_4)	$NH_2NH_2 \cdot H_2O$ Hydrazine Monohydrate, 98%, Sigma-Aldrich	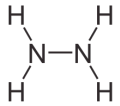
Sodium borohydride ($NaBH_4$)	$NaBH_4$ Sodium borohydride ReagentPlus®, 99%, Sigma-Aldrich	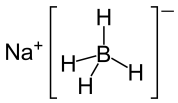
Tetrabutylammonium borohyride ($TBABH_4$)	$(CH_3CH_2CH_2CH_2)_4N(BH_4)$ Tetrabutylammonium borohydride 98%, Sigma-Aldrich	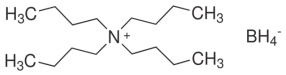
Phenyl Hydrazine	$C_6H_5NHNH_2$ Phenylhydrazine purum p.a., ≥95.0% (GC), Fluka	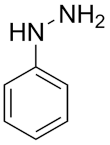

Figure 5.22: Reagents used in the non-aqueous bismuth synthesis approach.

Reagent	Formula (Trade name, Supplier)	Structural formula
High-Temperature Polyol-Thermal Decomposition Approach		
Polyvinyl-pyrrolidone (PVP)	$(C_6H_9NO)_n$ Polyvinylpyrrolidone, PVP, average Mw ~10 kD & ~ 55 kD, Sigma-Aldrich	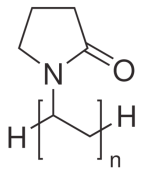
1,5-Pentanediol	$HO(CH_2)_5OH$ 1,5-Pentanediol, purum, ≥97.0% (GC), Fluka	
Diphenyl Ether	$(C_6H_5)_2O$ Molecular Diphenyl ether, ReagentPlus®, 99%, Sigma-Aldrich	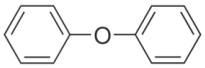
$Bi[N(SiMe_3)_2]_3$	Home Made	-
$NaN(SiMe_3)_2$ in THF	$NaN(SiMe_3)_2$ Sodium bis(trimethylsilyl)amide solution, 1.0 M in THF, Sigma-Aldrich	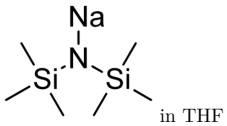 in THF
$NaN(SiMe_3)_2$	$NaN(SiMe_3)_2$ Sodium bis(trimethylsilyl)amide, 95%, Sigma-Aldrich	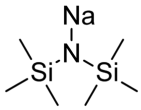
Ethylene Glycol (EG)	$HOCH_2CH_2OH$ Ethylene glycol (2-Methoxyethanol) ACS reagent, ≥99.5% (GC), Fluka	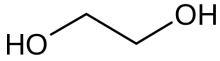
Tetrahydrofuran (THF)	C_4H_8O Tetrahydrofuran (THF)	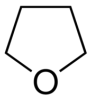
PHD-*co*-PVP	2 Pyrrolidone 1 ethenyl hexadecyl homopolymer Poly(1-vinylpyrrolidone)-graft- (1-hexadecene) Provider : ISP	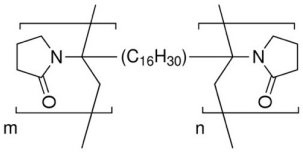
1-Octadecene (ODE)	$CH_3(CH_2)_{15}CH{=}CH_2$ 1-Octadecene (ODE) technical grade, 90%, Sigma-Aldrich	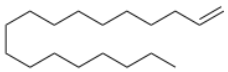
1,3-Diisopropyl-benzene (DIPB)	$C_6H_4[CH(CH_3)_2]_2$ 1,3-Diisopropylbenzene technical, ≥95% (GC), Sigma-Aldrich	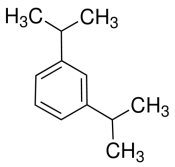
Chloroform	$CHCl_3$ Chloroform ACS grade, Sigma-Aldrich	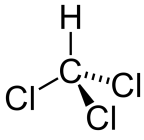

Figure 5.23: Reagents used in the high-temperature polyol-thermal decomposition (HTP-TD) synthesis approach.

Chapter 6

High-Pressure X-Ray Diffraction Studies on Synthesised Bismuth Nanoparticles

6.1 Introduction

As described in Chapter 4, commercially-available samples of nanomaterials were not of sufficient quality for the work in this thesis, and this led me to pursue the synthesis of my own nano-Bi samples, in collaboration with the University of St. Andrews, as described in Chapter 5.

Bismuth nanoparticles (nano-Bi) were synthesised using various methods. Higher-quality nano-Bi samples and improved HP-PXRD techniques have been obtained and developed over a period of approximately one year. In this chapter, the results of this work are described and are divided into four sections:

1. HP-PXRD experiments with bulk-Bi
2. HP-PXRD experiments with polydispersed nano-Bi
3. HP-PXRD experiments with monodispersed nano-Bi
4. HP-PXRD experiments with monodispersed nano-Bi on pressure re-increase

The principal aim is to determine the transition pressures and the crystal structures of nano-Bi at high pressure, particularly whether the incommensurate

Bi-III phase exists. To enable a direct comparison of the high-pressure behaviour of bulk-Bi, it was first necessary to perform a high-pressure diffraction study of nano-Bi and bulk-Bi using the same techniques as would be used for nano-Bi. The very different morphologies of the bulk-Bi and nano-Bi samples are illustrated in Fig. 6.1.

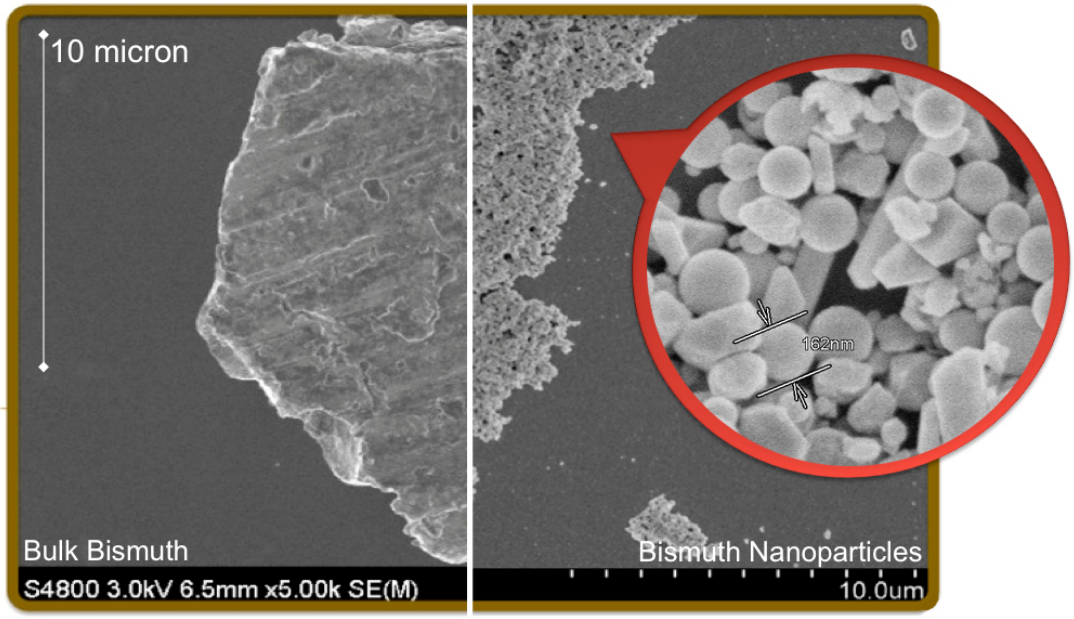

Figure 6.1: The substantial size difference between a bulk bismuth grain ($\sim$10μm) and bismuth nanoparticles (128(45) nm) produced in this study.

6.2 HP-PXRD Experiment with Bulk Bismuth (Bulk-Bi)

It is known from the literature that in bulk bismuth (bulk-Bi), Bi-I transforms at 2.55 GPa and 298 K to Bi-II, which has a monoclinic structure [Tonkov and Ponyatovsky, 2004]. On further compression, Bi-II transforms at 2.70 GPa [Tonkov and Ponyatovsky, 2004] to Bi-III, which was revealed by McMahon et al. [McMahon et al., 2007] to have an incommensurate host-guest structure comprising a body-centred tetragonal (bct) host and a bct guest component, as shown in Fig. 6.2. At 7.7 GPa, Bi-III transforms to a body-centred cubic (bcc) structure (Bi-V) [Aoki et al., 1982] and this phase is stable

to at least 220 GPa [Akahama et al., 2002]. The bulk bismuth phase diagram is shown in Fig. 6.3.

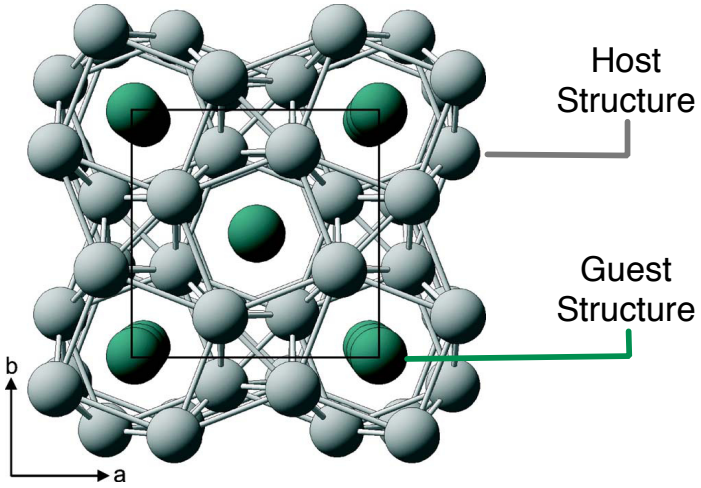

Figure 6.2: The incommensurate host-guest structure of Bi-III, as viewed down the tetragonal c-axis. The structure comprises a body-centred tetragonal (bct) host structure containing channels along the c axis. Contained within these channels are 1D chains of guest atoms which also have a bct structure [McMahon et al., 2007].

6.2.1 Method of HP-PXRD Data Collection with Bulk-Bi

Powder x-ray diffraction data were collected on beamline I15 at the Diamond synchrotron using a MAR345 image plate detector with an incident x-ray wavelength of 0.4124 Å. The incident beam size was 30 μm × 30 μm (the experimental details can be found in Appendix A.3).

The bulk-Bi (see Fig. 6.4) was material of 99.999% purity obtained from the Institute of Rare Metals, Russia. The sample was loaded with a methanol-ethanol (4:1) pressure transmitting medium into a ∼110 μm diameter hole in a tungsten gasket in a Merrill-Bassett-type [Merrill and Bassett, 1974] diamond-anvil cell (DAC) in an oxygen and water free glove box. The DAC was equipped with Boehler-Almax-type seats and diamond anvils, which provided a conical aperture (full angle) of 80°. A small piece of ruby (∼5 μm in diameter) was enclosed with the bismuth powder for pressure measurement via the ruby fluorescence technique [Mao et al., 1986].

The pressure in the cell was increased by tightening the three Allen screws

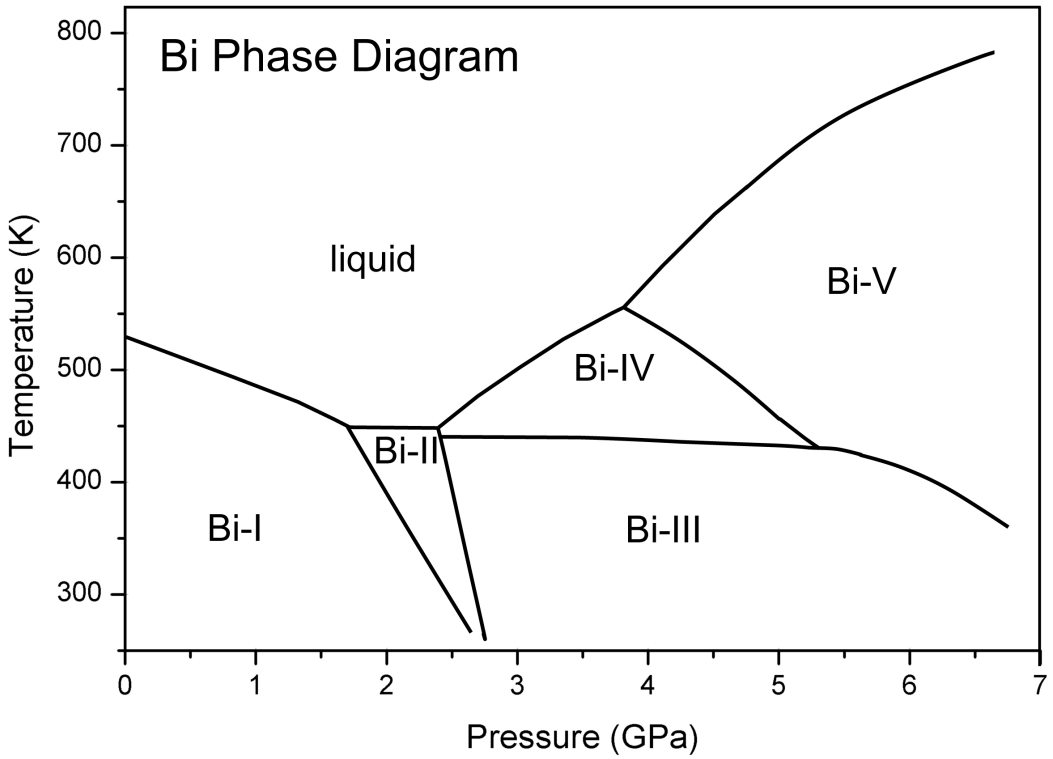

Figure 6.3: The phase diagram of bulk bismuth [Chaimayo et al., 2012].

equally to give 1-2 GPa pressure increments. An x-ray diffraction exposure was taken at every pressure step until the pressure reached 15 GPa. On pressure decrease, the screws were released to decrease the pressure in 1-2 GPa steps. X-ray diffraction exposures were taken at each step until they reached ambient pressure. Full details of the data collection method can be found in section 3.1.3.2.

6.2.2 Results and Discussion

6.2.2.1 On Pressure Increase

The purpose of this initial experiment was to repeat previous high-pressure investigations of bulk-Bi using exactly the same experimental and analysis methods as would be used to study the nano-Bi samples. The diffraction data from bulk-Bi on pressure increase are shown in Fig. 6.5, and the 1D integrated diffraction profiles obtained at each pressure are the same as those presented previously in the literature [Degtyareva, 2003, Degtyareva et al., 2004].

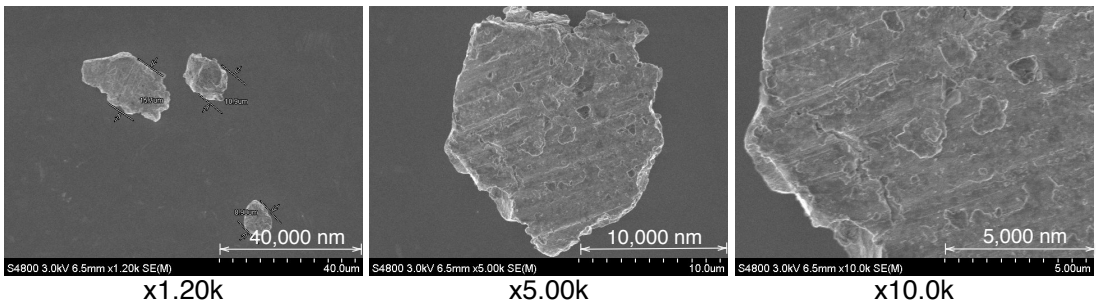

Figure 6.4: SEM images of bulk-Bi at different magnifications, ×1.20k (left), ×5.00k (middle) and ×10.0k (right). Each grain is more than 10,000 nm in diameter.

Analysis of the data in Fig. 6.5 reveals that the phase transitions are Bi-I→Bi-II at 2.6(1) GPa, Bi-II→Bi-III at 3.1(3) GPa, and Bi-III→Bi-V at 10.0(5) GPa. These transition pressures are determined as the first pressure at which the higher-pressure phase appears. It is evident that the Bi-I→Bi-II and Bi-II→Bi-III phase transitions pressures (P_{tr}) obtained from Fig. 6.5 are in excellent agreement with the existing literature, which has Bi-I→Bi-II at 2.55 GPa, Bi-II→Bi-III at 2.7 GPa. However, the transition of Bi-III→Bi-V was reported at 7.7 GPa in the literature [Degtyareva, 2003, Degtyareva et al., 2004], while the P_{tr} for the Bi-III→Bi-V transition obtained in this experiment is some 2 GPa higher than the value.

It should be noted, however, that in an experiment in [Degtyareva, 2003], Bi-III→Bi-V was found at 8.5(5) GPa while the generally accepted Bi-III→Bi-V P_{tr} is 7.7 GPa [Aoki et al., 1982]. These differences in P_{tr} could result from the different methods used to define P_{tr}. In this thesis, P_{tr} is defined as the pressure at which the new phase was first observed. The method of phase transition determinations were not mentioned in [Degtyareva, 2003, Degtyareva et al., 2004] or in [Aoki et al., 1982]; therefore, the P_{tr} of bulk-Bi reported in this thesis may simply not be the same compared to the numbers given by different authors.

Since 1982, it has been reported that bulk-Bi has a propensity to recrystallise on pressure increases at room temperature [Aoki et al., 1982]. Degtyareva et al. [Degtyareva et al., 2004] reported that when Bi-II transforms to Bi-III at room temperature, the bulk powder sample recrystalises from a fine powder, giving smooth Debye-Scherrer rings, to a polycrystalline form at 2.7 GPa and giving a highly textured and spotty 2D diffraction image from Bi-III. This is illustrated in

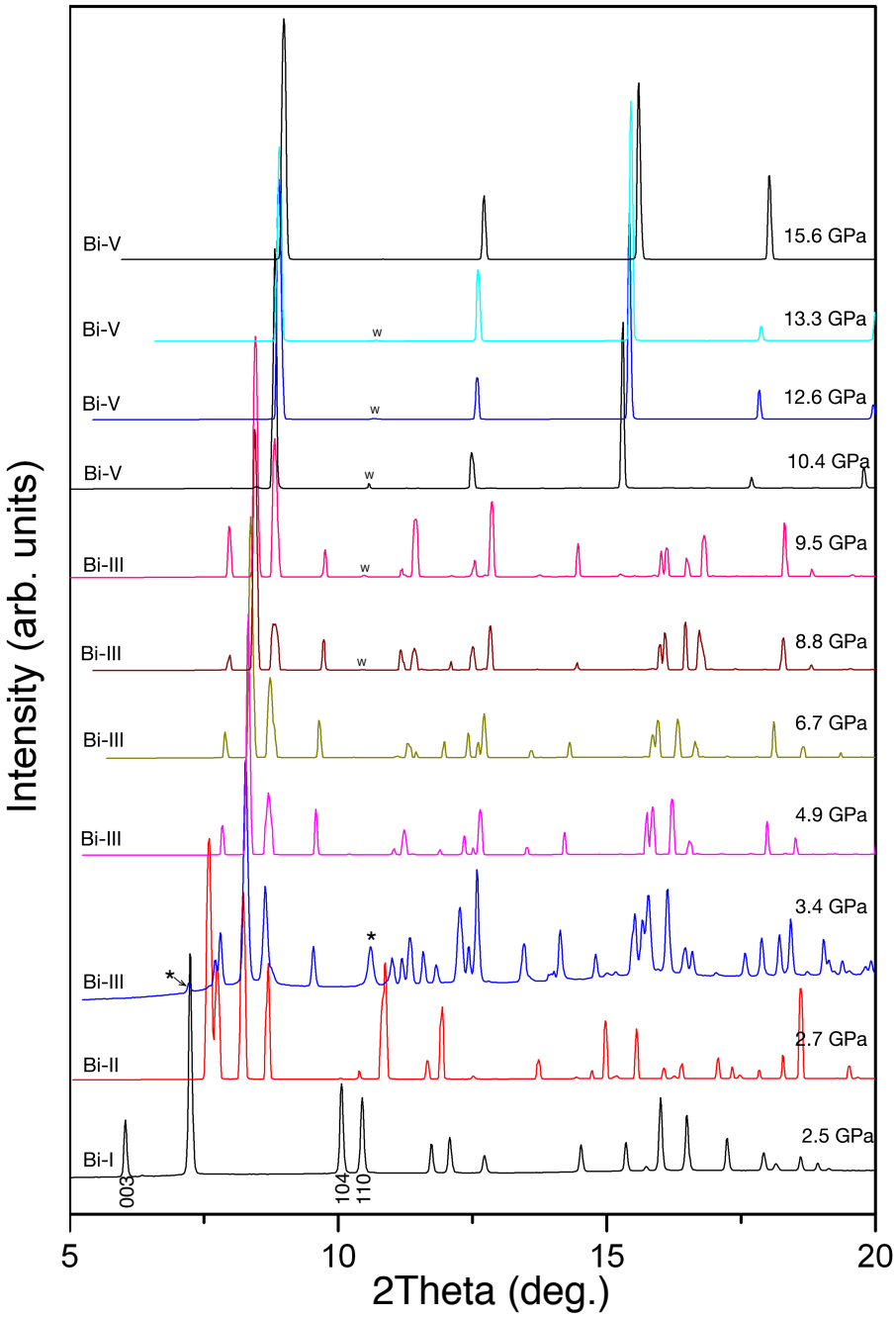

Figure 6.5: Waterfall plot of 1D integrated diffraction profiles obtained from bulk-Bi on pressure increase from ambient pressure to 15.6 GPa. The pressure was increased in 1-2 GPa steps. The diffraction patterns come from four phases, Bi-I, Bi-II, Bi-III and Bi-V. The asterisks (*) mark the positions of the unaccounted-for peaks and 'W' indicates peaks from the tungsten gasket. The peaks labelled (003), (104), and (110) are analysed in section 6.3.2.1

Fig. 6.6 which shows the 2D diffraction image from a sample of Bi-III at 6.7 GPa. The spotty nature of the Bi-III diffraction patterns means that there are many saturated pixels on the image plate (the maximum intensity of the image plate is only ∼65,000) and, as a result, the 1D integrated diffraction profiles have unusual peak shapes, with truncated tops. See, for example, the 4.9 and 6.7 GPa profiles in Fig. 6.5. Diffraction profiles of bulk-Bi-III with smooth Debye-Scherrer rings can only be obtained by compressing Bi-I directly into Bi-III at a low temperature, below the stability field of Bi-II [McMahon et al., 2000].

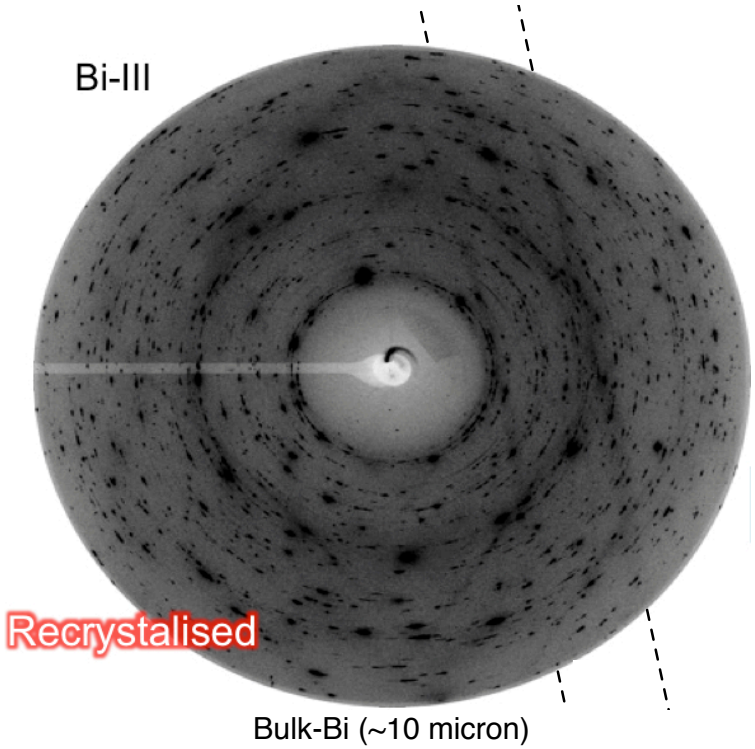

Figure 6.6: 2D diffraction image from Bi-III in bulk-Bi at 6.7 GPa. The 1D integrated diffraction profile of this image is shown in Fig. 6.5. The sample recrystalised at the transition to Bi-III, resulting in the spotty nature of the pattern. The inclined lines of diffuse scattering in the image arise from the scattering from the chains of guest atoms. The dashed lines are guides for the eye for the inclined lines of diffuse scattering.

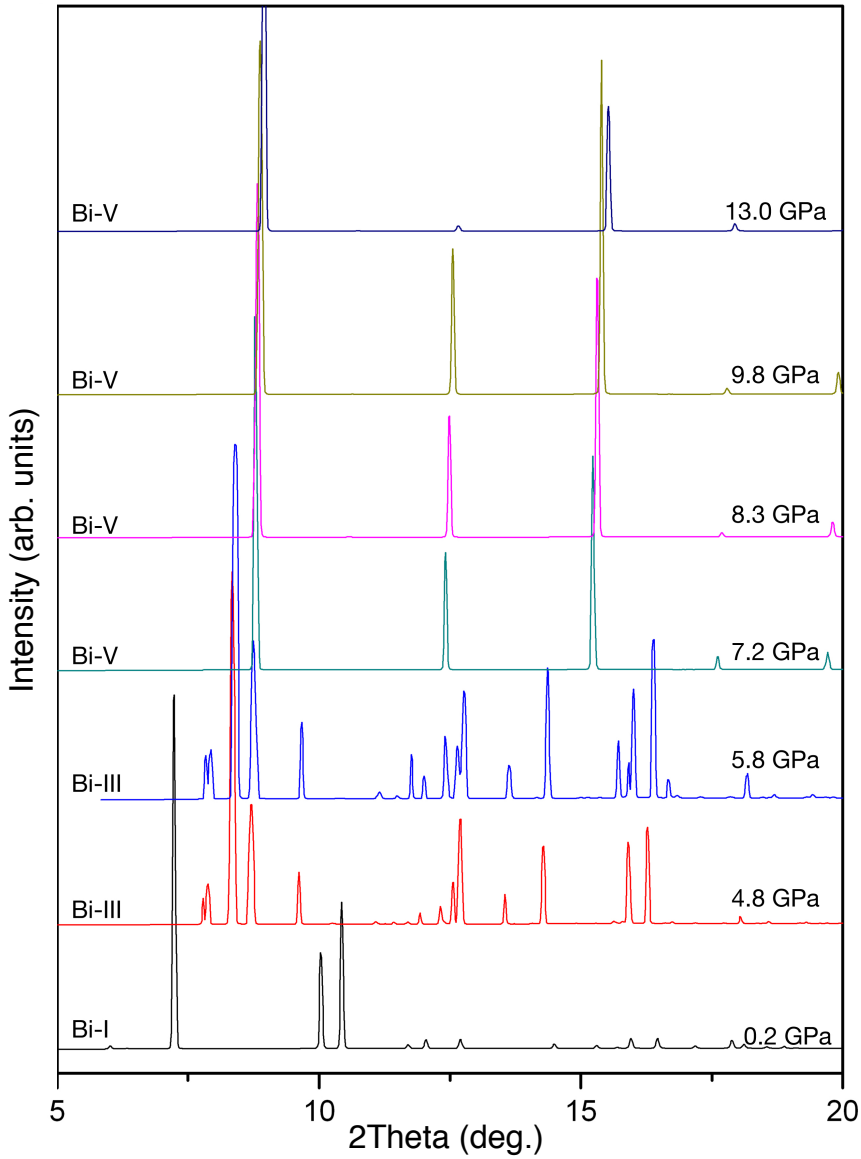

Figure 6.7: Waterfall plot of 1D integrated diffraction profiles obtained from bulk-Bi from 13.0 GPa to ambient pressure on pressure decrease. The pressure was decreased in 2-3 GPa steps. The different diffraction profiles come from three phases, Bi-V, Bi-III, and Bi-I.

6.2.2.2 On Pressure Decrease

As can be seen in Fig. 6.7, on pressure decrease from Bi-V, the reverse transition sequence is observed, and the results again agree with the literature [Degtyareva, 2003, Degtyareva et al., 2004]. Because of hysteresis (all of the pressure-induced phase transitions in Bi are first-order), the transition pressures on pressure decrease are lower than those obtained on pressure increase. The Bi-V→Bi-III transitions take place at 6.5(7) GPa, and Bi-III→Bi-I at 2.5(2.3) GPa.

It is important to note that Bi-II was not observed on pressure decrease, because a large pressure decrease resulted in the stability range of Bi-II being missed. Therefore, the Bi-III→Bi-II, and Bi-II→Bi-I transition pressures, and their hystereses, could not be obtained.

6.2.3 Conclusions of the HP-PXRD Experiment with Bulk-Bi

The bulk-Bi studied here shows the same behaviour as that reported previously in the literature, with the P_{tr} on pressure increase being very similar to those reported in [Degtyareva, 2003, Degtyareva et al., 2004]. The pressure hysteresis in the Bi-III→Bi-V transition has been found to be 2.7(1.1) GPa. The same high-pressure experimental techniques and analysis methods used to study bulk-Bi on beamline I15 at the Diamond synchrotron were then subsequently used to study nano-Bi at high pressures.

6.3 HP-PXRD Experiment with Polydispersed Nano-Bi

6.3.1 Method of HP-PXRD Data Collection with Polydispersed Nano-Bi

Powder x-ray diffraction data were collected on beamline I15 at the Diamond synchrotron using a MAR345 image plate detector and an incident x-ray wavelength of 0.4124 Å. The incident beam size was 30 μm x 30 μm (the experimental details can be found in Appendix A.3).

The nano-Bi was synthesised at the Department of Physics and Astronomy, the University of St. Andrews, UK, as described in Chapter 5, and was produced using the high-temperature polyol-thermal decomposition method (for more details see Appendix B.1.1). The nanoparticles were polydispersed with diameters of 128(45) nm and mostly had a spherical and faceted morphology, as illustrated in Fig. 6.8. This sample was first obtained and carried out in HP-PXRD experiment. However, better quality samples used in HP-PXRD experiments are presented in the next section (section 6.4).

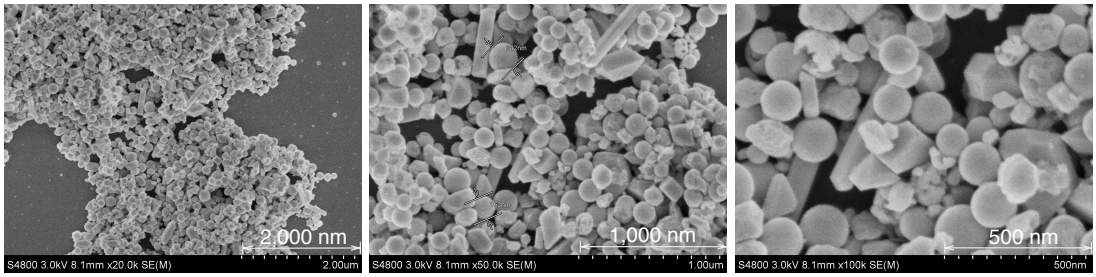

Figure 6.8: SEM images of the 128(45) nm polydispersed sample at different magnifications, ×20.0k (left), ×50.0k (middle), and ×100k (right).

The nano-Bi sample was loaded with a methanol-ethanol (4:1) pressure-transmitting medium into a ∼110 μm diameter hole in a tungsten gasket in a Merrill-Bassett-type [Merrill and Bassett, 1974] diamond-anvil cell (DAC) in an oxygen and moisture free glove box. The DAC was equipped with Boehler-Almax-type seats and diamond anvils, which provided a conical aperture (full angle) of 80°. A small piece of ruby (∼5 μm in diameter) was enclosed with the sample for pressure measurement via the ruby fluorescence technique [Mao et al., 1986].

6.3.2 Results and Discussion

6.3.2.1 On Pressure Increase

The x-ray diffraction patterns obtained on pressure increase revealed a considerable similarity between nano-Bi and bulk-Bi. Bi-I is observed from ambient pressure to 4.0(6) GPa, Bi-III from 3.2(2) GPa to 18.3(1.3) GPa and Bi-V from 12.2(1.7) GPa to 20.7(1) GPa (the highest pressure attained in this experiment), as illustrated in Fig. 6.9. In addition to the peaks from Bi-I, however, there are also some

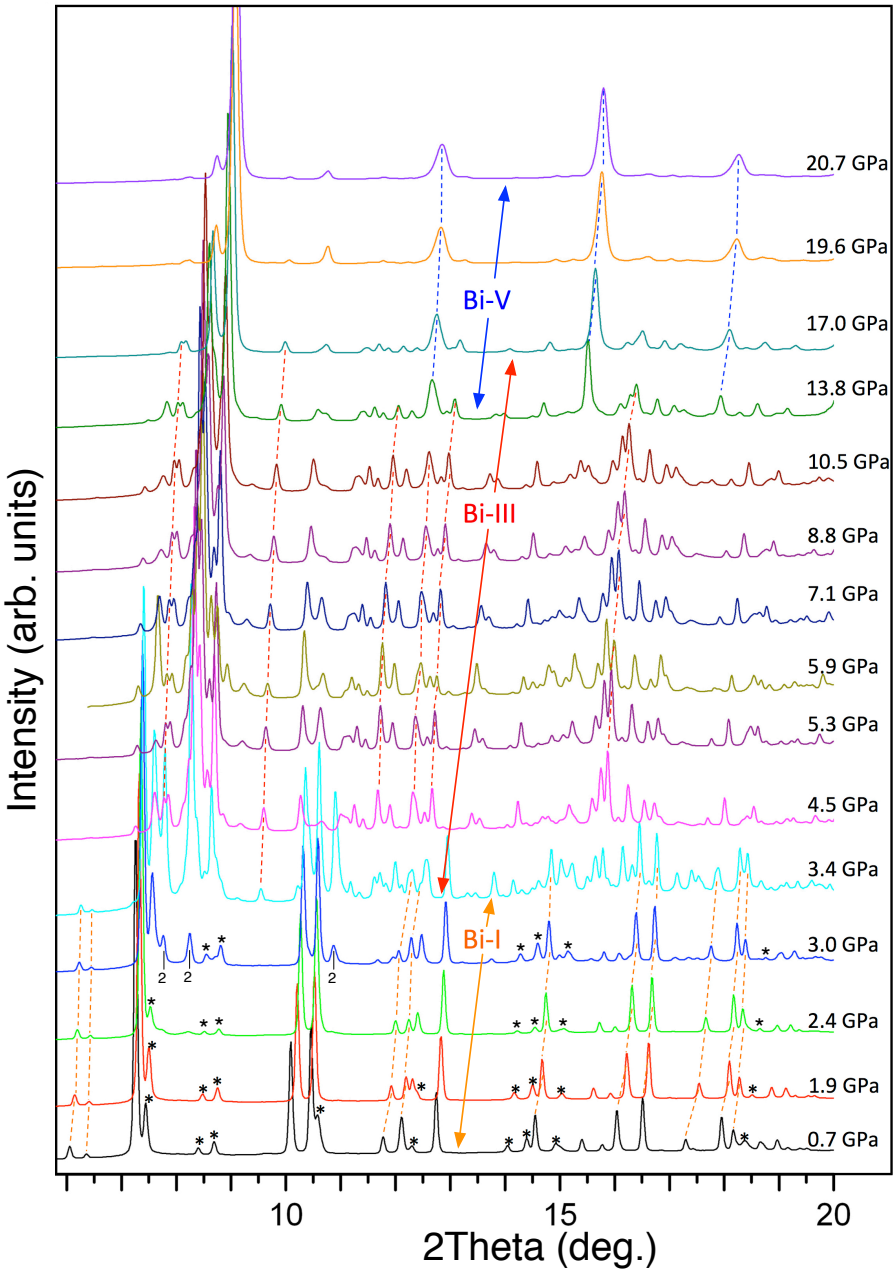

Figure 6.9: Waterfall plot of integrated diffraction profiles obtained from nano-Bi 128(45) nm on pressure increase from 0.7 to 20.7 GPa in increments of 1-2 GPa. The different diffraction profiles arise from three phases, Bi-I, Bi-III and Bi-V. The orange-dashed lines identify some diffraction peaks from Bi-I, the red-dashed lines identify some significant diffraction peaks from Bi-III, and the blue-dashed lines identify significant diffraction peaks from Bi-V. The diffraction peaks marked with asterisks (*) in the 0.7, 1.9, 2.4, 3.0 GPa profiles are from a bismuth oxide (Bi_2O_3) contaminant. The peaks labelled with '2' in the 3.0 GPa profile could be Bi-II peaks, but this is uncertain because they are also located close to the problematic Bi_2O_3 contaminant peaks.

additional peaks (which are identified with asterisks, '*' in Fig. 6.9) which are from Bi_2O_3, as confirmed by Rietveld refinement of the 0.7 GPa profile.

At 3.0 GPa, there are some peaks which are likely to be the (020), ($\bar{1}$11) and (220) peaks of Bi-II (from left to right), as labelled with '2' in Fig. 6.9. However, because the peaks are located very close to Bi_2O_3 peaks, a definite conclusion as to whether those peaks are from Bi-II cannot be made.

Phase coexistence is observed in the nano-Bi, as is evident from the mixed phase diffraction profiles. From Fig. 6.9, Bi-III is found to coexist with Bi-I at 3.4 GPa, along with some unidentified peaks. However, no phase coexistence of Bi-I and Bi-III was observed in bulk-Bi. Therefore, phase coexistence in nano-Bi exists over somewhat larger pressure ranges than in bulk-Bi.

From Fig. 6.9, between 1D integrated diffraction profiles at 3.4-17.0 GPa where Bi-III exists, the 1D integrated diffraction patterns have some peaks that cannot be explained by Bi-I, Bi-II or Bi-V. This phase is referred to as "complex Bi-III[1]" which comprises peaks from Bi-III and unaccounted-for additional peaks. This could be due to the behaviour of nano-Bi itself, or to the contamination of Bi_2O_3. The identity of the "complex Bi-III" phase will be addressed in section 6.4.2.2, as in the present sample the Bi_2O_3 contaminant makes detailed phase identification complicated.

The presence of Bi_2O_3 in the sample is linked to the nano-Bi sample-delivery method and the high level of oxygen (∼70-80 ppm) in the glove box used for the synthesis. The nano-Bi, contained in a closed-cap reaction tube sealed with paraffin tape, was delivered from the synthesis glove box at the University of St. Andrews directly to the DAC-loading glove box at The University of Edinburgh. It is very likely that oxygen may have leaked into the tube and formed Bi_2O_3. A second possibility could be the incidence of a high percentage of oxygen (∼70-80 ppm) in the synthesis environment itself, resulting in Bi_2O_3 formation. To avoid such contamination in later work, care was taken in monitoring oxygen levels during the synthesis, and an improved delivery method was implemented, which entailed the use of a vacuum chamber (with a small amount of argon) to store and transport the reaction tube.

To determine whether the particle size of the nano-Bi sample resulted in a broadening of the Bragg peaks, the full width at half maximum (FWHM) of three

[1]In this case, complex Bi-III refers to Bi-III plus an additional phase only. However, it does not have any meaning related to superlattice.

reflections (003), (104), and (110) (as shown in Fig. 6.5) from Bi-I in bulk-Bi are compared with that of the same three peaks from nano-Bi in Table 6.1. The width was determined using the XRDA software by fitting the peaks with a Gaussian function. On the the whole, the FWHM recorded from the bulk-Bi are smaller than those measured from the nano-Bi, as is to be expected from the Scherrer equation (see section 3.3.4 for more details about Scherrer equation).

Table 6.1: Comparison of the widths (FWHM) of the (003), (104), (110) Bragg peaks from bulk-Bi-I at 2.5 GPa and 128(45) nm nano-Bi-I at 2.4 GPa.

	FWHM of reflection (hkl) in 2θ (deg.)		
	(003)	(104)	(110)
Bulk-Bi	0.059(4)	0.069(5)	0.068(4)
Nano-Bi	0.073(11)	0.070(2)	0.073(2)

Figure 6.10: 2D diffraction image from complex Bi-III at 7.1 GPa, as obtained from 128(45) nm nano-Bi starting material, shows very good powder pattern. The few intense spots in the pattern arise from the diamond anvils of the pressure cell.

The incommensurate Bi-III phase is found to exist in nano-Bi from 3.2(2) GPa

to 18.3(1.3) GPa on pressure increase (as shown in Fig. 6.9) with some unaccounted-for additional peaks (which are labelled in Fig. 6.13). The 2D diffraction images from complex Bi-III at room temperature (Fig. 6.10) show strikingly-smooth powder patterns, in complete contrast to the very spotty diffraction patterns of Bi-III obtained using a bulk-Bi sample (see Fig. 6.6 for bulk-Bi-III). The very smooth Debye-Scherrer rings are maintained to the highest pressure studied with this sample (∼20 GPa) on pressure increase, and to ambient pressure on pressure decrease. To investigate the form of the nano-Bi sample after pressuring to 20 GPa and decompressing back to ambient pressure, the recovered sample was examined by SEM. After unloading from the DAC, the sample is still nano-crystalline, as can be seen from the SEM image in Fig. 6.11, which shows the recovered sample to be very similar in appearance to that of the as-loaded sample. It is believed that the pressure transmitting medium (PTM), methanol-ethanol (4:1), prevents the nanoparticles attaching to each other, thus preventing recrystallisation as the sample enters the Bi-III phase. This hypothesis might be tested by loading a nano-Bi sample without a PTM. The initial collapse of the gasket hole on first pressure increase would make the sample no longer to be nano-crystalline.

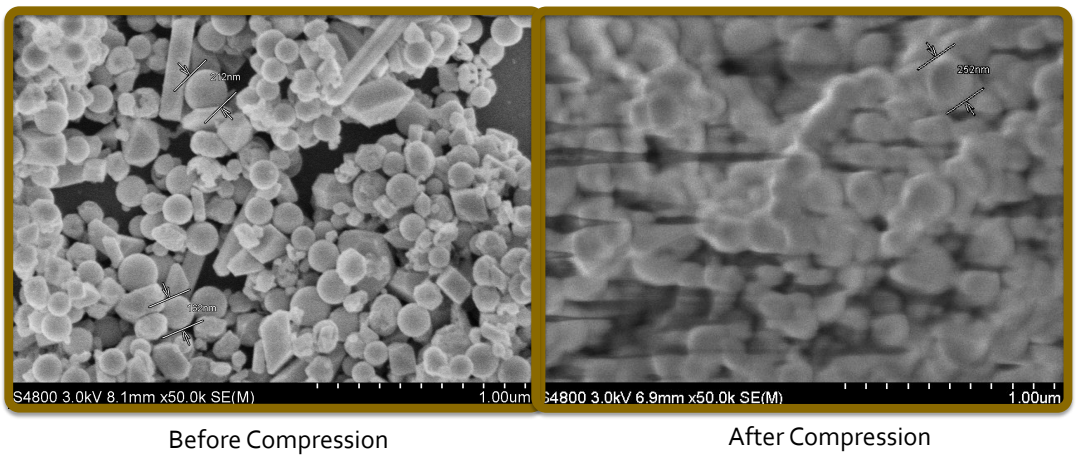

Figure 6.11: SEM images of a nano-Bi sample before pressure application (left) and on recovery from the gasket hole after pressure release (right). The nano-Bi sample remains nano-crystalline after recovery, with no evidence of larger crystal growth.

In nano-Bi, the Bi-III→Bi-V transition, as judged by the first appearance of diffraction peaks from Bi-V, is at 12.2(1.7) GPa, higher than the Bi-III→Bi-V tran-

sition pressure of bulk-Bi - (7.7 GPa) [Degtyareva, 2003, Degtyareva et al., 2004] or 10.0(5) GPa from the work described earlier in section 6.2.2. An increase in transition pressures with decreasing particle size is a well-known phenomenon in nanomaterials, with, for example, the P_{tr} of CdSe nanoparticles, increasing from 3.6 GPa to 4.9 GPa for crystallites decreasing from 2.1 nm to 1 nm in radius, while the transition pressure of bulk-CdSe is 2.0 GPa [Tolbert and Alivisatos, 1995b]. (A more extensive review on size-dependent P_{tr} can be found in section 2.4).

On further pressure increase, as shown in Fig. 6.9, Bi-III and Bi-V are found to coexist in the 13.8 GPa and 17.0 GPa profiles of nano-Bi, a much larger range than the coexistence range of 0.8(8) GPa that was observed in bulk-Bi (see Fig. 6.5). With further increases in pressure, all of the Bi-III eventually transforms to Bi-V, and single-phase Bi-V patterns were obtained above 19.6 GPa.

6.3.2.2 On Pressure Decrease

On pressure decrease from 19.5 GPa, see Fig. 6.12, the following phase transitions are observed: Bi-V→Bi-III at 6.2(2.5) GPa, Bi-III→Bi-II at 1.8(6) GPa, Bi-II→Bi-I at 1.8(6) GPa. It is notable that, in contrast to the pressure decrease experiment using bulk-Bi, Bi-II was observed in the nano-Bi, and was found to coexist with Bi-I at 1.2(1) GPa. It should be noted that due to the small stability range of Bi-II, both the Bi-III→Bi-II and Bi-II→Bi-I transitions were found to occur in the same pressure range of 2.3-1.2 GPa.

Unfortunately, from Fig. 6.12, it is not possible to determine whether Bi-V coexists with Bi-III or not on pressure decrease, and over what pressure range, because the pressure step between the last appearance of Bi-V (8.7 GPa) and the first appearance of Bi-III (3.7 GPa) is too large. However, no coexistence between Bi-III and Bi-II is observed, while Bi-II and Bi-I do coexist, as mentioned above.

It is known from the literature that Bi_2O_3, which has a monoclinic structure at ambient conditions, transforms to an amorphous phase at 20.7 GPa [Chouinard and Desgreniers, 2000], and that this process is irreversible. As can be seen from Fig. 6.9 and Fig. 6.12, Bi_2O_3 clearly exists in the Bi-I patterns on pressure increase (see Fig. 6.9). However, peaks from Bi_2O_3 are not present in the ambient-pressure patterns obtained after pressure decrease (see Fig. 6.12). This absence of Bi_2O_3 peaks on pressure decrease is most likely due to its transformation to the amorphous form of Bi_2O_3, as reported by Chouinard et

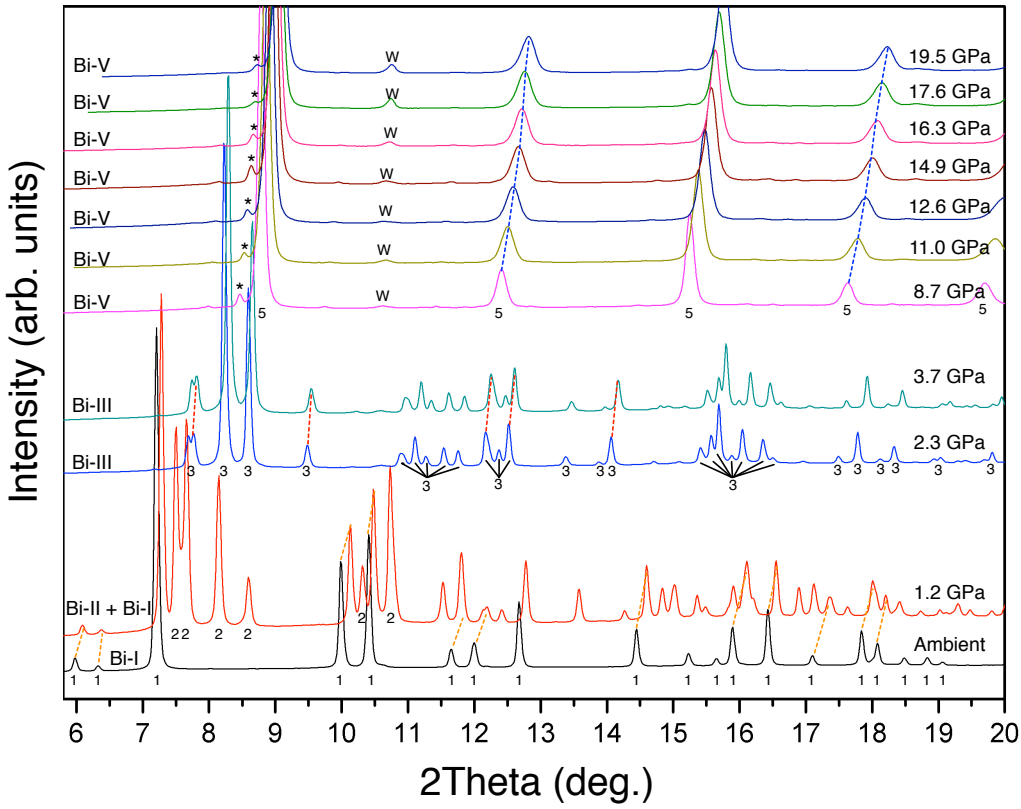

Figure 6.12: Waterfall plot of 1D integrated diffraction profiles obtained from nano-Bi 128(45) nm on pressure decrease from 19.5 GPa to ambient pressure in 1-2 GPa steps. Four phases are observed, Bi-V, Bi-III, Bi-II and Bi-I, with peaks from the different phases marked below the profiles with 5, 3, 2 and 1, respectively. Bi-II is observed as a mixed-phase profile with Bi-I. The orange-dashed lines indicate the progression of peaks from Bi-I, the red-dashed line highlights some of the significant peaks of Bi-III, and the blue-dashed line shows some of the Bi-V peaks. The asterisk '*' labels the residual Bi-III peaks. The 'W' marks the positions of tungsten gasket peaks. There is no evidence of any peaks in the profiles from Bi_2O_3 due to its amorphisation at high pressure, as reported in [Chouinard and Desgreniers, 2000].

al. [Chouinard and Desgreniers, 2000]. Further experiments were conducted to determine whether Bi_2O_3 nanoparticles have a crystalline-amorphous transition, and whether the transition is reversible or not in nanoparticles (see Appendix A.1).

The waterfall plot of 1D integrated diffraction profiles obtained on pressure decrease (Fig. 6.12) reveals that single-phase Bi-III profiles can be obtained at 3.7 and 2.3 GPa, unlike on pressure increase where the complex Bi-III was observed, as described earlier.

It is unclear why the nano-Bi behaves differently on pressure decrease compared to pressure increase, as regards the existence of single-phase Bi-III samples. Due to the lack of data between 8.7-3.7 GPa on pressure decrease. A hypothesis can be made once the diffraction patterns between ∼9-3 GPa are observed. Therefore, this phenomenon will be discussed in section 6.4.2.3.

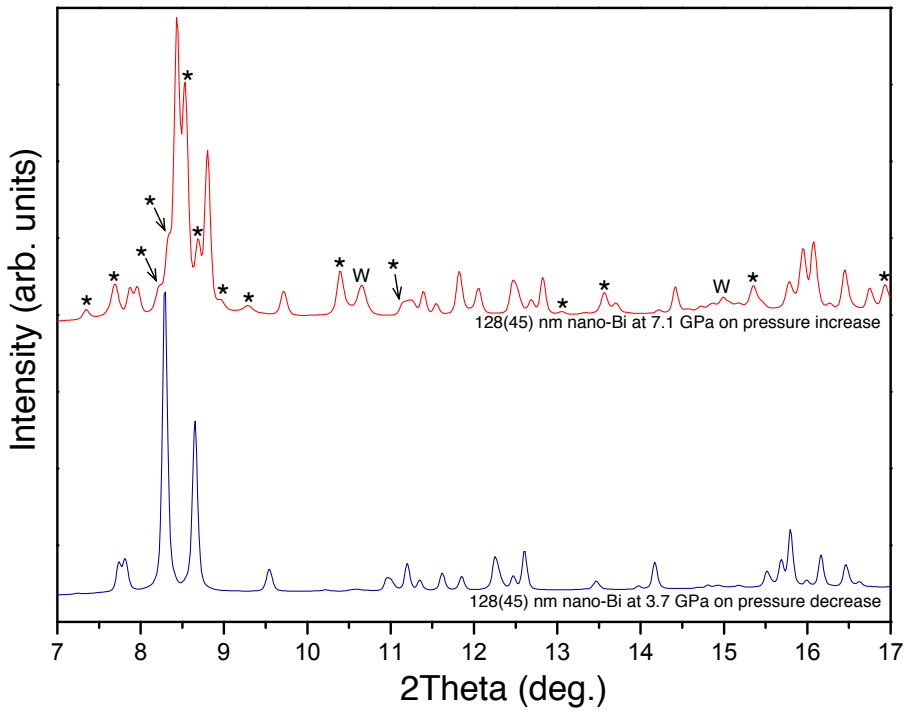

Figure 6.13: 1D integrated diffraction profiles of (top) nano-Bi at 7.1 GPa on pressure increase, (bottom) nano-Bi at 3.7 GPa on pressure decrease. Asterisks (*) indicate unaccounted-for peaks. The 'W' labels tungsten gasket peaks.

6.3.2.3 Structural Refinement with Polydispersed Nano-Bi

Fig. 6.13 illustrates the 128(45) nm complex Bi-III diffraction pattern obtained at 7.1 GPa on pressure increase. 21 peaks, from 7°-17° in 2θ, of the observed reflections (except the peaks with '*' and 'W') of nano-Bi could be indexed on the same superspace group of Bi-III as reported for bulk-Bi in [McMahon et al., 2007], which is an incommensurate host-guest structure with $a = 8.496(1)$ Å, $c = 4.152(1)$ Å, and $q = 1.306(1)$, as refined using the Le Bail method. The refinement of Bi-III on pressure increase shows that there is a Bi-III phase in this complex Bi-III phase. Regarding the additional phase, the refinement was made possible by using the masking tool in the JANA2006 software to ignore the non-related peaks (as labelled with '*' and 'W').

To avoid the extra phase seen in pressure increase in Fig. 6.13 (top), the 1D integrated diffraction profile at 3.7 GPa on pressure decrease was used to do a full Rietveld refinement[2], as the pattern is clean Bi-III phase (or single-phase Bi-III). With this pattern, the nano-Bi could be indexed on the same superspace group of Bi-III reported for bulk-Bi in [McMahon et al., 2007], which is an incommensurate host-guest structure with $a = 8.643(1)$ Å, $c = 4.225(1)$ Å, and $q = 1.308(1)$, as refined using the Rietveld method with $R_{wp} = 5.5\%$. However, the lattice parameters (a, c, and q-vector) of nano-Bi are slightly different from those of bulk-Bi which are $a = 8.635(1)$ Å, $c = 4.219(1)$ Å, and $q = 1.310(1)$ at 3.6 GPa [Degtyareva et al., 2004].

6.3.3 Conclusions

In general, the synthesised nano-Bi behaves almost the same as bulk-Bi does in terms of phase transition order, and the structures of each phase.

The incommensurate Bi-III structure (body-centred tetragonal (bct) host and bct guest) does exist on both pressure increase and decrease in nano-Bi. A full Rietveld refinement was able to be performed because no recrystallisation of this phase is found when using nano-Bi on pressure decrease.

On pressure increase, incommensurate Bi-III is found to exist with unaccounted-for additional peaks. Bi-III and the additional peaks are the so-called complex Bi-III phase, which exists over a wide range of pressures (15.1(15) GPa). On the

[2]refinement of atomic positions and thermal parameters.

other hand, on pressure decrease, only single-phase Bi-III patterns were found to be present only in a much narrower pressure range (4.5(3.0) GPa).

The best possible full Rietveld refinement can only be done with these clean Bi-III on pressure decrease, because it has no other additional peaks to affect the refinement. It is unfortunate that clean Bi-III does not exist on pressure increase due to the wide pressure range of stability which would help us to understand incommensurate structure (Bi-III) vs. pressure more easily.

The additional peaks in complex Bi-III could be due to the nature of the nano-Bi itself or resulting from Bi_2O_3 contamination. This issue is investigated in the next section. The coexistence regions of Bi-I-Bi-II and Bi-II-Bi-III and especially Bi-III-Bi-V are all larger than those found in the bulk. The phase coexistence also makes phase transition determination harder than it should be. The large coexistence of phases might arise from the polydispersed nature of the sample.

To overcome these issues, therefore, monodispersed nano-Bi is needed, as described in the next section.

6.4 HP-PXRD Experiments with Monodispersed Nano-Bi

The work described in the previous section on the polydispersed sample revealed that the phases observed at high pressure were the same as those found in the bulk, although the transition pressures were higher than those seen in the bulk material and the phases were found to coexist over larger pressure ranges. In order to determine what effect the polydispersed nature of the sample has on these phenomena, and to determine what effect that the sample size has on the transition pressures and crystal structures, particularly the incommensurate Bi-III phase, it is necessary to conduct similar high-pressure experiments on a range of different monodispersed samples, synthesised using the methods described in Chapter 5.

6.4.1 Method of HP-PXRD Data Collections with Monodispersed Nano-Bi

The diffraction and analysis methods used in this section were almost the same as those described in section 6.3.1 using the x-ray wavelengths mentioned in Appendix A.3. The only difference was that the samples were not loaded in a glove box, as this was no longer felt to be necessary.

Nano-Bi particles of various sizes were synthesised in the Department of Physics and Astronomy, the University of St. Andrews, UK. The nano-Bi samples had diameters of 51(6) nm, 52(15) nm, 92(13) nm, and 138(27) nm (see Chapter 5 section 5.5 and Appendix B.1.1 for the synthesis details). The particles have sizes and shapes shown in Fig. 6.14. Moreover, the size distribution can be seen in Fig. 5.19.

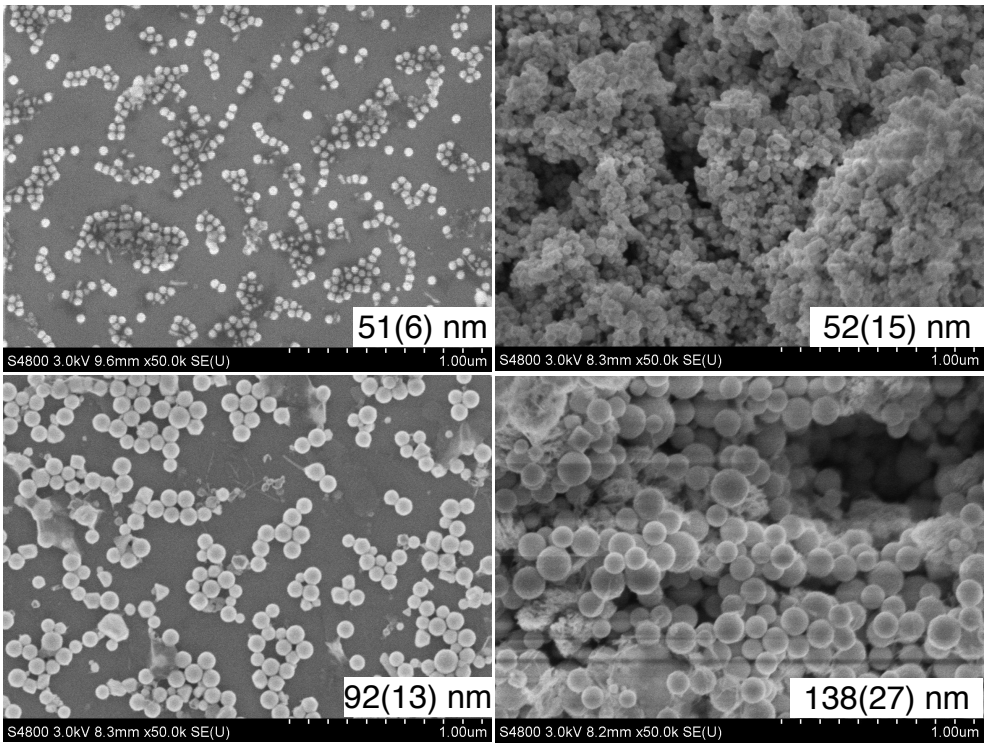

Figure 6.14: SEM images of the 51(6) nm, 52(15) nm, 92(13) nm, and 138(27) nm monodispersed samples at ×50.0k magnification. These samples were synthesised using high-temperature polyol-thermal decomposition method (HTP-TD).

6.4.2 Results and Discussion

6.4.2.1 On Pressure Increase

Analysis of the peak widths of the (104) and (110) reflections from the Bi-I phase in the four monodispersed samples revealed that the peak width increases with the reduction in the particle size, as expected from the Scherrer equation - see Table 6.2. In the 51(6) nm sample, the peak widths are some 50% broader than in the bulk sample. Given the complexity of the diffraction patterns of Bi-II and Bi-III, and the need to make accurate measurements of peak positions in order to accurately determine the lattice parameters and q-vector, too much additional width (from using still smaller particle sizes) may have been an issue. Any future studies with smaller particles will need to take such issues into account.

Table 6.2: The width (FWHM) of the (104), and (110) reflections from the Bi-I phase of bulk-Bi and monodispersed nano-Bi. All samples were measured at ambient pressure, except the 138(27) nm which was measured at 0.57 GPa.

	FWHM of reflection (hkl) in 2θ (deg.)	
	(104)	(110)
Bulk-Bi	0.054(1)	0.049(0)
138(27) nm	0.062(2)	0.060(2)
92(13) nm	0.080(2)	0.082(4)
52(15) nm	0.097(3)	0.101(4)
51(6) nm	0.106(11)	0.102(20)

For clarity, only waterfall plots of the 1D integrated diffraction profiles of 138(27) nm nano-Bi (see Fig. 6.15 and Fig. 6.19) are shown in this section. The reader can find the waterfall plots of all the other samples in Appendix A.2. This is because the experiment on the 138(27) nm nano-Bi sample was conducted in very small pressure steps (1-3 GPa) throughout the pressure application, from ambient pressure to 23 GPa on pressure increase and back down to ambient. Moreover, the basic characteristics of the 1D integrated diffraction profiles of all the nano-Bi samples are quite similar. Therefore, the plot of the 138(27) nm nano-Bi is the most representative of all nano-Bi.

In general, all of the monodispersed nano-Bi samples show the same behaviour as obtained with the 128(45) nm polydispersed nano-Bi sample (described in

section 6.3). The Bi-I, Bi-III, and Bi-V phases were all identified on pressure increase. It should be noted that in this section Bi-II was also recognised on pressure increase for the first time, as shown in Fig. 6.15. Again, large regions of phase coexistence exist in all samples, and such coexistence might not therefore arise as a result of polydispersed samples. Single-size nano-Bi is needed to investigate this phenomenon.

The smaller the particle size, the higher the values of P_{tr} seen for the Bi-I→Bi-II, Bi-II→Bi-III and Bi-III→Bi-V phase transitions - see Fig. 6.16. The differences are greatest in the transitions to Bi-III and Bi-V, which increase from 3.8 and 11.8 GPa in the 138(27) nm sample, to 4.0 and 12.9 GPa in the 92(13) nm, to 4.8 and 13.1 GPa in the 52(15) nm sample, and to 4.7 and 14.5 GPa in the 51(6) nm sample. This is the same behaviour seen in P_{tr} in other nanomaterials, such as CdSe [Tolbert and Alivisatos, 1995a], Se [Dai et al., 2011], and Te [Deng et al., 2008] (see section 2.4 for further details).

As with the polydispersed sample described in section 6.3.2, the 2D diffraction images obtained from the 51, 52, 92, 138 nm samples while they are in phase complex Bi-III (between ∼4 to 14 GPa), (see Fig. 6.17) have extremely smooth Debye-Scherrer rings rather than the "spotty" images obtained when using bulk-Bi (compare to Fig. 6.6 for bulk-Bi). The smoothness of the rings again reflects the lack of recrystallisation and annealing in the nano-crystalline samples.

While diffraction peaks from a Bi_2O_3 contaminant were observed in the polydispersed 128(45) nm Bi sample, no such Bi_2O_3 peaks were observed in any of the monodispersed samples, as can be seen in the Bi-I 1D integrated diffraction patterns in Fig. 6.15, Fig. 6.21 (and Fig. A.2 and Fig. A.3 in Appendix A.2). The oxide peaks were absent despite the samples being loaded under air and not in a glove box. This provided strong evidence that, as suggested earlier, the bismuth oxide observed in the polydispersed sample arose during the synthesis process, rather than from the sample-delivery method.

Although there are no diffraction peaks from Bi_2O_3, the Bi-I profiles from the 52(15) nm and 92(13) nm samples contain some unexpected broad bumps between 7.5° - 9.5° in 2θ (with $\lambda = 0.4141$ Å for 52(15) nm and 0.4146 Å for 92(13) nm), as shown in Fig. 6.21 in section 6.5 and Fig. A.3 in Appendix A.2. These are likely to arise from residual organic material used in the synthesis of the samples. In future studies, nuclear magnetic resonance (NMR) analysis might be used to

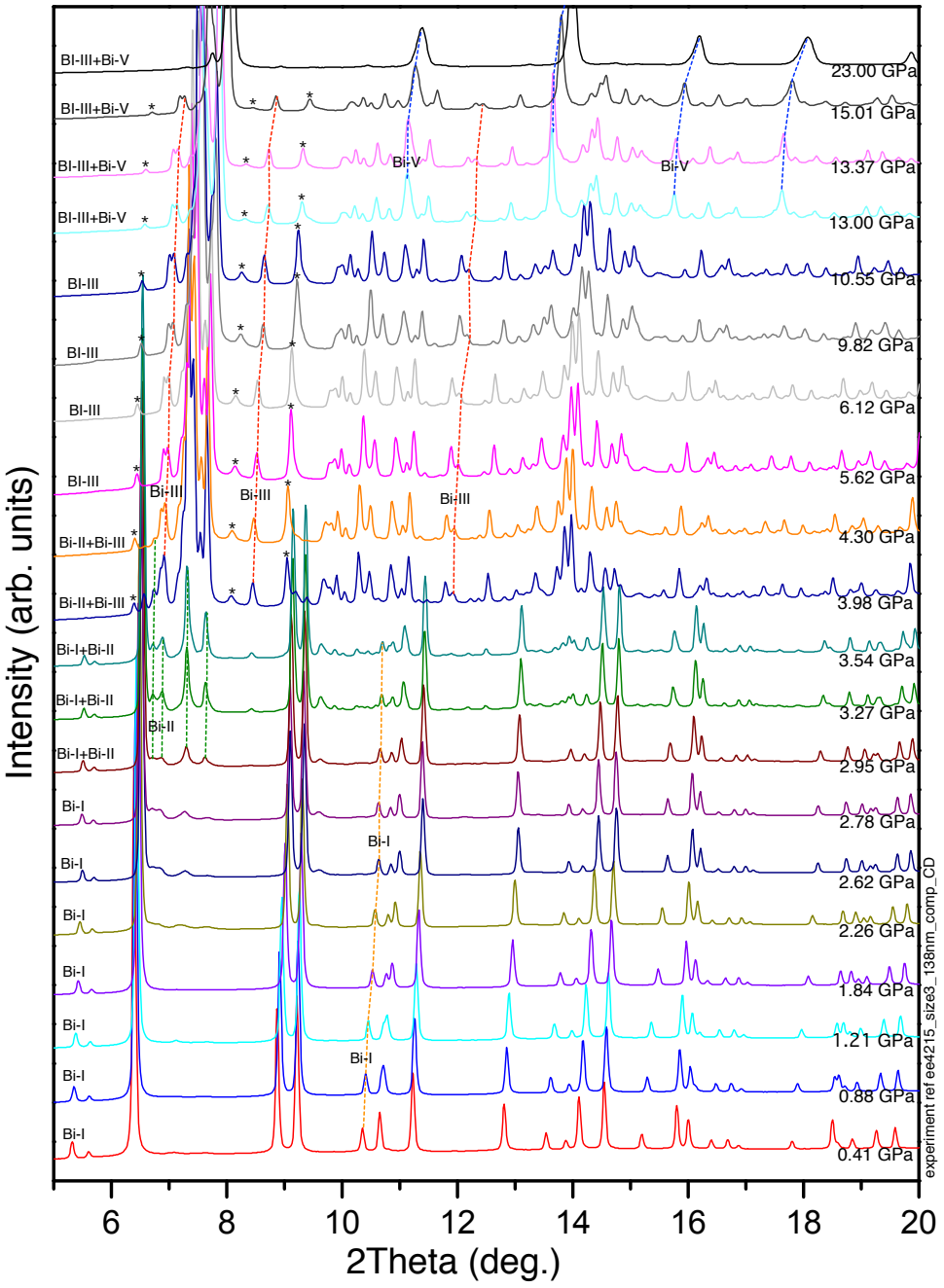

Figure 6.15: Waterfall plot of 1D integrated profiles obtained from the 138(27) nm nano-Bi on pressure increase to 23 GPa. The pressure was increased in 1-3 GPa steps. The diffraction patterns come from four phases, Bi-I, Bi-II, Bi-III, and Bi-V. The orange-, green-, red-, and blue-dashed lines indicate the progression of peaks from Bi-I, Bi-II, Bi-III, and Bi-V, respectively. The asterisks (*) mark the positions of the unaccounted-for peaks.

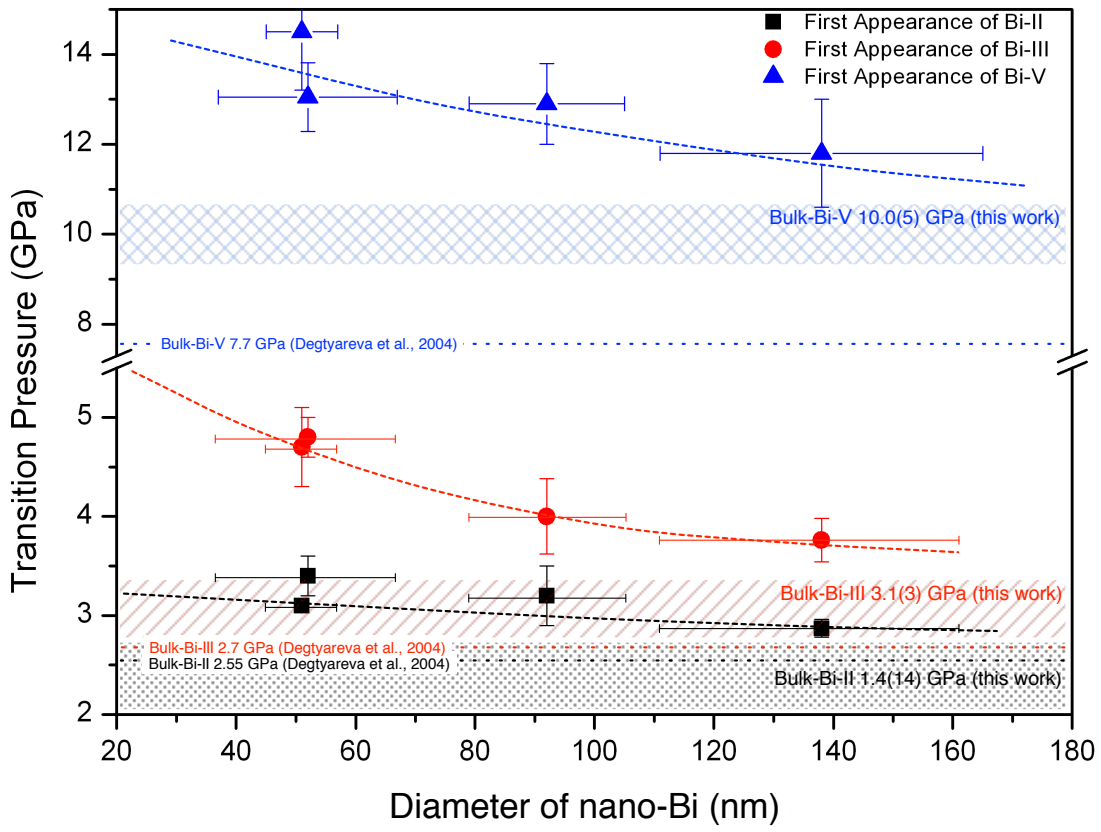

Figure 6.16: Transition pressures (P_{tr}) on pressure increase observed in nano-Bi, as defined by the pressure at the first appearance of higher pressure phase as a function of nanoparticle diameter (nm). The black squares (■), red solid circles (●), and blue triangles (▼), represent the first appearance of Bi-II, Bi-III, and Bi-V, respectively. 250-300 nm nano-Bi is predicted to have the same phase transition pressures as bulk material, as determined by extrapolation.

investigate the presence and identity of residual organic materials, but this is beyond the scope of the current study.

As shown in Fig. 6.18, there is very large coexistence of Bi-I with Bi-II, Bi-II with complex Bi-III, and complex Bi-III with Bi-V on pressure increase. The coexistence of phases in all samples is larger than that observed in bulk-Bi. It is worth mentioning that the data form the 138 nm presented in Fig. 6.15 and Fig. 6.19 is not included in Fig. 6.18, but another set of 138 nm data (which are in Fig. A.4, Fig. A.7 and Fig. A.12 in Appendix A.2) are presented in Fig. 6.18.

It should be noted that the complex Bi-III, which comprises Bi-III and some other unaccounted-for peaks, exists up to 24.1(2.8) GPa, 21.2(1.3) GPa,

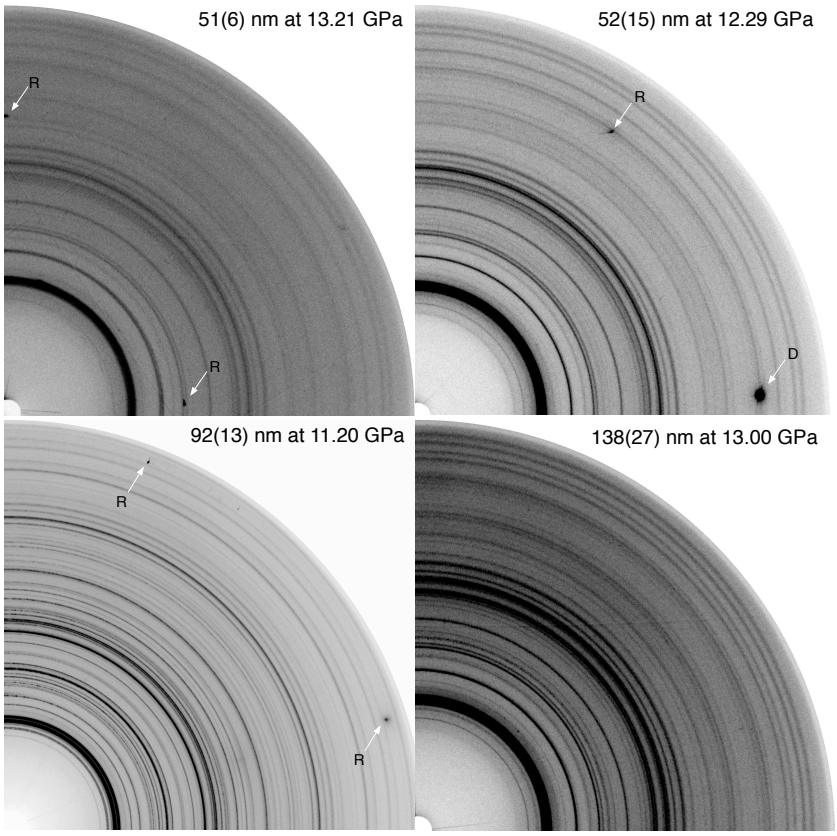

Figure 6.17: Four quarters of 2D diffraction images of the complex Bi-III phase from 51, 52, 93, 138 nm samples near 11-13 GPa. The image shows the smoothness of the Debye Scherrer rings. 'R' denotes a diffraction spot from ruby. A diamond reflection is labelled by 'D'.

30.1(1) GPa, and 20.0(3.0) GPa in the 51(6) nm, 52(15) nm, 92(13) nm, and 138(27) nm samples, respectively. These pressure are some ∼3 times larger than the upper pressure limit[3] of Bi-III in bulk which is 10.0(5) GPa.

6.4.2.2 Indexing of Unaccounted-for Peaks

Attempts were made to index the 10 unaccounted-for peaks using the indexing software DICVOL [Boultif and Louër, 2004]. Solutions were sought in cubic, tetragonal, hexagonal, orthorhombic and monoclinic crystal systems up to a unit cell volume of 300 Å^3. Despite many and extensive attempts, no solution was

[3]Upper pressure limit of Bi-III : the highest pressure at which the Bi-III exists either coexisting with another phase or as a single phase.

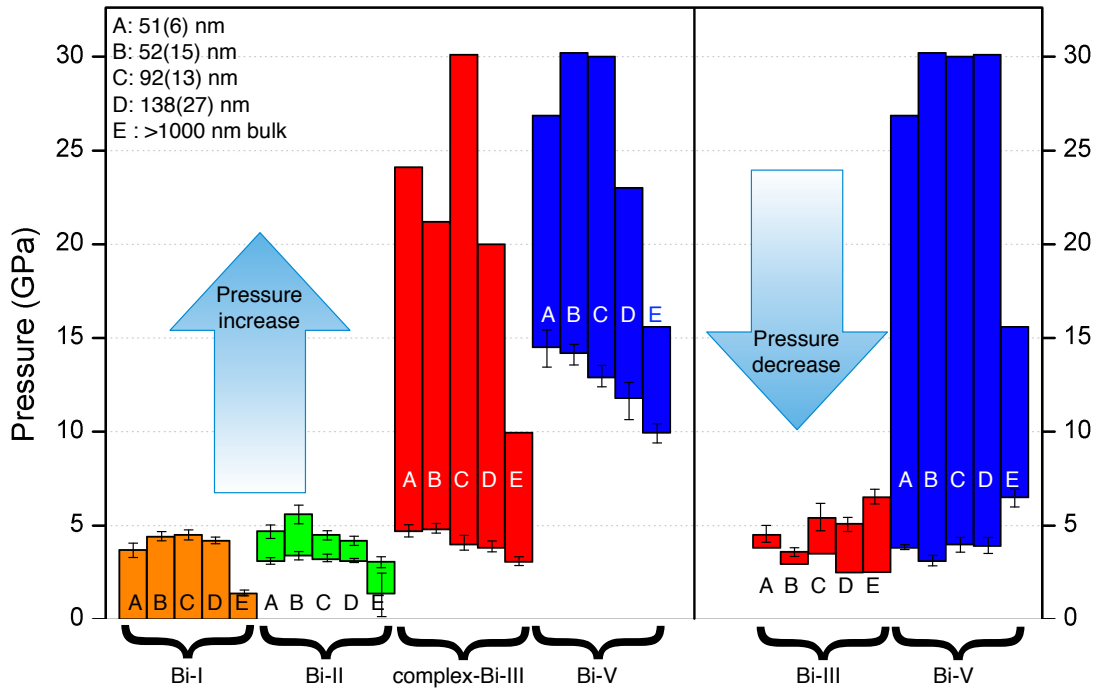

Figure 6.18: Pictorial representation of the P_{tr} in nano-Bi and bulk-Bi at room temperature on both pressure increase and decrease. The coexistence regions in nano-Bi are larger than those found in bulk-Bi, as seen by the degree of overlap between the bars representing different samples. A, B, C, D and E denote the 51, 52, 92, 138 nm and bulk-Bi samples, respectively.

found. *Ab initio* indexing of powder profiles is a challenging problem in high-pressure diffraction studies, as any systematic *hkl*-dependent shift in the peak positions (such as arises from deviatoric stress) can make indexing impossible [McMahon et al., 2003].

6.4.2.3 On Pressure Decrease

It should be noted that only a data set from the 138 nm sample has been carried out with pressure decrease until ambient pressure, as shown in Fig. 6.19, because the other samples, 51 nm, 52 nm, 92 nm and another data set of 138 nm samples, have been carried out on pressure decrease until a single phase of Bi-III was obtained for the purpose of repressurising which is described in section 6.5.

On pressure decrease from 18.99 GPa in the 138(27) nm sample, see Fig. 6.19, the following phase transitions are observed: Bi-V→Bi-III at 4.45(11) GPa and

Bi-III→Bi-II at 1.49(77) GPa. The Bi-II→Bi-I transition pressure cannot be determined because Bi-II was found to coexist with Bi-I in the 0.72 GPa profile, and the small stability range of Bi-II. The 138 nm sample reveals that single-phase Bi-III can be obtained in a narrow range of pressure (shown in Fig. 6.19), unlike on pressure increase where only the complex Bi-III was observed (see Fig. 6.15). This is the same behaviour found in the 128(45) nm sample described in section 6.3.2.

By considering the Bi-V→Bi-III P_{tr} of 52 nm (Fig. 6.23), 51 nm, 92 nm, 138 nm in Fig. A.5, Fig. A.6, and Fig. A.7 in Appendix A.2, respectively, the smaller the particle size, the lower the values of P_{tr} seen for the Bi-V→Bi-III phase transitions - in Fig. 6.20.

It is unclear why the nano-Bi behaves differently on pressure decrease compared to pressure increase, as regards the existence of single-phase Bi-III samples. One hypothesis is that the sample has some polydispersity, i.e. 27 nm for 138(27) nm sample. Therefore, each particle size in the sample has a different P_{tr}, which leads to the phase coexistence over wider pressure range than in bulk-Bi. On pressure decrease, sample at Bi-V phase was released in pressure from ∼19 GPa all the way to ∼3.5 GPa. The super-cooling-like effect might happen leading Bi-V to exist down to 3.59 GPa resulting in 8.5(1.6) GPa in hysteresis. Then, the Bi-V transform abruptly to Bi-III near 4.00-3.59 GPa, resulting in the clean Bi-III profiles on pressure decrease.

6.4.2.4 Difficulty in Investigating the Incommensurate Structure of Bi-III

Due to phase coexistence over a large range of pressures, and additional peaks in the complex Bi-III phase on pressure increase (see Table 6.3), it was initially difficult to be completely sure of the existence of Bi-III on pressure increase. However, by using the structure solution of bulk-Bi [McMahon et al., 2007], the peaks from Bi-III could be identified in the diffraction patterns using the Le Bail Method, along with some other phases. The result is similar to what is shown in Fig. 6.13.

The diffraction patterns from complex Bi-III are not suitable for studying the structural details of Bi-III because the unaccounted-for additional peaks make it difficult to observe all of the Bi-III diffraction peaks and might affect the nature of Bi-III. In addition, while strikingly-clean diffraction patterns from Bi-III are

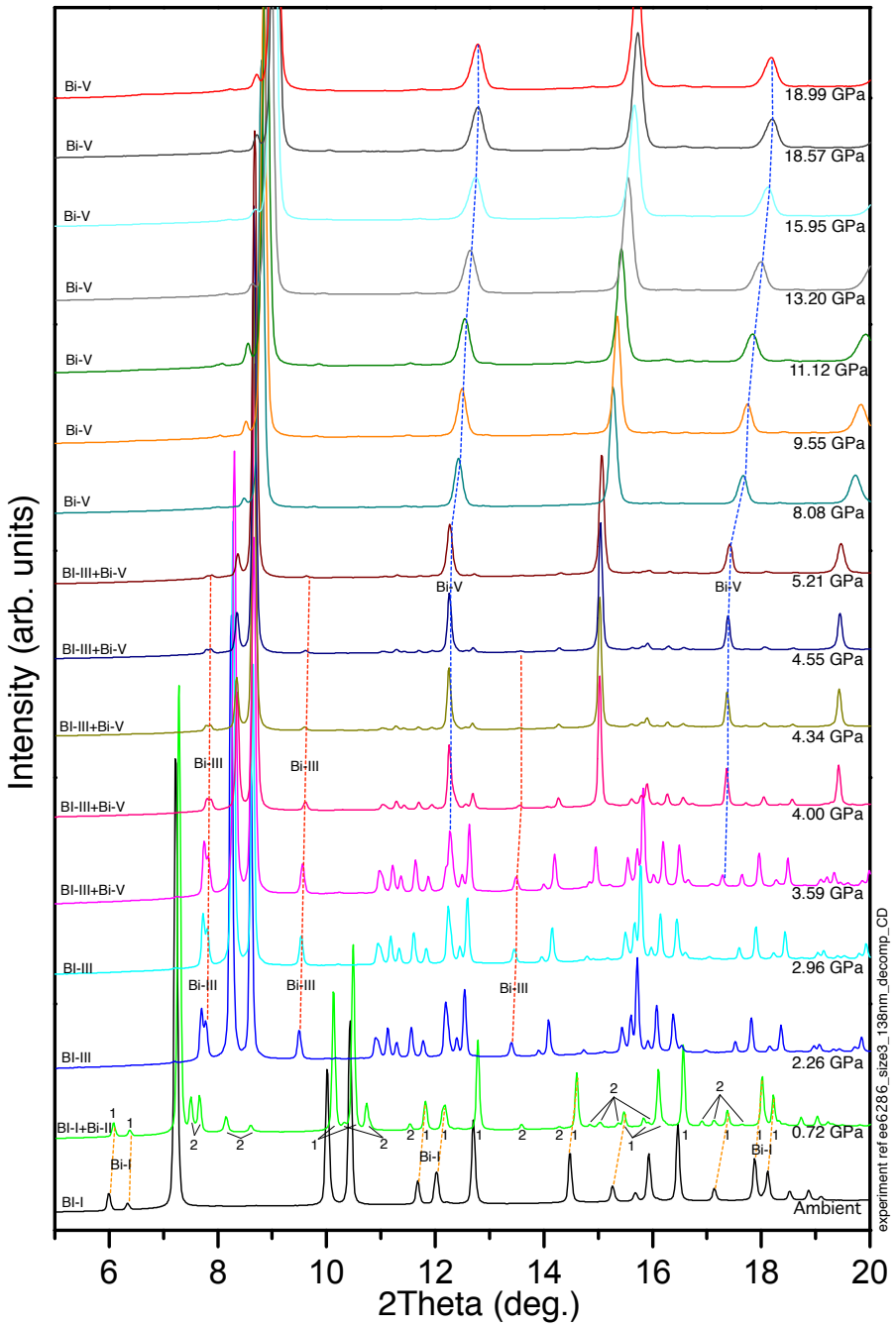

Figure 6.19: Waterfall plot of 1D integrated profiles obtained from the 138(27) nm nano-Bi on pressure decrease from 18.99 GPa to ambient pressure. The pressure was decreased in 1-3 GPa steps. The diffraction patterns come from four phases, Bi-I, Bi-II, Bi-III, and Bi-V. The orange-, green-, red-, and blue-dashed lines indicate the progression of peaks from Bi-I, Bi-II, Bi-III, and Bi-V, respectively. Some Bi-I and Bi-II peaks are highlighted with '1' and '2'.

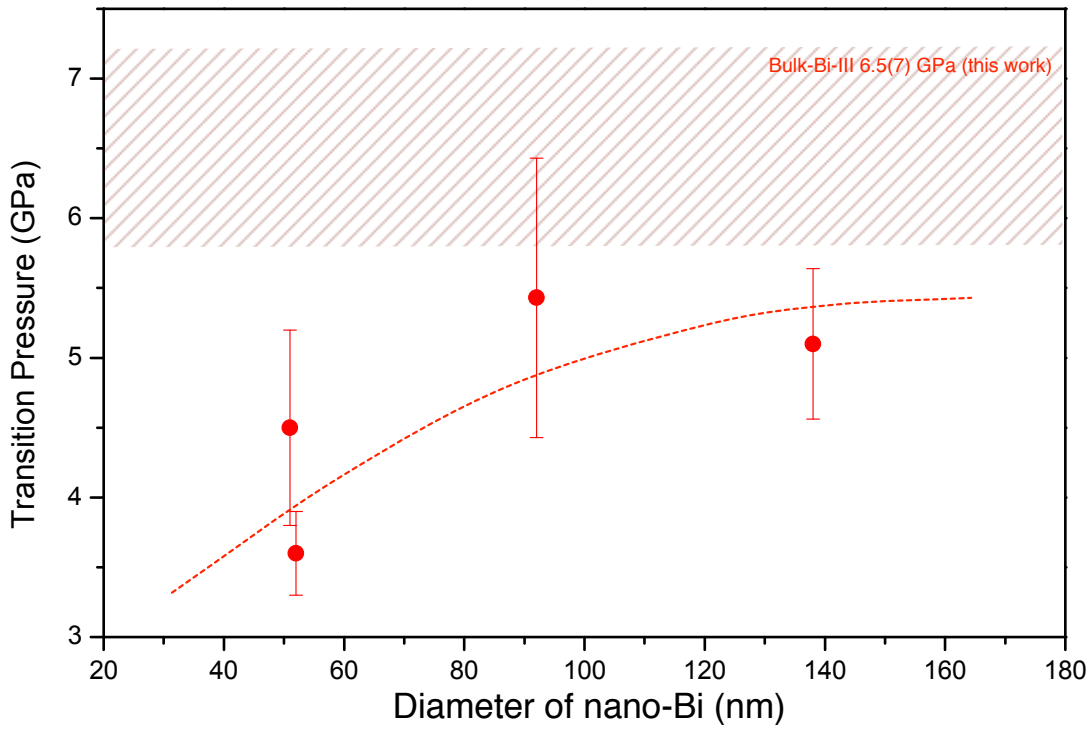

Figure 6.20: Transition pressure (P_{tr}) on pressure decrease of Bi-V→Bi-III, as defined by the pressure at the first appearance of Bi-III (●), are shown as a function of nanoparticle diameter (nm). The dashed line is a guide for the eye. The trend of P_{tr} decreases as size decreases. A 250-300 nm particle size of nano-Bi is predicted to have the same phase transition pressure as the bulk material, as determined by extrapolation.

Table 6.3: Complex Bi-III existence range on pressure increase (Bi-III for bulk-Bi)

	Pressure Range (GPa)	
	Start	End
Bulk-Bi	3.1(3)	10.0(5)
138(27) nm	3.8(2)	20.0(30)
92(13) nm	4.0(4)	30.1(1)
52(15) nm	4.8(2)	21.2(13)
51(6) nm	4.7(4)	24.1(28)

observed on pressure decrease, they are found only in the very narrow pressure range of ∼2-4 GPa. Complex Bi-III on pressure increase and the narrow range of single-phase Bi-III profiles on pressure decrease are thus the main difficulties

which obstruct the study of the incommensurate structure in nano-Bi, which ideally needs single-phase Bi-III profiles over a large range of pressure (more than ∼2-4 GPa).

6.4.3 Conclusions

Different sizes of nano-Bi samples have been synthesised. They exhibit the same behaviour as the nano-Bi 128(45) nm sample described in section 6.3 and have the Bi-I, Bi-II, complex Bi-III, and Bi-V phases on pressure increase.

However, those samples have no traces of bismuth oxide due to changing the bismuth synthesis method and reducing the oxygen level in the synthesis glove box from 60-70 ppm to 1-2 ppm.

Single-phase Bi-III profiles exist only in a very narrow range of pressure on pressure decrease, making it hard to study the incommensurate structure in Bi-III. Therefore, we had to find a way to get single-phase Bi-III samples over a wider range of pressures, and thus the pressure dependent incommensuration in nano-Bi can be studied.

6.5 HP-PXRD Experiments with Monodispersed Nano-Bi on Pressure Re-Increase

While the results of the previous section showed the existence of the incommensurate Bi-III phase in the monodispersed samples, and the greatly increased existence range of Bi-III on pressure increase, it also showed that Bi-III coexists with the unaccounted-for peaks from ∼3 GPa and with Bi-V from 14-18 GPa, making detailed analysis of Bi-III very difficult. However, having established the existence of Bi-III in nano-Bi, it was now essential to determine its structure and pressure dependence in some detail for comparison with the literature results on bulk-Bi. Of key importance is the value and pressure dependence of the incommensurate q-vector, a key structural parameter in describing the incommensurate structures [Nelmes et al., 1999, McMahon et al., 2001, Hejny and McMahon, 2003, McMahon et al., 2006].

In the previous studies of incommensurate Bi-III in bulk-Bi by Degtyareva et al. [Degtyareva et al., 2001, Degtyareva, 2003, Degtyareva et al., 2004], the value of the q-vector was extracted from x-ray diffraction data by calculating $q = c_h/c_g$, when c_h and c_g are the c-axis lattice parameter of the host and the guest component, respectively, of the structure. In bulk-Bi-III, the q-vector was determined over a pressure range of 2.7-8.3 GPa [Degtyareva et al., 2004], and was found to decrease with pressure. While the existence of Bi-III to much higher pressures in nano-Bi would enable the pressure dependence of q to be extended to well above 10 GPa. The phase coexistence with Bi-V (starting from 14-18 GPa) and the existence of some other undetermined additional phase with diffraction peaks (unaccounted-for peaks) near the main Bi-III peaks makes its determination difficult. In addition, the mixed-phase nature of the sample may affect the measured lattice parameters, leading to erroneous values of q.

These problems can be overcome by obtaining a single-phase sample of Bi-III on pressure decrease from Bi-V (see Fig. 6.23), and then repressurising it (see 6.24).

6.5.1 Method of HP-PXRD Data Collections with Monodispersed Nano-Bi on Pressure Re-Increase

The diffraction and analysis methods used in this section were almost the same as those described in section 6.3.1 using the x-ray wavelength mentioned in Appendix A.3.

The aim of the experiment was to obtain a single-phase pattern of Bi-III by first compressing a sample to 25-30 GPa to obtain single-phase Bi-V, then decreasing the sample pressure carefully to obtain a single-phase sample of Bi-III at ∼2-3 GPa. Single-phase Bi-III patterns were obtained for the 52 nm, 92 nm, 138 nm samples, while the 51 nm sample was found to have Bi-V coexisting with Bi-III until the lowest pressure on pressure decrease. Once such samples of Bi-III were obtained, they were then repressurised to ∼25-30 GPa, where 30 GPa is the maximum pressure of a Merrill-Bassett DAC equipped with 400 μm culet diamonds.

Subsequent least-squares (LS) analysis of the peak positions in the diffraction profiles was used to determine the lattice parameters of the host and guest phases, from which the compressibility and the pressure dependence of the q-vector could be obtained. The LS analysis was carried out using UnitCell.

6.5.2 Results and Discussion

6.5.2.1 Single Phase of Bi-III on Pressure Re-increase

For clarity, only waterfall plots of the 1D integrated diffraction profiles of 52(15) nm nano-Bi on pressure increase (see Fig. 6.21, Fig. 6.22), on pressure decrease (see Fig. 6.23), and on pressure re-increase (see Fig. 6.24 and Fig. 6.25) are shown in this section as it is the most representative of all nano-Bi. However, the waterfall plots of the 1D integrated diffraction profiles obtained on pressure re-increase of the other samples can be found in Appendix A.2, Fig. A.8, Fig. A.9, Fig. A.10, Fig. A.11 and Fig. A.12. In almost all cases, the lowest pressure profiles are from single-phase Bi-III samples (except the 51 nm sample, which was found to have Bi-V coexisting with Bi-III until the lowest pressure on pressure decrease).

From Fig. 6.24 and Fig. 6.25, which show the diffraction data obtained on re-compressing of the 52(15) nm sample, it is clear that single-phase Bi-III profiles are still obtained at pressures up to 14.28 GPa. This is some 4 GPa higher than

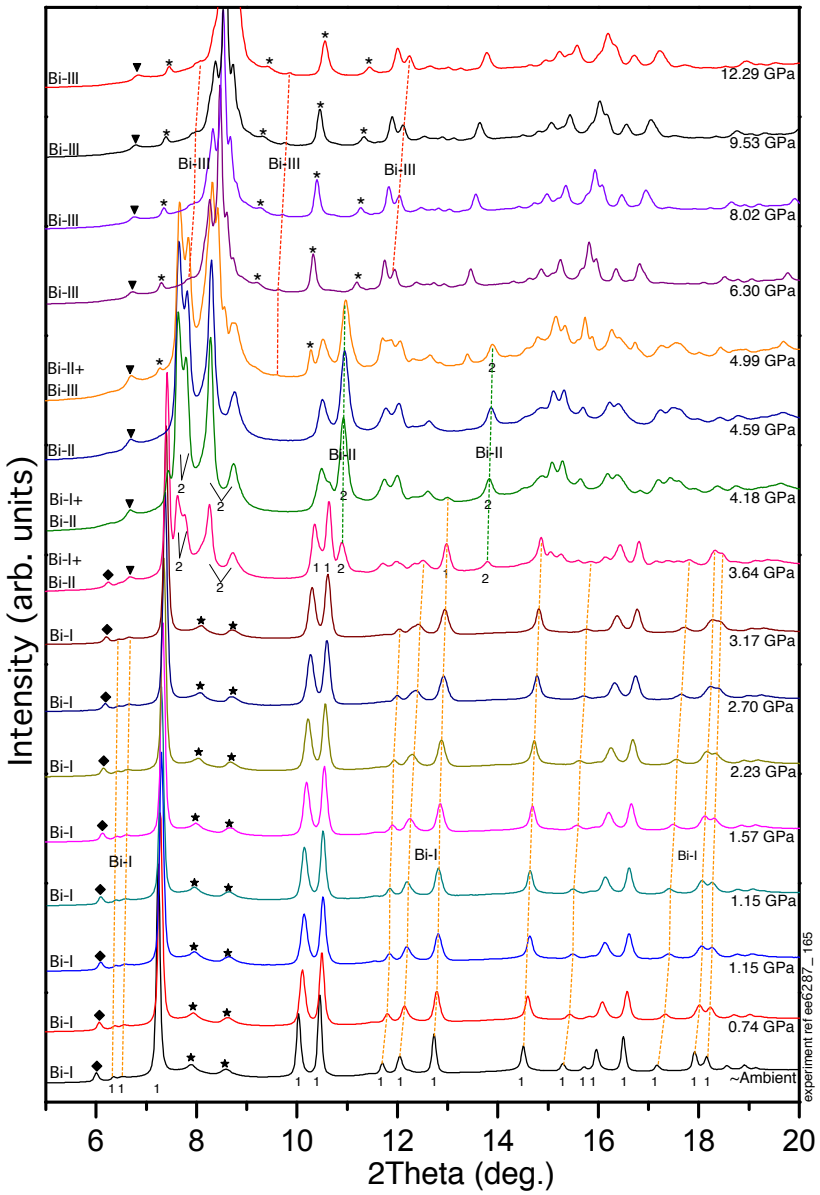

Figure 6.21: Waterfall plot of 1D integrated profiles obtained from the 52(15) nm nano-Bi on pressure increase to ∼12 GPa. Further plots to a maximum pressure of 30 GPa, as given in Fig. 6.22. The pressure was increased in 1-3 GPa steps between ambient pressure and 12 GPa. The diffraction patterns come from three phases, Bi-I, Bi-II, and Bi-III. The orange-, green-, and red-dashed lines indicate the progression of peaks from Bi-I, Bi-II and Bi-III, respectively. The (⧫), (▼), (*) symbols mark the positions of the unaccounted-for peaks. Some Bi-I and Bi-II peaks are highlighted with '1' and '2'. The two small bumps suggest the presence of organic materials in the sample, as labelled with ('★)'.

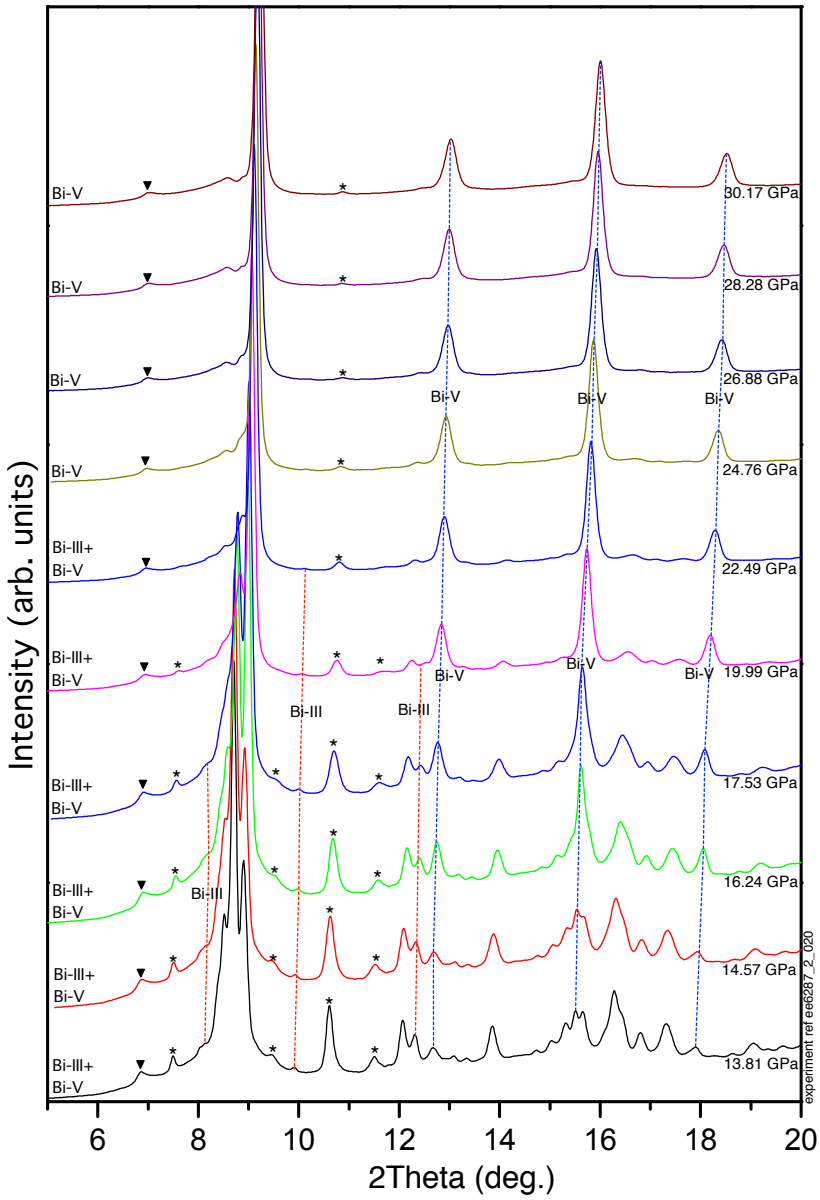

Figure 6.22: Waterfall plot of 1D integrated profiles obtained from the 52(15) nm nano-Bi on pressure increase to ∼30 GPa (continues from ∼12 GPa in Fig. 6.21). The pressure was increased in 1-3 GPa steps between 14 and 30 GPa. The diffraction patterns come from two phases, Bi-III, and Bi-V. The red-, and blue-dashed lines indicate the progression of peaks from Bi-III and Bi-V, respectively. The (▼), (*) symbols mark the positions of the unaccounted-for peaks.

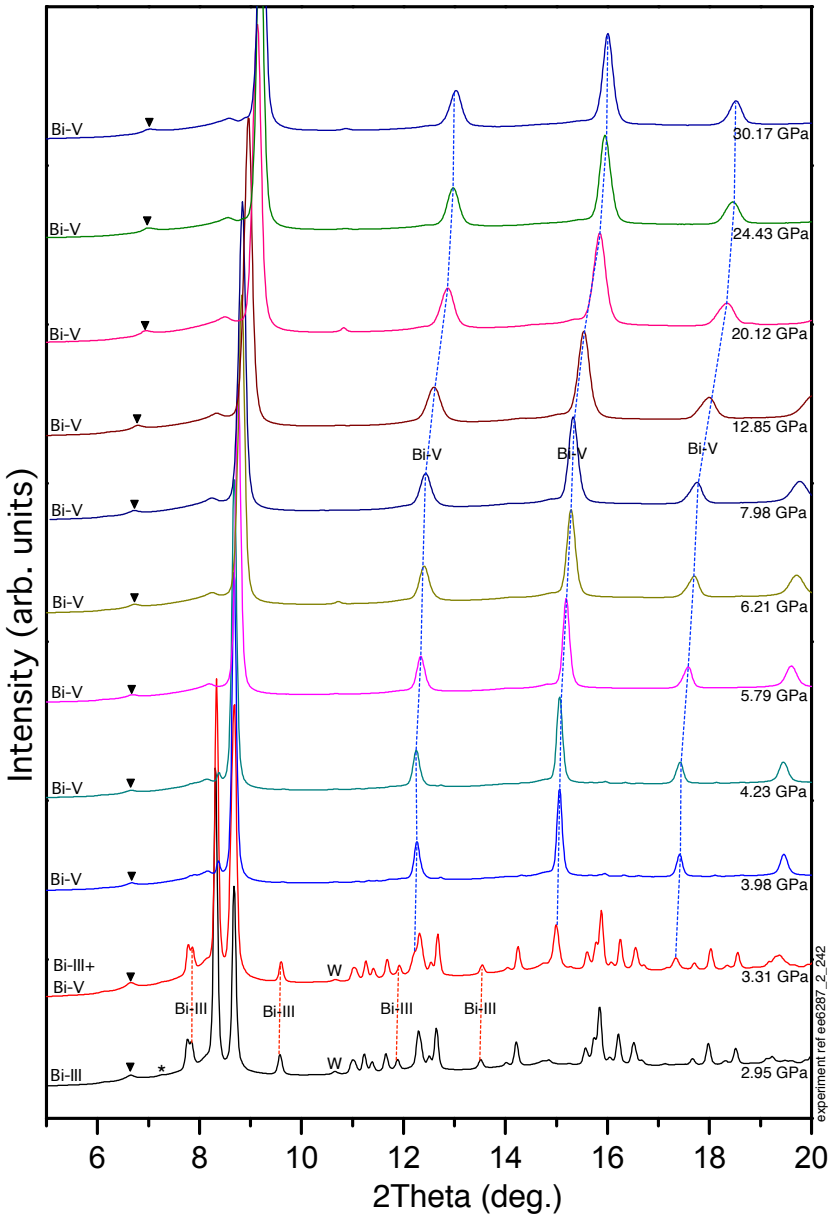

Figure 6.23: Waterfall plot of 1D integrated profiles obtained from the 52(15) nm nano-Bi on pressure decrease from 30.17 GPa to ambient pressure. The pressure was decreased in large pressure steps at the beginning of decompression, but smaller steps when reaching Bi-III. The diffraction patterns come from two phases, Bi-III and Bi-V. The red- and blue-dashed lines indicate the progression of peaks from Bi-III and Bi-V, respectively. The (▼), (*) symbols mark the positions of the unaccounted-for peaks. The 'W' labels tungsten gasket peaks.

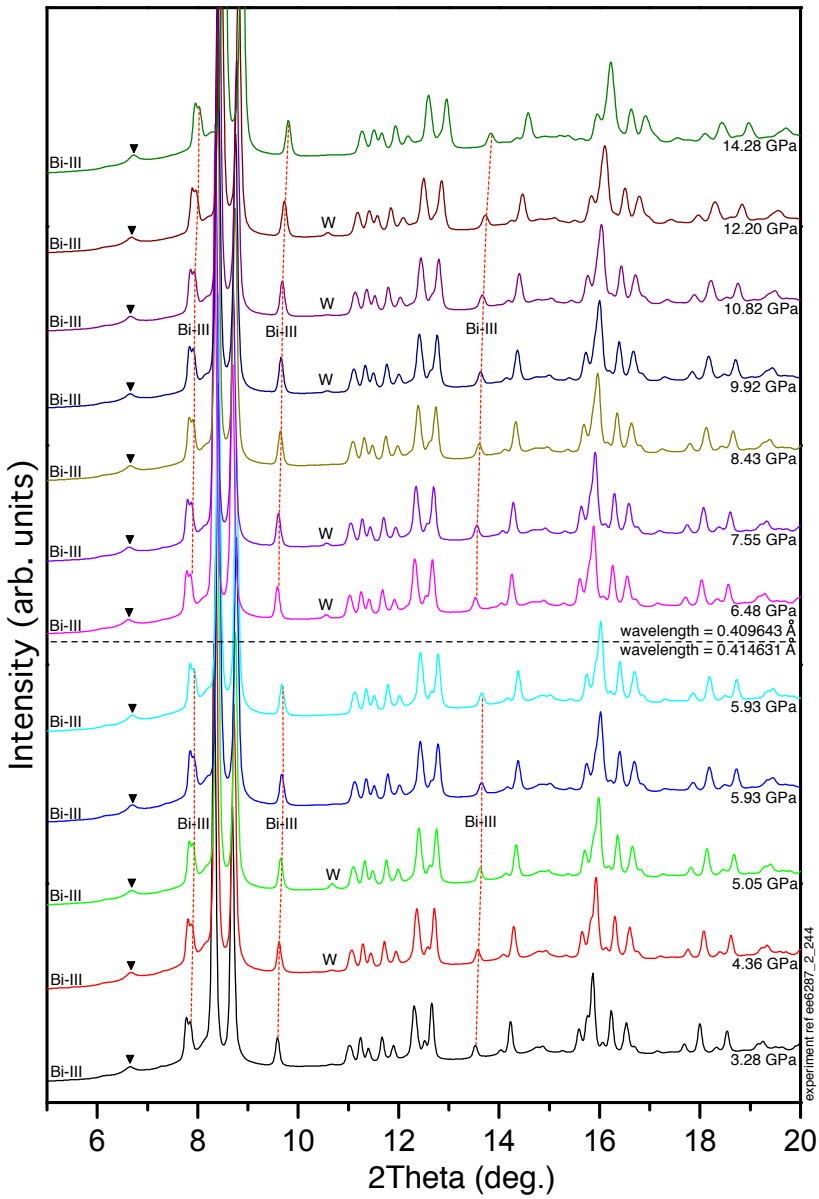

Figure 6.24: Waterfall plot of 1D integrated profiles obtained from the 52(15) nm nano-Bi on pressure re-increase from 3.28 to 14.28 GPa. The pressure was increased in 1-2 GPa steps. The diffraction patterns come only from one phase, Bi-III. The red-dashed lines indicate the progression of peaks from Bi-III. The (▼) symbol marks the positions of the unaccounted-for peaks. The 'W' labels tungsten gasket peaks.

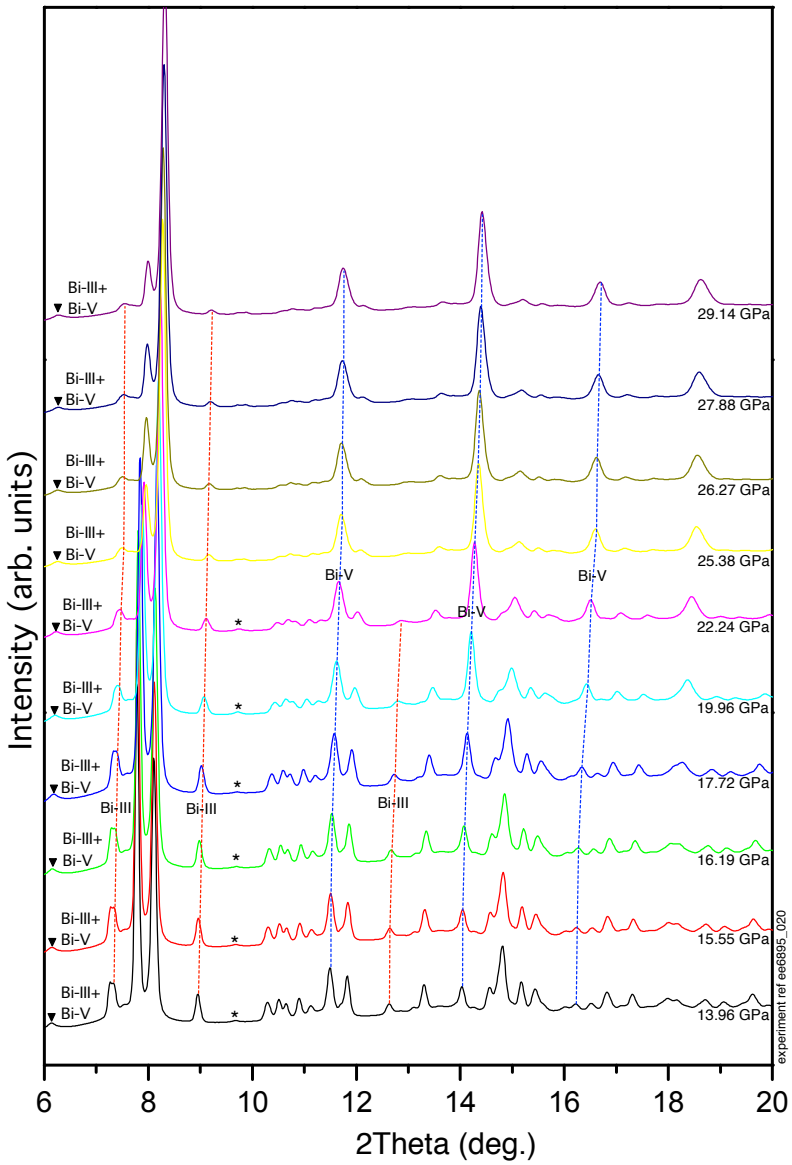

Figure 6.25: Waterfall plot of 1D integrated profiles obtained from the 52(15) nm nano-Bi on pressure re-increase from 13.96 to 29.14 GPa. The pressure was increased in 1-2 GPa steps. The diffraction patterns come from two phases, Bi-III and Bi-V. The red- and blue-dashed lines indicate the progression of peaks from Bi-III and Bi-V, respectively. The (▼), (*), symbols mark the positions of the unaccounted-for peaks. The sample at 13.96 GPa was identical to that of 14.28 GPa in Fig. 6.24. The difference in pressures is due to a slight decrease in the sample pressure in the two months between the experiments. It should be noted that Bi-V peaks have appeared at 13.96 GPa in the profile. This shows the sluggishness of phase transition of nano-Bi, as also found in the nanomaterials of SnO_2 [Jiang et al., 2001b], Te [Deng et al., 2008] and Ga_2O_3 [Wang et al., 2010].

the upper pressure limit that Bi-III is observed in bulk-Bi.

In addition, the profiles obtained on re-compression contain none of the unaccounted-for peaks from complex Bi-III phase which were observed to coexist with Bi-III on initial pressure increase, as described in section 6.3.2.2.

The same greatly-increased stability range of the Bi-III is observed in the other re-compressed samples - as can be seen in Appendix A.2, in Fig. A.8, Fig. A.9, Fig. A.10, Fig. A.11 and Fig. A.12. The upper pressure limit of the Bi-III phase cannot be determined because, in all samples, Bi-III still exists at the maximum pressures attained in the experiments, which are 30, 29, 27, and 27 GPa for the 51, 52, 92, and 138 nm samples, respectively. This can be seen in the pictorial representation of the P_{tr} at room temperature on pressure re-increase in Fig. 6.26. Therefore, the upper pressure limit of the existence range of Bi-III could be determined when larger maximum pressures are attained. In addition, the P_{tr} of the Bi-III→Bi-V transition on pressure re-increase are 14.1(2), 18.2(1.1), and 18.5(2.3) GPa for the 52, 92, and 138 nm, respectively.

It is clear from Fig. 6.25 that the width of the diffraction peaks increases with increasing pressure. The upper hydrostatic pressure range for the PTM used in this experiment (methanol-ethanol (4:1)) is up to 10 GPa [Klotz et al., 2009] and the peak broadness observed in Fig. 6.25 almost certainly arises from non-hydrostatic strains within the sample chamber, which can be confirmed by the increasing broadening of ruby spectra above 14 GPa on pressure re-increase (see Fig. 6.27).

The 1D integrated profiles from single-phase samples of Bi-III of bulk and nano-samples are shown in Fig. 6.28. The profiles are very similar, indicating the similarity of Bi-III from nano-Bi and from bulk-Bi. The structure of nano-Bi-III is the same as that of bulk-Bi-III, as reported in [McMahon et al., 2000, Degtyareva et al., 2004] after Rietveld refinement. Nevertheless, at very high pressure, i.e. more than 14-18 GPa, it is apparent that Bi-V appears along with the single phase of Bi-III.

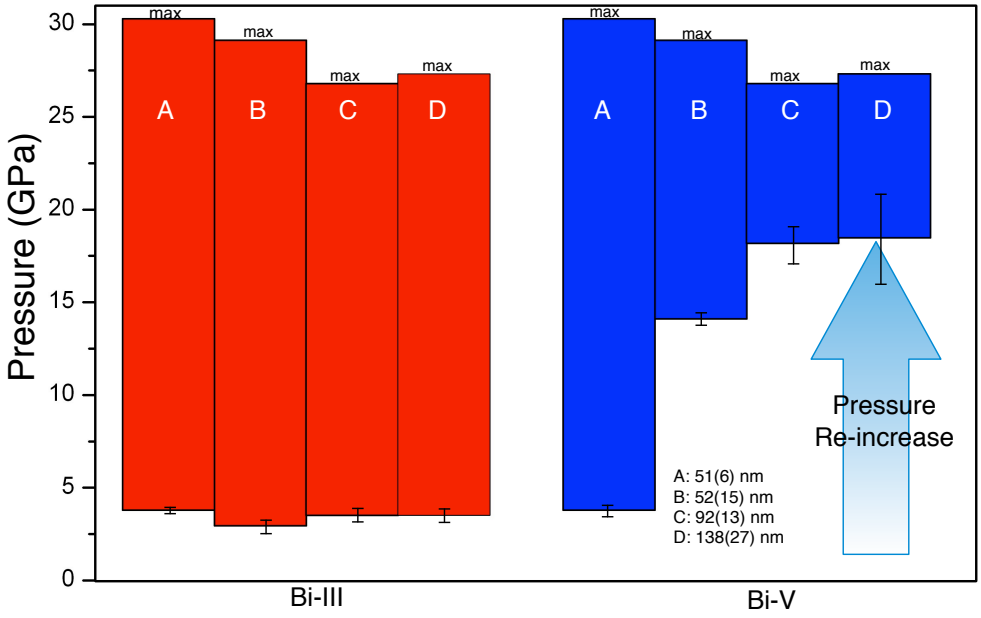

Figure 6.26: Pictorial representation of the P_{tr} in nano-Bi and bulk-Bi at room temperature on pressure re-increase. It should be noted that Bi-V still exists at the lowest pressure at which the 51(6) nm was studied (3.8 GPa) since pressure decrease and therefore Bi-V coexists with Bi-III for the whole range of pressure re-increase. The coexistence regions in nano-Bi can be seen by the degree of overlap between the bars representing different samples. A, B, C, and D denote the 51, 52, 92, and 138 nm samples, respectively.

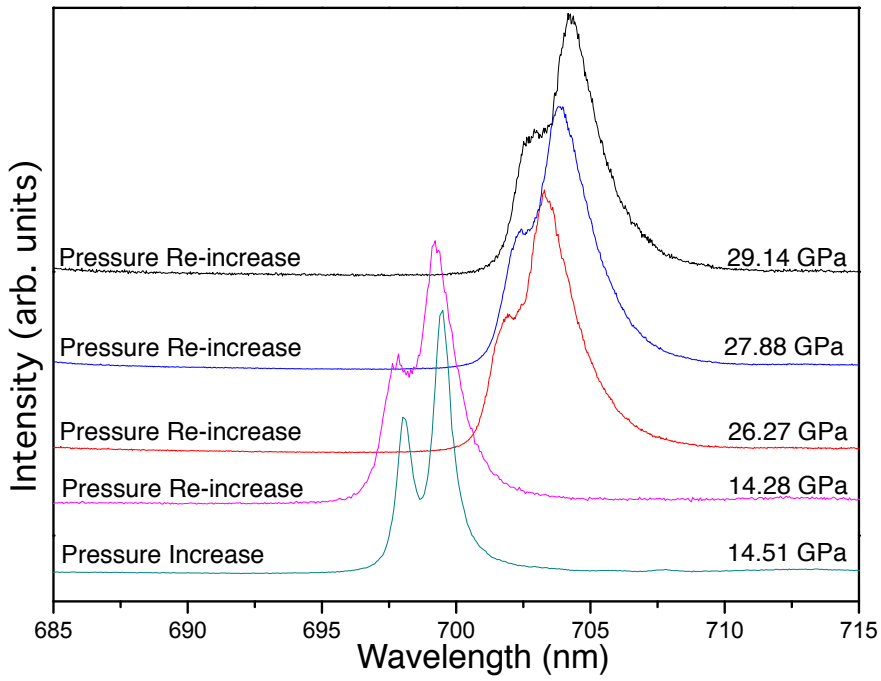

Figure 6.27: Ruby spectra measured during the HP-PXRD experiment on the 52(15)nm sample. At 14.51 GPa on initial pressure increase, the spectrum from the ruby is a sharp doublet. On pressure re-increase at the same pressure (14.28 GPa), the doublet is considerably broader, indicating non-hydrostatic conditions. At pressures above 25 GPa, the ruby spectra are much broader still.

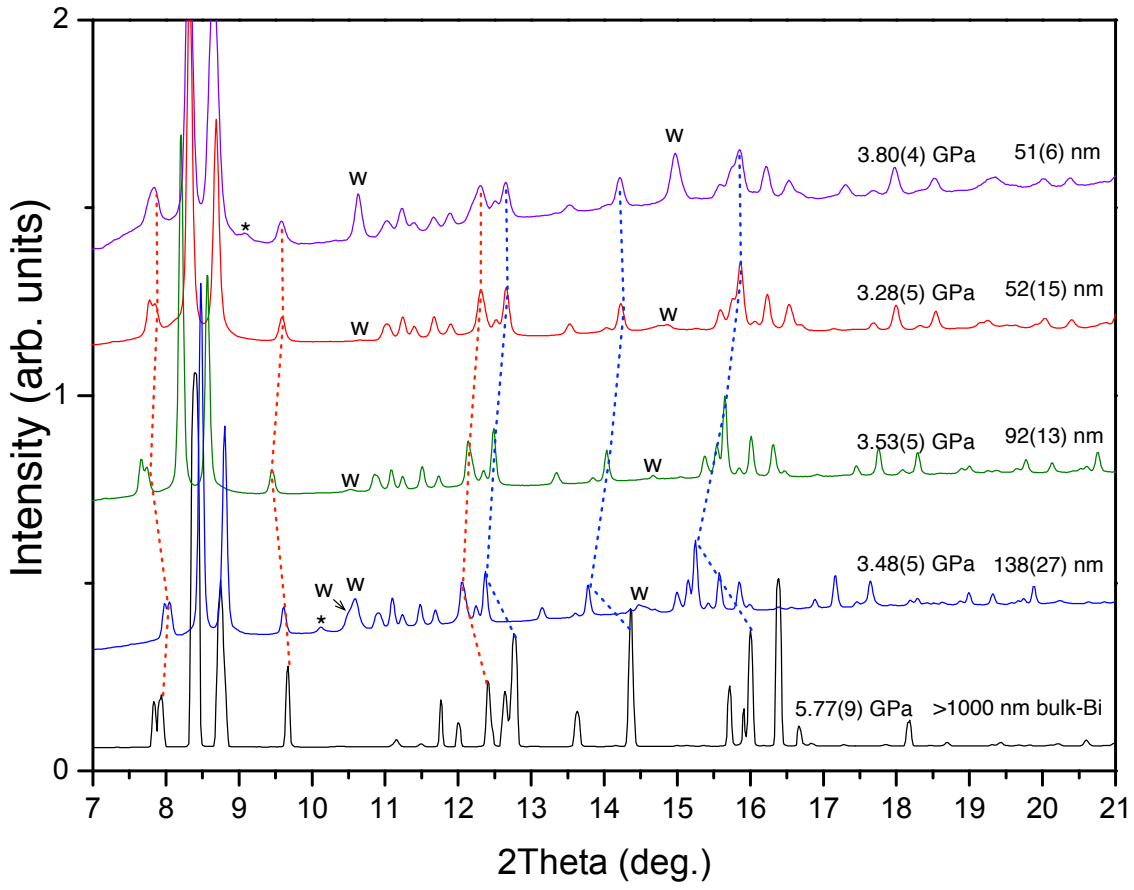

Figure 6.28: Comparison of 1D integrated diffraction profiles from Bi-III obtained from both bulk and various sizes of nano-Bi sample. Each diffraction profile was obtained in a different synchrotron beamtime, which utilised different x-ray wavelengths. This causes all of the Bi-III patterns to be slightly shifted with respect to each other. Diffraction peaks from the tungsten gasket are marked with 'W'. The red-dashed lines highlight the most intense guest-component peaks, while the blue-dashed lines highlight some peaks from the host component. It should be noted that an unusual 'W' peak located at lower 2θ exists in 138(27) nm profile. Moreover, non-Bi peak (marked with (*)) presented in 51(6) nm and 138(27) nm are ones of the unaccounted-for peaks observed in complex Bi-III on pressure increase.

6.5.2.2 Compressibility of Nano-Bi-III

At high pressures, the compressibility of nano-gold and nano-silver have been found to depend on the size of the sample crystallites [Gu et al., 2008]. In 10 nm Ag and 30 nm Au, the bulk moduli (K_0) were reported to be 121(6) GPa and 290(8) GPa, respectively, compared to the bulk-Ag and bulk-Au values of 116 GPa [Syassen and Holzapfel, 1978] and 171 GPa [Takemura, 2001], respectively.

The compressibility of Bi-III as obtained from the four nano-samples, and from bulk-Bi [Degtyareva et al., 2004] are shown in Fig. 6.29. Because there are two chain of guest atoms within each host unit cell of Bi-III, the total number of atoms in the host unit cell is $8 + 2\times(c_h/c_g)$ [McMahon et al., 2007]. As c_h and c_g are pressure dependent, so is the number of atoms in the host unit cell.

In the main, the compressibility of nano-Bi is clearly lower than bulk-Bi. Therefore, nano-Bi has a higher bulk modulus compared to that in the bulk. The bulk moduli (K_0) of the four samples, as obtained by fitting the compressibility curves to a Birch-Murnaghan equation of state, are 77(2), 72(3), 75(3) and 66(3) GPa for the 51 nm, 52 nm, 92 nm, and 138 nm samples, respectively, while that of the bulk is 53(1) GPa [Degtyareva et al., 2004]. As previously reported for nano-gold and nano-silver [Gu et al., 2008], nano-Bi has a higher bulk modulus with the smaller particle sizes.

6.5.2.3 Size Dependent - Pressure Independence of the Incommensurate Wave Vector (q-vector) of Nano-Bi-III

In earlier studies of bulk-Bi-III, the incommensurate q-vector (c_h/c_g) was determined over its full stability range of 2.7 to 8.3 GPa [Degtyareva, 2003, Degtyareva et al., 2004], and this is shown in Fig. 6.30, along with the pressure dependence of q obtained over the pressure range of ∼3 up to 30 GPa from the 51(6) nm, 52(15) nm, 92(13) nm, and 138(27) nm samples of nano-Bi-III.

The q-vector in nano-Bi-III is pressure independent over its full pressure range up to ∼30 GPa. This would seem to be a different behaviour to that seen in bulk-Bi-III, where the q-vector was concluded to slightly decrease over the pressure range of 2.7-8.3 GPa. However, the limited pressure range of the bulk-Bi-III data makes it difficult to state with confidence that the pressure dependences are different. Either an extended pressure range for the bulk-Bi-III data, perhaps by re-compressing bulk-Bi-III, or a lower uncertainty would be needed to make a

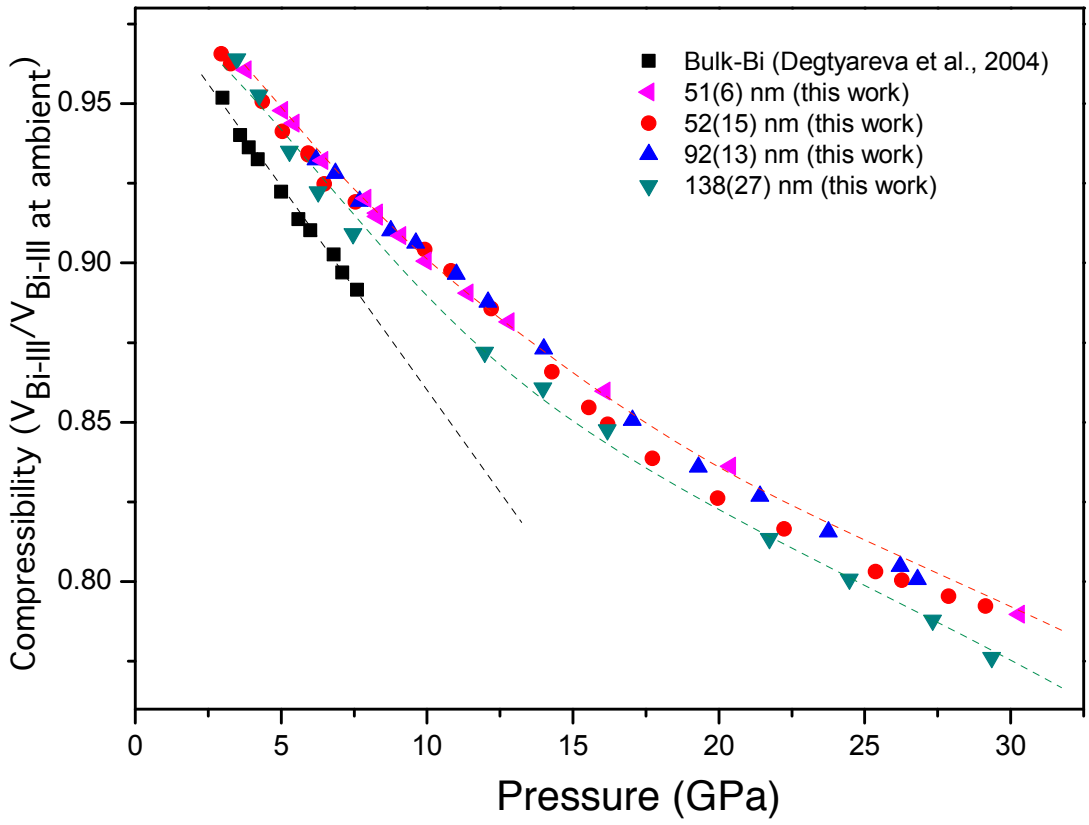

Figure 6.29: The compressibility of the four monodispersed nano-Bi samples (this work) and bulk-Bi [Degtyareva et al., 2004]. The dashed lines are guide to the eye. Although the pressure range of the compressibility of bulk-Bi-III is smaller than that of the four nano-Bi-III samples, it clearly has higher compressibility (lower bulk modulus) than the nano-Bi-III phases. All nano-Bi samples have slightly size-dependent compressibility over the pressure range as regards to the proximity of data points from each sample. Error bars are smaller than the plotting symbols ($\sim$0.001).

more definitive statement.

Over the remarkably-large existence range of Bi-III in nano-Bi of 3-30 GPa, the q-vector of nano-Bi samples can be seen to be pressure independent, particularly in comparison to the incommensurate wave vector measured previously in bulk-Rb-IV and bulk-Ba-IV, both of which are highly pressure dependent (see Fig. 6.31).

From Fig. 6.30, it should be, noted, however, that the 52 nm sample exhibits a somewhat different trend to the rest of the nano-Bi samples. Although re-examination of the data was carried out, the unusual trend still persisted. Moreover,

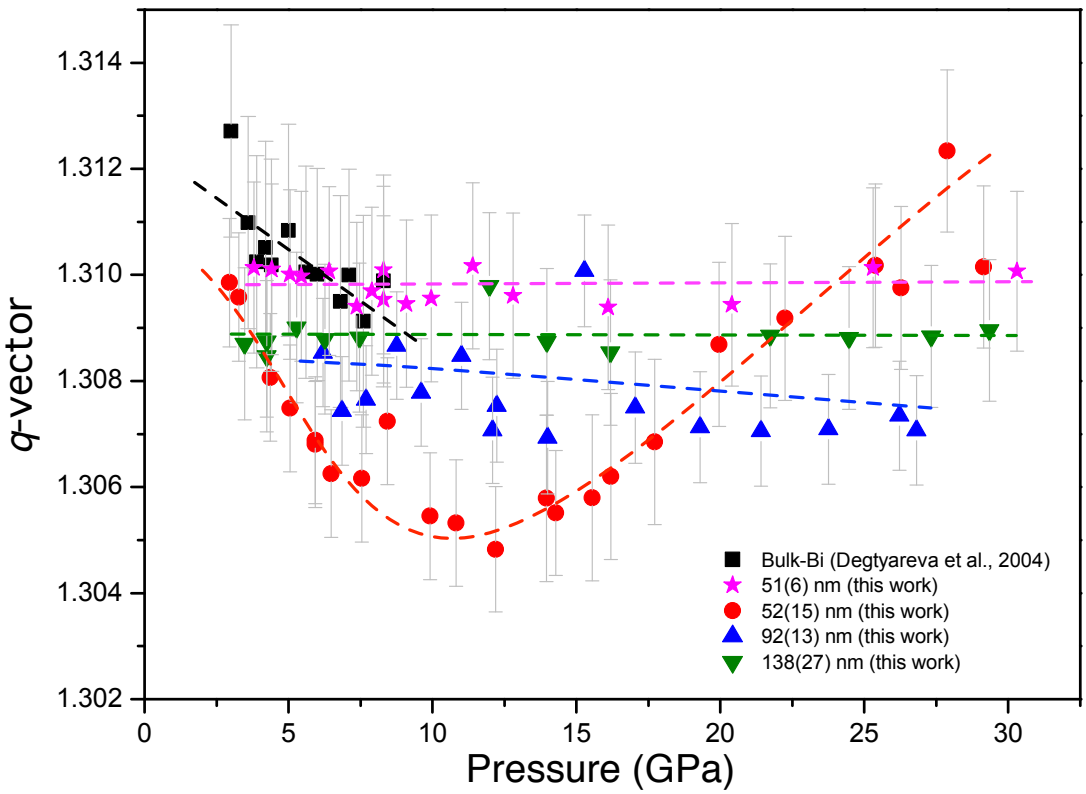

Figure 6.30: Pressure independence of the incommensurate wave vector (q-vector) of all nano-Bi-III samples, with that of bulk-Bi-III [Degtyareva et al., 2004] for comparison. The q-vector of the nano-Bi-III phase is pressure independent overs its extended pressure range of ∼30 GPa. In bulk-Bi-III, the stability range is much smaller, and a previous linear fit (black dashed line) to the data points suggested that q-vector is pressure dependent. The dashed lines corresponding to the nano-Bi data are guides to the eye.

the 51 nm nano-Bi was synthesised using a different method to the rest of the samples, i.e., the 52 nm, 92 nm, and 138 nm samples, and the results in Fig. 6.30 may suggest that the synthesis method might affect the crystallographic properties.

The 52 nm sample exhibited the smallest q-vector among all the samples between 8-15 GPa, the larger values were from the 92 and the 138 nm samples. The largest q-vector was from the bulk material. Due to the variation of the q-vector over the large pressure range from the 52 nm sample, it is hard to conclude on any systematic variation of the q value with particle size in nano-Bi. However, between 8-15 GPa, these values suggest a trend of the incommensurate wave vector of the nanoparticles with particle size, where decreasing the size of the

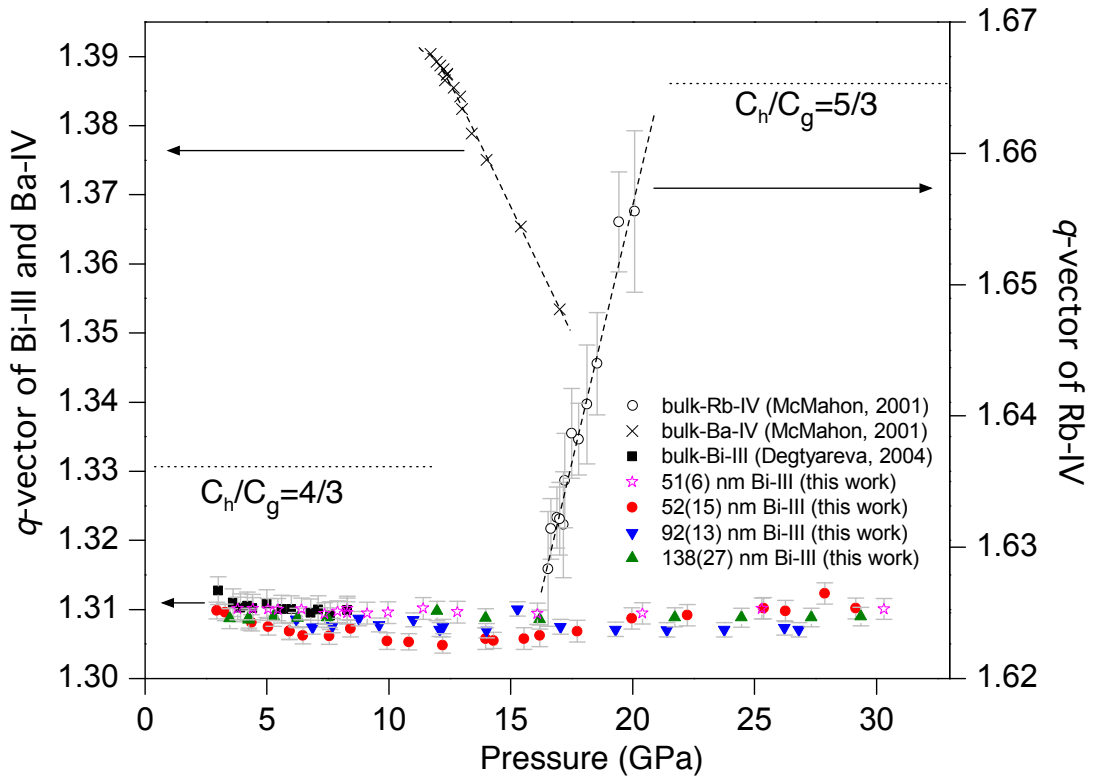

Figure 6.31: Pressure dependence of incommensurate wave vector (q-vector) of all nano-Bi-III samples in comparison with that of bulk-Bi-III [Degtyareva et al., 2004], bulk-Ba-IV and bulk-Rb-IV [McMahon et al., 2001]. The dashed lines are guides to the eye.

particles leads to a smaller q-vector.

6.5.2.4 Pressure Independence of axial ratio c_h/a_h in Nano-Bi-III

In Fig. 6.32, the axial ratio c_h/a_h of all the nano-Bi samples is found to vary between 0.488 to 0.490, staying almost pressure-independent. In bulk-Bi-III, the stability range is much smaller, and a previous fit to the data point suggested that c_h/a_h was more pressure dependent, as shown by the dashed line in Fig. 6.32. The pressure-independent trend of c_h/a_h in nano-Bi means that the host unit cell of nano-Bi has isotropic compression in a substantial range of pressure (∼3-30 GPa).

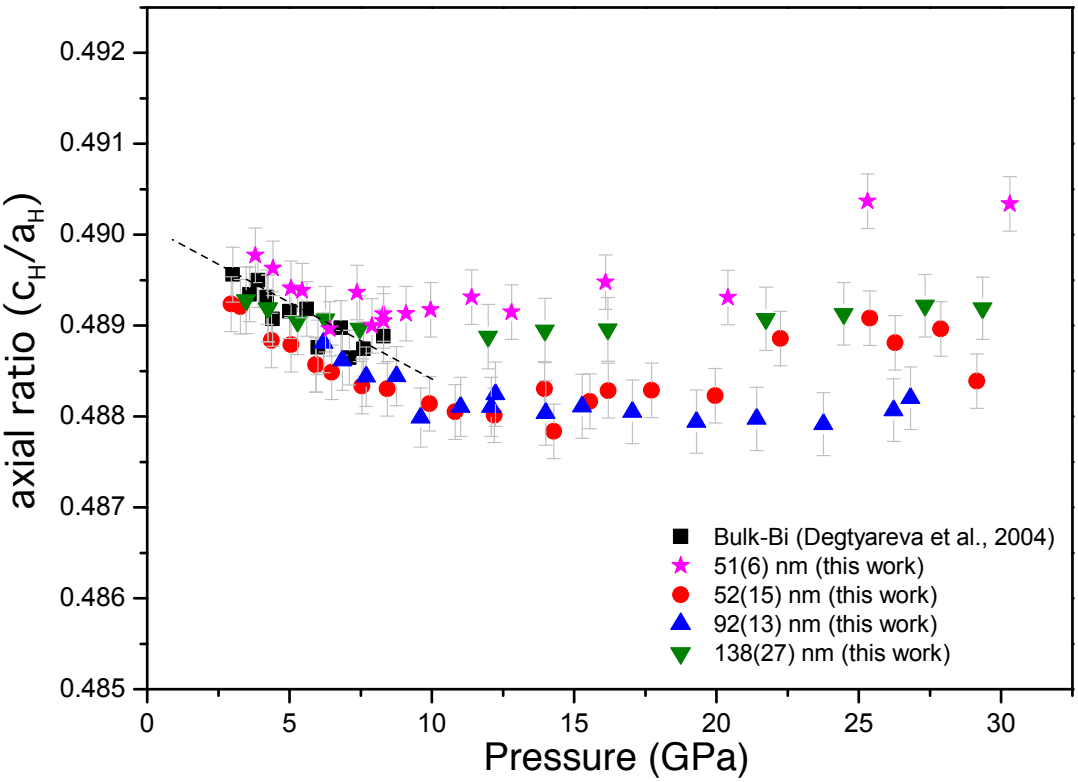

Figure 6.32: Pressure dependence of the axial ratio (c_h/a_h) of all nano-Bi-III samples, along with pressure dependence of c_h/a_h from bulk-Bi-III [Degtyareva et al., 2004] for comparison. The c_h/a_h of the nano-Bi-III phase is pressure independent over its extended pressure range of ∼30 GPa. The dashed line shows the linear fit to c_h/a_h in bulk-Bi and highlighting the decrease in c_h/a_h over pressure range 2.7-8.3 GPa [Degtyareva et al., 2004].

6.5.3 Conclusions

Nano-Bi samples exhibit single Bi-III phase only over a very narrow range of pressure on pressure decrease, greatly limiting the pressure range over which this phase can be studied. However, when the repressurising technique was introduced, single-phase Bi-III patterns were obtained from ∼3 GPa to 14-18 GPa, and consequently coexisted with Bi-V from 14-18 GPa to the maximum pressure achieved in the experiments (∼30 GPa). The repressurising technique led us to obtain a large existence range of Bi-III, which is some ∼5 times larger than that of bulk-Bi-III, resulting in a better understanding of nano-Bi-III behaviours.

The very large coexistence of phases (from 2 to 17 GPa) in nano-Bi, represented

as a pictorial representation of the P_{tr} (Fig. 6.18 and Fig. 6.26), occurs only in nano-Bi, not in the bulk, where the largest coexistence of bulk-Bi has the pressure range of ∼0.3 GPa.

Our current results which is the compressibility of nano-Bi-III expand on the prior work of Degtyareva et al. [Degtyareva et al., 2004] on bulk-Bi-III. All of our results are greatly aided by the greater stability of nano-Bi-III compared to that of bulk-Bi-III which has much narrower stability. Nano-Bi-III samples are found to exhibit at lower compressibility (higher bulk modulus) than of bulk-Bi-III - an effect seen in compression studies of other nanomaterials. The differences in the compressibility of the different sizes of nano-Bi are quite small, and it is not possible to say whether there is a direct correlation between sample size and compressibility. However, the bulk modulus of nano-Bi obtained from fitting an equation of state suggests an increase in value as nanoparticles size decreases.

The incommensurate wavevector (q) is also found to depend on the particle size, with the value of the q decreasing with decreasing particle size between 8-15 GPa. However, the values of q are found to be much less pressure dependent than in the bulk material. In bulk-Bi-III, q decreases with pressure, that is, c_h is more compressible than c_g. In this case, as the pressure is increased, guest atoms are squeezed out of the chains and are presumably incorporated into the host structure, the so-called "toothpaste" effect. The pressure independence of q in nano-Bi-III suggests that this "toothpaste" effect is much smaller than in bulk-Bi-III.

While there is some evidence of size dependence in the bulk modulus, the compressibility of the host unit cell of Bi-III is found to be isotropic in all cases from 3 to 30 GPa. That is, the c_h/a_h ratio is pressure independent.

The repressurising technique used in this section may have wider application to high-pressure studies of other nanomaterials, particularly if the wide coexistence range of high-pressure phases is found to be a common phenomenon in high pressure. Previous studies of high-pressure Te show a wide coexistence range for Te-II and Te-III [Hejny and McMahon, 2003], even in the bulk material. It would be interesting to investigate this in nano-Te too when high-quality samples become available.

The smallest size of nano-Bi produced in this study was 51(6)nm. It would now be of extreme interest to look for size-dependent effects in much smaller

nanoparticles of Bi, i.e., 5-10 nm. Such samples may have larger, more extreme effects that could allow us to develop a better understanding about the size dependence properties in nanoparticles, particularly in incommensurate phases.

6.6 Conclusions

The incommensurate Bi-III phases exists in bismuth nanoparticles on pressure increase, pressure decrease and pressure re-increase. The repressurising process was the key experimental technique necessary to produce the single-phase samples of Bi-III necessary to study its structure. The phase transition pressures in nano-Bi were found to depend on the particle size: the smaller the nanoparticle size, the higher the transition pressures. The compressibility of nano-Bi was found to be lower than that of bulk Bi, while the q-vector was found to be less pressure dependent than in the bulk material. The value of the q-vector was found to get smaller as the particle size decreased during 8-15 GPa.

Chapter 7

Conclusions

The two main outcomes from the body of work contained in this thesis are the successful synthesis of high-quality bismuth nanoparticles, and the diffraction studies of these nanoparticles to pressures up to 30 GPa, as described in Chapter 5 and Chapter 6, respectively. Studies of bulk-Bi at high pressures have also been made for comparison with the studies of the nano-Bi. Since it was found that the quality of nanomaterials purchased from commercial suppliers was very poor, high-pressure diffraction studies of nano-Bi were only possible because the synthesis methods developed by the author allowed the production of high-quality samples with a range of different size.

Nano-Bi gives high-quality powder diffraction patterns over the entire pressure range used in the experiment, ambient pressure to 30 GPa. This is in contrast to bulk-Bi which, even when loaded into a pressure cell as a finely-ground polycrystalline starting material, recrystallises at 2.7 GPa on pressure increase into a sample containing large crystallites, resulting in powder-diffraction images with saturated pixels and relative peak intensities that are incorrect. Analysis of the nano-Bi at ambient pressure after compression and decompression showed that the nano-crystalline nature of the sample was retained, explaining the smooth powder rings. The smooth Debye-Scherrer rings obtained from nano-Bi meant that Rietveld (profile) refinement could be performed on all of the integrated diffraction patterns obtained at high pressure.

The series of transitions and structures found on compressing and decompressing nano-Bi is the same as that found in bulk materials, that is Bi-I, Bi-II, Bi-III, Bi-V. Although, on initial compression, nano-Bi is found to transform

to the incommensurate host-guest phase, Bi-III, the diffraction pattern from this phase contains diffraction peaks both from incommensurate Bi-III and some additional, unaccounted-for peaks. Attempts to fit these peaks as a separate phase, or as a distortion of Bi-III, were unsuccessful, and their identity remains unknown. However, if the Bi-III phase is accessed on pressure increase from a sample first compressed into Bi-V before decompressing back to Bi-I/Bi-II, single-phase patterns of Bi-III, with no additional peaks, are obtained. Rietveld refinement of Bi-III diffraction patterns obtained via this route show that the incommensurate structure is the same as that found in bulk-Bi.

Using the four different particle sizes of monodispersed samples synthesised in Chapter 5, we have investigated the size-dependence of the transition pressures, compressibility and the structural parameters of the incommensurate Bi-III phase. All of the nano-Bi samples exhibit phase coexistence over a much wider range of pressures (2-17 GPa) on pressure increase, decrease and re-increase compared to bulk-Bi samples, where the range of phase coexistence is typically only 0.5 GPa. Comparison of the phase transition pressures showed that as the size of the bismuth nanoparticles decreases, the transition pressures increase compared to those observed in bulk Bi. This increase in transition pressure with reducing particle size is the same effect seen in the majority of other nanomaterials with increasing pressure, most notably CdSe, Se and Te.

The increased phase transition pressures are most marked for the Bi-III phase, where, in contrast to the existence range of only 5 GPa seen in bulk Bi-III, a much wider existence range of 27 GPa is observed in nano-Bi-III. This five-times-greater existence range enables the structural parameters and compressibility of Bi-III to be studied over a pressure range comparable with other incommensurate phases in the elements.

The compressibility of nano-Bi-III is less than that of bulk-Bi-III, and is found to decrease further with decreasing particle size. This is the same behaviour seen in other nanomaterials. The incommensurate q-vector of all sizes of nano-Bi are found to be pressure independent but size dependent: the smaller the particle size of the nano-Bi-III, the smaller the value of q. The pressure independence of q means that there is no sign of its value converging to the commensurate values of $\frac{5}{4}$ or $\frac{4}{3}$ within the maximum pressure attained in this studies.

The pressure independence of the incommensurate wave vector in nano-Bi-III

could be caused by the high surface energy of the nanoparticles, which does not allow the atoms in the guest chains to be "squeezed out" of the host-structure channels under pressure, leading to a constant value of q-vector with pressure. The size dependence of q-vector might be due to different surface energy effects in the different particle sizes altering the arrangement of the host and guest structures, resulting in the different q-vector values.

While it was possible to synthesise four high-quality samples of nano-Bi particles during the timescale of this thesis, it would have been extremely interesting to synthesise much smaller nanoparticles with diameters of of 5-10 nm to see if more extreme effects on the phase transition pressures, coexistence ranges and incommensurate wave vector were obtained. The incommensurate wave vector might be lowered by reducing the particle size until it reached a commensurate value ($\frac{5}{4}$). However, it should be noted that having too small nanoparticles will lead to severe peak broadening in the diffraction profiles, which may prevent detailed analysis of the complex diffraction patterns from Bi-III. In addition to synthesising and studying smaller nano-particles, it would also be interesting to synthesise 250-300 nm nano-Bi, which the results of this thesis suggest that it should have the same phase transition pressures as bulk-Bi. The same particles should also have their compressibilities and incommensurate wave vectors studied for comparison with those found in the bulk. Although the work described in this thesis focused on nano-Bi, in light of the results it would now be extremely interesting to study other elemental systems where incommensurate phases are known to occur in the bulk, such as Te. This would require another substantial synthesis effort, however.

Finally, there are a variety of implications of the work described in this thesis on the wider studies of nanomaterials under high pressure. The most important is that the nanomaterials used must be well characterised, and produced in a very well-controlled manner. This suggests that nanoparticle synthesis will form an integral part of the research. Secondly, the behaviour of nanomaterials under high pressure might show a sluggishness during phase transitions that results in a wide coexistence of phases and also the presence of the unaccounted-for peaks. The repressurising technique used in the work described in this thesis may then allow one to get the single-phase patterns of the interesting phases.

Appendix A

High-Pressure X-Ray Diffraction Data

A.1 HP-PXRD Experiment with Bismuth Oxide Bulk and Nanoparticles

A.1.1 Method

From section 6.3.2.1, to confirm the amorphisation above 21 GPa of Bi_2O_3 which was previously reported by [Chouinard and Desgreniers, 2000], HP-PXRD of Bi_2O_3 has to be carried out.

Bulk- and nano-Bi_2O_3 were purchased from Sigma-Aldrich. The size of nano-Bi_2O_3 is claimed to be less than 100 nm. The experimental procedure is the same as reported in section 6.3.1 with technical details provided in Table A.1. The HP-PXRD experiments were conducted on pressure increase with very large ($\sim$5 GPa) pressure increment. The highest pressures in the experiments are 22 GPa for bulk-Bi_2O_3, and 21 GPa for nano-Bi_2O_3.

A.1.2 Results

From Fig A.1, α-Bi_2O_3 was observed in the diffraction patterns in bulk-Bi_2O_3 and nano-Bi_2O_3 at 0.1 GPa. However, bulk-Bi_2O_3 does not undergo amorphisation at the maximum pressure, 22 GPa, nor nano-Bi_2O_3 at 21 GPa as claimed by [Chouinard and Desgreniers, 2000]. This could be due to the overestimation of

pressure by the effect of non-hydrostatic condition in bulk-Bi_2O_3 and/or the size dependence phase transition in nano-Bi_2O_3.

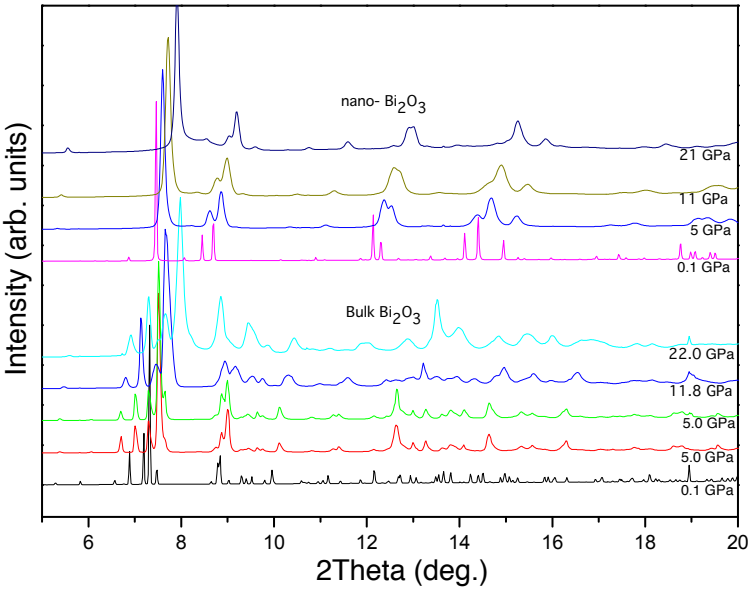

Figure A.1: (upper panel) Waterfall plot of 1D diffraction profiles obtained from nano-Bi_2O_3 on pressure increase from ambient to 21 GPa in 5 GPa steps. (lower panel) Waterfall plot of 1D integrated diffraction profiles obtained from bulk-Bi_2O_3 on pressure increase from ambient pressure to 22 GPa in 5 GPa steps. α-Bi_2O_3 phases are observed in both samples. There is no evidence of amorphisation at the highest pressure ~21 GPa, as reported in [Chouinard and Desgreniers, 2000].

A.1.3 Conclusions

The amorphous phase of nano-Bi_2O_3 has not been observed up to 22 GPa and 21 GPa in bulk- and nano-Bi_2O_3, respectively. Therefore, this experiment still cannot reproduce the result from [Chouinard and Desgreniers, 2000] which might be due to overestimation in pressure values in bulk- and nano-Bi_2O_3 and/or the higher transition pressure of nano-Bi_2O_3. However, the disappearance of Bi_2O_3 peaks on pressure decrease in section 6.3.2.1 from Fig. 6.12 is believed to be from the amorphisation of Bi_2O_3.

Future experiments should be done at a higher maximum pressure, e.g., 30 GPa, so that the questions of bulk- and nano-Bi_2O_3 crystalline-amorphous phase transition could be answered.

A.2 Waterfall Plots of 1D Integrated Diffraction Profiles

To simplify the layout of Chapter 6, and to aid readability, all waterfall plots of 1D integrated diffraction profiles are put in this appendix section.

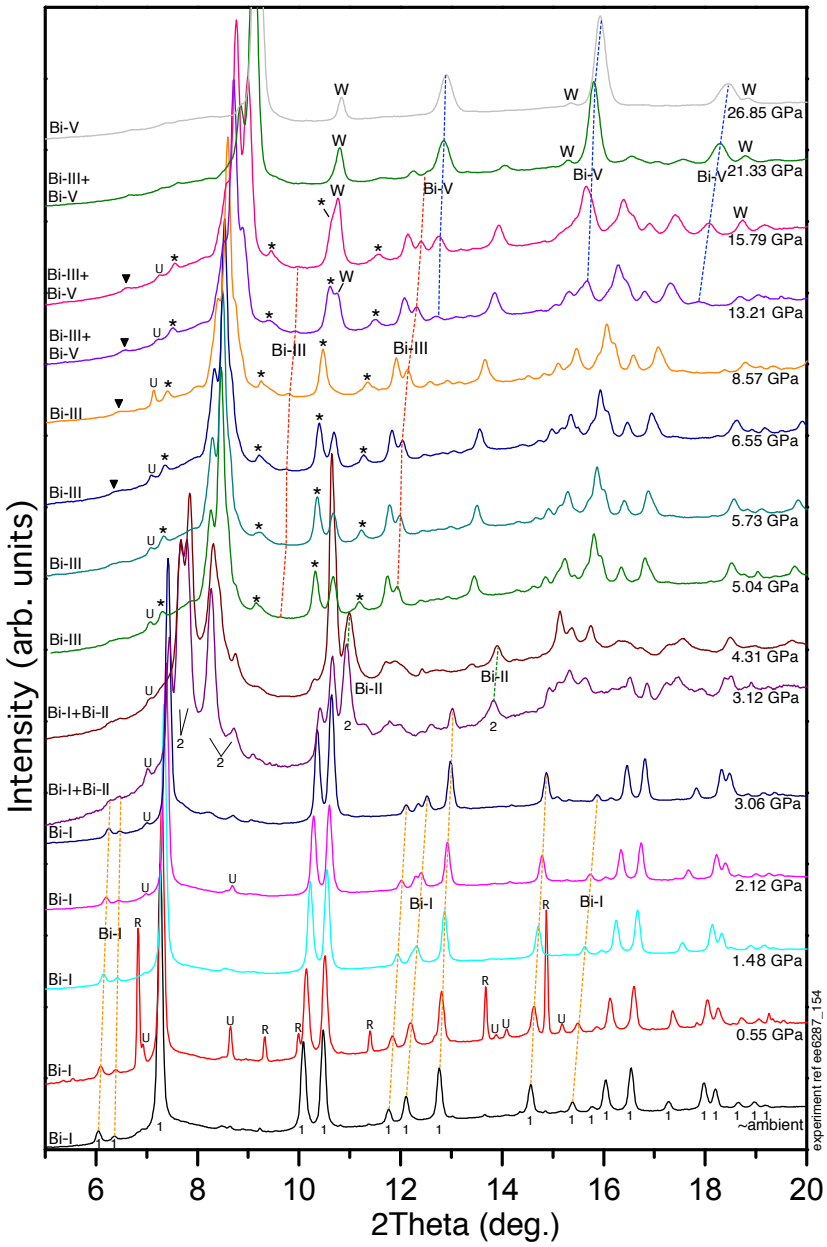

Figure A.2: Waterfall plot of 1D integrated diffraction profiles obtained from the 51(6) nm nano-Bi sample on pressure increase to ∼27 GPa. The pressure was increased in 1-3 GPa steps between ambient and 8 GPa and in 4-6 GPa steps between 8 GPa and 27 GPa. The diffraction patterns come from four phases, Bi-I, Bi-II, Bi-III, and Bi-V. The orange-, green-, red-, and blue-dashed lines indicate the progression of peaks from Bi-I, Bi-II, Bi-III, Bi-V, respectively. The asterisk (*), (▼) mark the position of the unaccounted-for peaks. The 'R' labels the positions of the ruby reflections. 'U' marks the undefined peaks which might be associated with ruby peaks. The 'W' indicate the position of the gasket (tungsten) reflections. Some Bi-II peaks are labelled with '2' to make them easy to be noticed.

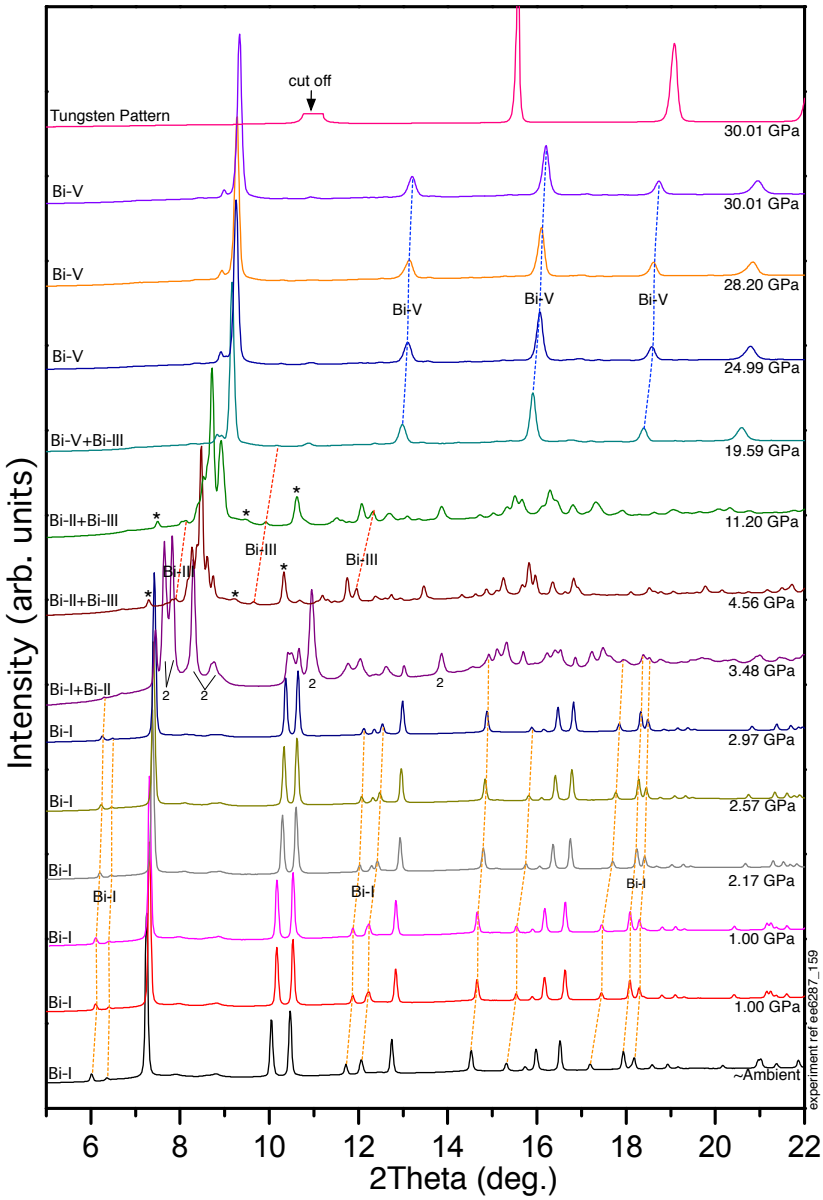

Figure A.3: Waterfall plot of 1D integrated diffraction profiles obtained from the 92(13) nm nano-Bi sample on pressure increase to ∼30 GPa. The pressure was increased in 1 GPa steps between ambient and 5 GPa and in 5 to 10 GPa steps between 5 GPa and 30 GPa. The diffraction patterns come from four phases, Bi-I, Bi-II, Bi-III, and Bi-V. The orange-, red-, and blue-dashed lines indicate the progression of peaks from Bi-I, Bi-III, Bi-V, respectively. Some Bi-II peaks are labelled with '2' to make them easy to be noticed. The asterisk (*) marks the position of the unaccounted-for peaks. At the top of the graph, a tungsten diffraction pattern is provided to assist identifying the non-Bi peaks from tungsten gasket reflections.

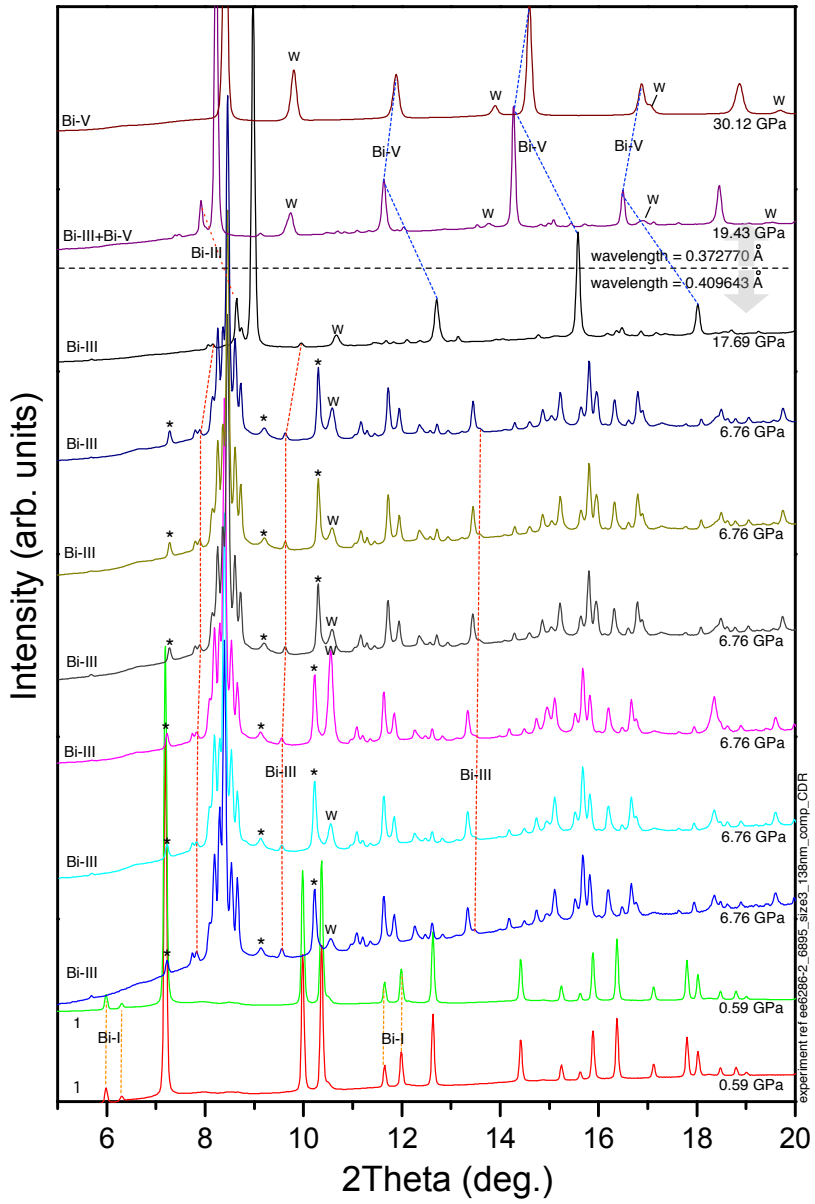

Figure A.4: Waterfall plot of 1D integrated diffraction profiles obtained from the 138(27) nm nano-Bi sample on pressure increase to ∼30 GPa. The pressure was increased very rapidly up to 30 GPa. The diffraction patterns come from three phases, Bi-I, Bi-III, and Bi-V. The orange-, red-, and blue-dashed lines indicate the progression of peaks from Bi-I, Bi-III, Bi-V, respectively. The asterisk (*) marks the position of the unaccounted-for peaks. The 'W' indicates the positions of the gasket (tungsten) reflections. The repetition of diffraction profiles at 6.76 GPa suggest that the sample is not homogenous because the peak at 10.8° in 2θ does not consistently appear in all patterns at 6.76 GPa.

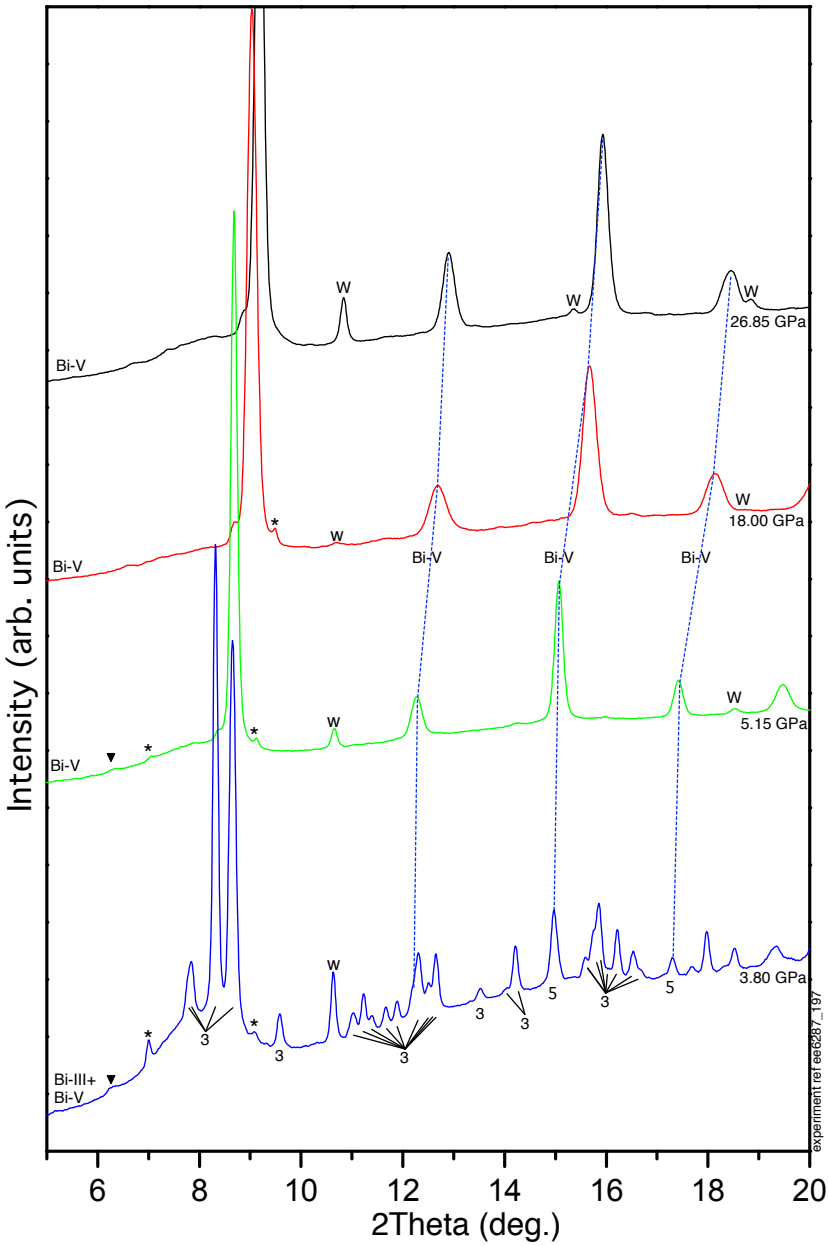

Figure A.5: Waterfall plot of 1D integrated diffraction profiles obtained from the 51(6) nm nano-Bi sample on pressure decrease from 26.85 GPa to ambient pressure. The pressure was decreased in a very large steps (2-13 GPa). The diffraction patterns come from two phases, Bi-III and Bi-V. Some Bi-III peaks are labelled with '3'. The blue-dashed lines indicate the progression of peaks from Bi-V. The (▼) and (*) mark the position of the unaccounted-for peaks. The 'W' indicates the positions of the gasket (tungsten) reflections.

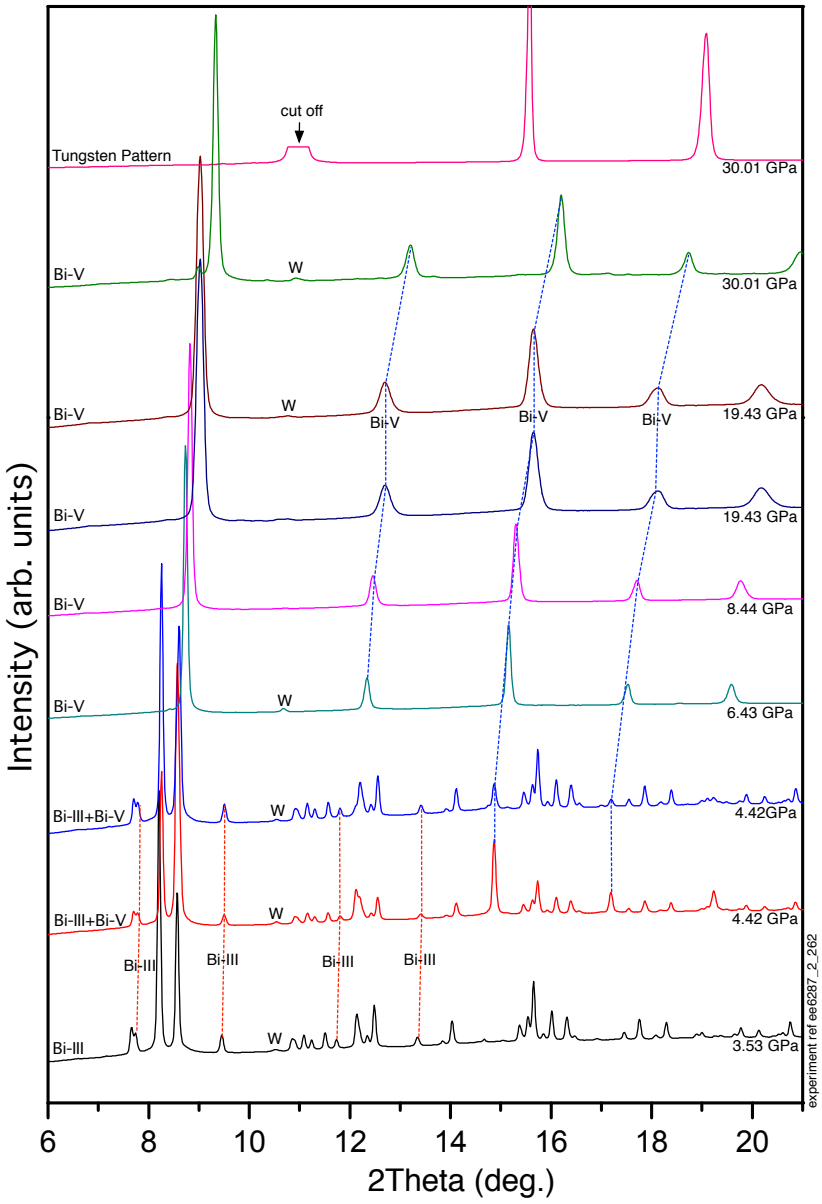

Figure A.6: Waterfall plot of 1D integrated diffraction profiles obtained from the 92(13) nm nano-Bi sample on pressure decrease from 30.01 GPa to 3.53 GPa. The pressure was decreased in large pressure steps at the beginning of decompression, but smaller steps when reaching Bi-III. The diffraction patterns come from two phases, Bi-III and Bi-V. The red- and blue-dashed lines indicate the progression of peaks from Bi-III and Bi-V, respectively. At the top of the graph, a tungsten diffraction pattern is provided to assist identifying the non-Bi peaks from tungsten gasket reflections. The 'W' indicates the positions of the gasket (tungsten) reflections.

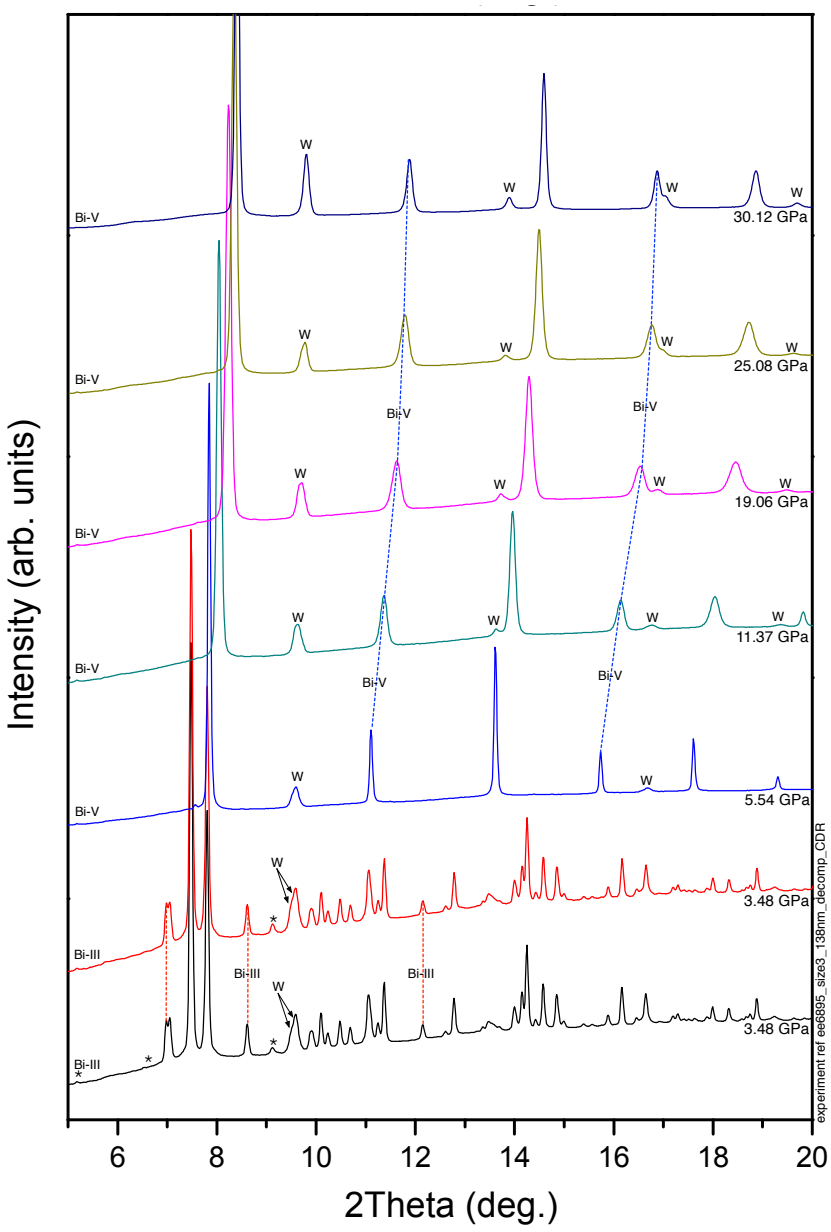

Figure A.7: Waterfall plot of 1D integrated diffraction profiles obtained from the 138(27) nm nano-Bi sample on pressure decrease from 30.12 GPa to 3.48 GPa. The pressure was decreased in large pressure steps at the beginning of decompression, but smaller steps when reaching Bi-III. The diffraction patterns come from two phases, Bi-III and Bi-V. The red- and blue-dashed lines indicate the progression of peaks from Bi-III and Bi-V, respectively. The 'W' indicate the position of the gasket (tungsten) reflections. The (*) marks the position of the unaccounted-for peaks.

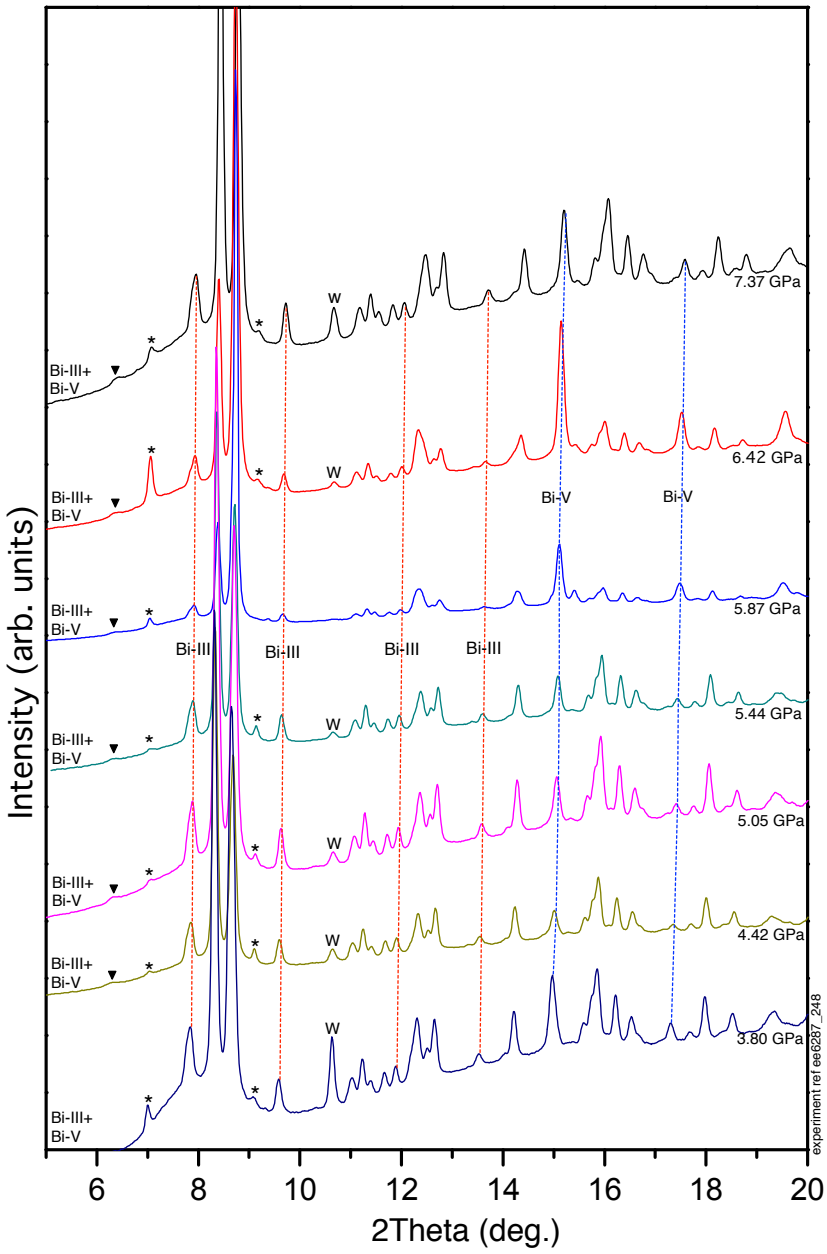

Figure A.8: Waterfall plot of 1D integrated diffraction profiles obtained from the 51(6) nm nano-Bi sample on pressure re-increase from 3.80 GPa to 7.37 GPa. The pressure was increased in 1-2 GPa. The diffraction patterns come from two phases, Bi-III and Bi-V. The red- and blue-dashed lines indicate the progression of peaks from Bi-III and Bi-V, respectively. The (▼) and (*) mark the position of the unaccounted-for peaks. The 'W' indicate the position of the gasket (tungsten) reflections. It should be noted that Bi-V exists at the lowest pressure (3.80 GPa) on pressure re-increase, because single phase Bi-III pattern could not be obtained from pressure decrease step.

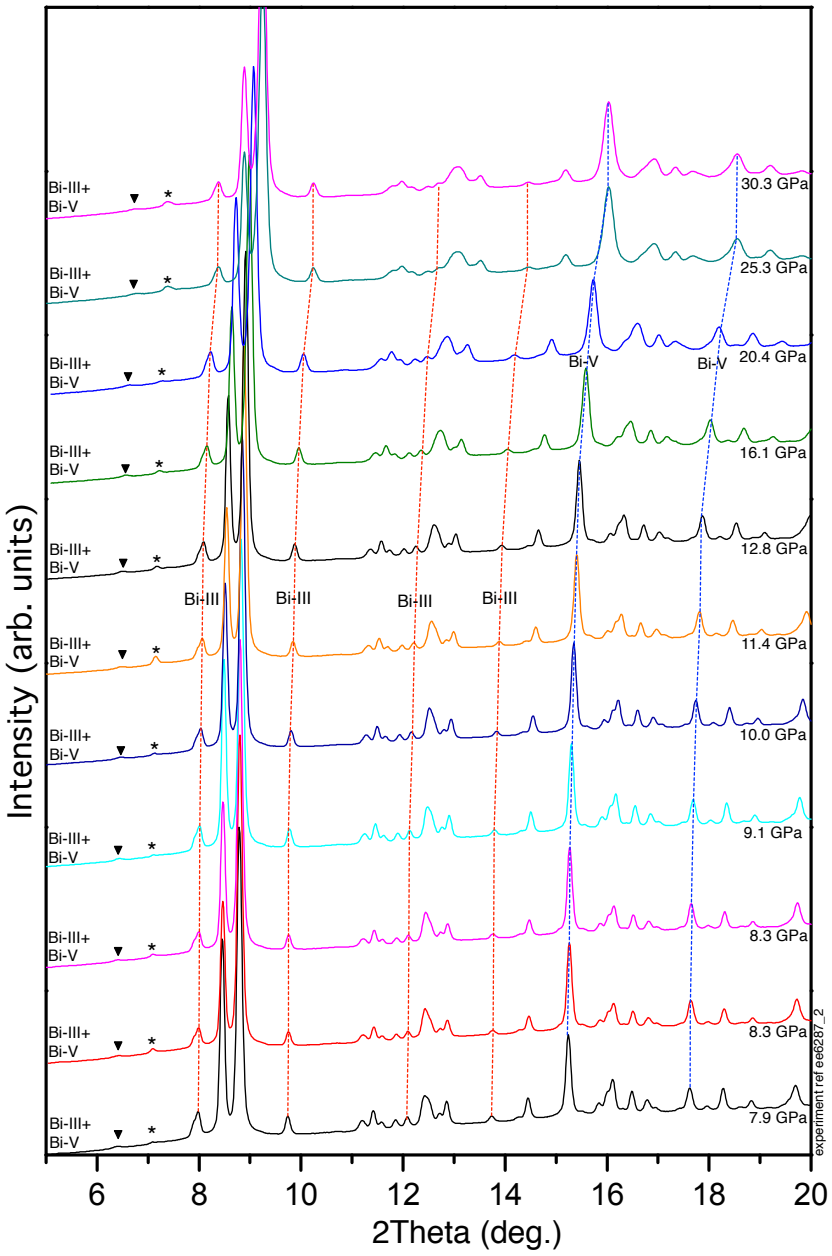

Figure A.9: Waterfall plot of 1D integrated diffraction profiles obtained from the 51(6) nm nano-Bi sample on pressure re-increase from 7.9 GPa to 30.3 GPa. The pressure was increased in 1-2 GPa between 7.9 and 12.8 GPa and in 4-5 GPa steps between 12.8 GPa and 30.3 GPa. The diffraction patterns come from two phases, Bi-III and Bi-V. The red- and blue-dashed lines indicate the progression of peaks from Bi-III and Bi-V, respectively. The (▼) and (*) mark the position of the unaccounted-for peaks.

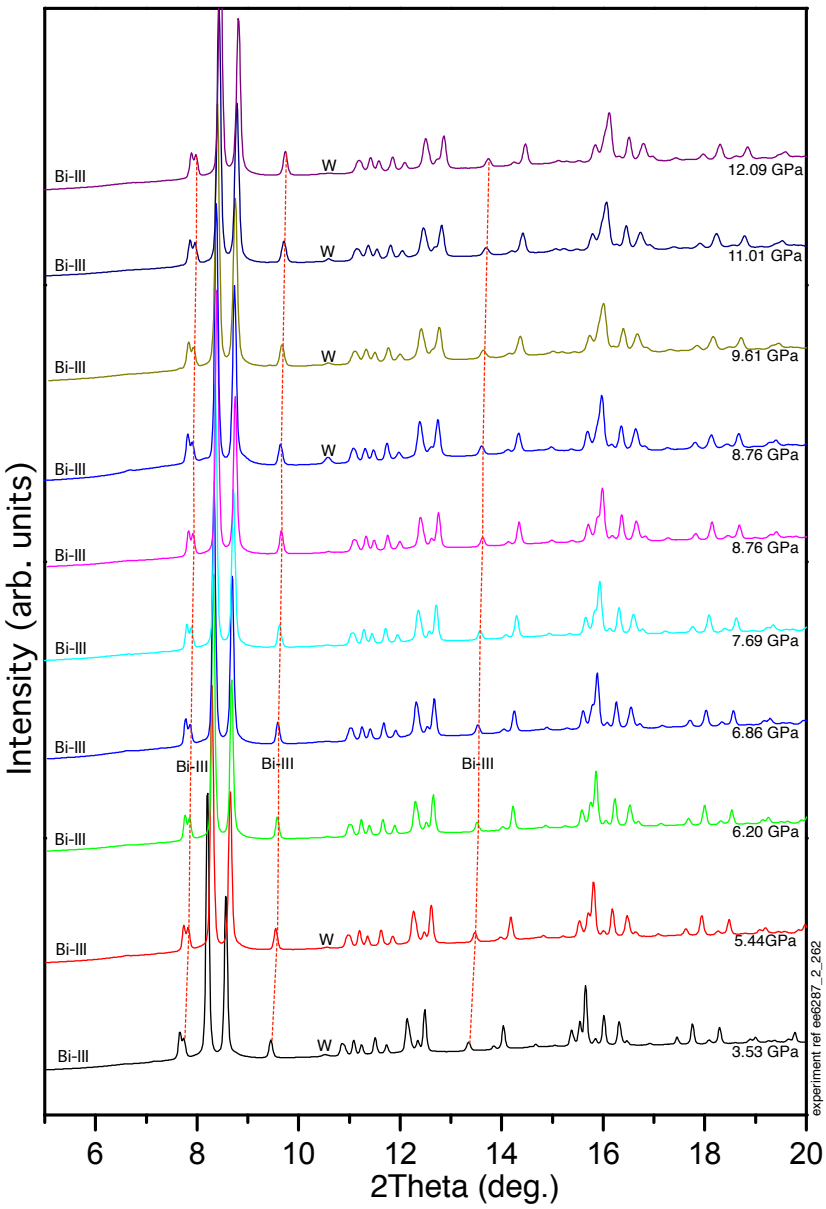

Figure A.10: Waterfall plot of 1D integrated diffraction profiles obtained from the 92(13) nm nano-Bi sample on pressure re-increase from 3.53 to to 12.09 GPa. The pressure was increased in 1-2 GPa steps. The diffraction patterns come only from one phase, Bi-III. The red-dashed lines indicates the progression of peaks from Bi-III. The 'W' marks the positions of the gasket (tungsten) peaks.

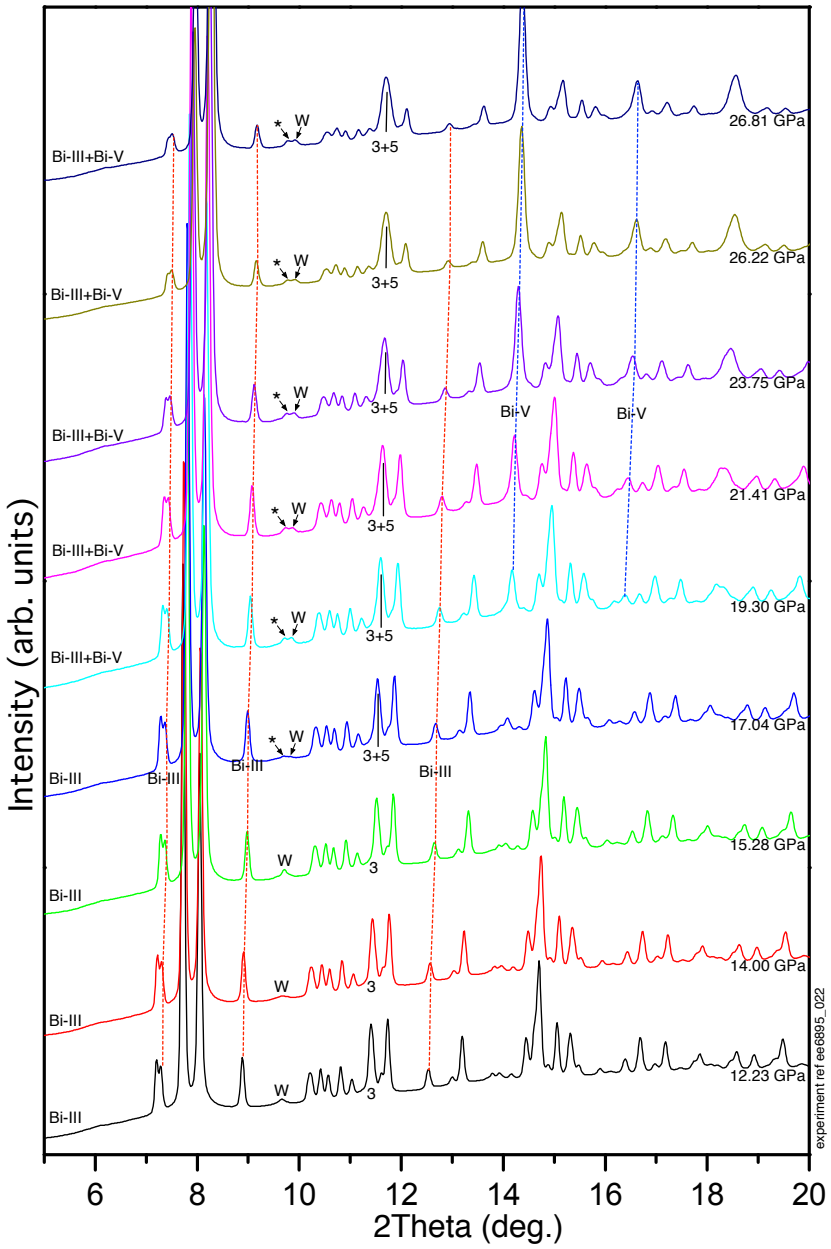

Figure A.11: Waterfall plot of 1D integrated diffraction profiles obtained from the 92(13) nm nano-Bi sample on pressure re-increase from 12.23 to to 26.81 GPa. The pressure was increased in 1-2 GPa steps. The diffraction patterns come from two phases, Bi-III and Bi-V. The red- and blue-dashed lines indicate the progression of peaks from Bi-III and Bi-V, respectively. '3' indicates a peak of Bi-III and '3+5' labels the overlapping peak of Bi-III and BI-V. The (*) marks the position of the unaccounted-for peaks. The 'W' marks the positions of the gasket (tungsten) peaks.

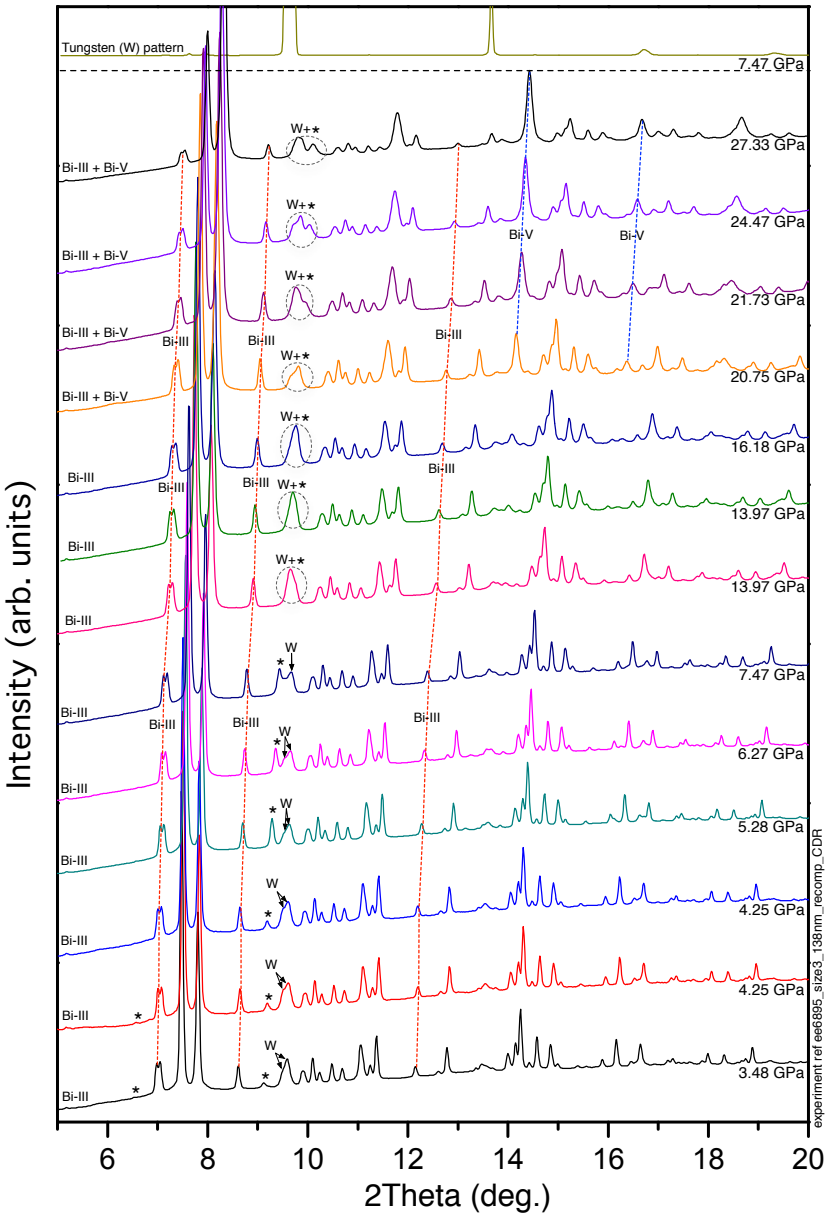

Figure A.12: Waterfall plot of 1D integrated diffraction profiles obtained from the 138(27) nm nano-Bi sample on pressure re-increase from 3.48 to to 27.33 GPa. The pressure was increased in 1-2 GPa steps. The diffraction patterns come from two phases, Bi-III and Bi-V. The red- and blue-dashed lines indicate the progression of peaks from Bi-III and Bi-V, respectively. The (*) marks the position of the unaccounted-for peaks. The 'W' indicates the positions of the gasket (tungsten) reflections. At the top of the graph, a tungsten diffraction pattern is provided to assist identifying the non-Bi peaks from tungsten gasket reflections. It should be noted that an unusual 'W' peak located at lower 2θ angle exists in 138(27) nm diffraction profiles on pressure re-increase.

A.3 Beamtime Technical Data

The experiments described in this thesis have the synchrotron experimental details according to Table A.1.

Table A.1: HP-PXRD experiments details from all samples presented in this thesis. P_{inc}, P_{dec}, P_{reinc} refer to pressure increase, decrease and re-increse, respectively.

Sample	Pressure	Experiment Ref.	Synchrotron	Wavelength (Å)
10 nm Se (commercial)	P_{inc}	hs3090K	ID09A, ESRF	0.3738 Å
10 nm Se (commercial)	P_{dec}	hs3090L	ID09A, ESRF	0.4142 Å
70 nm Se (commercial)	P_{inc}, P_{dec}	hs3090L	ID09A, ESRF	0.4142 Å
10 nm lyophilised Se (commercial)	P_{inc}	hs3090M	ID27, ESRF	0.2647 Å
40 nm Bi (commercial)	P_{inc}	hs3090M	ID27, ESRF	0.3738 Å
bulk-Bi	P_{inc}, P_{dec}	ee1638	I15, Diamond	0.4124 Å
128(45) nm Bi	P_{inc}, P_{dec}	ee1638	I15, Diamond	0.4124 Å
51(6) nm Bi	P_{inc}, P_{dec}, P_{reinc}	ee6287	I15, Diamond	0.4141 Å
51(6) nm Bi	P_{reinc}	ee6287-2	I15, Diamond	0.4146 Å
52(15) nm Bi	P_{inc}	ee6287	I15, Diamond	0.4141 Å
52(15) nm Bi	P_{inc}, P_{dec}, P_{reinc}	ee6287-2	I15, Diamond	0.4146 Å
52(15) nm Bi	P_{reinc}	ee6287-2	I15, Diamond	0.4096 Å
52(15) nm Bi	P_{reinc}	ee6895	I15, Diamond	0.3728 Å
92(35) nm Bi	P_{inc}, P_{dec}	ee6287-2	I15, Diamond	0.4146 Å
92(35) nm Bi	P_{dec}, P_{reinc}	ee6287-2	I15, Diamond	0.4096 Å
92(35) nm Bi	P_{reinc}	ee6895	I15, Diamond	0.3728 Å
138(27) nm Bi set 1	P_{inc}	ee4215	I15, Diamond	0.3643 Å
138(27) nm Bi set 1	P_{dec}	ee6286	I15, Diamond	0.4133 Å
138(27) nm Bi set 2	P_{inc}	ee6287-2	I15, Diamond	0.4096 Å
138(27) nm Bi set 2	P_{inc}, P_{dec}, P_{reinc}	ee6895	I15, Diamond	0.3728 Å
< 100 nm Bi_2O_3	P_{inc}	hs4039	ID09A, ESRF	0.4148 Å
bulk Bi_2O_3	P_{inc}	hs4039	ID09A, ESRF	0.4148 Å

Appendix B

Synthesis Details

B.1 Chemical Synthesis Procedures

In a typical synthesis, the work process can be described as: synthesis, washing, and characterisations.

B.1.1 Synthesis : Details of Chemical Reagents Used in Each Approach

Selected of successful synthesis recipes are provided in Fig. B.1, B.2, B.3, B.4, B.5, and B.6 for each approach described in Chapter 5.

Ref. R2(5)	Molecular Weight (g/Mol)	Mole (mol)	Mass (g)	Volume (mL)	Ratio to Bi^{3+}	Concentration (mol/L)
NaAOT (in isooctane)	444.56	0.001	0.4446	10.00	3	0.1
a -split NaAOT solution		0.0006		6.00		
b- split NaAOT solution		0.0004		4.00		
a- $Bi(NO_3)_3 \bullet 5H_2O$	485.07	0.000333333	0.1617			0.033333333
w	10					0.033333333
a- H_2O	18	0.0043	0.0780	0.0780		
b- H_2O		0.0040	0.0720			
b- $NaBH_4$	37.83	0.000666667	0.0252		2	

Ref. R3(1)	Molecular Weight (g/Mol)	Mole (mol)	Mass (g)	Volume (mL)	Ratio to Bi^{3+}	Concentration (mol/L)
NaAOT (in isooctane)	444.56	0.005	2.2228	10.00	2.5	0.5
a -split NaAOT solution		0.0033		6.67		
b- split NaAOT solution		0.00167		3.33		
a - $BiCl_3$	315.54	0.002	0.6311			0.2
w	2					0.2
a- H_2O	18	0.0067	0.1200	0.1200		
b- H_2O		0.0033	0.0600			
b- $NaBH_4$	37.83	0.001	0.0378		0.5	

Ref. R4(1)	Molecular Weight (g/Mol)	Mole (mol)	Mass (g)	Volume (mL)	Ratio to Bi^{3+}	Concentration (mol/L)
NaAOT (in isooctane)	444.56	0.005	2.2228	10.00	2.5	0.5
a -split NaAOT solution		0.003333333		6.67		
b- split NaAOT solution		0.001666667		3.33		
a - BiClO	260.43	0.002	0.5209			0.2
w	2					0.2
a- H_2O	18	0.0067	0.1200	0.1200		
b- H_2O		0.0033	0.0600			
b- $NaBH_4$	37.83	0.001	0.0378		0.5	

Figure B.1: Aqueous bismuth synthesis approach using NaAOT.

Ref. R3(2)	Molecular Weight (g/Mol)	Mole (mol)	Mass (g)	Volume (mL)	Ratio to Bi^{3+}	Concentration (mol/L)
NP5 (in isooctane)	441	0.001	0.4410	10.00	4	0.1
a -split NaAOT solution		0.0006		6.00		
b- split NaAOT solution		0.0004		4.00		
a - $BiCl_3$	315.54	0.00025	0.0789			0.025
w	2					0.025
a- H_2O	18	0.0012	0.0216	0.0216		
b- H_2O		0.0008	0.0144			
b- $NaBH_4$	37.83	0.0005	0.0189		2	

Ref. R4(3)	Molecular Weight (g/Mol)	Mole (mol)	Mass (g)	Volume (mL)	Ratio to Bi^{3+}	Concentration (mol/L)
NP5 (in isooctane)	441	0.001	0.4410	10.00	4	0.1
a -split NP5 solution		0.0007		7.00		
b- split NP5 solution		0.0003		3.00		
a - BiClO	260.43	0.00025	0.0651			0.025
w	2					0.025
a- H_2O	18	0.0014	0.0252	0.0252		
b- H_2O		0.0006	0.0108			
b- $NaBH_4$	37.83	0.0005	0.0189		2	

Figure B.2: Aqueous bismuth synthesis approach using NP5.

Ref. R5 (SYN. no 9)	Molecular Weight (g/Mol)	Mole (mol)	Mass (g)	Volume (mL)	Ratio to Bi^{3+}	Concentration (mol/L)
Toluene						
Decanoic Acid	172.26	0.00100	0.1723	7.000		
Dodecylamine	185.35	0.00100	0.1854	2.000		
Bismuth Acetate	386.11	0.00010	0.0386			0.0100
Toluene				1.000		
N_2H_4 monohydrate	50.06	0.00010	0.0108	0.005		
Toluene				1.000		
Phenyl Hydrazine	108.14	0.00100	0.0180	0.010		
H_2O	18	0.00100	0.0180			
Toluene				1.000		
$NaBH_4$	37.83	0.00010	0.0038			
H_2O	18	0.00100	0.0180			
Toluene				1.000		
$TBABH_4$	257.31	0.00010	0.0257			
H_2O	18	0.00100	0.0180			

Figure B.3: Non-aqueous bismuth synthesis spproach.

Ref. R10(2) SYN34.1	Molecular Weight (g/Mol)	Mole (mol)	Mass (g)	Volume (mL)	Ratio to Bi^{3+}	Concentration (mol/L)
PVP	55000					
Unit $(C_6H_9NO)_n$	109	0.006	0.698	0.698	16	0.6400
$Bi(NO_3)_3$ $5H_2O$	485.07	0.0004	0.1940			0.0400
$FeCl_3$	162.2	0.0000	0.0006		0.01	
1,5-pentanediol or Etyleneglycol (EG)				8.526		

Figure B.4: High-temperature polyol and thermal decomposition synthesis approach.

	Ref. R11	Molecular Weight (g/Mol)	Mole (mol)	Mass (g)	Volume (mL)	Molar Ratio (/Bi)	Concentration. (mol/L)
	PVP Stock Solution	55000					
	PVP			12.5568	12.557		
	1,5 Pentanediol				167.443		
A	Per synthesis…						
	PVP Units $(C_6H_9NO)_n$	109	0.00640	0.698	0.698	16.00	0.6038
B	1,5 Pentanediol				9.302		
C	$Bi(NO_3)_3.5H_2O$	485.07	0.0004	0.1940			0.0377
	$Bi(CH_3CO2)_3$	386.11	0.0004	0.1544			
	$BiCl_3$	315.34	0.0004	0.1261			
	BiClO	260.43	0.0004	0.1042			
	$NaBiO_3$	279.97	0.0004	0.1120			
D	NaN(SiMe3)2 in 1 M THF solution		0.0002		0.600		

Figure B.5: High-temperature polyol - thermal decomposition synthesis approach.

	Ref. R12	Molecular Weight (g/Mol)	Mole (mol)	Mass (g)	Volume (mL)	Molar Ratio (/Bi)	Concentration (mol/L)
A	$Bi(CH_3CO2)_3$	386.11	0.00025	0.0965			0.0421
	$NaBiO_3$	279.97	0.00025	0.0700			
	$BiCl_3$	315.34	0.00025	0.0788			
B	THF			0.5	0.562		
	PHD-*co*-PVP Stock Solution	25	% wt				
	PHD-*co*-PVP			26.25			
	1-octadecene			78.75	99.810		
C	PHD-*co*-PVP Stock Solution per synthesis			5.000	5.940		
D	NaN(SiMe3)2	183.38	0.00075	0.1375		3	
	NaN(SiMe3)2		0.00113	0.2063		4.5	
	NaN(SiMe3)2		0.00225	0.4126		9	

Figure B.6: High-temperature thermal decomposition (Buhro's procedure) synthesis approach.

B.1.2 Washing Procedures

After any synthesis, a majority of the particles will have similar diameters. Moreover, unreacted substrate, aggregation, and aggregation also remain in the synthesis solution.

To get rid of unwanted substances from the synthesised solution, sonication[1] and centrifugation[2] are the standard methods in common laboratory operations used to purify synthesised samples by the chemist and biologist.

This is the method used to get rid of unwanted materials, i.e., (sorted from lightest to heaviest) excess solvent, excess organic surfactant, unreacted substrate, aggregation (clustered nanoparticles), and aggregation of nanoparticles in forms of plate or clump.

The process of washing consists of five steps, as follows:

- Washing Solution: the mixture of good and bad solvent for nanoparticles are used in different ratios to vary the solubility of nanoparticles in the washing solution. For example, nano-Bi is well soluble in toluene, the NPs will be dispersed all over in the solution. In contrast, if acetone was used (bad solvent for nano-Bi), the NPs would aggregate at the bottom of the container. Therefore a mixture of good and bad solvents are used to disperse NPs in the washing solution and, however, leave enough ability for NPs to settle down at the bottom of the container after centrifugation.

- Mixing: After putting the washing solution into the system, the solution is shaken to mix the nanoparticles with the washing solution homogeneously and then sonicated to detach fused or clustered nanoparticles.

- Centrifugation: This is the step to separate the heavy (nanoparticles, cluster, aggregation (plate)) and light element (excess organic materials or reagents). The centrifuge will apply a centrifugal force to the solution so that the NPs and clusters or plates that are heavy will go to the bottom of the tube, the lighter elements will be at the top. The centrifugal force used is dependent on size of the NPs and should be adjusted for optimal performance. In this thesis, 2500-4000 rpm speed was used for 30-60 minutes duration.

[1]Sonication is the use of ultrasonic waves to agitate particles in a sample, for breaking particles clusters for mixing colloid with solvent.

[2]Centrifugation is a process that use centrifugal force to sediment heavy particles out of the light part of the solution.

- Decantation: After a successful centrifugation, the sample will be separated into two regions. The top region is called the "supernatant" and the bottom region is called the "pellet". The supernatant contains all the light elements, such as excess organic materials and solvent, while the pellet consists of the nanoparticles, clusters and aggregations (plates). The supernatant was removed using a micro pipet. And then the process from washing solution to decantation were repeated 3-10 times, depending on the synthesis.

- Re-suspension: re-suspension should always be performed in order to keep NPs for further use, e.g. for SEM or for HP-PXRD. The clean NPs were re-suspended in appropriate volume of toluene (4 mL) or isooctane (4 mL). Sonication was applied to re-suspend the settled NPs into solution.

All washing procedures can be found in Table B.1, Table B.2, Table B.3, and Table B.4.

Table B.1: Washing procedure of aqueous bismuth synthesis approach : 3 mL of chloroform or isooctane is used to re-disperse after the washing.

Time	Solvent 1	Solvent 2	Centrifuge speed (rpm)	Centrifuge duration (minutes)
1	10 mL Ethanol	-	3750	5

Table B.2: Washing procedure of non-aqueous bismuth synthesis approach : 2 mL of toluene or isooctane is used to re-disperse after the washing.

Time	Solvent 1	Solvent 2	Centrifuge speed (rpm)	Centrifuge duration (minutes)
1	0.5 mL Toluene	20 mL Methanol	3950	20
2	5 mL Toluene	20 mL Methanol	3950	20

Table B.3: Washing procedure of high-temperature polyol-thermal decomposition bismuth synthesis approach : 2 mL of toluene is used to re-disperse after the washing.

Time	Solvent 1	Solvent 2	Centrifuge speed (rpm)	Centrifuge duration (minutes)
1	-	10 mL Methanol	3950	30
2	5 mL Toluene	10 mL Methanol	3950	30
3	5 mL Toluene	10 mL Methanol	3950	30
4	5 mL Toluene	10 mL Methanol	3950	30
5	5 mL Toluene	10 mL Methanol	3950	30

Table B.4: Washing procedure of high-temperature thermal decomposition bismuth synthesis approach (Buhro's protocol): 2mL toluene is used to re-dispersed after the washing.

Time	Solvent 1	Solvent 2	Centrifuge speed (rpm)	Centrifuge duration (minutes)
1	4 mL Toluene	16 mL Methanol	3750	30
2	3 mL Toluene	15 mL Methanol	3750	60
3	3 mL Toluene	15 mL Methanol	3750	30
4	5 mL Toluene	15 mL Methanol	3750	30

B.2 Characterisation Techniques

Synthesis using the trial and error approach is strongly recommended to establish the characterisation process during synthesis, because monitoring what happens in each step can lead us to understand the mechanism of Bi nanoparticles growth, which will benefit the further syntheses. Therefore, the intermediate or end products of all the syntheses in this study have been characterised by scanning electron microscopy (SEM) at The University of St. Andrews and by in-house x-ray diffraction at the University of Edinburgh. Both tools have contributed considerably to this study because the facilities were made available for unlimited access and supported by experts.

B.2.1 Scanning Electron Microscopy (SEM)

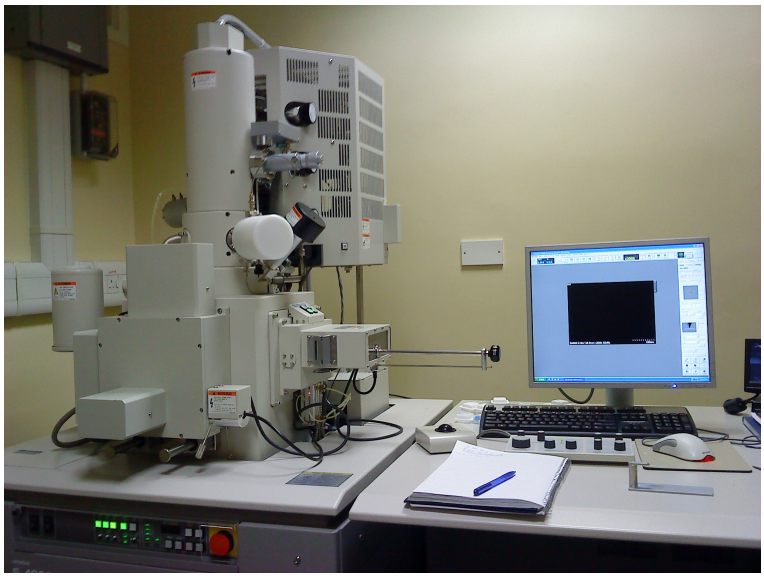

Figure B.7: Hitachi S-4800 SEM used in this thesis is located at School of Physics and Astronomy, the University of St. Andrews.

SEM is the main tool used in this study to justify whether the synthesised nanoparticles are close to ideal[3] or not. In all SEM sessions, every sample had their image captured at 0.05k, 0.1k, 0.5k, 1.2k, 5.0k, 20.0k, 50k and 100k as

[3]Ideal nanoparticles in this study are spherical and monodispersed.

standard magnifications. This will allow all the SEM images and all samples to be compared.

Size and shape determinations by SEM are usually carried out after the sample has already been washed, and the nanoparticle solution was dropped on to a Si substrate, then dried by spin coating and later put under vacuum. A sample was imaged using 0.05k, 0.1k, 0.5k, 1.2k, 5.0k, 20.0k, 50k and 100k of magnification. At 100k-200k magnification, where the edge of each nano particle in the sample could be defined, each particle in the frame has its diameter measured. Approximately 400-1000 individual particles are measured for each sample (see Fig. B.8). Size distribution histograms can be plotted which are consequently fitted by a Gaussian function. The FWHM/2 of the distribution is used to define the uncertainties of the diameter.

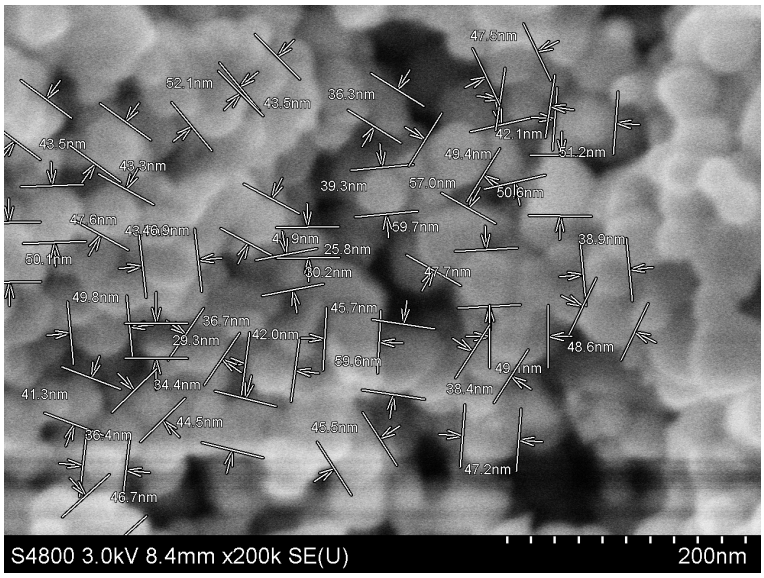

Figure B.8: SEM image showing measured nanoparticles using a measurement tool in the SEM software.

B.2.2 Transmission Electron Microscopy (TEM)

TEM has normally been used at the end of all characterisations to measure the size of the synthesised nanoparticles, because TEM can give larger magnification and better-defined edges compared to SEM. However, due to the very high cost per hour for using TEM and the free access available to SEM, TEM was not

employed as much as SEM, although TEM could have served the study with its better performance.

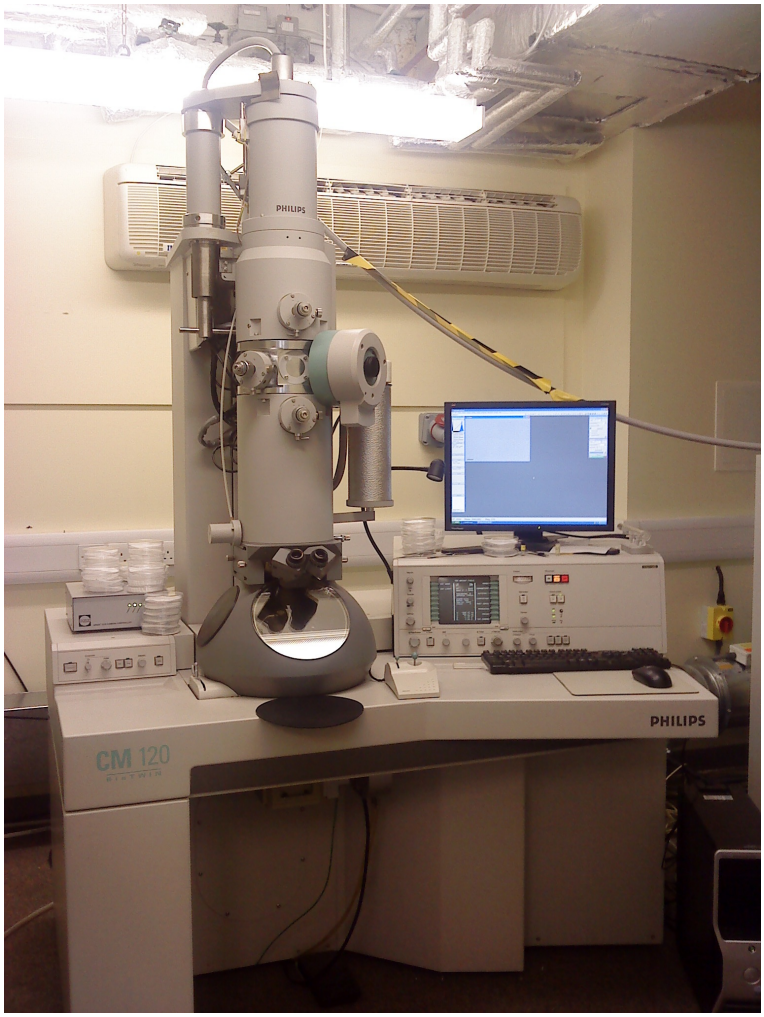

Figure B.9: Philips CM120 Transmission electron microscope (20-120 kV operating voltage) used in the study in this thesis is located at Institute of Molecular Plant Sciences, King's Building, The University of Edinburgh.

B.2.3 In-house X-Ray Diffraction (In-house XRD)

In-house XRD is conveniently accessible in the Centre for Science at Extreme Conditions (CSEC), Edinburgh, UK. The machine is a powder diffractometer consisting of a point detector, x-ray tube, and goniometer. In-house XRD has been used to determine the chemical components of the synthesised products. EVA^{TM},

the x-ray analysis software from Bruker, has been used to analyse powder x-ray diffraction pattern. This process is to ensure that only bismuth nanoparticles have been obtained (without any contamination).

If any contamination is found in a sample, as was the case in most samples, the reagent used in the synthesis recipe will also be characterised as well to identify whether the contamination exists in the unreacted substrate or not.

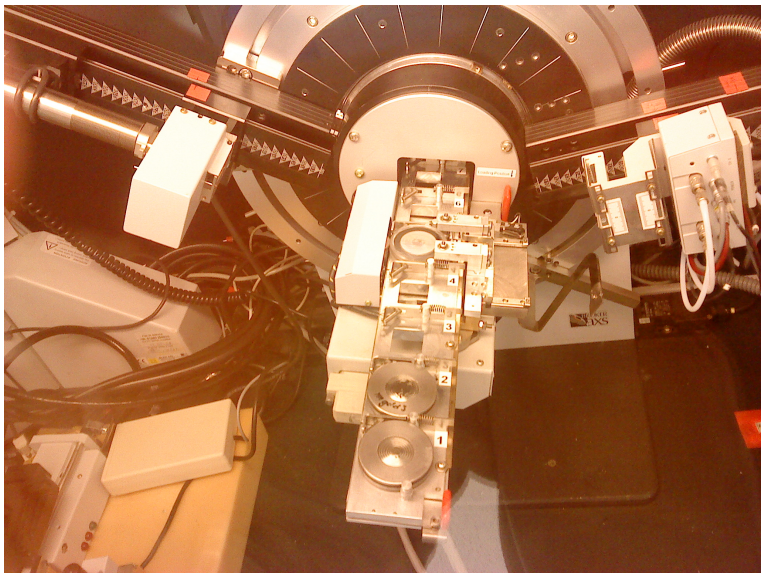

Figure B.10: The Bruker D8 X-ray diffractometer used in this thesis, located at the Centre for Science at Extreme Conditions, King's Building, The University of Edinburgh.

Appendix C

Publications

The author of this PhD thesis has contributed to two scientific publications. The papers listed below have been attached to this thesis after the bibliography.

- Chaimayo, W., Lundegaard, L. F., Loa, I., Stinton, G. W., Lennie, A. R., and McMahon, M. I. (2012). High-Pressure, high-temperature single-crystal study of Bi-IV. *High Pressure Research*, 32(3):442.

- Jimlim, P., Bovornratanaraks, T., Chaimayo, W., Pratontep, S., (2011). Effect of nano particle sizes on high pressure Raman scattering in nanocrystalline cerium dioxide. *Modern Physics Letter B*, 25(31):2399.

From the work described in this thesis, Chapter 5 could result in two chemistry publications and Chapter 6 could result in one high-pressure physics paper.

Bibliography

[Ato, 2012] Shape Software (2012). Atoms Software. www.shapesoftware.com/00_Website_Homepage

[Adams, 2012] Adams, D. M. (2012). Diacell Products, Easylab Technologies Ltd. www.easylab.co.uk

[Akahama and Kawamura, 2010] Akahama, Y. and Kawamura, H. (2010). Pressure calibration of diamond anvil Raman gauge to 410 GPa. *Journal of Physics: Conference Series*, 215:012195.

[Akahama et al., 2002] Akahama, Y., Kawamura, H., and Singh, A. K. (2002). Equation of state of bismuth to 222 GPa and comparison of gold and platinum pressure scales to 145 GPa. *Journal of Applied Physics*, 92(10):5892–5897.

[Alivisatos, 1996] Alivisatos, A. P. (1996). Perspectives on the physical chemistry of semiconductor nanocrystals. *Journal of Physical Chemistry*, 100(31):13226–13239.

[André et al., 2002] André, P., Charra, F., Chollet, P. A., and Pileni, M. P. (2002). Dipolar response of metallic copper nanocrystal islands, studied by twostep nearfield microscopy. *Advanced Materials*, 14(8):601–604.

[Andrievski and Glezer, 2001] Andrievski, R. A. and Glezer, A. M. (2001). Size effects in properties of nanomaterials. *Scripta Materialia*, 44(8-9):1621–1624.

[Anwar et al., 2003] Anwar, J., Frenkel, D., and Noro, M. G. (2003). Calculation of the melting point of NaCl by molecular simulation. *Journal of Chemical Physics*, 118(2):728–735.

[Aoki et al., 1982] Aoki, K., Fujiwara, S., and Kusakabe, M. (1982). Stability of the bcc structure of bismuth at high-pressure. *Journal of the Physical Society of Japan*, 51(12):3826–3830.

[Bandyopadhyay and Ming, 1996] Bandyopadhyay, A. and Ming, L. (1996). Pressure-induced phase transformations in amorphous selenium by x-ray diffraction and Raman spectroscopy. *Physical Review B*, 54(17):12049–12056.

[Baroli et al., 2007] Baroli, B., Ennas, M. G., Loffredo, F., Isola, M., Pinna, R., and Lopez-Quintela, M. A. (2007). Penetration of metallic nanoparticles in human full-thickness skin. *Journal of Investigative Dermatology*, 127(7):1701.

[Berkowitz and Kneller, 1969] Berkowitz, A. E. and Kneller, E. (1969). *Magnetism Metallurgy*, volume 1. Academic Press.

[Besson et al., 1992] Besson, J. M., Nelmes, R. J., Hamel, G., Loveday, J. S., Weill, G., and Hull, S. (1992). Neutron powder diffraction above 10 GPa. *Physica B: Condensed Matter*, 180:907–910.

[Boehler and Hantsetters, 2004] Boehler, R. and Hantsetters, K. D. (2004). New anvil designs in diamond-cells. *High Pressure Research*, 24(3):391–396.

[Booker and Boysen, 2005] Booker, R. D. and Boysen, E. (2005). *Nanotechnology for Dummies*. John Wiley & Sons.

[Borodko et al., 2006] Borodko, Y., Habas, S. E., Koebel, M., Yang, P., Frei, H., and Somorjai, G. A. (2006). Probing the interaction of poly (vinylpyrrolidone) with platinum nanocrystals by UV-Raman and FTIR. *Journal of Physical Chemistry B*, 110(46):23052–23059.

[Boultif and Louër, 2004] Boultif, A. and Louër, D. (2004). Powder pattern indexing with the dichotomy method. *Journal of Applied Crystallography*, 37(5):724–731.

[Bovornratanaraks et al., 2006] Bovornratanaraks, T., Allan, D. R., Belmonte, S. A., McMahon, M. I., and Nelmes, R. J. (2006). Complex monoclinic superstructure in Sr-IV. *Physical Review B*, 73(14):144112.

[Bri, 1964] Nobel Foundation (1964). Bridgman Biography. www.nobelprize.org/-nobel_prizes/physics/laureates/1946/bridgman-bio.html

[Bridgman, 1950] Bridgman, P. W. (1950). Bakerian Lecture : Physics above 20,000 kg/cm^2. *Proceedings of the Royal Society of London. Series A, Mathematical and Physical Sciences*, 203(1072):1–17.

[Bridgman, 1952] Bridgman, P. W. (1952). The resistance of 72 elements, alloys and compounds to 100,000 kg/cm^2. *Proceedings of the American Academy of Arts and Sciences*, 81(4):165–251.

[Brister, 1997] Brister, K. (1997). X-ray diffraction and absorption at extreme pressures. *Review of Scientific Instruments*, 68:1629.

[Bruchez Jr et al., 1998] Bruchez Jr, M., Moronne, M., Gin, P., Weiss, S., and Alivisatos, A. P. (1998). Semiconductor nanocrystals as fluorescent biological labels. *Science*, 281(5385):2013–2016.

[Brumlik et al., 1994] Brumlik, C., Menon, V., and Martin, C. (1994). Template synthesis of metal microtubule ensembles utilizing chemical, electrochemical, and vacuum deposition techniques. *Journal of Materials Research*, 9(05):1174–1183.

[Brust et al., 1994] Brust, M., Walker, M., Bethell, D., Schiffrin, D. J., and Whyman, R. (1994). Synthesis of thiol-derivatised gold nanoparticles in a two-phase liquid-liquid system. *Journal of the Chemical Society, Chemical Communications*, (7):801–802.

[Bundy, 2000] Bundy, F. P. (2000). The Diamond Makers. *Physics Today*, 53:58–59.

[Callister Jr, 2001] Callister Jr, W. D. (2001). *Fundamentals of Materials Science and Enegineering*. John Wiley & Sons, 5^{th} edition.

[Caracas and Gonze, 2005] Caracas, R. and Gonze, X. (2005). First-principle study of materials involved in incommensurate transitions. *Zeitschrift für Kristallographie*, 220(5-6):511–520.

[Carotenuto et al., 2009] Carotenuto, G., Hison, C. L., Capezzuto, F., Palomba, M., Perlo, P., and Conte, P. (2009). Synthesis and thermoelectric characterisation of bismuth nanoparticles. *Journal of Nanoparticle Research*, 11(7):1729–1738.

[Cason et al., 2001] Cason, J. P., Miller, M. E., Thompson, J. B., and Roberts, C. B. (2001). Solvent effects on copper nanoparticle growth behavior in AOT reverse micelle systems. *Journal of Physical Chemistry B*, 105(12):2297–2302.

[Chaimayo et al., 2012] Chaimayo, W., Lundegaard, L. F., Loa, I., Stinton, G. W., Lennie, A. R., and McMahon, M. I. (2012). High-pressure, high-temperature single-crystal study of Bi-IV. *High Pressure Research*, 32(3):442.

[Chapuis, 2010] Chapuis, G. (2010). Introduction to Aperiodic Crystals.

[Chen et al., 2002] Chen, B., Penwell, D., Benedetti, L. R., Jeanloz, R., and Kruger, M. B. (2002). Particle-size effect on the compressibility of nanocrystalline alumina. *Physical Review B*, 66(14):144101.

[Chen, 1997] Chen, C. (1997). Size dependence of structural metastability in semiconductor nanocrystals. *Science*, 276(5311):398–401.

[Chen, 2011] Chen, S. (2011). *FePt Nanoparticles Synthesis and Biomedical Application*. PhD thesis, School of Physics and Astronomy, North Haugh, St. Andrews, KY16 9SS, Scotland.

[Chen et al., 2008] Chen, Z., Sun, C. Q., Zhou, Y., and Ouyang, G. (2008). Size dependence of the pressure-induced phase transition in nanocrystals. *Journal of Physical Chemistry C*, 112(7):2423–2427.

[Chen and Derking, 1993] Chen, Z. X. and Derking, A. (1993). TiO_2 thin films by chemical vapour deposition: control of the deposition process and film characterisation. *Journal of Materials Chemistry*, 3(11):1137–1140.

[Cheng et al., 2009] Cheng, G., Wu, J., Xiao, F., Yu, H., Lu, Z., Yu, X., and Chen, R. (2009). Synthesis of bismuth micro-and nanospheres by a simple refluxing method. *Materials Letters*, 63(26):2239–2242.

[Chirea et al., 2009] Chirea, M., Cruz, A., Pereira, C. M., and Silva, A. F. (2009). Size-dependent electrochemical properties of gold nanorods. *Journal of Physical Chemistry C*, 113(30):13077–13087.

[Chouinard and Desgreniers, 2000] Chouinard, C. and Desgreniers, S. (2000). Bi_2O_3 under hydrostatic pressure: observation of a pressure-induced amorphization. *Solid State Communications*, 113(3):125–129.

[Clark et al., 2005] Clark, S. M., Prilliman, S. G., Erdonmez, C. K., and Alivisatos, A. P. (2005). Size dependence of the pressure-induced gamma to alpha structural phase transition in iron oxide nanocrystals. *Nanotechnology*, 16(12):2813–2818.

[Crespo et al., 2004] Crespo, P., Litrán, R., Rojas, T., Multigner, M., Fuente, J. D. L., Sánchez-López, J., García, M., Hernando, A., Penadés, S., and Fernández, A. (2004). Permanent magnetism, magnetic anisotropy, and hysteresis of thiol-capped gold nanoparticles. *Physical Review Letters*, 93(8):087204.

[Dai et al., 2011] Dai, R. C., Luo, L. B., Zhang, Z. M., and Ding, Z. J. (2011). Raman studies of selenium nanowires under high pressure. *Materials Research Bulletin*, 46(3):350–354.

[Datchi et al., 2009] Datchi, F., Giordano, V. M., Munsch, P., and Saitta, A. M. (2009). Structure of carbon dioxide phase IV: breakdown of the intermediate bonding state scenario. *Physical Review Letters*, 103(18):185701.

[Degtyareva, 2003] Degtyareva, O. (2003). *X-ray diffraction studies of complex high-pressure phases of Bi, Sb, and Ga*. PhD thesis, School of Physics and Astronomy, Centre for Science at Extreme Conditions (CSEC), King's Building, Mayfield Road, University of Edinburgh, EH9 3JZ.

[Degtyareva et al., 2001] Degtyareva, O., McMahon, M. I., and Nelmes, R. J. (2001). Crystal structure of the high pressure phase of Bismuth Bi-III. *Materials Science Forum*, 378-3:469–474.

[Degtyareva et al., 2004] Degtyareva, O., McMahon, M. I., and Nelmes, R. J. (2004). High-pressure structural studies of group-15 elements. *High Pressure Research*, 24(3):319–356.

[Demortiere et al., 2011] Demortiere, A., Panissod, P., Pichon, B. P., Pourroy, G., Guillon, D., Donnio, B., and Begin-Colin, S. (2011). Size-dependent properties of magnetic iron oxide nanocrystals. *Nanoscale*, 3(1):225–232.

[Deng et al., 2008] Deng, Z., Bao, Z., Cao, L., Chen, D., Tang, F., Wang, F., Liu, C., Zou, B., and Muscat, A. J. (2008). Spherical hexagonal tellurium nanocrystals: Fabrication and size-dependent structural phase transition at high pressure. *Nanotechnology*, 19(4):045707.

[Desgreniers and Lagarec, 1998] Desgreniers, S. and Lagarec, K. (1998). XRDA 3.1 - a program for x-ray diffraction analysis on a PC. *Journal of Applied Crystallography*, 31(1):109–110.

[Dick et al., 2002] Dick, K., Dhanasekaran, T., Zhang, Z. Y., and Meisel, D. (2002). Size-dependent melting of silica-encapsulated gold nanoparticles. *Journal of the American Chemical Society*, 124(10):2312–2317.

[Diemente, 1997] Diemente, D. (1997). Why is bismuth subchloride soluble in acid? *Journal of Chemical Education*, 74(4):398.

[Eastoe et al., 1996] Eastoe, J., Stebbing, S., Dalton, J., and Heenan, R. K. (1996). Preparation of colloidal cobalt using reversed micelles. *Colloids and Surfaces A: Physicochemical and Engineering Aspects*, 119(2-3):123–131.

[Eastoe et al., 1994] Eastoe, J., Steytler, D. C., Robinson, B. H., Heenan, R. K., North, A. N., and Dore, J. C. (1994). Structure of cobalt aerosol-OT reversed micelles studied by small-angle scattering methods. *Journal of the Chemical Society, Faraday Transactions*, 90(17):2497–2504.

[Eremets, 1996] Eremets, M. I. (1996). *High Pressure Experimental Methods*. Oxford University Press.

[Evans et al., 2009] Evans, S. R., Loa, I., Lundegaard, L. F., and McMahon, M. I. (2009). Phase transitions in praseodymium up to 23 GPa: An x-ray powder diffraction study. *Physical Review B*, 80(13):134105.

[Fanfair and Korgel, 2005] Fanfair, D. D. and Korgel, B. A. (2005). Bismuth nanocrystal-seeded III-V semiconductor nanowire synthesis. *Crystal Growth & Design*, 5(5):1971–1976.

[Feynman, 1992] Feynman, R. P. (1992). There's plenty of room at the bottom (reprinted). *Journal of Microelectromechanical Systems*, 1(1):60 –66.

[Fujihisa et al., 2006] Fujihisa, H., Akahama, Y., Kawamura, H., Ohishi, Y., Shimomura, O., Yamawaki, H., Sakashita, M., Gotoh, Y., Takeya, S., and Honda, K. (2006). O_8 cluster structure of the epsilon phase of solid oxygen. *Physical Review Letters*, 97(8):085503.

[Goldstein et al., 1992] Goldstein, A. N., Echer, C. M., and Alivisatos, A. P. (1992). Melting in semiconductor nanocrystals. *Science*, 256(5062):1425–1427.

[Goncharenko, 2005] Goncharenko, I. N. (2005). Evidence for a magnetic collapse in the epsilon phase of solid oxygen. *Physical Review Letters*, 94(20):205701.

[Grebinski et al., 2004] Grebinski, J. W., Richter, K. L., Zhang, J., Kosel, T. H., and Kuno, M. (2004). Synthesis and characterization of Au/Bi core/shell nanocrystals: A precursor toward II-VI nanowires. *Journal of Physical Chemistry B*, 108(28):9745–9751.

[Grüenwald and Dellago, 2009] Grüenwald, M. and Dellago, C. (2009). Nucleation and growth in structural transformations of nanocrystals. *Nano Letters*, 9(5):2099–2102.

[Gu et al., 2008] Gu, Q. F., Krauss, G., Steurer, W., Gramm, F., and Cervellino, A. (2008). Unexpected high stiffness of Ag and Au nanoparticles. *Physical Review Letters*, 100(4):045502.

[Guillaume et al., 2011] Guillaume, C. L., Gregoryanz, E., Degtyareva, O., McMahon, M. I., Hanfland, M., Evans, S., Guthrie, M., Sinogeikin, S. V., and Mao, H. K. (2011). Cold melting and solid structures of dense lithium. *Nature Physics*, 7(3):211–214.

[Guo et al., 2008] Guo, Q., Zhao, Y., Wang, Z., Skrabalak, S. E., Lin, Z., and Xia, Y. (2008). Size dependence of cubic to trigonal structural distortion in silver micro- and nanocrystals under high pressure. *Journal of Physical Chemistry C*, 112(51):20135–20137.

[Gupta and Rana, 2012] Gupta, D. C. and Rana, P. (2012). Study of semiconducting nanomaterials under pressure. *Journal of Molecular Modeling*, 18(7):3341–3350.

[Haase and Alivisatos, 1992] Haase, M. and Alivisatos, A. P. (1992). Arrested solid-solid phase transition in 4-nm-diameter cadmium sulfide nanocrystals. *Journal of Physical Chemistry*, 96(16):6756–6762.

[Hall, 1960] Hall, H. T. (1960). Ultrahighpressure, hightemperature apparatus: the"belt". *Review of Scientific Instruments*, 31(2):125–131.

[Hammersley et al., 1996] Hammersley, A. P., Svensson, S. O., Hanfland, M., Fitch, A. N., and Hausermann, D. (1996). Two-dimensional detector software: From real detector to idealised image or two-theta scan. *High Pressure Research*, 14:235–248.

[He et al., 2005] He, Y., Liu, J. F., Chen, W., Wang, Y., Wang, H., Zeng, Y. W., Zhang, G. Q., Wang, L. N., Liu, J., Hu, T. D., Hahn, H., Gleiter, H., and Jiang, J. Z. (2005). High-pressure behavior of SnO_2 nanocrystals. *Physical Review B*, 72(21):212102.

[Heinz and Jeanloz, 1984] Heinz, D. L. and Jeanloz, R. (1984). The equation of state of the gold calibration standard. *Journal of Applied Physics*, 55(4):885–893.

[Hejny et al., 2006] Hejny, C., Falconi, S., Lundegaard, L. F., and McMahon, M. I. (2006). Phase transitions in tellurium at high pressure and temperature. *Physical Review B*, 74(17):174119.

[Hejny and McMahon, 2003] Hejny, C. and McMahon, M. I. (2003). Large structural modulations in incommensurate Te-III and Se-IV. *Physical Review Letters*, 91(21):215502.

[Hiramatsu and Osterloh, 2004] Hiramatsu, H. and Osterloh, F. E. (2004). A simple large-scale synthesis of nearly monodisperse gold and silver nanoparticles with adjustable sizes and with exchangeable surfactants. *Chemistry of Materials*, 16(13):2509–2511.

[Holland and Redfern, 1997] Holland, T. J. B. and Redfern, S. A. T. (1997). Unit cell refinement from powder diffraction data; the use of regression diagnostics. *Mineralogical Magazine*, 61(1):65–77.

[Holzapfel, 2005] Holzapfel, W. B. (2005). Progress in the realization of a practical pressure scale for the range 1-300 GPa. *High Pressure Research*, 25(3):227–227.

[Husband et al., 2012] Husband, R. J., Loa, I., Stinton, G. W., Evans, S. R., Ackland, G. J., and McMahon, M. I. (2012). Europium-IV: An incommensurately-modulated crystal structure in the lanthanides. *Physical Review Letters (Accepted)*.

[Ichiyanagi and Yamada, 2005] Ichiyanagi, Y. and Yamada, S. (2005). The size-dependent magnetic properties of Co_3O_4 nanoparticles. *Polyhedron*, 24(16-17):2813–2816.

[IUCr, 1992] IUCr (1992). Report of the executive committee for 1991. *Acta Crystallographica Section A*, 48(6):922–946.

[Jackson and Mckenna, 1990] Jackson, C. L. and Mckenna, G. B. (1990). The melting behavior of organic materials confined in porous solids. *Journal of Chemical Physics*, 93(12):9002–9011.

[Jacobs et al., 2001] Jacobs, K., Zaziski, D., Scher, E. C., Herhold, A. B., and Alivisatos, A. P. (2001). Activation volumes for solid-solid transformations in nanocrystals. *Science*, 293(5536):1803–1806.

[Jamieson et al., 1959] Jamieson, J. C., Lawson, A. W., and Nachtrieb, N. D. (1959). New device for obtaining xray diffraction patterns from substances exposed to high pressure. *Review of Scientific Instruments*, 30(11):1016–1019.

[Janssen et al., 2007] Janssen, T., Chapuis, G., and Boissieu, M. D. (2007). *Aperiodic Crystals: From Modulated Phases to Quasicrystals*. ISBN: 0198567774. Oxford University Press.

[Jiang et al., 2001a] Jiang, J., Olsen, J. S., and Gerward, L. (2001a). Grain-size and alloying effects on the pressure-induced bcc-to-hcp transition in nanocrystalline iron. *Materials Transactions*, 42(8):1571–1574.

[Jiang et al., 1999a] Jiang, J. Z., Gerward, L., Frost, D., Secco, R., Peyronneau, J., and Olsen, J. S. (1999a). Grain-size effect on pressure-induced semiconductor-to-metal transition in ZnS. *Journal of Applied Physics*, 86(11):6608–6610.

[Jiang et al., 2001b] Jiang, J. Z., Gerward, L., and Olsen, J. S. (2001b). Pressure induced phase transformation in nanocrystal SnO_2. *Scripta Materialia*, 44(8-9):1983–1986.

[Jiang et al., 2000a] Jiang, J. Z., Gerward, L., Secco, R., Frost, D., Olsen, J. S., and Truckenbrodt, J. (2000a). Phase transformation and conductivity in nanocrystal PbS under pressure. *Journal of Applied Physics*, 87:2658.

[Jiang et al., 2000b] Jiang, J. Z., Olsen, J. S., Gerward, L., Frost, D., Rubie, D., and Peyronneau, J. (2000b). Structural stability in nanocrystalline ZnO. *Europhysics Letters*, 50:48.

[Jiang et al., 1999b] Jiang, Q., Shi, H. X., and Zhao, M. (1999b). Melting thermodynamics of organic nanocrystals. *Journal of Chemical Physics*, 111(5):2176.

[Katrusiak, 2007] Katrusiak, A. (2007). High-pressure crystallography. *Acta Crystallographica Section A*, 64(1):135–148.

[Khachadorian et al., 2011] Khachadorian, S., Papagelis, K., Scheel, H., Colli, A., Ferrari, A. C., and Thomsen, C. (2011). High pressure Raman scattering of silicon nanowires. *Nanotechnology*, 22:195707.

[Khanna and Linderoth, 1991] Khanna, S. N. and Linderoth, S. (1991). Magnetic behavior of clusters of ferromagnetic transition metals. *Physical Review Letters*, 67(6):742–745.

[Kiang, 2000] Kiang, C. H. (2000). Electron irradiation induced dimensional change in bismuth filled carbon nanotubes. *Carbon*, 38(11-12):1699–1701.

[Kittel, 2004] Kittel, C. (2004). *Introduction to Solid State Physics*. John Wiley & Sons, 8^{th} edition.

[Klotz et al., 2009] Klotz, S., Chervin, J. C., Munsch, P., and Marchand, G. L. (2009). Hydrostatic limits of 11 pressure transmitting media. *Journal of Physics D: Applied Physics*, 42(7):075413.

[Klotz et al., 2010] Klotz, S., Strässle, T., Cornelius, A. L., Philippe, J., and Hansen, T. (2010). Magnetic ordering in solid oxygen up to room temperature. *Physical Review Letters*, 104(11):115501.

[Koch, 1993] Koch, C. C. (1993). The synthesis and structure of nanocrystalline materials produced by mechanical attrition: A review. *Nanostructured Materials*, 2(2):109–129.

[Krahne et al., 2011] Krahne, R., Morello, G., Figuerola, A., George, C., Deka, S., and Manna, L. (2011). Physical properties of elongated inorganic nanoparticles. *Physics Reports*, 501(3-5):75–221.

[Kroto et al., 1985] Kroto, H. W., Heath, J. R., O'Brien, S. C., Curl, R. F., and Smalley, R. E. (1985). C_{60}: Buckminsterfullerene. *Nature*, 318(6042):162–163.

[Krstic et al., 2007] Krstic, V., Rikken, G. L. J. A., Kaempgen, M., Roth, S., and Beukes, J. A. (2007). Tellurium nanocylinders under pressure: Effects of the geometry of nanostructures. *Advanced Materials*, 19(8):1101–1104.

[Kumar et al., 2007] Kumar, R. S., Cornelius, A. L., and Nicol, M. F. (2007). Structure of nanocrystalline ZnO up to 85GPa. *Current Applied Physics*, 7(2):135–138.

[LeBail, 1992] LeBail, A. (1992). Extracting structure factors from powder diffraction data by iterating full pattern profile fitting. In Prince, E. and Stalick, J. K., editors, *Accuracy in Powder Diffraction II, Special Publication (NIST)*, 846:213.

[Lee et al., 2008] Lee, C., Wei, X., Kysar, J. W., and Hone, J. (2008). Measurement of the elastic properties and intrinsic strength of monolayer graphene. *Science*, 321(5887):385–388.

[Leff et al., 1996] Leff, D. V., Brandt, L., and Heath, J. R. (1996). Synthesis and characterization of hydrophobic, organically-soluble gold nanocrystals functionalized with primary amines. *Langmuir*, 12(20):4723–4730.

[Legrand et al., 2000] Legrand, J., Petit, C., Bazin, D., and Pileni, M. P. (2000). Collective effect on magnetic properties of 2D superlattices of nanosized cobalt particles. *Applied Surface Science*, 164(1-4):186–192.

[Lesar, 1979] Lesar, R. (1979). Raman spectroscopy of solid nitrogen up to 374 kbar. *Solid State Communications*, 32(2):131–134.

[Li et al., 2001] Li, Y. B., Xie, S. S., Zou, X. P., Tang, D. S., Liu, Z. Q., Zhou, W. Y., and Wang, G. (2001). Large-scale synthesis of beta-SiC nanorods in the arc-discharge. *Journal of Crystal Growth*, 223(1):125–128.

[Lide, 2008] Lide, D. (2008). *Handbook of Physics and Chemistry*, volume 76. CRC Press, Boca Raton, USA

[Liebermann, 2011] Liebermann, R. C. (2011). Multi-anvil, high pressure apparatus: a half-century of development and progress. *High Pressure Research*, 31(4):493–532.

[Liu et al., 2007] Liu, J. F., He, Y., Chen, W., Zhang, G. Q., Zeng, Y. W., Kikegawa, T., and Jiang, J. Z. (2007). Bulk modulus and structural phase transitions of wurtzite CoO nanocrystals. *Journal of Physical Chemistry C*, 111(1):2–5.

[Liu et al., 2006] Liu, J. F., Yin, S., Wu, H. P., Zeng, Y. W., Hu, X. R., Wang, Y. W., Lv, G. L., and Jiang, J. Z. (2006). Wurtzite-to-rocksalt structural transformation in nanocrystalline CoO. *Journal of Physical Chemistry B*, 110(43):21588–21592.

[Lobban et al., 1998] Lobban, C., Finney, J. L., and Kuhs, W. F. (1998). The structure of a new phase of ice. *Nature*, 391(6664):268–270.

[Lövestam et al., 2010] Lövestam, G., Rauscher, H., Roebben, G., Klüttgen, B. S., Gibson, N., Putaud, J. P., and Stamm, H. (2010). Considerations on a definition of nanomaterial for regulatory purposes. *JRC Reference Report*, 24403:202010–1.

[Lundegaard, 2008] Lundegaard, L. F. (2008). *High-pressure diffraction studies of rubidium phase IV*. PhD thesis, King's Building, Mayfield Road, University of Edinburgh, EH9 3JZ.

[Lundegaard et al., 2006] Lundegaard, L. F., Weck, G., McMahon, M. I., Desgreniers, S., and Loubeyre, P. (2006). Observation of an O-8 molecular lattice in the epsilon phase of solid oxygen. *Nature*, 443(7108):201–204.

[Ma et al., 2010] Ma, D., Zhao, J., Li, Y., Su, X., Hou, S., Zhao, Y., Hao, X., and Li, L. (2010). Organic molecule directed synthesis of bismuth nanostructures with varied shapes in aqueous solution and their optical characterization. *Colloids and Surfaces A: Physicochemical and Engineering Aspects*, 368:105–111.

[Mao and Bell, 1978] Mao, H. K. and Bell, P. M. (1978). High-pressure physics: sustained static generation of 1.36 to 1.72 megabars. *Science*, 200(4346):1145–1147.

[Mao et al., 1988] Mao, H. K., Hemley, R. J., Wu, Y., Jephcoat, A. P., Finger, L. W., Zha, C. S., and Bassett, W. A. (1988). High-pressure phase diagram and equation of state of solid helium from single-crystal x-ray diffraction to 23.3 GPa. *Physical Review Letters*, 60(25):2649–2652.

[Mao et al., 1986] Mao, H. K., Xu, J., and Bell, P. M. (1986). Calibration of the ruby pressure gauge to 800 kbar under quasi-hydrostatic conditions. *Journal of Geophysical Research*, 91(B5):4673–4676.

[Martin, 1994] Martin, C. R. (1994). Nanomaterials: A membrane-based synthetic approach. *Science*, 266(5193):1961–1966.

[Martin et al., 1994] Martin, T. P., Naher, U., Schaber, H., and Zimmermann, U. (1994). Evidence for a size dependent melting of sodium clusters. *Journal of Chemical Physics*, 100(3):2322–2324.

[Matkasymova et al., 2009] Matkasymova, A., Omurzak, E., and Sulaimankulova, S. (2009). Nanorods of metallic bismuth and antimony by the impulse plasma in liquid. *Journal of Cluster Science*, 20(1):153–158.

[McMahon, 2011] McMahon, M. I. (2011). High-pressure crystallography. *Topics in Current Chemistry*, 315:69–110.

[McMahon et al., 2003] McMahon, M. I., Degtyareva, O., Hejny, C., and Nelmes, R. J. (2003). New results on old problems: The use of single-crystals in high-pressure structural studies. *High Pressure Research*, 23(3):289–299.

[McMahon et al., 2000] McMahon, M. I., Degtyareva, O., and Nelmes, R. J. (2000). Ba-IV-type incommensurate crystal structure in group-V metals. *Physical Review Letters*, 85(23):4896–4899.

[McMahon et al., 2007] McMahon, M. I., Degtyareva, O., and Nelmes, R. J. (2007). Incommensurate modulations of Bi-III and Sb-II. *Physical Review B*, 75(18):184114.

[McMahon et al., 2004] McMahon, M. I., Hejny, C., Loveday, J. S., Lundegaard, L. F., and Hanfland, M. (2004). Confirmation of the incommensurate nature of Se-IV at pressures below 70 GPa. *Physical Review B*, 70(5):054101.

[McMahon and Nelmes, 2006] McMahon, M. I. and Nelmes, R. J. (2006). High-pressure structures and phase transformations in elemental metals. *Chemical Society Reviews*, 35(10):943–963.

[McMahon et al., 2006] McMahon, M. I., Nelmes, R. J., Schwarz, U., and Syassen, K. (2006). Composite incommensurate K-III and a commensurate form: Study of a high-pressure phase of potassium. *Physical Review B*, 74(14):140102.

[McMahon et al., 2001] McMahon, M. I., Rekhi, S., and Nelmes, R. J. (2001). Pressure dependent incommensuration in Rb-IV. *Physical Review Letters*, 87(5):055501.

[Merrill and Bassett, 1974] Merrill, L. and Bassett, W. A. (1974). Miniature diamond anvil pressure cell for single crystal xray diffraction studies. *Review of Scientific Instruments*, 45(2):290–294.

[Mezouar, 2010] Mezouar, M. (2010). Synchrotron high-pressure high-temperature techniques. *High-Pressure Crystallography from Fundamental Phenomena to Technological Application*, NATO Science for Peace and Security Series B-Physics and Biophysics:23–33. 41^{st} Course of the International School of Crystallography.

[Ming et al., 1983] Ming, L. C., Manghnani, M. H., Balogh, J., Qadri, S. B., Skelton, E. F., and Jamieson, J. C. (1983). Gold as a reliable internal pressure calibrant at high temperatures. *Journal of Applied Physics*, 54(8):4390–4397.

[Mirebeau, 2007] Mirebeau, I. (2007). Magnetic neutron diffraction under high pressure. *Comptes Rendus Physique*, 8(7-8):737–744.

[Moggach et al., 2008] Moggach, S. A., Allan, D. R., Parsons, S., and Warren, J. E. (2008). Incorporation of a new design of backing seat and anvil in a Merrill-Bassett diamond anvil cell. *Journal of Applied Crystallography*, 41(2):249–251.

[Nanda, 2009] Nanda, K. K. (2009). Size-dependent melting of nanoparticles: Hundred years of thermodynamic model. *Pramana*, 72(4):617–628.

[Narygina et al., 2011] Narygina, O., Mcbride, E., Stinton, G., and McMahon, M. (2011). Melting curve of potassium to 22 GPa. *Physical Review B*, 84(5):054111.

[Nelmes et al., 1999] Nelmes, R. J., Allan, D. R., McMahon, M. I., and Belmonte, S. A. (1999). Self-hosting incommensurate structure of barium IV. *Physical Review Letters*, 83(20):4081–4084.

[Nelmes et al., 1993] Nelmes, R. J., McMahon, M. I., Hatton, P. D., Crain, J., and Piltz, R. O. (1993). Phase-transition in InSb at presssure up to 5 GPa. *Physical Review B*, 47(1):35–54.

[Novoselov et al., 2004] Novoselov, K. S., Geim, A. K., Morozov, S. V., Jiang, D., Zhang, Y., Dubonos, S. V., Grigorieva, I. V., and Firsov, A. A. (2004). Electric field effect in atomically thin carbon films. *Science*, 306(5696):666–669.

[Olsen et al., 1999] Olsen, J. S., Gerward, L., and Jiang, J. Z. (1999). On the rutile/alpha-PbO_2-type phase boundary of TiO_2. *Journal of Physics and Chemistry of Solids*, 60(2):229–233.

[Ould-Ely et al., 2005] Ould-Ely, T., Thurston, J. H., Kumar, A., Respaud, M., Guo, W., Weidenthaler, C., and Whitmire, K. H. (2005). Wet-chemistry synthesis of nickel-bismuth bimetallic nanoparticles and nanowires. *Chemistry of Materials*, 17(18):4750–4754.

[Palosz et al., 2004] Palosz, B., Stel'makh, S., Grzanka, E., Gierlotka, S., Pielaszek, R., Bismayer, U., Werner, S., and Palosz, W. (2004). High pressure x-ray diffraction studies on nanocrystalline materials. *Journal of Physics: Condensed Matter*, 16(5):S353–S377.

[Park et al., 2007] Park, T. J., Papaefthymiou, G. C., Viescas, A. J., Moodenbaugh, A. R., and Wong, S. S. (2007). Size-dependent magnetic properties of single-crystalline multiferroic $BiFeO_3$ nanoparticles. *Nano Letters*, 7(3):766–772.

[Patterson, 1939] Patterson, A. (1939). The Scherrer formula for x-ray particle size determination. *Physical Review*, 56(10):978–982.

[Petricek et al., 2006] Petricek, V., Dusek, M., and Palatinus, L. (2006). The crystallographic computing system. *JANA2006*, Institute of Physics, Praha, Czech Republic.

[Piermarini et al., 1973] Piermarini, G. J., Block, S., and Barnett, J. D. (1973). Hydrostatic limits in liquids and solids to 100 kbar. *Journal of Applied Physics*, 44(12):5377.

[Pong et al., 2007] Pong, B. K., Elim, H. I., Chong, J. X., Ji, W., Trout, B. L., and Lee, J. Y. (2007). New insights on the nanoparticle growth mechanism in the citrate reduction of Gold (III) salt: Formation of the Au nanowire intermediate and its nonlinear optical properties. *Journal of Physical Chemistry C*, 111(17):6281–6287.

[Proctor et al., 2009] Proctor, J., Gregoryanz, E., Novoselov, K., Lotya, M., Coleman, J., and Halsall, M. (2009). High-pressure Raman spectroscopy of graphene. *Physical Review B*, 80(7):073408.

[Qadri et al., 1996] Qadri, S. B., Yang, J., Ratna, B. R., Skelton, E. F., and Hu, J. Z. (1996). Pressure induced structural transitions in nanometer size particles of PbS. *Applied Physics Letters*, 69(15):2205–2207.

[Rao et al., 1992] Rao, C. N., Vijayakrishnan, V., Santra, A. K., and Prins, M. W. J. (1992). Dependence of the reactivity of Ag and Ni clusters deposited on solid substrates on the cluster size. *Angewandte Chemie International Edition*, 31(8):1062–1064.

[Rekhi et al., 2001] Rekhi, S., Saxena, S., Ahuja, R., Johansson, B., and Hu, J. (2001). Experimental and theoretical investigations on the compressibility of nanocrystalline nickel. *Journal of Materials Science*, 36(19):4719–4721.

[Reppert et al., 2007] Reppert, J., Rao, R., Skove, M., He, J., Craps, M., Tritt, T., and Rao, A. M. (2007). Laser-assisted synthesis and optical properties of bismuth nanorods. *Chemical Physics Letters*, 442(4-6):334–338.

[Richards et al., 2010] Richards, V. N., Shields, S. P., and Buhro, W. E. (2010). Nucleation control in the aggregative growth of bismuth nanocrystals. *Chemistry of Materials*, 23(2):137–144.

[Roduner, 2006] Roduner, E. (2006). Size matters: why nanomaterials are different. *Chemical Society Reviews*, 35(7):583–592.

[Rong et al., 2006] Rong, C., Li, D., Nandwana, V., Poudyal, N., Ding, Y., Wang, Z. L., Zeng, H., and Liu, J. P. (2006). Size-dependent chemical and magnetic ordering in L1(0)-FePt nanoparticles. *Advanced Materials*, 18(22):2984–2988.

[San-Miguel, 2006] San-Miguel, A. (2006). Nanomaterials under high-pressure. *Chemical Society Reviews*, 35(10):876–889.

[Sanchez et al., 2000] Sanchez, C., Ribot, F., Rozes, L., and Alonso, B. (2000). Design of hybrid organic-inorganic nanocomposites synthesized via sol-gel chemistry. *Molecular Crystals and Liquid Crystals*, 354(1):143–158.

[Sanloup et al., 2008] Sanloup, C., Gregoryanz, E., Degtyareva, O., and Hanfland, M. (2008). Structural transition in compressed amorphous sulfur. *Physical Review Letters*, 100(7):75701.

[Schedin et al., 2007] Schedin, F., Geim, A. K., Morozov, S. V., Hill, E. W., Blake, P., Katsnelson, M. I., and Novoselov, K. S. (2007). Detection of individual gas molecules adsorbed on graphene. *Nature Materials*, 6(9):652.

[Shimizu et al., 1998] Shimizu, K., Suhara, K., Ikumo, M., Eremets, M. I., and Amaya, K. (1998). Superconductivity in oxygen. *Nature*, 393(6687):767–769.

[Shukla et al., 2003] Shukla, N., Liu, C., Jones, P. M., and Weller, D. (2003). FTIR study of surfactant bonding to FePt nanoparticles. *Journal of Magnetism and Magnetic Materials*, 266(1):178–184.

[Sitec, 2012] Sitec (2012). SITEC-Sieber Engineering AG, Aschbach 7 CH-8124 Maur / Zurich, Switzerland. www.sitec-hp.ch

[Soltanzadeh and Morsali, 2010] Soltanzadeh, N. and Morsali, A. (2010). Sonochemical synthesis of a new nano-structures bismuth(III) supramolecular compound: New precursor for the preparation of bismuth(III) oxide nano-rods and bismuth(III) iodide nano-wires. *Ultrasonics Sonochemistry*, 17(1):139–144.

[Son et al., 2010] Son, J. S., Park, K., Han, M. K., Kang, C., Park, S.-G., Kim, J.-H., Kim, W., Kim, S.-J., and Hyeon, T. (2010). Large-scale synthesis and characterization of the size-dependent thermoelectric properties of uniformly sized bismuth nanocrystals. *Angewandte Chemie International Edition*, 50(6):1363–1366.

[Stoller et al., 2008] Stoller, M. D., Park, S., Zhu, Y., An, J., and Ruoff, R. S. (2008). Graphene-based ultracapacitors. *Nano Letters*, 8(10):3498–3502.

[Stubenrauch et al., 2008] Stubenrauch, C., Wielpütz, T., Sottmann, T., Roychowdhury, C., and Disalvo, F. J. (2008). Microemulsions as templates for the synthesis of metallic nanoparticles. *Colloids and Surfaces A: Physicochemical and Engineering Aspects*, 317(1-3):328–338.

[Sun et al., 2011] Sun, Y., Yang, W., Ren, Y., Wang, L., and Lei, C. (2011). Multiple-step phase transformation in silver nanoplates under high pressure. *Small*, 7(5):606–611.

[Švancara et al., 2010] Švancara, I., Prior, C., Hočevar, S. B., and Wang, J. (2010). A decade with bismuthbased electrodes in electroanalysis. *Electroanalysis*, 22(13):1405–1420.

[Syassen and Holzapfel, 1978] Syassen, K. and Holzapfel, W. B. (1978). Isothermal compression of Al and Ag to 120 kbar. *Journal of Applied Physics*, 49(8):4427–4430.

[Takemura, 2001] Takemura, K. (2001). Evaluation of the hydrostaticity of a helium-pressure medium with powder x-ray diffraction techniques. *Journal of Applied Physics*, 89(1):662.

[Talapin et al., 2002] Talapin, D. V., Rogach, A. L., Mekis, I., Haubold, S., Kornowski, A., Haase, M., and Weller, H. (2002). Synthesis and surface modification of amino-stabilized CdSe, CdTe and InP nanocrystals. *Colloids and Surfaces A: Physicochemical and Engineering Aspects*, 202(2-3):145–154.

[Taneja et al., 2002] Taneja, P., Ayyub, P., and Chandra, R. (2002). Size dependence of the optical spectrum in nanocrystalline silver. *Physical Review B*, 65(24):245412.

[Tharamani et al., 2008] Tharamani, C. N., Thejaswini, H. C., and Sampath, S. (2008). Synthesis of size-controlled Bi particles by electrochemical deposition. *Bulletin of Materials Science*, 31(3):207–212.

[Tolbert and Alivisatos, 1994] Tolbert, S. and Alivisatos, A. P. (1994). Size dependence of a first order solid-solid phase transition: The wurtzite to rock salt transformation in CdSe nanocrystals. *Science*, 265(5170):373–376.

[Tolbert and Alivisatos, 1995a] Tolbert, S. and Alivisatos, A. P. (1995a). High-pressure structural transformations in semiconductor nanocrystals. *Annual Review of Physical Chemistry*, 46(1):595–626.

[Tolbert and Alivisatos, 1995b] Tolbert, S. and Alivisatos, A. P. (1995b). The wurtzite to rock salt structural transformation in CdSe nanocrystals under high pressure. *Journal of Chemical Physics*, 102(11):4642–4656.

[Tolbert et al., 1996] Tolbert, S., Herhold, A. B., Brus, L. E., and Alivisatos, A. P. (1996). Pressure-induced structural transformations in Si nanocrystals: Surface and shape effects. *Physical Review Letters*, 76(23):4384–4387.

[Tonkov and Ponyatovsky, 2004] Tonkov, E. Y. and Ponyatovsky, E. G. (2004). *Phase Transformations of Elements Under High Pressure*. CRC Press, 1^{st} edition.

[Valden et al., 1998] Valden, M., Pak, S., Lai, X., and Goodman, D. W. (1998). Structure sensitivity of CO oxidation over model Au/TiO_2 catalysts. *Catalysis Letters*, 56(1):7–10.

[Valkenburg, 1962] Valkenburg, A. V. (1962). Visual observations of high pressure transitions. *Review of Scientific Instruments*, 33(12):1462–&.

[Wang and Buhro, 2010] Wang, F. and Buhro, W. E. (2010). An easy shortcut synthesis of size-controlled bismuth nanoparticles and their use in the SLS growth of high-quality colloidal cadmium selenide quantum wires. *Small*, 6(4):573–581.

[Wang et al., 2008] Wang, F., Tang, R., Yu, H., Gibbons, P. C., and Buhro, W. E. (2008). Size-and shape-controlled synthesis of bismuth nanoparticles. *Chemistry of Materials*, 20(11):3656–3662.

[Wang et al., 2010] Wang, H., He, Y., Chen, W., Zeng, Y. W., Stahl, K., Kikegawa, T., and Jiang, J. Z. (2010). High-pressure behavior of beta-Ga_2O_3 nanocrystals. *Journal of Applied Physics*, 107(3):033520.

[Wang et al., 2007] Wang, H., Liu, J. F., Wang, Y., Chen, W., Jiang, J. Z., Olsen, J. S., and Gerward, L. (2007). High-pressure structural behaviour of nanocrystalline Ge. *Journal of Physics: Condensed Matter*, 19(15):156217.

[Wang et al., 2004] Wang, J. W., Wang, X., Peng, C., and Li, Y. D. (2004). Synthesis and characterization of bismuth single-crystalline nanowires and nanospheres. *Inorganic Chemistry*, 43(23):7552–7556.

[Wang et al., 2006] Wang, W. Z., Poudel, B., Ma, Y., and Ren, Z. F. (2006). Shape control of single crystalline bismuth nanostructures. *Journal of Physical Chemistry B*, 110(51):25702–25706.

[Wang and Kim, 2008] Wang, Y. and Kim, K. (2008). Large-scale polyol synthesis of single-crystal bismuth nanowires and the role of NaOH in the synthesis process. *Nanotechnology*, 19:265303.

[Wang and Xia, 2004] Wang, Y. and Xia, Y. (2004). Bottom-up and top-down approaches to the synthesis of monodispersed spherical colloids of low melting-point metals. *Nano Letters*, 4(10):2047–2050.

[Wang et al., 2005] Wang, Y. W., Hong, B. H., and Kim, K. S. (2005). Size control of semimetal bismuth nanoparticles and the UV-visible and IR absorption spectra. *Journal of Physical Chemistry B*, 109(15):7067–7072.

[Website, 2009] Diamond Website. (2009). Components of the synchrotron machine http://www.diamond.ac.uk/Home/Technology/Components.html.

[Weck et al., 2002] Weck, G., Loubeyre, P., and LeToullec, R. (2002). Observation of structural transformations in metal oxygen. *Physical Review Letters*, 88(3):035504.

[Weir et al., 1959] Weir, C. E., Lippincott, E. R., Valkenburg, A. V., and Bunting, E. N. (1959). Infrared Studies in the 1- to 15-micron region to 30,000 atmospheres. *Journal of Research of the National Bureau of Standards. Section A*, 63(55-62).

[Wiley et al., 2004] Wiley, B., Herricks, T., Sun, Y., and Xia, Y. (2004). Polyol synthesis of silver nanoparticles: use of chloride and oxygen to promote the

formation of single-crystal, truncated cubes and tetrahedrons. *Nano Letters*, 4(9):1733–1739.

[Yamamoto and Hori, 2006] Yamamoto, Y. and Hori, H. (2006). Direct observation of the ferromagnetic spin polarization in gold nanoparticles: A review. *Reviews on Advanced Materials Science*, 12:23–32.

[Yamanaka et al., 2001] Yamanaka, T., Fukuda, T., Hattori, T., and Sumiya, H. (2001). New diamond anvil cell for single-crystal analysis. *Review of Scientific Instruments*, 72(2):1458–1462.

[Yarema et al., 2010] Yarema, M., Kovalenko, M. V., Hesser, G., Talapin, D. V., and Heiss, W. (2010). Highly monodisperse bismuth nanoparticles and their three-dimensional superlattices. *Journal of the American Chemical Society*, 132(43):15158–15159.

[Yu et al., 2003] Yu, W. W., Wang, Y. A., and Peng, X. (2003). Formation and stability of size-, shape-, and structure-controlled CdTe nanocrystals: Ligand effects on monomers and nanocrystals. *Chemistry of Materials*, 15(22):4300–4308.

[Zhang and Maginn, 2012] Zhang, Y. and Maginn, E. J. (2012). A comparison of methods for melting point calculation using molecular dynamics simulations. *Journal of Chemical Physics*, 136(14):144116.

[Zhao et al., 1991] Zhao, X. S., Schroeder, J., Persans, P. D., and Bilodeau, T. G. (1991). Resonant-raman-scattering and photoluminescence studies in glass-composite and colloidal CdS. *Physical Review B*, 43(15):12580.

High Pressure Research
Vol. 32, No. 3, September 2012, 442–449

Taylor & Francis
Taylor & Francis Group

High-pressure, high-temperature single-crystal study of Bi-IV

Wanaruk Chaimayo[a]*, Lars F. Lundegaard[a], Ingo Loa[a], Graham W. Stinton[a], Alistair R. Lennie[b] and Malcolm I. McMahon[a]

[a]*SUPA, School of Physics and Astronomy, and Centre for Science at Extreme Conditions, The University of Edinburgh, Mayfield Road, Edinburgh, EH9 3JZ, UK;* [b]*Daresbury Laboratory, Daresbury, Warrington WA4 4AD, UK*

(*Received 4 July 2012; final version received 15 August 2012*)

Bi-IV is the stable high-pressure, high-temperature phase of bismuth at ∼4 GPa and ∼500 K. It was first identified in 1958, but its structure has remained uncertain. An X-ray powder-diffraction study of Bi-IV reported the structure as monoclinic, but a subsequent reinterpretation of the same data concluded that the structure was *C*-centred orthorhombic (*oC*16), with the same atomic arrangement as in Cs-V and Si-VI. To resolve the uncertainty over the structure of Bi-IV, we investigated this phase at 3.2 GPa and 465 K by single-crystal synchrotron X-ray diffraction. All of the observed reflections could be indexed on the orthorhombic *oC*16 structure proposed by Degtyareva, with $a = 11.191(5)$ Å, $b = 6.622(1)$ Å and $c = 6.608(1)$ Å. The spacegroup was confirmed as *Cmce*. Refinement of the data resulted in an excellent fit ($R = 2.8\%$), and gave atomic coordinates very similar to those of the *oC*16 structures in Cs-V and Si-VI.

Keywords: bismuth; crystal structure; high-pressure; high temperature; X-ray diffraction

1. Introduction

Bismuth is the highest-atomic-number member of the group-15 elements, and its high-pressure, high-temperature behaviour has been studied for more than seven decades. The first investigation of the high-pressure phase transitions in Bi was made by Bridgman using shear-modulus and volume-discontinuity measurements [1,2]. He detected two clear transitions below 4 GPa and some evidence of a further transition at ∼4.3 GPa. Subsequent conductivity studies by Bridgman [3,4] and Bundy [5] showed that the Bi-I → Bi-II and Bi-II → Bi-III transitions at 2.5 and 2.7 GPa, respectively, are accompanied by sharp discontinuities in resistivity. These have been used subsequently as fixed points to calibrate high-pressure apparatuses [6]. Bridgman also identified further transitions at 4.5, 6.5 and 9 GPa from (small) volume discontinuities, but saw no accompanying changes in resistivity [4]. The lack of any such changes at these pressures was confirmed by Bundy [5], who saw only a single further transition at 12.5 GPa at room temperature.

However, Bundy identified another high-pressure, high-temperature phase above 450 K at 4 GPa [5], and this was subsequently confirmed by Klement et al. [7]. Since then, there have been

*Corresponding author. Email: wanaruk.chaimayo@ed.ac.uk

ISSN 0895-7959 print/ISSN 1477-2299 online

http://dx.doi.org/10.1080/08957959.2012.722214
http://www.tandfonline.com

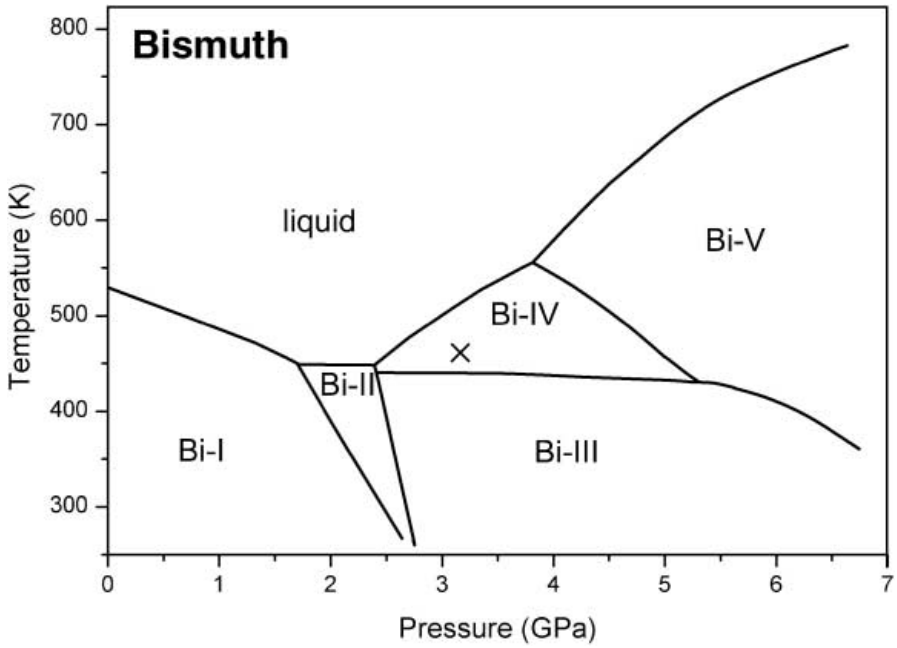

Figure 1. Phase diagram of bismuth adapted from [7]. The cross shows the *P–T* conditions at which the present single-crystal diffraction study was performed. Note that conflicting phase naming schemes have been used in the literature. In particular, Bi-IV has been denoted as Bi-VII in some of the earlier work.

numerous studies of Bi at high-pressures and temperatures [8, and references therein], and the presently accepted phase diagram and naming of the phases is as shown in Figure 1.

At ambient conditions, Bi-I has the rhombohedral As-type structure with two atoms per unit cell [8]. Bi-I transforms at 2.55 GPa and 298 K to Bi-II, which has a *C*-centred monoclinic structure with four atoms per unit cell [9]. On further compression, Bi-II transforms at 2.70 GPa to Bi-III [8], which was shown to have an incommensurate host–guest structure comprising a body-centred-tetragonal (bct) 'host' structure and an interpenetrating bct 'guest' component that is incommensurate with the host along their common *c*-axis [10,11]. The identification of Bi-III as incommensurate resolved a long-standing disagreement about the density of this phase [10]. At higher pressures, Bi-III transforms to a body-centred cubic (bcc) structure, Bi-V, at 7.7 GPa at 298 K [12], and this phase is stable to at least 220 GPa [13], the highest pressure to which Bi has been studied.

The phase Bi-IV has, in contrast to the room-temperature phases, attracted little attention. It was first assumed to be bcc by Klement et al. [7] by analogy with the phase diagram of thallium. The first diffraction study of Bi-IV was made by Fedotov et al. [14] at 2.85 GPa and 483 K using neutron diffraction. Most of their experiments were performed on powder samples, but they noted that a single-crystal of Bi-IV can be obtained by annealing close to the melting line, and some additional information was obtained from single-crystal diffraction. Fedotov et al. concluded that the Bi-IV structure was tetragonal, but there are a number of discrepancies between the observed and calculated peak positions [14].

Bi-IV remained unstudied for almost two decades, until Chen et al. [15] attempted to determine its structure by using the high-intensity X-ray beam from a synchrotron in order to overcome problems due to sample absorption. They identified 48 reflections which they indexed on a monoclinic unit cell containing 8 atoms with $a = 6.468(5)$ Å, $b = 6.578(5)$ Å, $c = 6.468(5)$ Å and $\beta = 118.88(6)^\circ$ at 3.9 GPa and 503 K.

Soon afterwards, and aided by the structure solutions of Cs-V [16] and Si-VI [17], Degtyareva [18] and Degtyareva et al. [19] reinterpreted the Bi-IV powder diffraction patterns of Chen et al. [15] as being from an orthorhombic *oC*16-*Cmce*[1] crystal structure, isostructural with Cs-V and

Si-VI. The pseudo-tetragonal *oC*16 structure of Degtyareva and the monoclinic structure of Chen et al. are very closely related [18].

Perhaps surprisingly, there has been no subsequent experimental re-examination of the structure of Bi-IV to confirm whether or not it is isostructural with Cs-V and Si-VI. This is almost certainly due to the difficulties in conducting powder X-ray diffraction experiments under high-pressure and high-temperature conditions, and the propensity of Bi powders to recrystallise even at room temperature [10,12]. While single-crystal X-ray diffraction techniques would seem the ideal method to study Bi-IV, the use of such techniques has many problems. First, the absorption of Bi is too high to study it at the wavelength (0.71 Å) available from standard X-ray tubes on in-house single-crystal diffractometers. Second, it is necessary to maintain constant pressure–temperature conditions during the full data collection period, which might be many hours. And, third, the standard beryllium plates that have been used for a long time to support the diamond anvils in pressure cells for single-crystal X-ray diffraction are weakened at high temperatures, and can also cause a strong, structured background.

These problems can all be overcome by using high-energy radiation from a synchrotron to decrease the sample absorption and the data collection time, and by using Boehler–Almax [20] seats for the diamond anvils to provide increased strength and maintain anvil alignment at high temperatures while simultaneously reducing the background [21]. Using such techniques, we have recently collected data from a single-crystal of oxygen at 15.9 GPa and 625 K [22]. In this paper, we describe the use of these single-crystal techniques to determine the detailed structure of Bi-IV at 3.2 GPa and 465 K.

2. Description of the experiment

Single-crystal X-ray diffraction data were collected on beamline 9.5 HPT at the Synchrotron Radiation Source (SRS) Daresbury Laboratory using a mar345 image plate detector and a wavelength of 0.44397 Å. The incident beam size was $30 \times 40\,\mu m^2$, and the Bi sample was material of 99.999% purity obtained from the Institute of Rare Metals, Russia. The sample was loaded without any pressure transmitting medium into a 180 μm diameter hole in a rhenium gasket in a Merrill–Bassett-type [23] diamond-anvil cell. The pressure cell was equipped with Boehler–Almax-type seats and diamond anvils, which provided a conical aperture (full angle) of 76°. A small piece of ruby was enclosed with the bismuth for pressure measurement via the ruby fluorescence technique [24], employing the temperature correction from [25]. The sample temperature was regulated by heating the entire pressure cell using an external heater.

The heater reduced the X-ray aperture on the incident beam side of the pressure cell to ±28°, and the use of a water-cooled cell base ensured that the alignment of the sample was unchanged during the 8 h data collection. The temperature of the sample was determined by a K-type thermocouple placed in contact with the rear of one of the diamond anvils.

An initial crystal of Bi-IV was grown by first melting a powdered sample of Bi-I at 1.3 GPa and 500 K, and then compressing the liquid into the stability region of Bi-IV at 3.8 GPa. This initial crystal was not entirely suitable for data collection, and a much higher quality crystal was obtained via heating–cooling cycles to and from the melt at 3.2 GPa. The diffraction pattern from the resulting high-quality crystal obtained at 3.2 GPa and 465 K is shown in Figure 2. The high quality of the crystal, combined with the intensity of the synchrotron X-ray beam and the strong scattering power of bismuth, meant that great care needed to be taken to ensure that sample reflections were not saturated. An exposure time of 10 s/frame and a 29 mm thick aluminium attenuator ensured that the reflections were not saturated. X-ray diffraction data from the Bi-IV crystal were collected in a sequence of contiguous ±0.25° oscillations over a total scan range of 50° around the vertical axis.

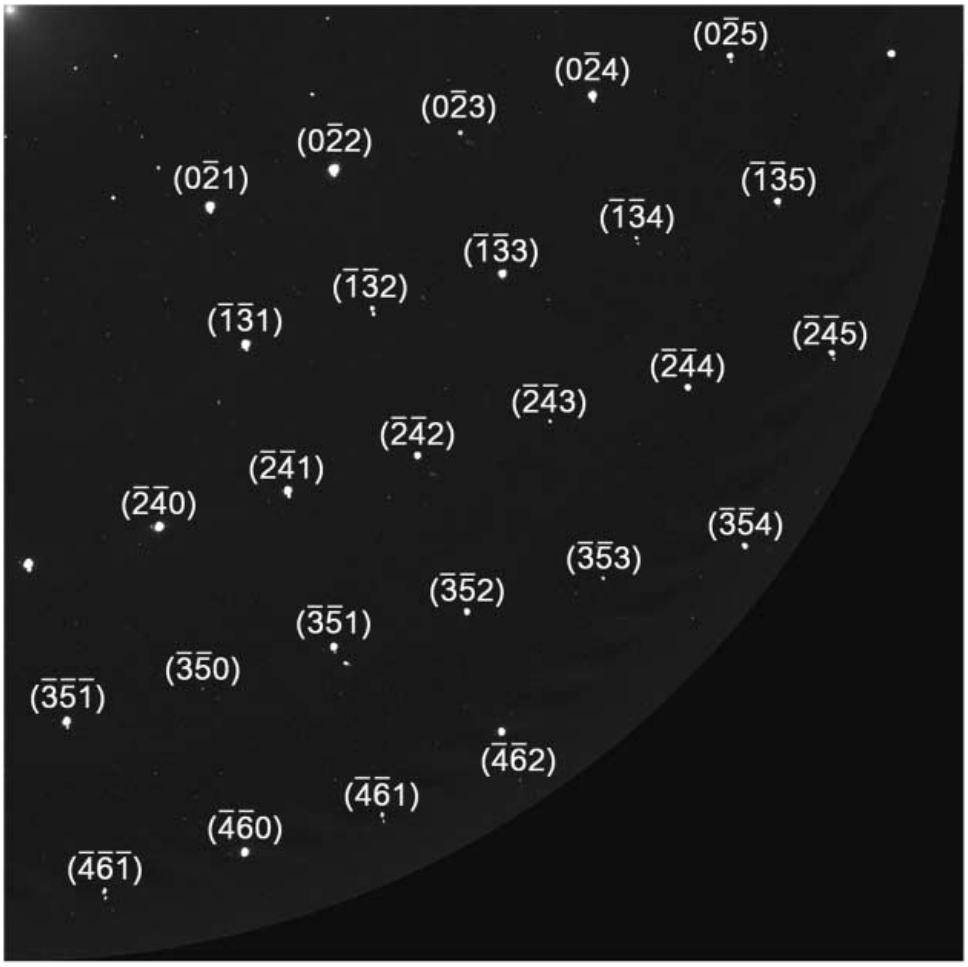

Figure 2. One quadrant of a composite image of 46 superimposed mar345 images selected from the overall 50° scan range to show representative data. Twenty-six observed reflections are indexed. The weak reflections in close proximity to some of the main reflections are from a second, much smaller crystal with a different orientation.

3. Results

The unit cell and orientation matrix of the crystal were determined from the positions of 159 reflections, and revealed Bi-IV to be orthorhombic with lattice parameters $a = 11.191(5)$ Å, $b = 6.622(1)$ Å and $c = 6.608(1)$ Å at 3.2 GPa and 465 K. Density considerations showed that there are 16 atoms per unit cell. With the exception of some very weak spots – which a later analysis showed to come from a second, much smaller crystal of Bi-IV with a different orientation – all of the observed reflections were accounted for by this orthorhombic unit cell.

The intensities of all accessible reflections to a minimum d-spacing of 0.75 Å were integrated using the SAINT+ program [26], and were corrected for decay of the intensity of the X-ray beam, changes in the illuminated sample volume, and absorption by the diamond anvils. No correction was made for the absorption of the sample. A total of 159 individual reflections were observable and analysis of the systematic absences showed them to be consistent with space groups $C2ce$ and $Cmce$. Averaging of symmetry-equivalent reflections gave 65 independent reflections with a good internal agreement between symmetry equivalent reflections, $R_{\rm sym}(F^2)$, of 5.3%.

The structure of Bi-IV was solved initially in the space group $Cmce$ by direct methods using the SIR92 software package [27]. This revealed the structure to comprise atoms on the 8d and 8f Wyckoff sites at $(x, 0, 0)$ and $(0, y, z)$, respectively, with $x = 0.21$, $y = 0.17$ and $z = 0.32$ at 3.2 GPa and 465 K. Subsequent least-squares refinement using SHELX [28], including two sets of anisotropic atomic displacement parameters, converged immediately to give an excellent fit,

Table 1. The refined structural parameters of Bi-IV at 3.2 GPa and 465 K in spacegroup *Cmce*.

	Site	*x*	*y*	*z*
Bi1	8*d*	0.2139(3)	0	0
Bi2	8*f*	0	0.1743(2)	0.3240(2)

Note: The refined lattice parameters are $a = 11.191(5)$ Å, $b = 6.622(1)$ Å and $c = 6.608(1)$ Å.

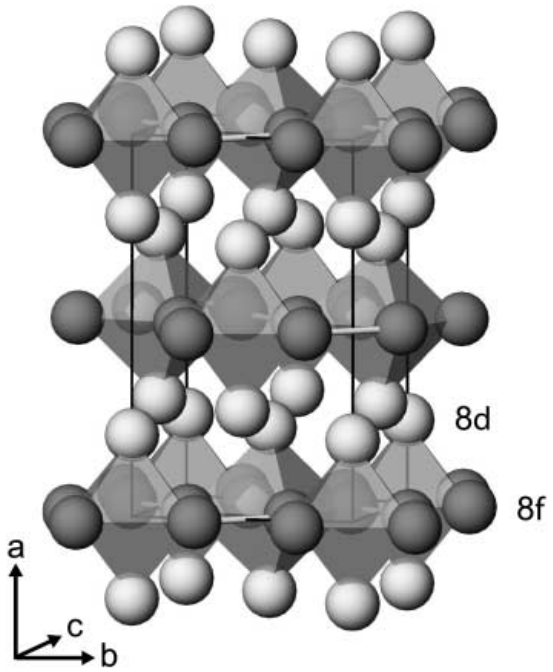

Figure 3. Perspective view of the Bi-IV crystal structure. The atoms on the 8*f* sites (shaded dark grey) form flat atomic layers, while the atoms on the 8*d* sites (shaded light grey) form buckled layers. The octahedra highlight the spatial arrangement of the atoms.

with an *R*-factor of $R_1(F > 4\sigma(F)) = 2.8\%$ and a goodness of fit of 1.20. The largest residual density in the Fourier difference map was $0.99\,e^-/Å^3$. Refinements in the lower-symmetry *C*2*ce* symmetry increased the number of refined parameters from 12 to 20, and showed all atoms to refine to within 1σ of the positions they would occupy in space group *Cmce*. The final refined structural parameters in space group *Cmce* are given in Table 1, and the refined structure is shown in Figure 3.

4. Discussion

As suggested by Degtyareva [18], Bi-IV has the same *oC*16 structure observed in other elements at high-pressure, Cs-V [16], Rb-VI [29], Si-VI [17], Ge [30] and, most recently, in K above 96 GPa [31]. There would thus seem to be close links between the high-pressure structural behaviour of the group 1 alkali metals Cs, Rb and K, the group 14 elements Si and Ge and the group 15 element Bi. Other structural similarities are also observed, particularly the incommensurate host–guest phases, which are observed in the alkali metals Na, K and Rb [32–34] and the group 15 elements As, Sb and Bi [10,35–37]. However, such structures have not been observed, at least not yet, in Si and Ge.

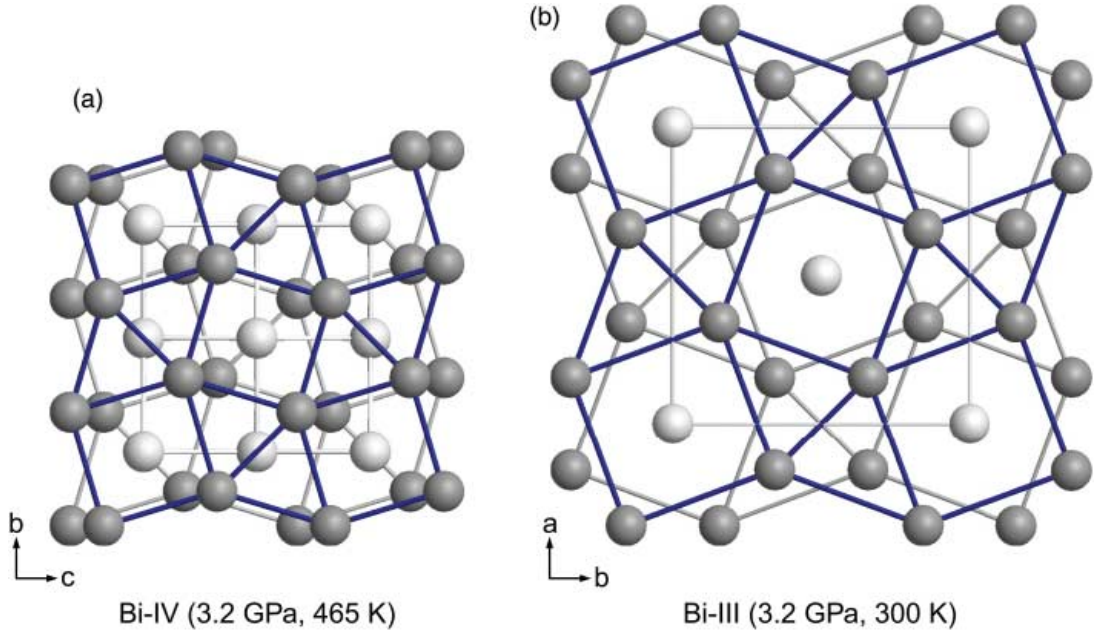

Figure 4. (a) The Bi-IV structure at 3.2 GPa seen looking down the *a*-axis, and (b) the Bi-III structure at the same pressure seen looking down the *c*-axis. The two structures are drawn to the same scale. In (a) the 8*f* atoms that comprise the flat 3^2434 nets are shaded dark grey, while the 8*d* atoms that comprise the buckled 4^4 nets are shaded light grey. In Bi-III, the host/guest atoms are shaded dark/light grey, respectively. Note that, contrary to what these particular projections suggest, the Bi-IV structure is less dense than Bi-III: In Bi-IV, the flat 8*f* layers alternate with the buckled 8*d* layers (Figure 3), whereas Bi-III has a dense stacking of the flat layers with guest atoms in the voids of the dense framework.

A perspective view of the *oC*16 structure is shown in Figure 3, which highlights the spatial arrangement of the atoms in terms of octahedral groups. The structure can be regarded both as a distorted face-centred cubic superstructure [16] and as a layered structure comprising flat planes of 8*f* atoms and buckled layers of 8*d* atoms. The former layers can be regarded as arrangements of triangles and squares (3^2434 nets) as shown in Figure 4(a), which depicts the structure viewed down the long *a*-axis. The shortest interatomic distance in Bi-IV, of 3.277 Å at 3.2 GPa and 465 K, is in this layer of atoms. Between these 3^2434 layers, the 8*d* atoms are arranged in buckled 4^4 nets which, because of the similarity of the *b* and *c* lattice parameters, are almost square.

Degtyareva [18] noted that the same nets are found in the host–guest composite structures: the host atoms are arranged in 3^2434 nets, while the guest atoms are arranged in 4^4 nets. Since her report, the structure of Bi-III has also been shown to be a host–guest composite structure [10], and the structures of Bi-III and Bi-IV are thus closely related.

The close similarity is shown in Figure 4, where the different nets of the two structures are highlighted. The 3^2434 nets in the two structures are clearly very similar, but their dimensions and relative alignment are different. In Bi-IV at 3.2 GPa and 465 K, the squares in the 3^2434 nets have sides of length 3.45 Å, while in Bi-III at the same pressure[2] the sides are some 34% longer at 4.62 Å. And the centres of the squares in the 3^2434 nets are aligned above each other in the Bi-III structure (forming the octagonal channels in which the 1D chains of guest atoms lie), whereas the squares are offset by $c/2$ in the Bi-IV structure. Finally, the flat 3^2434 layers of 8*f* atoms alternate with the buckled 4^4 layers of 8*d* atoms in Bi-IV (Figure 3), whereas Bi-III has a dense stacking of the flat 3^2434 layers with the guest atoms in the voids of the dense framework. The distance between the flat 3^2434 nets is therefore only 2.116 Å in Bi-III in contrast to 5.596 Å in Bi-IV.

The transition from the Bi-IV to the Bi-III structure thus involves a translation of half of the 8*f*-atom planes along the *c*-axis, along with half of the 8*d* atoms. The sides of the squares in the 8*f*-atom layers then expand by a third in order to accommodate the chains of guest atoms now running through the centres, while the spacing between the 8*f*-atom layers decreases by over a factor of two.

The close relationship between the structures of Bi-III and Bi-IV, and the ease of the temperature-induced transition between them, raises the possibility of transitions between these structures in other elements. As said, the alkali metals K and Rb have both high-pressure host–guest and *oC*16 phases. However, in both cases, the host structure has 16 atoms per unit cell, rather than the 8-atom variant found in As, Sb, Bi and Sc. Further examples of Bi-III to Bi-IV transitions are thus more likely to be found in this latter group of elements, perhaps at high temperatures, where little is known of the phase behaviour of these materials at the relevant pressures.

5. Conclusion

The long-uncertain structure of Bi-IV has been determined *in situ* at 3.2 GPa and 465 K using single-crystal X-ray diffraction techniques. As suggested by Degtyareva [18], the structure is orthorhombic (pseudo-tetragonal), with spacegroup *Cmce*, and is isostructural with Cs-V and Si-VI. The structural motifs of Bi-IV – the 3^2434 and 4^4 nets – are very similar to those found in the host–guest Bi-III structure.

Acknowledgements

This work is supported by research grants and a fellowship (I.L.) from the UK Engineering and Physical Sciences Research Council, and facilities were made available by the SRS, Daresbury Laboratory.

Notes

1. The double glide plane in spacegroup number 64 is now conventionally denoted with the symbol '*e*'. As a result, the spacegroup symbol has been changed from *Cmca* to *Cmce*.
2. The structure of Bi-III at 3.2 GPa and 300 K was obtained from interpolating the structural parameters given by Degtyareva et al. [37]. The structural parameters are: $a_H = 8.660$ Å, $c_H = 4.233$ Å, $c_G = 3.230$ Å, and $x = 0.157$.

References

[1] P.W. Bridgman, *Effects of high shearing stress combined with high hydrostatic pressure*, Phys. Rev. 48 (1935), pp. 825–847.
[2] P.W. Bridgman, *Polymorphism, principally of the elements, up to 50,000 kg/cm^2*, Phys. Rev. B 48 (1935), pp. 893–906.
[3] P.W. Bridgman, *The resistance of nineteen metals to 30,000 kg/cm^2*, Proc. Am. Ac. Arts Sci. 72 (1938), pp. 157–205.
[4] P.W. Bridgman, *The resistance of 72 elements, alloys and compounds to 100,000 kg/cm^2*, Proc. Am. Ac. Arts Sci. 81 (1952), pp. 165–251.
[5] F.P. Bundy, *Phase diagram of bismuth to 130,000 kg/cm^2, 500°C*, Phys. Rev. 110 (1958), pp. 314–318.
[6] D. Decker, W. Bassett, L. Merrill, H. Hall, and J. Barnett, *High-pressure calibration: A critical review*, J. Phys. Chem. Ref. Data 1 (1972), pp. 773–836.
[7] W. Klement, G.C. Kennedy, and A. Jayaraman, *Phase diagrams of arsenic, antimony, and bismuth at pressures up to 70 kbars*, Phys. Rev. 131 (1963), pp. 632–637.
[8] E.Y. Tonkov and E.G. Ponyatovsky, *Phase transformations of elements under high pressure*, Advances in Metallic Alloys, Vol. 4, CRC Press, 2005.
[9] R. Brugger, R. Bennion, and T. Worlton, *The crystal structure of bismuth-II at 26 kbar*, Phys. Lett. A 24 (1967), pp. 714–717.
[10] M.I. McMahon, O. Degtyareva, and R.J. Nelmes, *Ba-IV-type incommensurate crystal structure in group-V metals*, Phys. Rev. Lett. 85 (2000), pp. 4896–4899.
[11] M.I. McMahon, O. Degtyareva, and R.J. Nelmes, *Incommensurate modulations of Bi-III and Sb-II*, Phys. Rev. B 75 (2007), p. 184114.
[12] K. Aoki, S. Fujiwara, and M. Kusakabe, *Stability of the bcc structure of bismuth at high pressure*, J. Phys. Soc. Jpn. 51 (1982), pp. 3826–3830.
[13] Y. Akahama, H. Kawamura, and A.K. Singh, *The equation of state of Bi and cross-checking of Au and Pt scales to megabar pressure*, J. Phys., Condens. Matter 14 (2002), pp. 11495–11500.

[14] V.K. Fedotov, E.G. Ponyatovskiĭ, V.A. Somenkov, and S.S. Shil'shteĭn, *Neutron-diffraction investigation of the polymorphism of bismuth at pressures up to 30 kbar*, Fiz. Tverd. Tela 20 (1978), pp. 1088–1096.
[15] J.H. Chen, H. Iwasaki, and T. Kikegawa, *Structural study of the high-pressure—high-temperature phase of bismuth using high energy synchrotron radiation*, J. Phys. Chem. Solids 58 (1997), pp. 247–255.
[16] U. Schwarz, K. Takemura, M. Hanfland, and K. Syassen, *Crystal structure of cesium-V*, Phys. Rev. Lett. 81 (1998), pp. 2711–2714.
[17] M. Hanfland, U. Schwarz, K. Syassen, and K. Takemura, *Crystal structure of the high-pressure phase silicon VI*, Phys. Rev. Lett. 82 (1999), pp. 1197–1200.
[18] V.F. Degtyareva, *Crystal structure of a high-pressure phase in Bi-based alloys related to Si-VI*, Phys. Rev. B 62 (2000), pp. 9–12.
[19] V.F. Degtyareva, O. Degtyareva, and D.R. Allan, *Ordered Si-VI-type crystal structure in BiSn alloy under high pressure*, Phys. Rev. B 67 (2003), p. 212105.
[20] R. Boehler and K.D. Hantsetters, *New anvil designs in diamond-cells*, High Press. Res. 24 (2004), pp. 391–396.
[21] S.A. Moggach, D.R. Allan, S. Parsons, and J.E. Warren, *Incorporation of a new design of backing seat and anvil in a Merrill–Bassett diamond anvil cell*, J. Appl. Crystallogr. 41 (2008), pp. 249–251.
[22] L.F. Lundegaard, C.L. Guillaume, M.I. McMahon, E. Gregoryanz, and M. Merlini, *On the structure of high-pressure high-temperature η-O_2*, J. Chem. Phys. 130 (2009), p. 164516.
[23] L. Merrill and W.A. Bassett, *Miniature diamond anvil pressure cell for single crystal x-ray diffraction studies*, Rev. Sci. Instrum. 45 (1974), pp. 290–294.
[24] H.K. Mao, J. Xu, and P.M. Bell, *Calibration of the ruby pressure gauge to 800 kbar under quasi-hydrostatic conditions*, J. Geophys. Res. 91 (1986), pp. 4673–4676.
[25] D.E. McCumber and M.D. Sturge, *Linewidth and temperature shift of the R lines in ruby*, J. Appl. Phys. 34 (1963), pp. 1682–1684.
[26] *SMART, SAINT, ASTRO and XPREP, Data Collection and Processing Software for the SMART System*, (1995), Bruker AXS Inc., Madison, Wisconsin, USA.
[27] A. Altomare, G. Cascarano, C. Giacovazzo, and A. Guagliardi, *Completion and refinement of crystal structures with SIR92*, J. Appl. Crystallogr. 26 (1993), pp. 343–350.
[28] G.M. Sheldrick, *A short history of SHELX*, Acta. Crystallogr. A 64 (2008), pp. 112–122.
[29] U. Schwarz, K. Syassen, A. Grzechnik, and M. Hanfland, *The crystal structure of rubidium-VI near 50 GPa*, Solid State Commun. 112 (1999), pp. 319–322.
[30] K. Takemura, U. Schwarz, K. Syassen, M. Hanfland, N. Christensen, D. Novikov, and I. Loa, *High-pressure Cmca and hcp phases of germanium*, Phys. Rev. B 62 (2000), pp. R10603–R10606.
[31] L.F. Lundegaard, M. Marqués, G. Stinton, G.J. Ackland, R.J. Nelmes, and M.I. McMahon, *Observation of the oP8 crystal structure in potassium at high pressure*, Phys. Rev. B 80 (2009), p. 020101.
[32] L.F. Lundegaard, E. Gregoryanz, M.I. McMahon, C.L. Guillaume, I. Loa, and R.J. Nelmes, *Single-crystal studies of incommensurate Na to 1.5 Mbar*, Phys. Rev. B 79 (2009), p. 064105.
[33] M.I. McMahon, R.J. Nelmes, U. Schwarz, and K. Syassen, *Composite incommensurate K-III and a commensurate form: Study of a high-pressure phase of potassium*, Phys. Rev. B 74 (2006), p. 140102.
[34] M.I. McMahon, S. Rekhi, and R.J. Nelmes, *Pressure dependent incommensuration in Rb-IV*, Phys. Rev. B 87 (2001), p. 55501.
[35] U. Schwarz, L. Akselrud, H. Rosner, A. Ormeci, Y. Grin, and M. Hanfland, *Structure and stability of the modulated phase Sb-II*, Phys. Rev. B 67 (2003), p. 214101.
[36] O. Degtyareva, M.I. McMahon, and R.J. Nelmes, *Pressure-induced incommensurate-to-incommensurate phase transition in antimony*, Phys. Rev. B 70 (2004), p. 184119.
[37] O. Degtyareva, M.I. McMahon, and R.J. Nelmes, *High-pressure structural studies of group-15 elements*, High Press. Res. 24 (2004), pp. 319–356.

Modern Physics Letters B, Vol. 25, No. 31 (2011) 2399–2405

DOI: 10.1142/S0217984911027698

EFFECT OF NANO PARTICLE SIZES ON HIGH PRESSURE RAMAN SCATTERING IN NANOCRYSTALLINE CERIUM DIOXIDE

P. JIMLIM and T. BOVORNRATANARAKS*

Department of Physics, Faculty of Science, Chulalongkorn University, Bangkok 10330, Thailand
ThEP Center, CHE, 328 Si Ayutthaya Road, Ratchathewi, Bangkok 10400, Thailand
** thiti.b@chula.ac.th*

W. CHAIMAYO

SUPA, School of Physics and Astronomy, and Centre for Science at Extreme Conditions, University of Edinburgh, Mayfield Road, Edinburgh, EH9 3JZ, United Kingdom

S. PRATONTEP

KMITL College of Nanotechnology, King Mongkut's Institute of Technology Ladkrabang, Chalongkrung Road, Ladkrabang, Bangkok 10520, Thailand
kpsirapa@kmitl.ac.th

Received 21 December 2009

Nanocrystalline CeO_2 with different particle sizes has been studied under high pressure using Raman spectroscopy techniques and diamond anvil cell at room temperature. The pressure shift of the first-order Raman frequency for each particle sizes was measured. Linear dependence of the first order Raman frequency on pressure for each particle sizes has been observed. We found that the first order Raman frequency decreases with the decreasing particle sizes under ambient condition and the lattice constant increases with the decreasing particle size. The increasing molar fraction of oxygen vacancies with the decreasing particle size is responsible for the lattice expansion.

Keywords: Nanocrystalline; Raman scattering; cerium dioxide; high pressure.

1. Introduction

Cerium dioxide (CeO_2) has been extensively studied by scientist of various disciplines because of its multifold industry applications. It has potentially used in automotive three-way catalytic converters,[1] catalytic oxidation reactions,[2] solid oxide fuel cell electrolyte material,[3] gas sensors,[4] optical coatings,[5] sunscreen cosmetics,[6] insulating layer on silicon substrates,[7] and high storage capacitor devices.[8] Kourouklis *et al.*[9] have reported Raman spectroscopy results of CeO_2

*Corresponding author.

under high pressure up to 35 GPa. They have found that the first order Raman peak shifts to higher frequency with the increasing pressure. From their report, structural phase transition from fluorite phase to the orthorhombic $PbCl_2$ at 31 GPa has been proposed, which has also been confirmed by high pressure X-ray studies.[10] Saxena *et al.*[11] have studied the high-pressure Raman spectroscopy on nanocrystalline CeO_2 up to 36 GPa. The first order Raman peaks is founded to be increase with an increasing pressure. They have also reported the transition pressure around 26.5 GPa, which is less than that reported for the bulk CeO_2 at 31 GPa. Therefore, the effect of nano particle size on the transition pressure is an important key to understand high-pressure phenomenon of the nano scale materials. In this study, we have investigated nanocrystalline CeO_2 under high pressure up to 30 GPa at room temperature by Raman scattering.

2. Experiments

The nanocrystallines CeO_2 used in this experiment were commercial nanosized CeO_2, with the average particle size 10.5 nm, 36.8 nm, 53.2 nm, and 533.3 nm (produced by Sigma-Aldrich and Nanostructured & Amorphous Materials, Inc.). They were identified as the cubic fluorite structure with spacegroup *Fm3m* using X-ray diffraction.

Pressure was generated using a Merrill–Bassett type diamond anvil cell.[12] Diamond anvils with a 300 μm culet were used in a gasketed diamond anvil cell. The gasket consisted of a tungsten 270 μm thick, preindented to 30 μm. The hole of diameter 150 μm was drilled on the gasket by electric discharge machine (EDM).[13] The sample chamber is the loaded with the nano-CeO_2 powder and a single crystal of ruby chip ($\sim$5–10 μm) and flooded with pressure transmitting medium. The pressure transmitting medium is a mixture of 4:1 methanol: ethanol. A tungsten gasket sheet is compressed between two diamond culets. High pressures are generated in the pressure cell by applying force to the diamond culets using screws to drive two beryllium supporting discs together.[14] Pressure measurement were carried out using ruby fluorescence techniques of R_1 line calibrated by Mao *et al.*[15] The Raman spectra were collected by the CCD equipped Raman microscope (RENISHAW). The Raman spectra of 250–700 cm^{-1} with a spectral resolution of 1.7 cm^{-1} were recorded by using the 514.5 nm line from an Ar-ion laser with an average power of 50 mW.

3. Results and Discussion

At ambient pressure, nanocrystalline CeO_2 sample was confirmed to have a cubic fluorite structure with spacegroup *Fm3m* using angle dispersive X-ray diffraction techniques. This structure possess one triply degenerate Raman active optical phonon (F_{2g}) and two infrared-active phonons which are correspond to the LO and TO modes. Therefore, the first order Raman spectrum of CeO_2 is consists of only one Raman line. For the second order Raman spectrum, there are peaks at

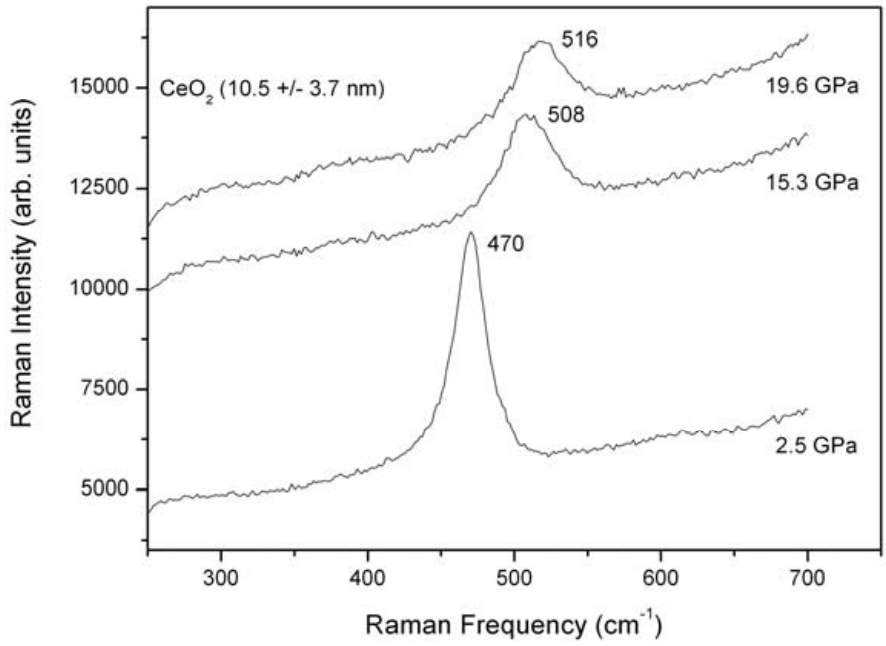

Fig. 1. The first order Raman peaks of CeO_2 (10.5 ± 3.7 nm) at three different pressures under room temperature. The Raman spectra were excited with the 514.5 nm line of an Ar-ion laser. (Integration time of 300 seconds.)

580, 660, 880, 1030, and 1160 cm^{-1} which are correspond to $\omega_{TO}(X)$ + LA(X), $\omega_R(X)$ + LA(X), $\omega_{LO} + \omega_{TO}$, $2\omega_R(X)$ and $2\omega_{LO}$, respectively.[9]

Figure 1 shows the Raman spectrum of nano-CeO_2 with the particle size 10.5 nm at three different pressures under room temperature. It shows the first order Raman peak (F_{2g}) shift to the higher frequency with the increasing pressure. The effect of pressure on the first order Raman spectra with different particle sizes are shown in Figs. 2 and 3. We observed that the frequency of the first order Raman peaks increases with increasing pressure which is in a good agreement with the linear fitting. This also caused by the pressure induced decrease of lattice constant. Additionally, we found that the first order Raman peak depend on the particle size under ambient condition as shown in Table 1. Figures 4 and 5 show the observed and calculated powder diffraction patterns of CeO_2 (10.5 nm and 53.2 nm) at ambient condition after the completion of the combined Rietveld refinement. When the particle size is decrease, the lattice constant increase (strain relative to the bulk) and the frequency of the first order Raman peak decrease. This is in good agreement with Zhang *et al.*,[16] as the lattice parameter increases with decreasing particle size when the particle size is smaller than 20 nm. The position of Raman peak was highly sensitive to the change in lattice parameters which also depend on particle size. If the uniform strain was assumed under hydrostatic pressure, the changes in lattice parameter can be calculated from $\Delta a/a_0 = -P/3B$ where P is pressure and B is the bulk modulus. If the changes in lattice parameter are taken into account, the shift of Raman peaks is given by

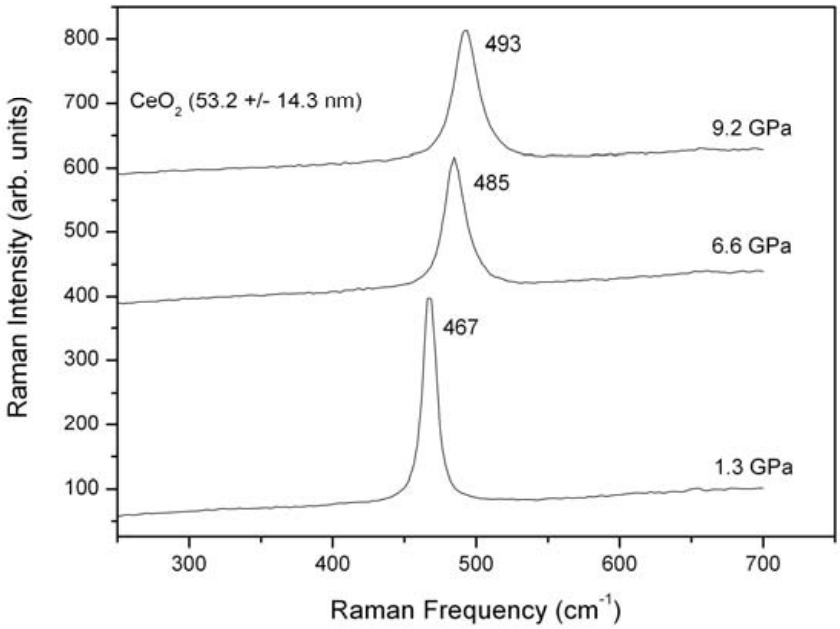

Fig. 2. The first order Raman peaks of CeO_2 (53.2 ± 14.3 nm) at three different pressures under room temperature. The Raman spectra were excited with the 632.8 nm line of an He–Ne laser. (Integration time of 80 seconds.)

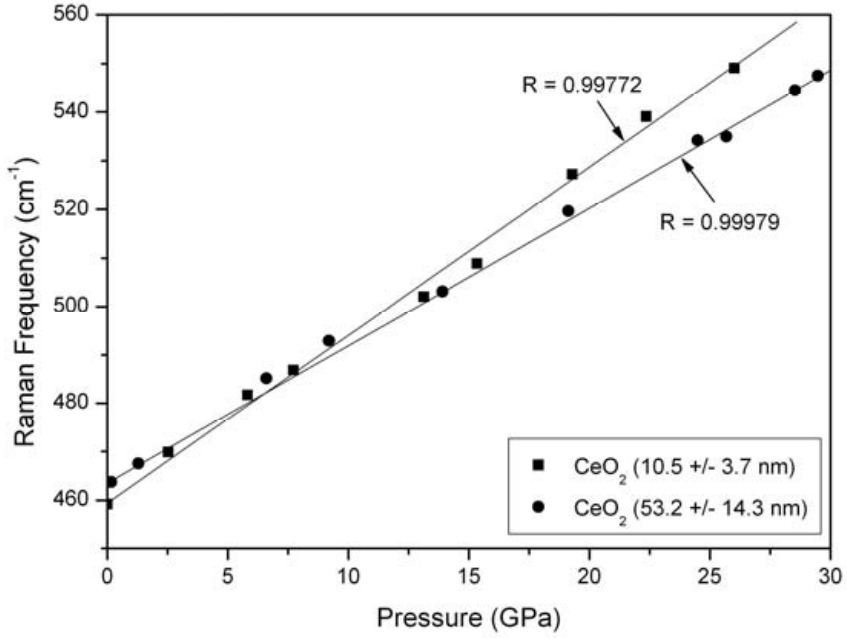

Fig. 3. The pressure dependence of the first order Raman peak in CeO_2 with particle size 10.5 nm and 53.2 nm at room temperature. R is the linear regression factor.

$\Delta\omega_i(q,x) = -3\gamma_i(q)\omega_i(q) \times [\Delta a/a_0]$, where ω_i is the phonon dispersion for the selected mode and $\gamma_i = -d\ln\omega_i/d\ln V = (B/\omega_i)(d\omega_i/dP)$.[18] This shift can be fully explained by the increasing lattice constant.[19]

Table 1. The first order Raman peak with difference particle sizes at ambient condition.

Average particle size	The first order Raman peak (cm^{-1})	Lattice constant (Å)	R_p	R_{wp}	R_{exp}
10.5 ± 3.7 nm[a]	460.62 ± 0.26[b]	5.43425(0)[c]	8.02%	11.23%	11.78%
36.8 ± 16.0 nm[a]	464.06 ± 0.03[b]	5.43159(5)[c]	7.82%	11.25%	11.34%
53.2 ± 14.3 nm[a]	464.01 ± 0.07[b]	5.43157(5)[c]	7.37%	10.79%	11.12%
533.3 ± 192.3 nm[a]	464.13 ± 0.01[b]	5.43053(5)[c]	8.23%	11.87%	10.89%
Bulk	465[d]	5.411[e]	—	—	—

[a]The average particle sizes were measured by using TEM.
[b]The first order Raman peak was obtained by fitting peaks with Pseudo-Voigtian function. They were collected by using Raman spectroscopy (NT-MDT, NTEGRA Spectra) at National Nanotechnology Center.
[c]X-ray diffraction patterns were collected by using X-ray diffractometer (Bruker, D8-Discover) at Scientific and Technological Research Equipment Centre. They were refined by using Rietveld Refinement.
[d]Reference 9.
[e]Reference 17.

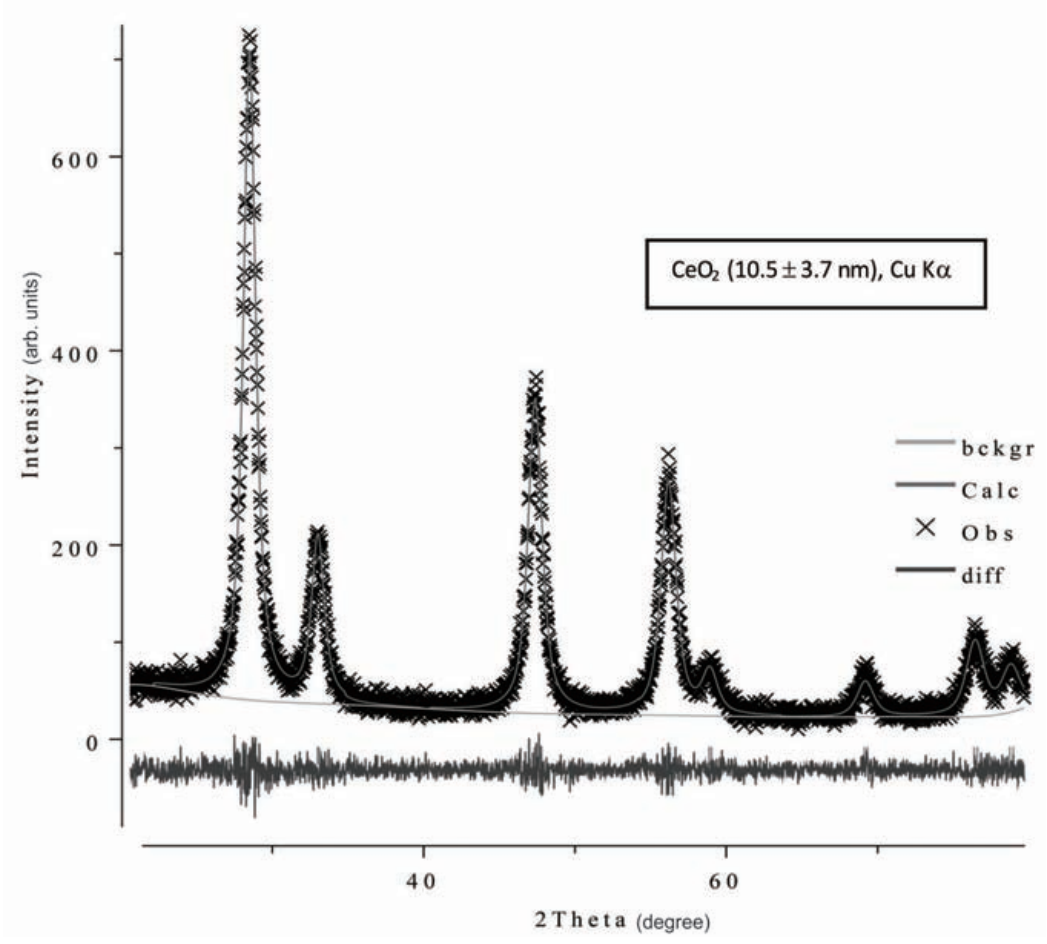

Fig. 4. The observed and calculated powder diffraction patterns of CeO_2 (10.5 ± 3.7 nm) after the completion of the combined Rietveld refinement. The data were collected from Bruker X-ray diffractometer in a step scan mode with a step $\Delta 2\theta = 0.02°$ at ambient condition.

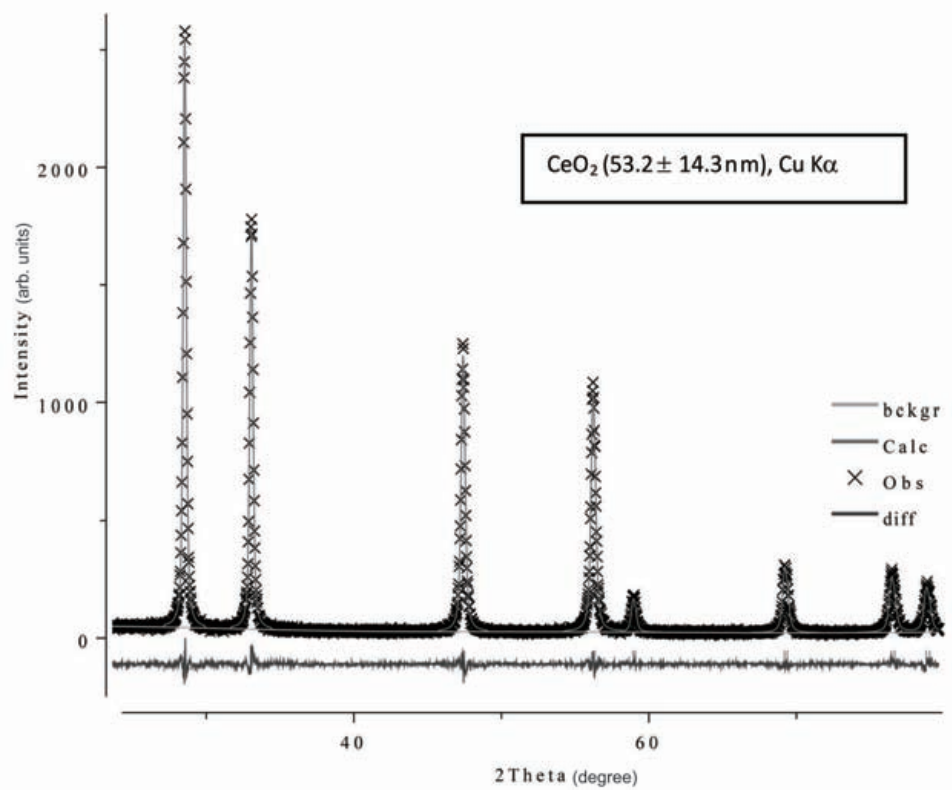

Fig. 5. The observed and calculated powder diffraction patterns of CeO_2 (53.2 ± 14.3 nm) after the completion of the combined Rietveld refinement. The data were collected from Bruker X-ray diffractometer in a step scan mode with a step $\Delta 2\theta = 0.02°$ at ambient condition.

The lattice expansion in small particles has been explained by Tsunekawa *et al.* and Zhou *et al.* Tsunekawa *et al.*[20] has investigated the influence of particle size on the Ce^{3+}/Ce^{4+} ratio in CeO_2 nanoparticles. In the report, the smaller the particle sizes, the more concentration of Ce^{3+} was presented. They explained this increase in terms of an associated reduction in the valence of the Ce^{4+} ions to Ce^{3+} ions caused by an increasing molar fraction of oxygen vacancy. Zhou *et al.*[21] has performed X-ray diffraction as well as TEM measurement and reported size-induced lattice relaxation in nanocrystalline CeO_2. The formation of oxygen vacancies and the associated Ce^{3+} is assumed to be the cause of lattice expansion with the decreasing particle size.

4. Conclusion

Effect of nano particle sizes on high pressure Raman scattering in nanocrystalline CeO_2 have been carefully investigated. The first order Raman frequency increases with increasing pressure. We found the first order Raman frequency decreases with decreasing particle size under ambient condition. The lattice constant increases with decreasing particle size. It is also caused by the decreasing particle size induced decrease of the first order Raman frequency. The increasing molar fraction of oxygen vacancies with the decreasing particle size is responsible for the lattice expansion.

Acknowledgments

The authors are grateful to the Office of the National Research Council of Thailand for financial support. X-ray diffraction facilities have been provided by Scientific and Technological Research Equipment Centre. Equipments have been developed under research grant supported by the National Synchrotron Light Research Institute (Public Organization). Raman Spectroscopy has been carried out at The National Nanotechnology Center and also at The Gem and Jewelry Institute of Thailand (Public Organization). T.B. acknowledges financial support from Thailand Research Fund contract number DBG5280002 and The Asahi Glass foundation. The authors acknowledge Dr. Wantana Klysubun, Dr. Valarak Saengsuwan, Mr. Komkilp Kotmool, and Mr. Rut Monotum for technical assistance.

References

1. E. Mamontov and T. Egami, *J. Phys. Chem. Solid* **61** (2000) 1345.
2. T. Tschope, J. Y. Ying and Y. M. Chiang, *Mater. Sci. Eng. A* **204** (1995) 267.
3. M. Mogensen, N. M. Sammes and G. A. Tompsett, *Solid State Ionics* **127** (2000) 63.
4. R. Bene, I. V. Perczel, F. Reti, F. A. Meyer, M. Fleisher and H. Meixner, *Sens. Actuator B* **71** (2000) 36; U. Lampe, J. Gerblinger and H. Meixner, *ibid.* **7** (1992) 787.
5. G. Haas, J. B. Ramsey and R. Thun, *J. Opt. Soc. Am.* **48** (1957) 324.
6. S. Yabe and T. Sato, *J. Solid. State. Chem.* **171** (2003) 7.
7. L. Tye and N. A. El-Masry, *Appl. Phys. Lett.* **65** (1994) 3081.
8. A. H. Morshed, M. Tomita, N. El-Masry, P. McLarty, N. P. Parikh and S. M. Bedair, in *Epitaxial Oxide Thin Films II*, eds. D. K. Fork, J. S. Speck, I. Shiosaki and R. M. Wolf, *Mater. Res. Soc. Symp. Proc.*, Vol. 401 (Material Research Society, Pittsburgh, 1996).
9. G. A. Kourouklis, A. Jayaraman and G. P. Espinosa, *Phys. Rev. B* **37** (1988) 4250.
10. S. J. Duclos, Y. K. Vohra, A. L. Ruoff, A. Jayaraman and G. P. Espinosa, *Phys. Rev. B* **38** (1988) 7755.
11. S. Rekhi and S. K. Saxena, *J. Appl. Phys.* **89** (2001) 2968.
12. A. Jayaraman, *Rev. Sci. Instrum.* **57** (1986) 1013.
13. H. E. Lorenzana, M. Bennahmias, H. Radousky and M. B. Kruger, *Rev. Sci. Instrum.* **65** (1994) 3540.
14. V. Saengsuwan, Postgraduate thesis, Chulalongkorn University, Bangkok, 2004.
15. H. K. Mao, P. M. Bell, J. Shaner and D. Steinberg, *J. Appl. Phys.* **49** (1978) 3276.
16. F. Zhang, S. Chan, J. E. Spanier, E. Apak, Q. Jin, R. D. Robinson and I. P. Herman, *Appl. Phys. Lett.* **80** (2002) 127.
17. Power Diffraction File, ed. W. F. McClune (JCPDS International Center for Diffraction Data, Swarthmore, PA, 1980).
18. W. H. Weber, K. C. Hass and J. R. McBride, *Phys. Rev. B* **48** (1993) 178.
19. J. E. Spanier, R. D. Robinson, F. Zhang, S.-W. Chan and I. P. Herman, *Phys. Rev. B* **64** (2001) 245407.
20. S. Tsunekawa, K. Ishikawa, Z.-Q. Li, Y. Kawazoe and A. Kasuya, *Phys. Rev. Lett.* **85** (2000) 3440.
21. X. D. Zhou and W. Huebner, *Appl. Phys. Lett.* **79** (2001) 3512.